

INTERNATIONAL DOCTORAL
SCHOOL OF THE USC

Alejandro
Carballosa Calleja

PhD Thesis

Emergent dynamics in complex networks: Synchronization, polarization and epidemics

Santiago de Compostela, 2023

Doctoral Programme in Materials Science

USC
UNIVERSIDADE
DE SANTIAGO
DE COMPOSTELA

ESCOLA DE DOUTORAMENTO
INTERNACIONAL DA USC

DOCTORAL THESIS

EMERGENT DYNAMICS IN COMPLEX NETWORKS: SYNCHRONIZATION, POLARIZATION AND EPIDEMICS

Alejandro Carballosa Calleja

Supervisor: Alberto Pérez Muñuzuri

PHD PROGRAMME IN MATERIAL SCIENCES

SANTIAGO DE COMPOSTELA

2023

USC
UNIVERSIDADE
DE SANTIAGO
DE COMPOSTELA

DECLARACIÓN DO AUTOR/A DA TESE

D./Dna. **Alejandro Carballosa Calleja**

Título da tese: **Emergent dynamics in complex networks: Synchronization, polarization and epidemics**

Presento a miña tese, seguindo o procedemento axeitado ao Regulamento, e declaro que:

1) A tese abarca os resultados da elaboración do meu traballo.
2) De ser o caso, na tese faise referencia ás colaboracións que tivo este traballo.
3) Confirmo que a tese non incorre en ningún tipo de plaxio doutros autores nin de traballos presentados por min para a obtención doutros títulos.
4) A tese é a versión definitiva presentada para a súa defensa e coincide a versión impresa coa presentada en formato electrónico

E comprométome a presentar o Compromiso Documental de Supervisión no caso de que o orixinal non estea na Escola.

En **Santiago de Compostela**, **23 de Outubro de 2023**.

Sinatura electrónica

USC
UNIVERSIDADE
DE SANTIAGO
DE COMPOSTELA

”At the heart of the Universe is a steady, insistent beat:
the sound of cycles in sync”
S. Strogatz

USC
UNIVERSIDADE
DE SANTIAGO
DE COMPOSTELA

Agradecementos/Acknowledgments

Botando a vista atrás, nestes catro anos xa dende que me iniciei nas *andanzas* do doutoramento, acontecéronme unha chea de cousas polas cales coñecín e afiancei amizade con persoas marabillosas que fixeron que esta tese fose moito máis levadeira. Gustaríame empregar esta pequena sección para recordalos e expresar o meu cariño e a miña máis sinceira gratitude. Ademáis, digo andanzas xa que me gustaría tamén frikear un pouco establecendo pequenos paralelismos entre esta etapa miña e aquela que viviron nun pasado remoto e mítico Frodo Bolsón e a súa Compañía do Anel, dende que marchou do seu fogar ata que conseguiu depositar o anel único nas terras desoladas e frías do señor escuro. Aínda que levo esta historia no corazón dende ben pequeno, nestes últimos anos volvín a ela máis dunha vez en busca de refuxio dos meus propios males, polo que en parte é tamén o meu modo de honrala. Penso ademáis que o meu carácter en xeral achégase moito a aquel dos *hobbits*, polo que o paralelismo é se cabe, moito máis acertado.

Así, gustaríame comezar con aqueles que comezaron estas andanzas ao meu carón, os meus Sam, Merry e Pippin, que me apoiaron e me impulsaron en incontables ocasións conseguindo sempre que tirase para diante incluso cando eu xa non podía máis. Basti, o meu Sam, a ti déboche moito, xa dende antes de todo isto. Por ser o outro lado da miña moeda, por deixarme ser e ao mesmo tempo non ser, forzándome a sacar o mellor de min cando eu mesmo negábame a intentalo. Alo, tocouche Merry, por ser a voz da razón, da honestidade e tamén da espontaneidade. Mantivéchesme no chan para que non perdese o camiño e acollíchesme con consello e refuxio cando máis o necesitaba. En volos dous sempre tiven unha casa na que estar moi ben arroupado, perdón por case quemala requentando unha pizza. Mar, os nosos camiños separáronse moi cedo pero sei que sempre poderemos contar o un co outro, sexa compartindo fotos de bichos simpáticos ou contándonos as penas. Creo que encaixas moi ben con Pippin, xa que nunca sabemos cal será a próxima locura coa que nos sorprendas.

Parte do resto da miña Compañía foron chegando pouco a pouco dende o Grupo de Física Non Lineal (o GFNL para os amigos), tamén cada un dende un sitio distinto. Da primeira etapa pre-COVID, gustaríame agradecer aos que foron os meus pilares iniciais, Darío, Dani, Irma, Mariamo e David. Aínda sen case coñecerme de nada, nunca dubidaron en botarme unha man con todo aquelo no que me atasquei, dende apuros informáticos e consellos vitais, ata o peor do papeleo burocrático. Tamén ao meu breve compañeiro de despacho e amigo Juanma, algún día remataremos o torneo de ping pong (que saibas que estiven entrenando todos estes anos, así que prepárate). Moi tristemente, durante a pandemia vímonos obrigados a abandoar os despachos e para cando voltei, a maioría deles xa seguira cada un o seu propio camiño. Non todos, sen embargo. A Sara, a cara alegre e brava do grupo, sempre disposta a escoitar os teus problemas ou ter charlas matinais de despacho. A Martiño e Damián, que aínda que separados por case todo un edificio de distancia sempre estiveron ahí para botar un cable ou unha caña cando fixese falta. Aos tres, grazas por facer de vanguardia e axudarme tanto nestes

USC UNIVERSIDADE DE SANTIAGO

últimos intres da tese. A Belén, pola complicidade, por entenderme tan ben e por compartir o meu sentido do humor. Marcaches un antes e un despois no grupo, e sen dúbida Santiago está moito mellor agora que contamos cunha segoviana coma ti. A Javi, polas tartas, os cotilleos, os ánimos e a hiperactividade. A Alba, pola cercanía, o cariño, e por facerme mirar o mundo con outros ollos, amosándome que hai moitas cousas boas agardando a ser descubertas tanto en min mesmo coma nos demais. A Manu, Santi, Martín , Ismael, Arnau, Carol, Adri, Alfredo, Mateo, Marcos e Vanessa. Grazas a todos polo apoio, os ánimos e por facer destes anos que o GFNL fose tamén unha segunda casa. Eu son o seguinte en abrir as ás e deixar este niño, pero levareivos a todos sempre moi preto do corazón. Alégrome de terme cruzado en todolos vosos camiños e agardo que saibades que sempre poderedes contar comigo para o que precisedes.

Ao meu director Alberto Pérez Muñuzuri (tocaríache ser Gandalf, se mo permites), por todos estes anos de guía e apoio, e por toda a confianza que depositaches en min en tantísimas ocasións. O traballo presentado nesta tese non podería ter sido realizado sen a súa supervisión e dedicación, polo que xa é tan mía coma súa. Grazas por terme dado a oportunidade e por ter sido o meu mentor nesta viaxe científica, agardo ter estado á altura.

Así mesmo, esta tese tampouco tería existido sen a financiación recibida durante estes últimos anos dende a Xunta de Galicia, baixo o programa de "Axudas de apoio á etapa predoutoral" da convocatoria 2020. A colaboración do Centro de Supercomputación de Galicia (CESGA) tamén foi esencial para o cómputo de gran parte dos resultados desta tese.

A Stefano Boccaletti, por acogerme bajo su ala durante mi estancia en Florencia, por tratarme con tanta generosidad y por enseñarme tanto sobre ciencia como sobre la historia, cultura y más importante si cabe, la gastronomía florentina. Hiciste que mi estancia allí fuera una de las mejores experiencias del doctorado. Como dicen en italiano, *sei davvero un tipo in gamba!* Talking about my research stay, I'd like to take the oportunity to thank also all the professors in the CNR of Firenze that made my stay there in overall a really great experience. Thanks to Stefano Focardi and Massimo Materassi for all the talks and discussions. And, of course, many thanks to Alessandro Torcini and Simona Olmi for all the help given and for getting so involved with the project.

Fóra do territorio universitario, gustaríame agradecer tamén á miña xente de Lugo (a Comarca), a Luis, Alberte, David, Carlos, Adrián e en especial a Fer, Mateo, Pablo, Álex e Antía (que aínda que ela non é de Lugo, xa case). Sepárannos uns cantos kilómetros de distancia, pero aínda así cada vez que nos xuntamos parece que o tempo non pasara, e iso valóroo moito. Sen vós tería perdido o rumbo hai xa moito o tempo. Fóchedes sempre un dos meus principais pilares para manterme a flote. Unhas simples grazas quédanse curtas.

A Vicky, Pablo B., e Cósima (non son de Lugo pero tamén son parte da miña Comarca) por todo o que foi e por todo o que será! Aínda que o tempo nos levara por camiños moi diferentes e afastados, alégrome moito de que a nosa amizade tampouco se mermase nin co tempo nin cos kilómetros. Sempre teredes un oquiño no meu corazón.

A Novoa e a Isaac (Legolas e Gimli supoño), por acollerme coma un máis baixo o voso teito durante tantas noites de simposio e convocatorias. Fúchedes un respiro moi necesario, e alégrome moito de poder contar convosco no que veña. Tamén ao resto dos de Pontereas que fixéchedes que aquel ano fose tan especial, e en particular a Sara, Uxía, Iria e Mateo.

Por último e por suposto, á miña familia, aos meus pais Julio e Alicia e ao meu irmán Andrés. Grazas por todo o apoio dende neno e por crer en min, sen vós xa nin tería podido comezar a andar este camiño.

Igual que nas andanzas de Frodo, cada ano que pasaba a tese (o anel) volveuse unha carga

máis e máis pesada que me levou por moitos camiños insospeitados. Grazas a axuda de toda esta Compañía, fun capaz de chegar ao monte do destino e depositala. Quérovos moito a todos.

USC
UNIVERSIDADE
DE SANTIAGO
DE COMPOSTELA

USC
UNIVERSIDADE
DE SANTIAGO
DE COMPOSTELA

Contents

Summary v

Resumen ix

Resumo extenso xiii

General Objectives xix

1 Introduction 1
- 1.1 Complex systems and self-organization . . . 1
- 1.2 Nonlinear dynamics . . . 4
- 1.3 Networks . . . 7
- 1.4 Synchronization . . . 11
- 1.5 Spatio-temporal pattern formation in biology . . . 12
- 1.6 Epidemic processes in networks . . . 14

2 Methods 17
- 2.1 Graph theory and complex networks . . . 17
- 2.2 The Kuramoto model for synchronization phenomena . . . 20
- 2.3 The Belousov-Zhabotinsky reaction . . . 25
  - 2.3.1 Photosensitive variant of the BZ reaction . . . 28
- 2.4 Linear stability analysis. Equilibrium points and growth factors . . . 31

I Collective behavior in periodic oscillators: Synchronization and applications. 37

Motivation and specific objectives 39

3 The Kuramoto model with higher order interactions 41
- 3.1 Introduction . . . 41
- 3.2 Methods . . . 42
  - 3.2.1 Model . . . 42
  - 3.2.2 Coherence indicators . . . 43
  - 3.2.3 Simulation protocols . . . 43
  - 3.2.4 Mean field analysis . . . 44
- 3.3 Results . . . 48

USC UNIVERSIDADE DE SANTIAGO DE COMPOSTELA

3.3.1 Dynamical regimes . . . 48
3.3.2 Transitions to the coherent state . . . 51
3.3.3 Multistability and clustered regimes . . . 62
3.4 Summary and conclussions . . . 64

4 Intermittency regimes in chemical oscillators with local interactions 67
4.1 Introduction . . . 67
4.2 Methods . . . 69
4.2.1 Model . . . 69
4.2.2 Numerical details . . . 71
4.3 Results . . . 72
4.4 Summary and conclusions . . . 83

5 Photosensitive control of arrays of chemical oscillators 85
5.1 Introduction . . . 85
5.2 Methods . . . 86
5.2.1 Experimental setup . . . 86
5.2.2 Preparation of the silica gel and the BZ catalyst free solution . . . 88
5.2.3 Periodic pulses and coupled networks . . . 89
5.3 Results . . . 90
5.3.1 Characterization of the experimental setup . . . 90
5.3.2 Synchronization control by means of periodic pulses . . . 91
5.3.3 Networks of coupled oscillators . . . 94
5.4 Summary and conclussions . . . 97

II Collective behavior in diffusive processes: Opinion formation and epidemic spreading 99

Motivation and specific objectives 101

6 Polarized opinion structures in complex networks 103
6.1 Introduction . . . 103
6.2 Model . . . 105
6.2.1 Numerical details . . . 106
6.3 Polarization measures . . . 107
6.3.1 Growth rates . . . 107
6.3.2 Polarization degree . . . 109
6.4 Results . . . 109
6.5 Conclusions . . . 116

7 Evaluating risk descriptors in metapopulation epidemiologic models 119
7.1 Introduction . . . 120
7.2 Risk prediction for the Galician municipalities . . . 121
7.2.1 Galician spatial network . . . 121
7.2.2 Epidemiological network model . . . 124
7.2.3 Growth rates of the epidemic outbreaks . . . 128

USC UNIVERSIDADE DE SANTIAGO DE COMPOSTELA

7.2.4 Parameter estimation and model validation . . . 129
7.2.5 Results . . . 131
7.3 Risk prediction for the Spanish network . . . 135
7.3.1 Spanish spatial network . . . 135
7.3.2 Age-structure epidemic model . . . 136
7.3.3 Metapopulation network and mobility map . . . 138
7.3.4 Growth rates in the Spanish network . . . 139
7.3.5 Results . . . 141
7.4 Summary and conclusions . . . 149

8 Coupling opinions with epidemic models **151**
8.1 Introduction . . . 151
8.2 Analysis and reconstruction of the social networks . . . 152
8.2.1 Opinion model . . . 157
8.3 Opinion biased SIR model . . . 161
8.4 Epidemic Results . . . 163
8.5 Conclusions . . . 173

9 Summary and Conclusion **175**

Appendices **179**

A **181**
A.1 Growth rates of the age-structure SEIR model . . . 181

B **185**
B.1 Numerical integration of ODEs . . . 185

List of publications **189**

Copyright permissions **191**

List of Figures **213**

List of Tables **215**

Bibliography **234**

USC UNIVERSIDADE DE SANTIAGO DE COMPOSTELA

USC
UNIVERSIDADE
DE SANTIAGO
DE COMPOSTELA

Summary

"The whole is greater than the sum of its parts" is probably the most cited quote within the complex systems' literature but, although it leaves out most of the important features, it is a very nice quote for a summary. This almost newly-born field of science battles reductionism and focuses on the macro-scale, emergent properties of nature that cannot be understood by dissecting the system of study in its more basic elements. The communication among these elements transforms them into parts of something greater, and the many forms that this communication may arise are of equal importance.

In this thesis, we revolve around this idea and examine in different contexts the interplay between individual dynamics and interaction patterns among system units. Complex networks, formed by nodes and links, are the perfect mathematical substrate to study such systems as they allow to bestow a set of internal dynamics in each node and store all the information regarding connectivity patterns in a square matrix. As a result, local couplings between units lead to global dynamics of collective behavior, with different levels of coherence depending on different factors. Through the chapters in this thesis we will analyze profoundly these collective states, studying the conditions for their emergence and their stability. In this sense, we will see how different network structures induce new dynamical regimes and modify the phase transitions between them. We will study which configurations favor coherence between the dynamical units, and which ones favor the emergence of differentiated states. With this in mind, the contents of this thesis are summarized in the following:

Chapter 1. Introduction

In this first chapter we review the context and relevant background for this work. We start by pondering on the definition of complexity and review important features common to all of them: emergence, self-organization, feedback, adaptation, robustness and memory. Then we proceed with the mathematical principles used to understand and work with complex systems: nonlinear dynamics and complex networks. Finally, we give some thought to the emergent phenomena studied along the several chapters: synchronization, instabilities and epidemic spreading.

Chapter 2. Methods

The technical aspects and the common tools used along the thesis are presented here. We review here the basics of graph theory and complex networks, reference models such as the Kuramoto model for phase oscillators or the dynamics and history of the Belousov-Zhabotinsky chemical reaction. Further theoretical concepts of nonlinear dynamics are described here, such as the linear stability analysis of the system's fixed points.

USC
UNIVERSITAT DE SANTIAGO

Chapter 3. The Kuramoto model with higher order interactions

Our first chapter of Results is dedicated to the emergent property of synchronization, exploring from theoretical and numerical perspectives, the effect of introducing a higher order network term in the Kuramoto model for phase oscillators, i.e., the universal paradigm of synchronization phenomena. New dynamical regimes in the form of two-clusters, abrupt phase transitions and multistability emerges as a consequence. We also explore different distributions for the natural frequencies of the oscillators, paying close attention to the phase transitions and the partial synchronization regime. More in particular, we start with unimodal distributions and from there study bimodal ones with increasing distances between the two modes. Of especial interest for this chapter will be the study of two types of clustering regimes that emerge because of the higher order term, with one of them living in a region that is prohibited in the classical Kuramoto model.

Chapter 4. Intermittency regimes in chemical oscillators with local interactions

Next, we move on to a type of oscillators that are a bit more complicated but less abstract. Within them, there is a continuous chemical exchange between auto-catalytic and inhibiting reactants that lead to observable oscillations. This is the famous Belousov-Zhabotinski reaction, from which several experimental set-ups and numerical models have appeared in the decades from its discovery. Here we present a numerical setup where oscillators move randomly in a two-dimensional pool with a finite velocity and a fixed radius of interaction. In this way, we study the effect of local diffusion in the synchronous collective behavior, an effect which is usually overlooked in favor of the mean-field interaction of all the population. Here, we find that in low-mixing conditions, a series of blurred phase transitions appear with unique intermittent but synchronized regimes.

Chapter 5. Photosensitive control of arrays of chemical oscillators

In this chapter we focus on the experimental aspects of the Belousov-Zhabotinsky reaction. Here we consider the photosensitive version of the reaction, where a Ruthenium catalyst is fixed into silica gels. These gels are deposited in very small wells that are carved accurately in a glass plate with laser ablation. In this way, we configure an array of chemical oscillators that can be stimulated through light pulses which either excite or inhibit the firing of the oscillators. Our final aim is to establish feedback loops between the oscillators in order to propose this setup as a method to study experimentally networks of chemical oscillators. For this purpose, we characterize the system in depth and show the synchronization of simple network structures as validation of the method. In a nutshell, this chapter is devoted to present the experimental results obtained regarding the control of synchronization dynamics.

Chapter 6. Polarized opinion structures in complex networks

From here on, we focus on the collective behavior of another type of dynamics: opinion formation and the emergence of polarized structures in social networks. Despite having been studied for several decades and with quite a few mechanisms having been proposed for its

USC DE COMPOSTELA

origin, there is not yet a clear and central explanation for this phenomenon. Here we propose the Turing instability as a tracer of the onset of this polarization, a widely known mechanism in biology that explains the origin of many differentiation processes. As this mechanism is closely connected to the network topology, we study the onset of polarization for different network structures by means of linear stability analysis and the spectra of the network Laplacian matrix. We find that scale-free networks show higher potentiality for polarization because of the large heterogeneity in the connectivity distributions. In this case, the transition to the full-polarized state grows monotonically as more and more nodes become polarized, while on the other hand, for random connectivity distributions the transition to the full-polarized state is abrupt, with the area of emergence being more limited in the parameter space.

Chapter 7. Evaluating risk descriptors in metapopulation epidemiologic models

In this chapter, we consider another system that can potentially self-organize and exhibit collective coherent behavior in the form of pandemic waves. In this way, we first analyze the impact of the first waves of COVID-19 in the autonomous community of Galicia and later on the whole national territory of Spain. Using a metapopulation model with SIR-like dynamics, we reconstruct the spatial network of cities and roads of the territory accounting for the geographical features of each locality. After fitting it with cumulative incidence data, we simulate the advance of the epidemic spread across the whole net of municipalities. At the same time, using linear stability theory and the geographical and demographical information of each node, we develop a risk descriptor that aims to predict the probability of suffering a new outbreak in each locality. The aim of this descriptor is to give a quick and efficient benchmark where one could try different strategies to reduce the risk in critical municipalities. To this end is devoted the second part of this chapter, where we examine the the risks factors om more complex scenarios where age compartments are also considered. Within this model, we consider different confinement strategies that reduce contacts between individuals, either within the localities or between the different localities.

Chapter 8. Coupling opinions with epidemic models

In this last chapter of results, the aim now is on the one hand, to measure directly the opinion distributions from real social networks at different moments in time, while on the other, to evaluate the impact that differentiated distribution of opinions may have in the dynamics of an epidemiological model. In this way, we consider that the opinion value is related to the degree of concern about the disease and regulates the actions that individuals take against it. For example, to follow or not to follow social distancing measures. In this sense we ponder the following question: can we find traces in the online social activity that, in the case of an epidemic outbreak, the population will try to self-organize in order to prevent it? If it is impossible to avoid the presence of rogues and contrarians, is there a way to minimize their effects? We try to simulate this scenario by incorporating the information obtained from the opinion distributions into an epidemic model as a weighted network where the infection process is biased by the opinion values: nodes with the opinion of following social distancing are virtually isolated. We show that even small levels of increased awareness against the disease can have a quantitative impact in the evolution of the disease, while a polarized opinion distribution may interestingly halt or

USC

enhance its advance, depending on some parameters.

Chapter 9. Summary and Conclusion

Finally, we wrap up this thesis by summarizing the main conclusions of the work carried out along the thesis, reflecting on its implications and commenting on the future work.

USC
UNIVERSIDADE DE SANTIAGO DE COMPOSTELA

Resumen

”El todo es más que la suma de sus partes” es probablemente, la cita más repetida en la literatura sobre los sistemas complejos. Con todo, si bien es verdad que omite una gran parte de las características principales de estos sistemas, es una muy buena cita para un resumen. Este campo de la ciencia cuenta con no muchos años de edad y combate el reduccionismo centrándose en las propiedades emergentes de la naturaleza a escala macroscópica, propiedades que no pueden entenderse si se disecciona el sistema de estudio en sus elementos más básicos. La comunicación entre estos elementos los transforma en partes de algo más grande, por lo que las distintas formas en las que pueda surgir esta comunicación son de igual importancia.

En esta tesis, giramos en torno a esta idea y examinamos en diferentes contextos la interacción entre las dinámicas individuales y los patrones de interacción entre ellas. Las redes complejas, formadas por nodos y enlaces, son el sustrato matemático perfecto para estudiar este tipo de sistemas ya que permiten dotar de un conjunto de dinámicas internas a cada nodo y almacenar toda la información relativa a los patrones de conectividad en una matriz cuadrada. Como resultado, los acoplamientos locales entre unidades pueden conducir a una dinámica global de comportamientos colectivos, con diferentes niveles de coherencia según distintos factores únicos a cada sistema. A lo largo de los capítulos de esta tesis analizaremos en profundidad estos estados colectivos, estudiando las condiciones para su aparición y su estabilidad. En este sentido, veremos cómo diferentes estructuras de redes inducen nuevos regímenes dinámicos y modifican las transiciones de fase entre ellos. Estudiaremos qué configuraciones favorecen la coherencia entre las unidades dinámicas y cuáles favorecen la emergencia de estados diferenciados. Teniendo esto en cuenta, los contenidos de esta tesis se resumen en lo siguiente:

Capítulo 1. Introducción

En este primer capítulo revisamos el contexto y los antecedentes relevantes para este trabajo. Comenzamos reflexionando sobre la definición de complejidad y revisamos importantes rasgos comunes a todos los sistemas complejos: emergencia, autoorganización, retroalimentación, adaptación, robustez y memoria. Luego procedemos con los principios matemáticos utilizados para comprender y trabajar con sistemas complejos: dinámica no lineal y redes complejas. Finalmente, reflexionamos sobre los fenómenos emergentes estudiados a lo largo de los distintos capítulos: sincronización, inestabilidades y propagación de epidemias.

Capítulo 2. Métodos

Aquí se presentan los aspectos más técnicos y las herramientas comunes utilizadas a lo largo de la tesis. Revisaremos fundamento básicos de teoría de grafos y redes complejas, así

USC UNIVERSIDADE DE SANTIAGO

como modelos de referencia como el modelo de Kuramoto para osciladores de fase o la historia y la dinámica de la reacción química de Belousov-Zhabotinsky. Aquí se describen también conceptos teóricos de la dinámica no lineal, como el análisis de estabilidad lineal de los puntos fijos del sistema.

Capítulo 3. El modelo de Kuramoto con interacciones de orden superior

Nuestro primer capítulo de Resultados está dedicado a la propiedad emergente de la sincronización, explorando desde perspectivas teóricas y numéricas el efecto de introducir un término de red de orden superior en el modelo de Kuramoto para osciladores de fase, i.e., el paradigma universal de los fenómenos de sincronización. Como consecuencia, se observan nuevos regímenes dinámicos en forma de dos *clusters* síncronos, transiciones de fase abruptas y multiestabilidad. También consideraremos diferentes distribuciones para las frecuencias naturales de los osciladores, prestando especial atención a las transiciones de fase y al régimen de sincronización parcial. Más en concreto, estudiaremos desde distribuciones unimodales hasta distribuciones bimodales con distancias crecientes entre los dos modos. De especial interés en este capítulo será el estudio de dos tipos de regímenes de agrupamiento (*clustering*) que surgen debido al término de orden superior, uno de los cuales habita en una región que está prohibida en el modelo clásico de Kuramoto.

Capítulo 4. Regímenes de intermitencia en osciladores químicos con interacciones locales

A continuación, consideramos un tipo de osciladores que son un poco más complicados pero algo menos abstractos. En ellos hay un intercambio químico continuo entre reactivos autocatalíticos e inhibidores que conducen a la aparición de oscilaciones observables. Esta es la famosa reacción de Belousov-Zhabotinski, a partir de la cual han surgido diversas configuraciones experimentales y modelos numéricos incluso en las décadas posteriores a su descubrimiento. Aquí presentamos una configuración numérica donde los osciladores se mueven aleatoriamente en una caja bidimensional con una velocidad finita y un radio de interacción fijo. De esta manera, estudiamos el efecto de la difusión local en los comportamientos síncronos, un efecto que generalmente se pasa por alto en favor de la interacción de campo medio con toda la población. Aquí, encontramos que en unas condiciones bajas de mezclado podemos observar una serie de transiciones de fase borrosas y regímenes intermitentes pero sincronizados únicos.

Capítulo 5. Control fotosensible de conjuntos de osciladores químicos

En este capítulo nos centramos en los aspectos experimentales de la reacción de Belousov-Zhabotinsky. Aquí consideramos la versión fotosensible de la reacción, donde un catalizador de rutenio se fija en geles de sílice. Al mismo tiempo, estos geles se depositan en pocillos muy pequeños que se tallan con precisión en una placa de vidrio mediante ablación láser. De esta manera, podemos disponer de una serie de osciladores químicos que pueden estimularse mediante pulsos de luz que excitan o inhiben el disparo de las oscilaciones. Nuestro objetivo es establecer bucles de retroalimentación entre ellos, de tal forma que este sistema pueda ser empleado para el estudio experimental de redes de osciladores químicos. Para

ello, caracterizamos a fondo las propiedades de los osciladores y enseñamos la sincronización de estructuras de red simples para validar el método. En otras palabras, este capítulo está dedicado a presentar los resultados experimentales obtenidos en el control de las dinámicas de sincronización.

Capítulo 6. Estructuras de opinión polarizadas en redes complejas

A partir de aquí nos centramos en el comportamiento colectivo de otro tipo de dinámicas: la formación de opinión y la emergencia de estructuras polarizadas en las redes sociales. A pesar de haber sido estudiado durante varias décadas y que varios mecanismos se hayan postulado para su origen, aún no hay una explicación clara o completa para este fenómeno. Aquí proponemos la inestabilidad de Turing como rastreador del inicio de esta polarización, un mecanismo ampliamente conocido en biología que explica el origen de muchos procesos de diferenciación. Como este mecanismo está estrechamente relacionado con la topología de la red, estudiamos el inicio de la polarización para diferentes estructuras de red mediante análisis de estabilidad lineal y el espectro de autovalores de la matriz Laplaciana de la red. Entre otras cosas, encontramos que las redes libres de escala tienen una mayor potencialidad de polarización debido a la gran heterogeneidad en las distribuciones de conectividad. Al mismo tiempo, estas redes muestran una transición monótona al estado de polarización total, mientras que en aquellas distribuciones de conectividad con carácter más aleatorio la transición al estado totalmente polarizado es abrupta, con un área de emergencia más limitada en el espacio de parámetros.

Capítulo 7. Evaluación de descriptores de riesgo en modelos epidemiológicos metapoblacionales

En este capítulo, consideramos otro sistema con alto potencial para autoorganizarse y exhibir un comportamiento colectivo coherente en forma de ondas pandémicas. De este modo, analizamos en primer lugar el impacto de las primeras oleadas de COVID-19 en la comunidad autónoma de Galicia y posteriormente en todo el territorio nacional de España. Utilizando un modelo metapoblacional con dinámicas tipo SIR, reconstruimos la red espacial de ciudades y caminos del territorio teniendo en cuenta las características geográficas de cada localidad. Tras ajustarlo con datos de incidencia acumulada, simulamos el avance de la epidemia por toda la red de municipios. Paralelamente, utilizando la teoría de la estabilidad lineal y la información geográfica y demográfica de cada nodo, desarrollamos un descriptor de riesgo que busca predecir la probabilidad de sufrir un nuevo brote en cada localidad. El objetivo de este descriptor es proporcionar un punto de referencia rápido y eficiente donde se puedan probar diferentes estrategias para reducir el riesgo en los municipios críticos. Para este fin dedicamos la segunda parte de este capítulo, donde analizamos los factores de riesgo en escenarios más complejos donde también se consideran compartimentos de edad. Dentro de este modelo, se considerarán diferentes estrategias de confinamiento que reducen los contactos interpersonales, ya sea dentro de las localidades o entre ellas.

USC UNIVERSIDADE DE SANTIAGO DE COMPOSTELA

Capítulo 8. Acoplo de opiniones con modelos epidemiológicos

En este último capítulo de resultados, el objetivo ahora es, por un lado, medir directamente las distribuciones de opinión en redes sociales en diferentes momentos en el tiempo; y por otro, evaluar el impacto que una distribución diferenciada de opiniones puede tener en la dinámica de un modelo epidemiológico. De esta forma, consideramos que el valor de la opinión está relacionado con el grado de preocupación o alarma por una enfermedad, regulando así las acciones que los individuos toman frente a ella. Por ejemplo, esta opinión puede significar el seguir o no medidas de distanciamiento social. En este sentido nos planteamos la siguiente pregunta: ¿podemos encontrar en la red la existencia de una huella digital de que, en caso de un brote epidémico, la población intentará autoorganizarse para detenerlo? Si es imposible evitar la presencia de negacionistas y contrarios, ¿hay alguna manera de minimizar sus efectos? Para simular esto incorporamos la información obtenida de las distribuciones de opinión en un modelo epidémico donde el proceso de infección está sesgado por los valores de opinión: los nodos con la opinión de seguir el distanciamiento social están prácticamente aislados, mientras que aquellos con una opinión contraria estarán totalmente expuestos a contagiarse. Entre otras cosas, mostramos que incluso pequeños niveles de mayor conciencia contra la enfermedad pueden tener un impacto cuantitativo en la evolución de la pandemia, mientras que una distribución de opinión polarizada puede retrasar o fomentar su avance, en función de unos parámetros concretos.

Capítulo 9. Resumen y conclusión

Finalmente, concluimos esta tesis resumiendo las principales conclusiones del trabajo realizado a lo largo de la tesis, reflexionando sobre sus implicaciones y comentando el trabajo futuro por hacer.

USC
UNIVERSIDADE DE SANTIAGO DE COMPOSTELA

Resumo extenso

"O todo é máis que a suma das súas partes" é probablemente, a cita máis repetida na literatura sobre os sistemas complexos. Con todo, se ben é certo que omite unha gran parte das características principais de este tipo de sistemas, é unha moi boa cita para un resumo. Certas dinámicas como a autorregulación dun sistema, a formación de patróns espazo-temporais ou a propagación persistente no tempo de ondas biolóxicas son o resultado da sinerxia entre un elevado número de compoñentes que son capaces de adaptar a súa función entre eles. Estas dinámicas adoitan recibir o nome de emerxentes xa que son propiedades únicas que xorden da colectividade das partes e polo tanto, non se poden entender a través dun estudo reducionista destas últimas. Noutras palabras, da comunicación entre as partes xorde unha transformación, de tal xeito que as distintas formas nas que se produce esta comunicación son de igual importancia e deben ser estudadas no seu conxunto.

Nesta tese, xiramos arredor desta idea e examinamos en diferentes contextos a interacción entre as dinámicas individuais e os patróns de interacción entre elas. Os sistemas complexos poden atoparse de forma ubicua na natureza, tanto entre seres vivos (ecosistemas, poboacións de bacterias ou redes neuronais) coma entre seres inanimados (osciladores químicos, láseres ou circuítos electrónicos), e aínda que cada sistema sexa en natureza distinto do anterior, todos comparten certas propiedades transversais. Unha das máis importantes quizais sexa o seu modo de organizarse, xeralmente en forma de redes ou grafos onde os nodos conforman os elementos unitarios e os vértices os tipos de interaccións existentes entre eles. Por outra banda, para poder ser entendidos en profundidade, estes procesos requiren de ferramentas e modelos matemáticos que sexan capaces de describir correctamente a evolución temporal do sistema. Estes modelos atopan o seu nexo común na rama das matemáticas que estuda os sistemas dinámicos de tipo non lineal, xa que en todos eles podemos atopar mecanismos similares que controlan o crecemento, o decaemento, a colaboración ou a competición entre as distintas variables do sistema, xa sexan especies animais ou concentracións de reactivos. Poñendo todo en común, a teoría de grafos complexos resulta nun substrato matemático idóneo para estudar este tipo de sistemas, permitíndonos dotar dun conxunto de dinámicas internas a cada nodo e almacenar toda a información relativa aos patróns de conectividade nunha matriz cadrada. Como resultado, os axustes locais entre as unidades do sistema poden conducir a unha dinámica global de comportamentos colectivos, con diferentes niveis de coherencia segundo distintos factores únicos a cada sistema. Ao longo dos capítulos desta tese, analizaremos en profundidade estes estados colectivos estudando tanto as condicións para a súa aparición como a súa estabilidade. Para isto, propoñeranse tres dos campos máis estudados na literatura dos sistemas complexos: o estudo de osciladores periódicos, a formación de opinións e a epidemioloxía. A través do uso das mesmas ferramentas matemáticas, amosaremos que estes campos non están tan lonxe como aparentan e estudaremos a fondo as dinámicas emerxentes de cada un. Veremos como diferentes estruturas de redes inducen novos réximes ou modifican as

USC

transicións de fase entre eles, estudaremos que configuracións favorecen a coherencia entre as unidades dinámicas e cales favorecen a emerxencia de estados diferenciados.

Dunha banda, os procesos de sincronización conforman unha das principais formas de auto-organización nas que os elementos base dun sistema son capaces de axustar os seus ritmos propios aos do resto dando lugar á emerxencia de oscilacións grupais coherentes. Deste xeito, estudar a sincronización dun sistema consiste en estudar a comunicación entre as súas distintas partes, entendendo cales son as condicións que levan a estas últimas a poñerse dacordo en forma dun sistema completamente sincronizado. Entre os casos máis estudados, por poñer un par de exemplos de gran importancia biolóxica, atópanse as agrupacións de neuronas das que xorden a memoria ou a consciencia, ou os marcapasos cardíacos, cuxa boa coordinación resulta nun corazón san que latexa de forma estable. Así mesmo, estudar a sincronización destes sistemas tamén consiste en comprender que pode rompela, resultando no mal funcionamento dos órganos. Doutra banda, os procesos de formación de opinión poden dar lugar tamén a dinámicas globais altamente coordinadas, como sería o caso do consenso, ou a dinámicas opostas pero moi coordinadas entre si, como sería o caso da polarización. Do estudo destes procesos ao longo do tempo, unha das observacións máis atopadas na literatura é que a polarización da sociedade parece estar na alza nas últimas décadas (sobre todo en temas directamente relacionados coa política). Polo tanto, debullar cales son os mecanismos que levan a esta dinámica emerxente é clave para entender o por que destes sucesos e eventualmente frealos. Finalmente, a epidemioloxía estuda cales son as condicións necesarias para que dunha pequena semente de infectados poida xurdir unha epidemia a gran escala. Moitas variables, dende a propia viralidade da infección ata a facilidade que teña para propagarse inflúen altamente nos procesos epidémicos, polo que requírense de modelos cada vez máis sofisticados para reproducir de forma fidedigna a evolución dunha pandemia. O seu estudo no eido das redes complexas non só permite entender mellor estes procesos se non que a través de estratexias que controlen e modifiquen os vértices da rede pódense estudar tamén formas de controlar e parar un gromo a punto de brotar.

Para o estudo destes tres sistemas, expoñeranse diversas ferramentas teóricas e computacionais que axuden a acadar os obxectivos propostos. O estudo teórico realizarase dende o punto de vista da física estatística e da dinámica non lineal de sistemas, xa que o obxecto de estudo consiste nunha poboación moi grande de elementos que interactúan entre si e cuxo comportamento pode modelarse a través de ecuacións diferenciais altamente non lineais. Entre as ferramentas matemáticas que proporcionan as anteriores teorías, atoparanse con frecuencia nesta tese o estudo de transicións de fase, a criticalidade, a análise de estabilidade dos puntos fixos así como o estudo das posibles solucións analíticas do sistema. Dende o estudo computacional, buscarase integrar numericamente as ecuacións diferenciais dos modelos nunhas condicións o máis próximas posibles ás reais en cada caso, co fin de validar os susoditos modelos teóricos á vez que distinguir as distintas rexións do espazo de fases do sistema. En tódolos sistemas considerados, a topoloxía da rede terá unha clara influencia na emerxencia dos estados colectivos, con distintas topoloxías dando lugar a modificacións cuantitativas deste espazo de fases. Polo tanto, o uso destas ferramentas computacionais será clave para entender e detallar os mecanismos debidos á rede complexa que afectan ás dinámicas colectivas. Por exemplo, no caso dos osciladores químicos, o estudo computacional do sistema axudará a discernir detalladamente as condicións exactas que poden dar lugar aos distintos réximes de sincronización completa ou de *clustering*, ao mesmo tempo que axudará a adiantarse aos posibles resultados dun futuro estudo experimental. No caso da formación de opinións e da

epidemioloxía, a rede complexa actúa coma un substrato físico onde se poden propagar as variables, polo que a estrutura da rede estará directamente relacionada coa difusión delas e co estado final do sistema. Como veremos nos distintos capítulos desta tese, distintas topoloxías de rede resultarán en distintos estados de polarización (uns máis leves ca outros) e en distintos ritmos de propagación de enfermidades. Tendo todo isto en conta, os contidos desta tese distribúense nos seguintes capítulos:

Capítulo 1. Introdución

Neste primeiro capítulo revisaremos o contexto e os antecedentes relevantes para este traballo. Comezaremos reflexionando sobre a definición de complexidade e revisaremos importantes trazos comúns a todos os sistemas complexos: emerxencia, auto-organización, retroalimentación, adaptación, robustez e memoria. Logo, procederemos a introducir os principios matemáticos utilizados ao longo da tese para comprender e traballar cos sistemas complexos: a dinámica non lineal de sistemas e as redes complexas. Finalmente, reflexionaremos brevemente sobre os fenómenos emerxentes estudados ao longo dos distintos capítulos: sincronización, inestabilidades e propagación de epidemias.

Capítulo 2. Métodos.

Aquí presentaranse os aspectos máis técnicos e as ferramentas comúns utilizadas ao longo da tese. Comezaremos facendo unha breve revisión dos fundamentos máis básicos da teoría de redes complexas, caracterizando as súas propiedades principais e comentando os distintos tipos de topoloxía máis estudados na literatura. Tamén revisaranse aquí modelos de referencia de gran importancia para esta tese, como o modelo de Kuramoto para osciladores de fase que representa o paradigma universal dos fenómenos de sincronización. Doutra banda, introduciremos a historia e a dinámica da reacción química de Belousov-Zhabotinski, a cal examinaremos nesta tese tanto dende o puntos de vista numérico coma do experimental. Finalmente, describiremos tamén aquí conceptos teóricos chave da dinámica non lineal como é a análise de estabilidade lineal dos puntos fixos do sistema.

Capítulo 3. O modelo de Kuramoto con interaccións de orde superiores

O noso primeiro capítulo de Resultados estará dedicado á propiedade emerxente da sincronización, explorando dende perspectivas teóricas e numéricas o efecto de introducir un termo de rede de orde superior no modelo de Kuramoto para osciladores de fase. Como consecuencia da nova non linealidade engadida, os osciladores experimentarán unha forza a maiores que impulsará a súa sincronización e resultará en transicións de fase abruptas. Doutra banda, xa que este novo termo tradúcese tamén na introdución dun segundo harmónico nas oscilacións, observarase a emerxencia de novos réximes dinámicos en forma de dous *clusters* síncronos. Co fin de caracterizar a fondo estas novas transicións e estados, exploraremos diferentes distribucións para as frecuencias naturais dos osciladores, comezando por distribucións unimodais e seguindo con distribucións bimodais con distancias crecentes entre os dous modos. Do mesmo xeito, realizarase un extenso estudo analítico baseado na resolución auto-consistente do sistema que permitirá obter as solucións do sistema. De especial interese neste capítulo será a aparición da multiestabilidade entre os distintos réximes e o estudo

USC UNIVERSIDADE

dos dous tipos de estados de agrupamento (*clustering*) que xorden debido ao termo de orde superior, dos cales, un habita nunha rexión que está prohibida no modelo clásico de Kuramoto.

Capítulo 4. Réximes de intermitencia en osciladores químicos con interacción locais

A continuación, neste capítulo consideraremos un tipo de osciladores que son un pouco máis complicados pero menos abstractos e máis achegados á realidade. Neles, hai un intercambio químico continuo entre reactivos autocatalíticos e inhibidores que conducen á aparición de oscilacións observables. Esta é a dinámica da famosa reacción de Belousov-Zhabotinski, a partir da cal xurdiron unha multitude de configuracións experimentais e modelos numéricos incluso décadas posteriormente ao seu descubrimento. De feito, a configuración numérica considerada aquí está baseada nunha configuración experimental onde unha poboación de micro-esferas de plástico están cargadas co catalizador que activa a reacción. Dado que os cambios entre o estado oxidado e o estado reducido do catalizador (debidos á reacción BZ) afectan á cor deste, as oscilacións de cada partícula son claramente observables e medibles. Nas simulacións presentadas neste capítulo, os osciladores poden moverse aleatoriamente nunha caixa bidimensional cunha velocidade finita e un radio de interacción fixo. A maiores, tamén discretizamos en partículas de fluído a solución circundante ás partículas, a cal actúa en si mesma coma outro oscilador que acopla as partículas entre si. Este sistema vainos permitir estudar o efecto da difusión local nos comportamentos síncronos, un efecto que xeralmente se pasa por alto en favor dunha interacción de campo medio con toda a poboación onde a solución circundante afecta a todas ás partículas ao mesmo tempo. Atoparemos aquí que debido ás condicións de pouco mesturado dadas polas velocidades baixas dos osciladores e os radios pequenos de interacción, aparecerán unha serie de transicións de fase ruidosas e novos réximes intermitentes pero sincronizados que non aparecen no modelo de campo medio. Entre estes novos estados, atoparemos un par deles que cremos poden ser de alto interese físico, onde observamos oscilacións espontáneas de moi alta amplitude seguidas de oscilacións máis pequenas de moi alta frecuencia. Doutra banda, tamén amosaremos outro estado periódico no tempo que é moi similar, onde estas oscilacións espontáneas son seguidas dun cese total da actividade oscilatoria.

Capítulo 5. Control fotosensible de conxuntos de osciladores químicos

Neste capítulo centrarémonos nos aspectos experimentais da reacción de Belousov-Zhabotinsky. Aquí detallaremos o proceso seguido para fabricar a poboación de osciladores químicos descrita no epígrafe anterior, pero considerando agora unha versión fotosensible da reacción, onde un catalizador de rutenio fíxase en xeles de sílice en vez das micro-esferas . Ao mesmo tempo, estes xeles depositanse en pocillos moi pequenos que se tallan con alta precisión nunha placa de vidro mediante ablación láser. Desta forma, podemos dispoñer dunha serie de osciladores químicos que poden estimularse mediante pulsos de luz que ou ben excitan ou inhiben o disparo das oscilacións. O noso obxectivo é establecer bucles de retroalimentación entre eles de tal xeito que este sistema poida ser empregado no estudo experimental de redes de osciladores químicos. Para iso, caracterizaremos a fondo as propiedades dos osciladores e amosaremos a sincronización de estruturas de rede simples para validar o método. Noutras palabras, este capítulo estará dedicado a presentar os resultados

experimentais obtidos no campo do control das dinámicas de sincronización.

Capítulo 6. Estruturas de opinión polarizadas nas redes complexas

A partir deste capítulo centrarémonos no comportamento colectivo doutro tipo de dinámicas máis achegadas á esfera humana e social: a formación de opinións e a emerxencia de estruturas polarizadas nas redes sociais. A pesar de ter sido un foco de estudo durante varias décadas e que varios mecanismos se haxan postulado para a súa orixe, aínda non hai unha explicación clara e completa para este fenómeno. Aquí propoñeremos a inestabilidade de Turing como rastrexador do inicio desta polarización, un mecanismo amplamente coñecido en bioloxía que explica a orixe de moitos procesos de diferenciación. Como este mecanismo está estreitamente relacionado coa topoloxía da rede, estudaremos o inicio da polarización para diferentes estruturas de rede mediante análises de estabilidade lineal e o espectro de autovalores da matriz laplaciana da rede. Entre outras cousas, atoparemos que as redes libres de escala teñen unha maior potencialidade de polarización debido á gran heteroxeneidade nas distribucións de conectividade. Ao mesmo tempo, observaremos que estas redes amosan unha transición monótona ao estado de polarización total, mentres que naquelas distribucións onde a conectividade segue un carácter máis aleatorio, a transición ao estado totalmente polarizado é abrupta, cunha área de emerxencia máis limitada no espazo de parámetros.

Capítulo 7. Evaluación de descritores de risco en modelos epidemiolóxicos metapoboacionais

Neste capítulo, consideramos outro sistema con alto potencial para a auto-organización e a exhibición dun comportamento colectivo coherente en forma de ondas pandémicas. Deste xeito, analizaremos en primeiro lugar o impacto das primeiras ondas da COVID-19 na comunidade autónoma de Galicia e posteriormente en todo o territorio nacional de España. Utilizando un modelo metapoboacional con dinámicas tipo SIR, reconstruiremos a rede espacial de cidades e estradas do territorio tendo en conta as características xeográficas de cada localidade. Tras axustalo con datos de incidencia acumulada, simularemos o avance da epidemia por toda a rede de municipios observando que municipios sofren dunha maior incidencia. Paralelamente, utilizando a teoría da estabilidade lineal e a información xeográfica e demográfica de cada nodo, desenvolveremos un descritor de risco que buscará predicir a probabilidade de ocorrencia dun novo gromo de infección en cada localidade. Cómpre dicir que este factor é independente da evolución real da pandemia e correlaciónase ben tanto coas simulacións como cos datos analizados. Doutra banda, ao estar calculado por medios analíticos, o seu tempo de cómputo e ínfimo. O obxectivo deste descritor é polo tanto, proporcionar un punto de referencia rápido e eficiente onde se poidan probar diferentes estratexias para reducir o risco de municipios críticos sen a necesidade de custosos recursos computacionais ou longos tempos de simulación. Unha vez presentado e validado este factor de risco, a segunda parte deste capítulo dedicarase a analizar os factores de risco en escenarios máis complexos onde tamén se considerarán compartimentos de idade. Dentro deste modelo, consideraranse diferentes estratexias de confinamento que permiten reducir os contactos, xa sexa dentro das localidades ou entre elas, e analizaremos cales son as máis optimas para diminuír o risco de novos gromos.

USC
UNIVERSIDADE DE SANTIAGO DE COMPOSTELA

Capítulo 8. Acoplo de opinións con modelos epidemiolóxicos

Neste capítulo, o obxectivo agora será, dunha banda, medir directamente as distribucións de opinión en redes sociais en diferentes momentos no tempo; e doutra banda, avaliar o impacto que unha distribución diferenciada de opinións pode ter na dinámica dun modelo epidemiolóxico. Deste xeito, consideraremos que o valor obtido na opinión estará relacionado directamente co grao de preocupación ou alarma por unha enfermidade, regulando as accións que os individuos toman fronte a ela. Por exemplo, esta opinión poderá significar seguir ou non as medidas de distanciamento social. Neste sentido, consideraremos a seguinte cuestión: podemos atopar na rede a existencia de pegadas dixitais de que en caso de ocorrencia dun gromo epidémico a poboación tentará autoorganizarse para detelo? Se é imposible evitar a presenza de negacionistas e contrarios, hai algunha maneira de minimizar os seus efectos? Para simular isto, o primeiro que faremos será recoller unha ampla mostra de datos da rede social *Twitter* durante dous meses distintos onde poderíamos asumir que a actividade na rede foi marcada por eventos socio-políticos: unhas eleccións nacionais e o inicio da pandemia da COVID-19. De cada rede obteremos unha distribución de opinión distinta, e incorporaremos a esta información nun modelo epidémico que ocorra nos nodos e vértices dunha rede complexa de tal xeito que o proceso de infección estea nesgado polos valores da opinión: os nodos coa opinión de seguir o distanciamento social estarán practicamente illados, mentras que aqueles coa opinión de non seguilo terán moitas máis probabilidades de contaxiarse. Para contrastar os resultados obtidos, tamén realizaremos un estudo máis a fondo xerando distribucións de opinións sintéticas onde podamos medir máis detalladamente a súa diferenciación, así como realizaremos o mesmo análise na rede social de Twitter portuguesa e considerando outro modelo epidémico un tanto máis complexo. Entre outras cousas, amosaremos que incluso pequenos niveis de maior conciencia contra a enfermidade poden ter un impacto cuantitativo na evolución da pandemia, mentres que unha distribución de opinión polarizada pode tanto frear como fomentar o seu avance, en función duns parámetros concretos.

Capítulo 9. Resumo e conclusión

Finalmente, concluiremos esta tese resumindo as principais conclusións do traballo realizado ao longo da tese, reflexionando sobre as súas implicacións e comentando o traballo futuro por facer.

USC
UNIVERSIDADE DE SANTIAGO DE COMPOSTELA

General Objectives

This thesis, as outlined in the summary, undertakes an in-depth exploration of the intricate communication dynamics within large systems that lead to the emergence of complex phenomena, such as synchronization of periodic oscillators, polarization in opinion formation and epidemic waves in human populations. The main objective of this thesis is then to identify and quantify thoroughly the main mechanisms behind these processes. Moreover, it aims to analyze how an increase in the complexity of these mechanisms can induce modifications in the emergent features observed.

In that sense, the initial focus of the investigation lies in the field of synchronization. There, we examine the influence of different network structures on the coherent states exhibited by populations of oscillators. The aim is to identify how the introduction of more complex network architectures might either foster synchronization or drive new collective behaviors, reshaping the landscape of system solutions. As elucidated in the summary, this goal will be pursued in Chapters 3, 4 and 5, where we will study a diverse range of oscillator populations, ranging from the abstract (Kuramoto oscillators), to the tangible (chemical oscillators in a laboratory setting).

Subsequently, in Chapters 6, 7 and 8, our main goal extends into realms more closely aligned with human dynamics: opinion formation and epidemiology. In contrast to the earlier emphasis on enhancing synchronization, the primary objective here is the opposite. Here, the ultimate aim is not only to understand the mechanisms behind polarization and epidemic waves, but also to develop strategies for their effective control and mitigation.

In essence, this comprehensive exploration navigates through both theoretical and applied domains, bridging the abstract concepts of complex systems with real-world implications. Ranging the spectrum from abstract oscillators to the intricacies of societal dynamics, this thesis aspires to provide a holistic understanding of the interaction patterns shaping the behavior of complex systems across various scales.

USC
UNIVERSIDADE DE SANTIAGO DE COMPOSTELA

USC
UNIVERSIDADE
DE SANTIAGO
DE COMPOSTELA

Chapter 1

Introduction

1.1 Complex systems and self-organization

What have in common a very large group of insects, bacteria, living cells or humans? The answer could be that they are all alive, yes, but that is not the one that we are aiming at. When looked separately, they all have their unique traits and behaviors but at an abstract level, all these groups of living things share common features of complex collective behavior: synergy, intricate communication patterns and high levels of adaptation [Mitchell and Mitchell, 2011]. For example, a colony of ants formed by hundreds of individuals that communicate in a rather simple way between each other, operate really smoothly to seek food, fight intruders and in overall work together to preserve the colony. If a single individual gets separated from the group having lost the pheromone trail that indicates the way back, it will wander alone randomly facing a grim end. But in group however, they can even merge together to build bridges with their bodies or transport materials over hundreds of meters to construct intricate ground fortresses with many labyrinthine passages. Bees developed a complex hierarchical structure that adapts to the hive necessities: when the current queen accidently dies or is starting to fail, the colony acts swiftly to produce a new queen that keeps it all together. The functioning of neuron cells communicating with each other can be roughly simplified to a couple of rules, and yet when you sum a large number of them you obtain perception, awareness, emotion and other large-scale brain functions that cannot be understood from studying the neurons alone.

This type of remarkably **self-organization** behavior and the fascinating **emergent** properties that arise from many interacting likewise elements lie at the core of the complex systems' science. But what defines complexity and what exactly qualifies as a complex system? According to the Cambridge dictionary, complexity is "the state of having many parts and being difficult to understand or find an answer to", which can be a vague word used to refer to something that is just "complicated". This has been up to debate practically since the own emergence of the field and many authors have offered their perspectives from years working on it [Rosen, 1977, Newman, 2011, Ladyman et al., 2013, Bianconi et al., 2023, Estrada, 2023]. A suitable (and common) way to define a complex system consists in enumerating a list of properties that are shared always or at least often by these type of systems. We have already named two of the most important. That some kind of **spontaneous order** should emerge just from the interaction of the parts and without a clear central of control is, for [Ladyman et al., 2013], a necessary condition (but not sufficient) for a system to be complex. This spontaneous order is found in a myriad of ways in the form of spatio-temporal patterns,

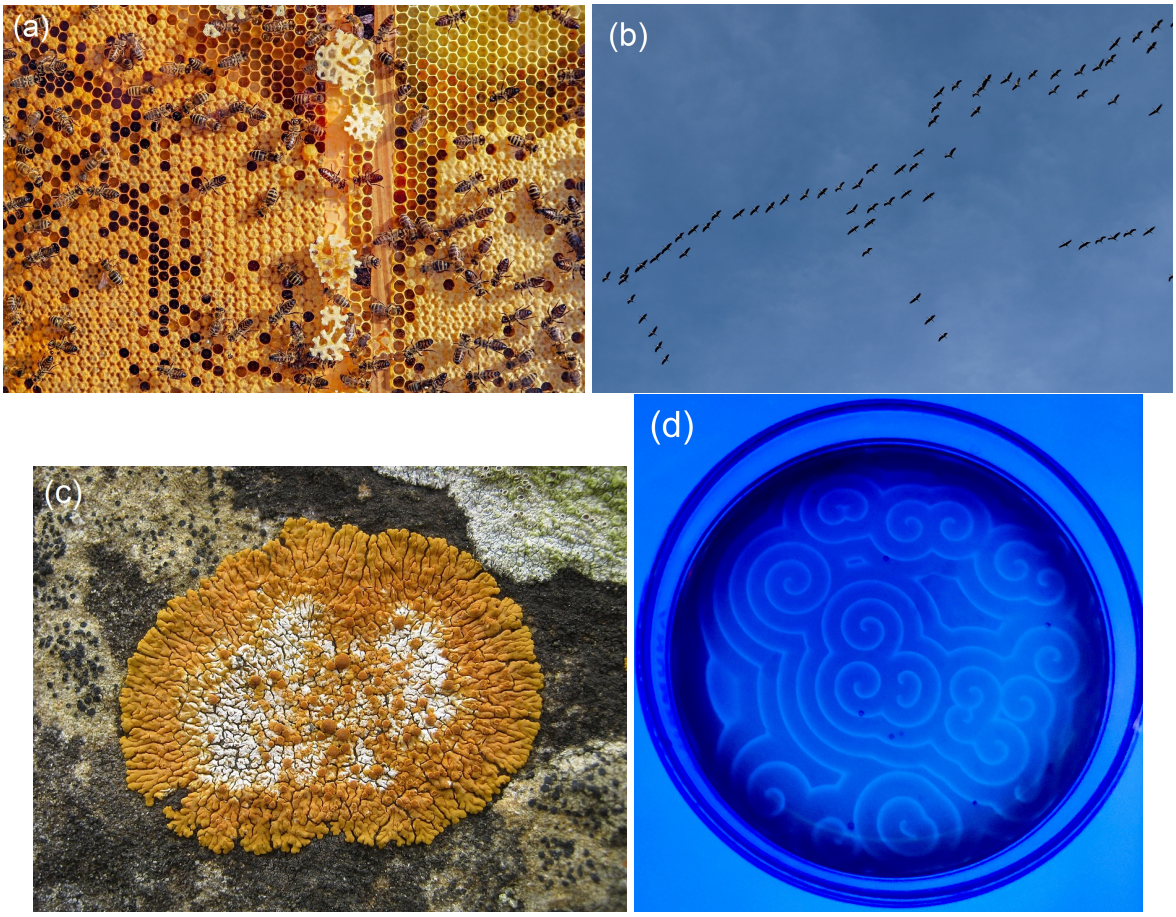


Figure 1.1: Examples of self-organization and spontaneous order in the form of spatiotemporal patterns in natural complex systems. (a) Beehive collective beehavior to produce and store honey in hexagonal formation, (b)Flock of migrating birds arranged in V-shape, (c) Licken growth under complex patterns and (d) auto-waves in the Belousov-Zhabotinsky reaction. Images (a) and (b) were taken from the copyright free repository `https://pixabay.com/`, image (c) from `https://commons.wikimedia.org/wiki/File:Variospora_flavescens_232782.jpg`, while image (d) is of own making.

periodicity or collective redistribution of any kind. In Figure 1.1 we show some examples of this. In fact, self-organization may not be just a rare phenomenon limited to living systems but a inherent property of the universe itself according to the marvellous ideas written in [Kauffman, 1996]. Kauffman's notion of "order for free" implies that once a certain threshold of complexity is increased, spontaneous order arises naturally. From molecules to cells, from cells to organisms, from organisms to ecosystems, societies and so on. Following this reasoning, another common feature to complex systems is that of **nestedness**, the existence of several levels of structures with different proprieties that also interact with each other.

Other important features to complex systems mentioned in [Bianconi et al., 2023, Ladyman et al., 2013] are that of **nonlinearity**, **feedback**, **adaptation** and **robustness**. **Nonlinearity** refers to the type of dynamics in the system, and probably it is easier to explain it stating first what is a linear system. If there is linearity, the output of the system is always proportional to the input, or in other words, the more the input the more the output. Reversely, with nonlinear dynamics, just small differences in the inputs can lead to disproportionate effects. The branch of mathematics that studies the stability of these systems and how they evolve in time has been key for the mathematical formalism of complex systems, and one could

reasonably say that it provides a language for their study [Pessoa, 2021]. Indeed, although nonlinearity is present in most of the complex systems studied to date, it has been argued that it is not neither a necessary nor a sufficient condition for complexity [Ladyman et al., 2013], since just linear dynamics in the presence of feedback can give raise to complex scenarios [MacKay, 2008]. This leads us to the following key idea. **Feedback** and **adaptation** give the system a fundamental property in complexity, the ability to regulate itself. Consider the flock of birds shown in Figure 1.1 (b). Each member of the group is aware of its neighbors and adjusts its course accordingly to the proximity to them, but, right after its own adjusting, its corresponding neighbors will do the same. Think also about a simplified ecosystem of two predator/prey species, let's say foxes and rabbits, where the first ones can only feed on the latter. In this case, a feedback loop is created establishing a clear dependence between the two species, since an increase in the rabbit population imply more food for the foxes that will increase their numbers accordingly. However, given some time, there will be an unavoidably excess of foxes which at some point may even extinguish the rabbits. Without any other source of food, the foxes will soon vanish too.

Finally, **robustness** and **fragility** refer in general to the system's ability to maintain (or not) its structure and function against external perturbations. In climate research for example, human activities induce certain perturbations that may have the potential to alter the state or development of an ecosystem, pushing them into qualitatively different states or modes of operation [Lenton et al., 2008]. The critical threshold at which this tiny perturbation results in large scale global fluctuations is usually referred to as a "tipping point" [Gladwell, 2006], with a current pressing question being: how far are we actually from these tipping points [Lenton et al., 2019]?. From another perspective, for A.Arenas *"robustness and fragility must be understood in terms of propagation. The more robust is the system to perturbations, the more difficult is to propagate in this system any other property from local to global, and the contrary for the fragility."* [Bianconi et al., 2023]. In network theory, the relation between the structural properties and percolation dynamics has been widely studied [Boccaletti et al., 2006], and a general logical result is that the less the distance between the nodes in the network, the faster the propagation of diseases or ideas in it.Another example of robustness comes from the notion of resilience and attack tolerance to either random or targeted attacks, which depend strongly on the network topology [Albert et al., 2000, Cohen et al., 2000].

In summary, a proper definition of a complex system as stated by [Ladyman et al., 2013] follows that it *"is an ensemble of many elements which are interacting in a disordered way, resulting in robust organization and memory"*, although we believe that one should also keep in mind that *"to understand a complex system (diverse community) of interacting players (oscillators, species, whatever) we must determine the (emergent) properties at the collective level (including coexistence and biodiversity). Not only do we need to consider interactions but we need to describe them richly enough for collective properties to be unraveled"* [Pessoa, 2021]. In this latter sense and very recently, [Estrada, 2023] reviews the necessity and sufficiency of all the previous considered notions, putting the emphasis simply in the interactions themselves. In his words, *"a complex system is defined as the system where there is a bidirectional non-separability between the identities of the parts and the identity of the whole. Thus, not only the identity of the whole is determined by the constituent parts, but also the identity of the parts are determined by the whole due to the nature of their interactions. That is, interactions act as transformers of the nature of the interacting objects and of the whole formed by them"*. In this sense, the flight of a solitary bird by its own can be described in terms

of purely classical mechanics, while a member of a flock becomes an adaptive element that eventually builds a self-organized group. A street cat becomes either predator or prey when facing a mouse or a dog, but it can also become an important part of a family if it is adopted by them.

Along this thesis, we will resonate thoughtfully with this idea of putting the spotlight in the interactions in order to fully comprehend the complex dynamics of the system and therefore, the emergent properties that come out of it. In this way, we will explore in some of the chapters how new or refined forms of interactions between the elements of our system may break or transform these properties; while in others we will focus on the effect that different structures with similar interactions have in the resulting emergent properties.

1.2 Nonlinear dynamics

"Nonlinear dynamical systems not only contribute to our view of how interacting elements behave, but defines both a language and a formal system to characterize emergent behaviors". [Pessoa, 2021]

If two elements of a system cooperate, compete or interchange information of any kind, mathematically this means the presence of non-linear terms. For example, while the natural growth of rabbits may be given by the linear function αX, with alpha being a growth rate and X the rabbit population, the amount of rabbits preyed by foxes at a given moment in time will depend both on the population of rabbits X and foxes Y at that given time: βXY, with β being the predation rate. The more realistic the model, the more nonlinear will be. Say for example we want to consider that there is a maximum sustainable capacity C given by the environment, and once the population surpasses this capacity it has to decrease. Then, we consider the classical logistic equation, $\alpha X(1 - X/C)$, widely used in ecology for modeling the growth of animal species. If these terms are included into differential equations, we can discover how will the species evolve in time. Are any of the species condemned to go extinct as we said earlier or can they coexist in time? Each of these possibilities is a different point of equilibrium of the system, and they can be found by studying the phase space of the solutions to these equations. In this way, we can reproduce the dynamical landscape of the model and understand or even predict the origin of certain outcomes. Thus, the study of nonlinear dynamical systems in fields as biology involved a revolution in population ecology with the seminal works of [Lotka, 1925, Volterra, 1928, Ricker, 1954], that later served to establish the roots for mathematical biology [May, 1973, Murray, 2002, Murray, 2003]. But it did not stop there. A certain revolution came in science from the pioneer modelling of the meteorological weather [Lorenz, 1963], theoretical neuroscience [Lapicque, 1907, Hodgkin and Huxley, 1952], epidemic spreading [Kermack et al., 1927], economy [Mantegna and Stanley, 2000], opinion dynamics [Degroot, 1974] and many other fields that can be described by means of differential equations. The beauty of it all is that from deeply understanding the math behind them, these seemingly disconnected fields that range from physics to social and health science were bridged together, creating a new interdisciplinary field of science.

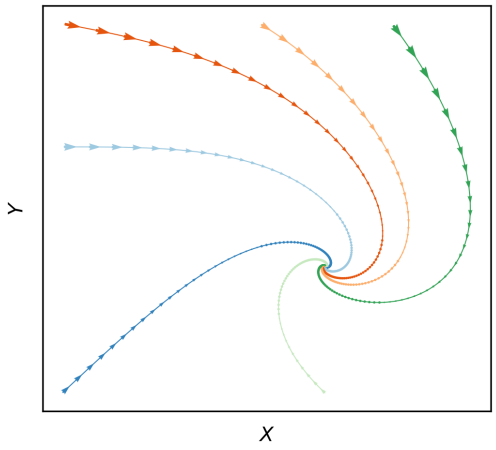
With this idea in mind, let us introduce formally the language in which we will communicate along this whole manuscript. For now we will give a general overview that we will apply later on with the models of the different chapters (for a detailed description we refer the interested reader to the seminal textbook by [Strogatz, 2015]). We have a set of interdependent

variables given by the vector state $\boldsymbol{x}(t) = (x_1(t), ..., x_n(t))$, that evolve in time accordingly to the following ordinary differential equations:

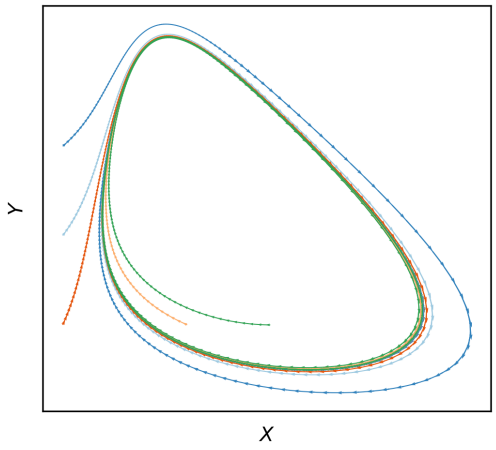
$$\frac{d\boldsymbol{x}(t)}{dt} = \boldsymbol{f}(\boldsymbol{x}(t); \gamma) \tag{1.1}$$

where the functions $\boldsymbol{f}(\boldsymbol{x}(t))$ correspond to internal and reaction dynamics, i.e., variable growth, decay, competition, etc; while the set of parameters γ and shape the rate of each one of them. As the system evolves, the vector state $\boldsymbol{x(t)}$ flows towards some direction of the state space, and what we are interested then is in knowing if a stationary state is reached and where. In other words, this happens when the dynamical flow stops, $\frac{d\boldsymbol{x}(t)}{dt} = \boldsymbol{f}(\boldsymbol{x}^*; \gamma) = 0$. The set of values $\boldsymbol{x}^*$ that satisfy the previous equation are termed the *fixed points* of the system and correspond to an equilibrium state. Depending on the parameters γ, a perturbation to this equilibrium may grow looking for another of the fixed points, or it can decay back to the former. In the latter case, if all perturbations damp out we say that $\boldsymbol{x}^*$ is an stable fixed point that attracts all trajectories in its vicinity. This type of stable attractor is illustrated in Figure 1.2(a), where we see different trajectories spiraling into the fixed point. Another possibility that we will find in the following chapters, is that from the variation of the parameters a bifurcation of the stability is encountered, and the stable fixed point $\boldsymbol{x}^*$ now becomes unstable. In this specific case, what we find is that $\boldsymbol{x}(t)$ flows towards a stable closed loop giving rise to oscillations in the variables through what is known as a Hopf bifurcation [Strogatz, 2015]. This stable loop, called a *limit cycle*, is of great importance as it gives an explanation for the emergence of many periodic behaviors in nature. It is illustrated in Figure 1.2(b), where we can see how trajectories starting both inside and outside the cycle end up circling in it. A final possibility is that the trajectories of $\boldsymbol{x}(t)$ wander around infinitely without stopping or repeating but enclosed within certain boundaries, as it is shown in Figure 1.2(c). In this case, if two adjacent trajectories at a given moment in time (the blue and the orange ones at the left white circle for example) separate exponentially a few moments later, then this type of aperiodic motion is termed chaotic. Examples of this motion are the famous butterfly of Lorenz [Lorenz, 1963] (which is the the one we are drawing) or the Rössler attractor [Rössler, 1976].

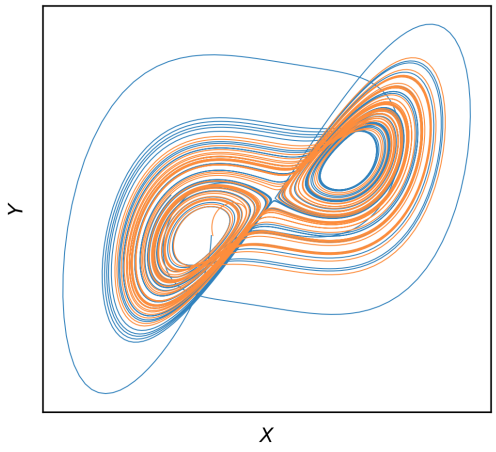
USC
UNIVERSIDADE DE SANTIAGO DE COMPOSTELA



(a) Stable fixed point



(b) Stable limit-cycle



(c) Lorenz's chaotic attractor

Figure 1.2: Phase space of different dynamical states in function of two variables X and Y of the system and different system parameters. Different colors represent trajectories originating at different initial conditions, with arrows in (a) and (b) denoting the direction of the flow towards the stable attractor. Note that the dynamics of (a,b) and (c) are obtained through different toy models in order to highlight these behaviors.

1.3 Networks

"The mystery of life begins with the intricate web of interactions, integrating the millions of molecules within each organism. The enigma of the society starts with the convoluted structure of the social network. The unpredictability of economic processes is rooted in the unknown interaction map behind the mythical market. Therefore, networks are the prerequisite for describing any complex system, indicating that complexity theory must inevitably stand on the shoulders of network theory." [Barabasi, 2002]

Going a step further, we will consider systems composed of N similar elements where each undergo the same local dynamics given by Eq. 1.1, but that will receive feedback from the dynamical state of the other units and that will adapt to them accordingly. A natural representation of this system of interactions comes in the form of networks and graph theory [Boccaletti et al., 2006]. With the explosion of social media in the last decade we are now pretty familiar with the concept of social networks, but networked systems go way beyond and the study of their transversal properties pervades science from microbiology to statistical physics [Strogatz, 2001]. Although graph theory had existed for a couple of centuries, the network representation of physical systems didn't actually emerge until the end of the 20th century, when computers were powerful enough to handle and investigate the datasets required to map real networks formed of thousands of nodes. It was like this that the veil was lifted, and research finally was able to focus on the topology of neural connectomes that explicit how the neurons are arranged [Yamamoto, 1991], on cellular and metabolic networks detailing the binding interactions between genes, proteins and metabolites [Kohn, 1999, Hartwell et al., 1999, Jeong et al., 2000], or in the explicit structure behind the Internet and the World Wide Web (WWW) at its earlier times [Albert et al., 1999, Faloutsos et al., 1999, Broder et al., 2000]. The differences between these networks are very clear: the internal dynamic of a neuron differs completely from that of a gene, and a cell is formed by organic matter while the documents that form the WWW are chunks of digital data. Thus, one would expect that their network structure differ too, but the striking fact observed when comparing all these systems together was that the organizing principles behind the network formations were the same, independently of their diversity in size and evolution. The network architecture of most real systems self-organize similarly sharing a lot of physical properties, therefore being possible to unify them by using a same set of mathematical tools [Barabási and Pósfai, 2016b]. Deeply understanding the network structure is of great importance because it directly affects the function of its elements, this is, their dynamics. As we said earlier, the network topology changes its robustness and therefore its ability to propagate information, diseases, electrical currents, etc, so revealing the exact relation between structure and function is key to understand the emergent phenomena.

However there are lots of delicate aspects that one must take into account when modelling networks. Again, we comment briefly here on some of them and leave the curious reader for detailed reviews or books in the subject (see e.g. [Boccaletti et al., 2006, Barabási and Pósfai, 2016b]). Reproducing the exact connectome of animals and humans is not hard only because there are millions and millions of neurons, but because the wiring between them are also considerably intricate and vary from one living being to another [Sporns et al., 2005]. Also in real networks, new links and rewirings are forming constantly in time which affect also to the dynamics of the whole system. In fact, the study of temporal networks is a problem so vast that it is becoming a subfield of its own

USC DE COMPOSTELA

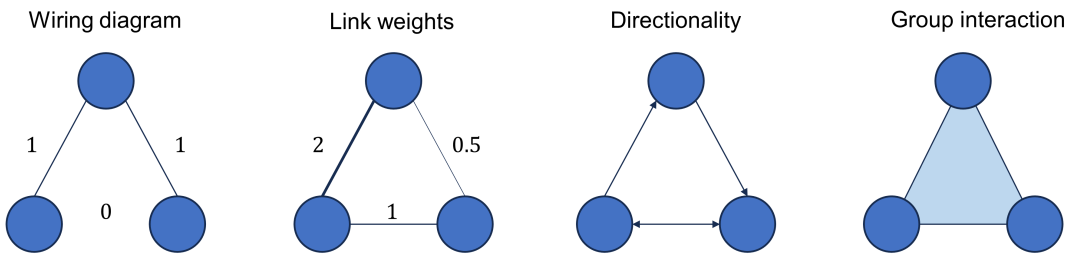


Figure 1.3: Relevant considerations of possible network interactions.

[Holme and Saramäki, 2012]. Nodes as well as links might be heterogeneous too, in the sense that the dynamics of each node may vary either with different values of the parameters γ or even having sets of completely different dynamics. Link heterogeneity can refer to the directionality of the links or to the intensity of them. Think for a second in your complete social network of acquaintances. In time, from school, university, work, sports and other activities that involve social exchange you have gathered a broad contact list in which there are stronger and weaker ties, from family and close friends to just one-time acquaintances. We can grasp intuitively in this way the concept of link *weights* w, which represent the intensity of the connection in the form of real numbers attached to the links (instead of plainly existing or not). At the same time, there may be some people that you know because you are following them on social media (or know them because are friends of friends) but they are not aware of you. In this case there is a unilateral connection with a given direction.

Another important concept that has been relevant recently is that of group interactions, usually termed as higher-order [Battiston et al., 2020]. Stablishing a link between a pair of nodes implies that the connection is strictly between those two nodes, but what if by some motive, the presence of more local connections induces stronger dynamical effects? Probably the more intuitive example is that of "peer-pressure": if all your group of friends wants to do something that you are not very convinced of, it is more likely that you will fall to their shenanigans if you found yourself surrounded by the group, than if they are texting you separately. In this same example, notice that the pressure you receive to change your opinion is not only stronger, but also the time scale of the communication is faster. This is, in the first case the information spreads across the whole group instantly while with straight pair-wise links, information must spread among all the connections individually. In Figure 1.3 we show a summary of the commented features, whose effects on the dynamics will be explored in many of the future chapters.

On the other hand, the large scale structure of the network is usually referred to as its *topology* and all its information is stored in a squared matrix called the adjacency matrix A_{ij}, as it gives the information on wheter two nodes i, j are adjacent or not. The network topology is mainly affected by how the network was constructed from scratch. Did all the nodes connect randomly by chance or were there some defined rules on its evolution? In the first type of networks, the distribution of links follows a Gaussian shaped curve, while in many real networks what we see is that the link distribution follows a power-law. The specific details on why does this occurs are presented in the Methods section, but for now what it is important is that the shape of this link distribution affects strongly the functioning of the system. Between other things, the conditions under which the emergent phenomena appears may change drastically. Therefore, a central core of this thesis will be to contrast how different network topologies

change the overall dynamics of the system. For this purpose, we consider that the coupling between our dynamical units is mediated directly by the adjacency matrix, with a coupling parameter K that modulates the strength of this coupling. This transforms eq.1.1 for each unit i into:

$$\frac{d\boldsymbol{x_i}(t)}{dt} = \boldsymbol{f}(\boldsymbol{x}(t);\gamma) + K\sum_{j}^{N} A_{ij}\boldsymbol{h}(\boldsymbol{x_i},\boldsymbol{x_j}) \qquad \text{with } i = 1,...,N \tag{1.2}$$

where $\boldsymbol{h}$ are the interaction functions between the states $\boldsymbol{x_i}$ and $\boldsymbol{x_j}$ that will depend on the system we are modelling. In Chapter 3 for example, we will see that this interaction function takes the form of a sinusoidal coupling $h(x_i,x_j) = \sin(x_j - x_i)$. In the rest of the chapters, we will mainly consider diffusive systems where our coupling function will correspond to Fick's law of diffusion $h(x_i,x_j) = x_j - x_i$. We will see that the parameter K will be usually related with the amount of order in the system, allowing us to study the phase transitions from the disordered state to the ordered one whose onset appears at a critical point K_c. For some systems we will see that this order comes in the form of clustering of elements that synchronize their internal rhythms, while in others the critical point signals the emergence of differentiated patterns.

USC
UNIVERSIDADE DE SANTIAGO DE COMPOSTELA

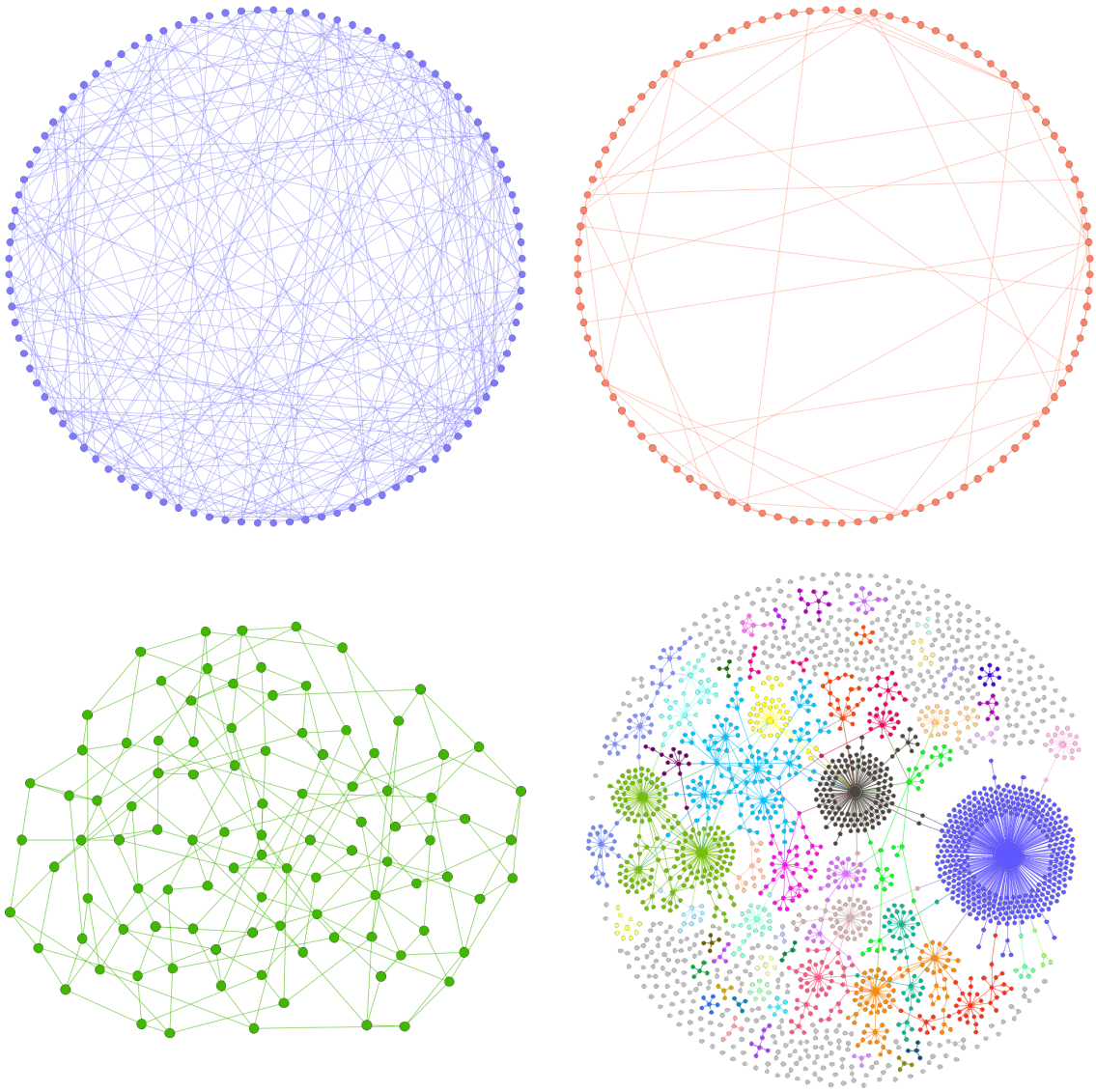


Figure 1.4: Different network topologies based on their interaction pattern. From left to right, fully random network, "small-world" network (top row), regular/grid network and scale-free network (bottom row). See Methods for their description.

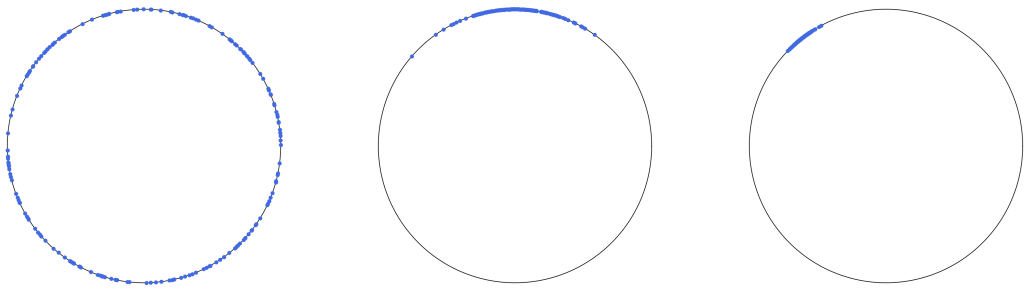
USC
UNIVERSIDADE DE SANTIAGO DE COMPOSTELA

1.4 Synchronization

"At the heart of the Universe is a steady, insistent beat: the sound of cycles in sync. It pervades nature at every scale from the nucleus to the cosmos. Every night along the tidal rivers of Malaysia, thousands of fireflies congregate in the mangroves and flash in unison, without any leader or cue from the environment.[...] Even our bodies are symphonies of rhythm, kept alive by the relentless, coordinated firing of thousands of pacemaker cells in our hearts. In every case, these feats of synchrony occur spontaneously, almost as if nature has an eerie yearning for order". [Strogatz, 2003]

Trying to explain persisting order in time, or in other words, synchronization phenomena, is one of the mean branches of the complex system's community that has marvelled scientists for many decades (including of course, the writer of this thesis). It even spans to centuries, with more than three hundred years since the physicist Christiaan Huygens was puzzled by *"two clocks hanging next to one another separated by one or two feet keep an agreement so exact that the pendulums always oscillate together without variation. After admiring this for a while, I finally figured out that it occurs through a kind of sympathy: mixing up the swings of the pendulums"*[Strogatz, 2003]. Huygens' study of this *sympathy* was one of first analysis of inanimate sync [Huygens1673], a topic that later from the late 20th century until today would experience and exploding interest with the study of new physical oscillators: lasers [Winful and Rahman, 1990, Li and Erneux, 1993, Sugawara et al., 1994, Roy and Thornburg, 1994], electrical generators and circuits [Chua et al., 1993, Jankowski et al., 1995, Nishikawa and Motter, 2015], Josepshon junctions [Watanabe and Strogatz, 1993, Filatrella et al., 2001] or chemical oscillators [Kuramoto, 1984, Yoshimoto et al., 1993, Kiss and Hudson, 2001, Kiss et al., 2002, Taylor et al., 2009] between many others (see [Rosenblum and Pikovsky, 2003] for a further review). As Strogatz said it, there is an inevitable tendency for synchrony in every system formed of rhytmic elements that are able to "hear" each other.

Another pioneer of the synchronization field was Arthur T. Winfree, who planted the seeds for the mathematical approach to the study of biological and circadian rhythms [Winfree, 2001]. He became aware of this universal tendency in periodic living systems and aimed for a tractable model of a mutually-coupled population of oscillators [Winfree, 1967]. Later on, inspired by the ideas of Winfree, Yoshiki Kuramoto focused on a simpler, more abstract model and showed how to solve it exactly [Kuramoto, 1984]. In the Methods section we will review the main



(a) $K = 0$ **(b)** $K = 2.5$ **(c)** $K = 10$

Figure 1.5: Collective synchrony in a set of phase oscillators for increasing values of the coupling strength K. Each blue point represents a different oscillator, whose phases are distributed in (a) between 0 and 2π.

aspects of this model as it will be at the core of great part of this thesis. For the moment let us just give a glimpse of its qualitative features. This simple model consisted in the following differential equation of a population of N coupled phase oscillators with phase θ_i,

$$\dot{\theta}_i = \omega_i + \frac{K}{N}\sum_{j=1}^{N}\sin(\theta_j - \theta_i) \qquad i = 1,...,N \tag{1.3}$$

where ω_i is the natural frequency of each oscillator. In absence of any coupling, it is clear that $\theta_i(t) = \omega_i t$ so each oscillator would evolve freely according to its own rhythm. However, at a certain critical value of the coupling K, those oscillators that have very close natural frequencies will suddenly group together, locking their phases and moving in unison. With further increasing K, more and more oscillators are allowed into the locked cluster until all form a "single giant oscillator". This sort of collective behavior is illustrated in Figure 1.5 for sufficiently large K, where a population of N coupled phase oscillators that are initially distributed around the circle, after given some time, they appear exactly locked in phase. Kuramoto did not know it at the time, but his model would end up becoming the paradigm for synchronization phenomena with new results and insights being obtained from it more than thirty years later. Some of them will be even presented along this manuscript in Chapter 3. The main importance of this model lied in that it presented for the first time, a quite simplistic model that allowed for analytical solution and therefor to provide a theory that could help to understand exactly why oscillators that have a different internal rhythm end up moving in unison after they have become entangled. In this way, with such a simple but yet effective model, the flashes of fireflies, the chirping of crickets, and the firing of pacemakers were all unified and understood [Acebrón et al., 2005].

1.5 Spatio-temporal pattern formation in biology

Another shape that equation 1.2 may take is that of reaction-diffusion systems

$$\frac{d\boldsymbol{x_i}(t)}{dt} = \boldsymbol{f}(\boldsymbol{x_i}(t);\gamma) + K\sum_{j}^{N} A_{ij}(\boldsymbol{x_i} - \boldsymbol{x_j}) \qquad \text{with } i = 1,...,N \tag{1.4}$$

where some species $\boldsymbol{x_i}$ may diffuse through the nodes of the network. The most striking feature of these systems is that, under some circumstances, they can exhibit spontaneous symmetry breaking and self-sustained spatio-temporal structures. This breaking of the spatial symmetry of the medium, was first predicted by Alan M. Turing in 1952 [Turing, 1952], where he described how patterns in the form of stripes and spots can arise naturally from a homogeneous, uniform state once diffusion is taken into account. With this, Turing explained the basic process of morphogenesis (this is, the biological process by which a cell, tissue or organism develops its shape), by stating the necessity of the diffusion of two different chemical signals with different diffusion rates, one slower that activates growth and other one much faster that inhibits it. As these conditions are quite ubiquitous in nature, the Turing instability present in reaction-diffusion systems represents one of the fundamental mechanisms that cause pattern-formation in biology [Koch and Meinhardt, 1994]. The Turing instability therefore can explain too the pigmentation so characteristic in animal skin: stripes in zebras and fish, spots in felines... Figure 1.6 shows some examples of Turing patterns, with spots in a

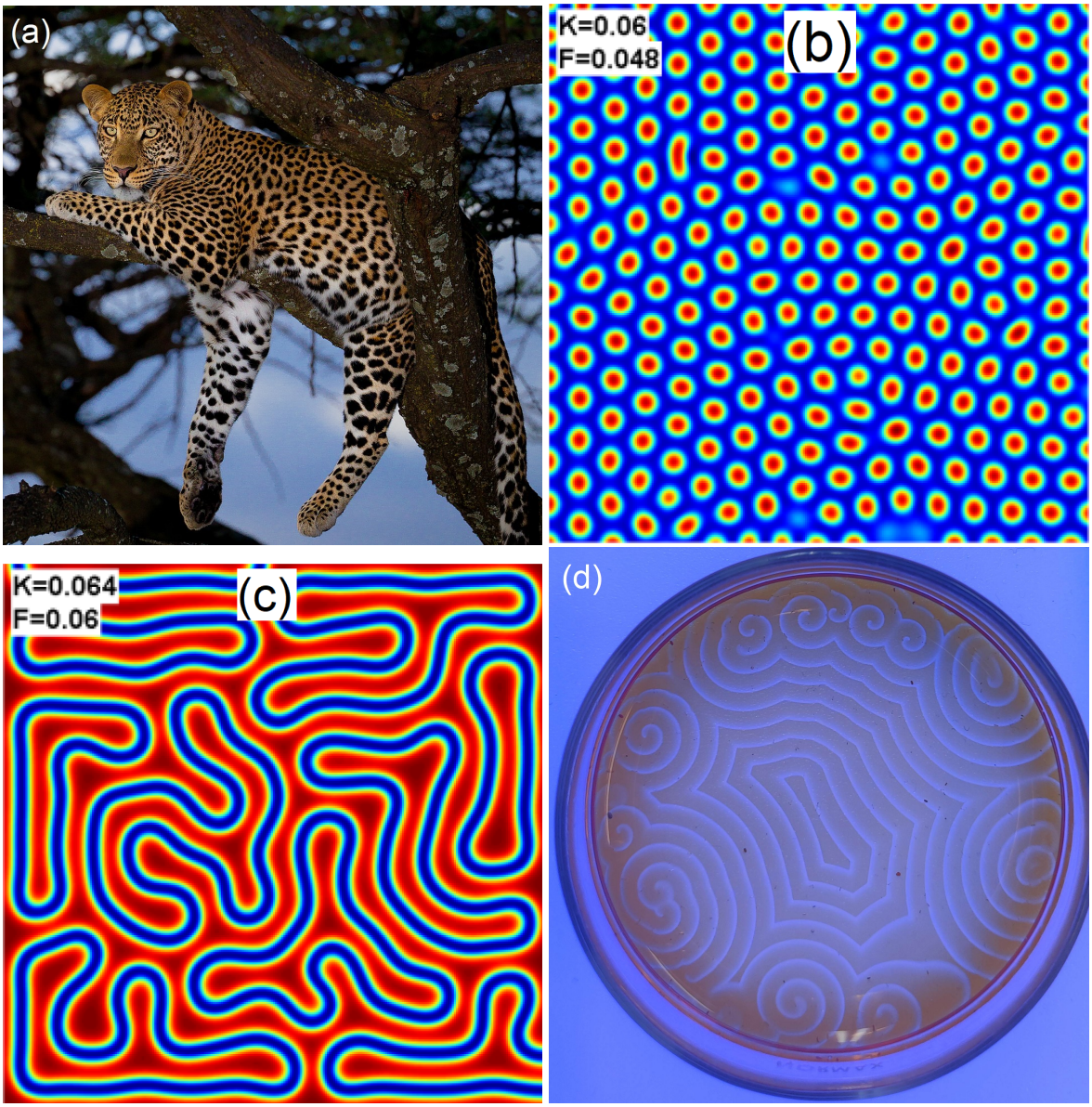


Figure 1.6: Examples of spatial Turing patterns: Black dots in a leopard skin (a), simulated dots (b) and stripes (c) with the CARD model. In (d), autowaves in the BZ reaction. Image (a) is originally by Sumeet Moghe from `https://en.wikipedia.org/wiki/Leopard#/media/File:African_leopard_male_(cropped).jpg`; (b) and (c) are lended by Dr. Alberto P. Muñuzuri, while image (d) is of own making.

USC
UNIVERSIDADE DE SANTIAGO DE COMPOSTELA

leopard skin (a) and dots and stripes in simulations of the CARD model (Cubic Autocatalytic Reaction-Diffusion) [Muñuzuri and Pérez-Mercader, 2022] (b,c). In this way, it is somehow paradoxical that the natural tendency of physical systems to drive the concentration gradients towards an homogeneous state, results in a spontaneous self-organization of the system under structured heterogeneous patterns.

On the other side, the experimental study of Turing patterns goes hand in hand with that of chemically active media, where there are usually activator and inhibitor reactants diffusing. This would be the case, for example, of the excitable dynamics of the Belousov-Zhabotinsky reaction [Zhabotinskii, 1964], from which Figure 1.1(d) and Figure 1.6(d) show examples also of its oscillatory behavior and its capability to sustain autowaves [Zhabotinsky and Zaikin, 1973]. The autowaves represent other of the fundamental mechanisms of nature to process and manage information transfer in biological systems [Vasiliev et al., 1987]. This constitutes them as the basis for the occurrence of morphogenesis in living organisms, and many other relevant examples as the propagation of nerve excitations and cardiac pulses in the heart's pacemaker cells [Zhabotinsky and Zaikin, 1973, Aliev and Panfilov, 1996, Gray and Jalife, 1996].

The Belousov-Zhabotinsky reaction will be a core element in our thesis, as its ability to show oscillations can be exploited to study synchronization phenomena. In Chapter 2, Methods, we will dedicate a whole section to review its experimental background and theory, as it will be the main object of study of Chapters 4 and 5. On the other hand, in Chapter 6, we will relate the symmetry breaking capacity of the Turing instability to induce differentiated patterns, with the social phenomenon of opinion polarization. Therefore, the explicit conditions necessary for a reaction-diffusion system to undergo the Turing instability are also described in detail in Chapter 2.

1.6 Epidemic processes in networks

Finally, the study of epidemic spreading dynamics on top of complex networks has been an extensive field of research within the complex systems literature, being a topic covered in several books and reviews [Keeling and Eames, 2005, Barrat et al., 2008, Pastor-Satorras et al., 2015]. One usual approach here is to consider that each node of the network is a single individual and that the edges between them are face-to-face interactions that occur daily, modelling the infective transmission of the disease as a stochastic process that occurs with a certain probability through the edges of the network. This scheme traces the mobility of the individuals [Wang et al., 2011], allowing for simulations of entire cities that scale down to the individual interactions with their closest circles and local neighborhoods. These interactions can be even more refined by adding geographical and demographical data to the nodes and simulating the daily interaction patterns [Perez and Dragicevic, 2009]. With this information at hand, one can effectively simulate the outcome of vaccination strategies targeting specific nodes or group of nodes [Dezső and Barabási, 2002, Martín et al., 2011], or analyze how non-pharmaceutical interventions (such as social distancing or mobility restrictions) can hinder the spread of the viral disease [Hoertel et al., 2020, Carballosa et al., 2020]. Note that these strategies that aim to restrain the diffusion of the epidemic dynamics usually imply altering the connectivity pattern of the network, either by blocking nodes that act as hubs or super spreaders within the network or by cutting down the number of interactions and/or edges between the nodes [Xiong and Li, 2017]. A different scheme considers nodes as entities where large subpopulations of individuals live, as is illustrated in Figure 1.7(a). In this way one

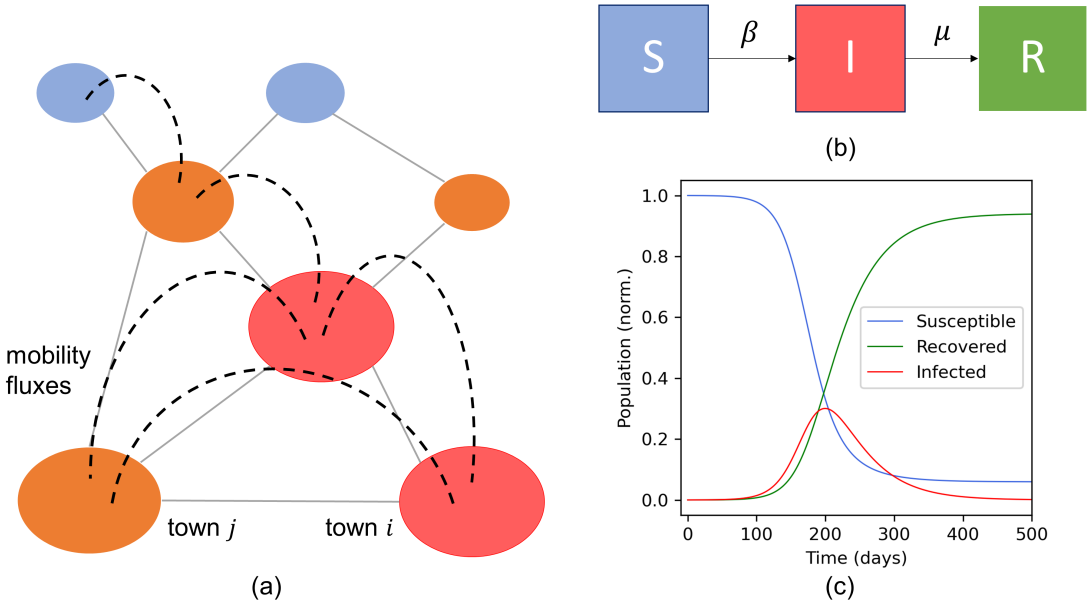


Figure 1.7: (a) Schematic of a metapopulation model, where each circle corresponds to a different population. In each town are nested the dynamics of the SIR model (b), where β represents the infectivity rate and μ the recovery rate. An example of the time evolution of its dynamics is shown in panel (c).

can attribute certain geographical characteristics to the nodes to naturally include the spatial distribution of a set of localities within a territory. This approach is known as *metapopulation network models* [Watts et al., 2005, Colizza et al., 2007, Colizza and Vespignani, 2008] and here the infective transmission process occurs locally, where one could think of individuals as particles interacting with each other. At the same time, these individuals are allowed to simultaneously travel through the edges of the network according to a set of rules and diffusing the disease through multiple nodes. These network models also allow the possibility of considering a deterministic nature to the infection process instead of the stochastic one, exploiting the features of the classic family of SIR-like models [Anderson and May, 1991] with an added spatial dimension [Calvetti et al., 2020].

The classic SIR model distributes the population into three exclusive compartments or boxes: Susceptible (S), Infected (I) and Recovered (R). Whenever there is an interaction between the first two, the probability of spreading the disease is given by the infectivity rate β. Simultaneously, infected individuals have a chance μ of being recovered at each time step. This is summarized in the diagram of Figure 1.7, along with the typical dynamics of the model. An important assumption of these models is that the whole population is homogeneously distributed within each compartment, and therefore all individuals from compartment S interact with all of compartment I. On one hand, if we are considering all the population of a country, this assumption can be partly overcome with the inclusion of the metapopulation network, breaking the spatial homogeneity and simulating the dynamics of the epidemics in a large heterogeneous population in a computationally affordable way. In Chapter 7, we consider these metapopulation network models to analyze the geographical spread of COVID-19 across the territories of Galicia and Spain. In this way, each of the nodes drawn in Figure 1.7(a) would correspond to each municipality, and the links would account for mobility flows between individuals. On

the other hand, if we aim for lower populations as just the ones in a city or less, introducing explicit network structures as the ones commented at the beginning of this subsection is a great choice to account for heterogeneities in the contact rates. This, is what we will do later on in Chapter 8.

USC
UNIVERSIDADE
DE SANTIAGO
DE COMPOSTELA

Chapter 2

Methods

In this chapter we introduce different aspects that will be used along the whole dissertation. We start by reviewing the basics of graph theory and several types of different network topologies. Then, we introduce the Kuramoto model for networks of phase-coupled oscillators, detailing the basic concepts of collective synchrony needed for the first part of the thesis. After this, some background on the history and the dynamics of the Belousov-Zhabotinsky chemical reaction is given. Finally, we outline the theoretical basis of the linear stability analysis needed to understand the later parts of this work.

2.1 Graph theory and complex networks

Another cornerstone of this thesis will be the mathematical representation of physical systems in the form of networks or graphs, where the system's elements are represented through nodes and their interactions through links. In general terms, the information on whether any two elements i and j from the system are connected is stored in the $N \times N$ adjacency matrix A_{ij} as follows

$$A_{ij} = \begin{cases} 1, & \text{if } i \text{ and } j \text{ are connected} \\ 0, & \text{if not} \end{cases} \tag{2.1}$$

or $A_{ij} = w_{ij}$ in case there are weighted links. In other words, the adjacency matrix contains the structure of the whole network, with any given row i being the list of connections of node i.

Summing across the elements of the rows or the columns, we obtain a first measure of how important is a given node within the total network in terms of its *connectivity degree*:

$$k_i = \sum_{j}^{N} A_{ij} \tag{2.2}$$

Unless the links are directed, the matrix A_{ij} is symmetric and therefore either the rows and the columns give the connectivity list. If they are directed however, the rows give the *out* connectivity, those nodes to which i is pointing to; while the columns give the *in* connectivity, those nodes that are pointing to i. In this case,

USC UNIVERSIDADE DE SANTIAGO DE COMPOSTELA

$$k_i^{in} = \sum_j^N A_{ij} \qquad\qquad k_i^{out} = \sum_j^N A_{ji} \tag{2.3}$$

When characterizing the network, it is of interest to talk about node and link centrality. In the first case, a preliminar measure of node centrality comes directly from the connectivity distribution, the largest the connectivity degree, the more central is the node. To understand link centrality however, we first need to talk about distances and *paths*. In a complex network there are no physical locations and therefore we must use the number of links between any two nodes to establish a metric of "distance". To reach a random node j from a given node i, there can be multiple paths that can be followed. Thus, we define the **shortest path length** ℓ_{ij} as the minimal number of links needed to reach node j from node i. Notice that there can be multiplicity in the number of shortest paths that connect nodes $i-j$. In function of the number of shortest paths that cross a given node or link, one can also determine the degree of centrality of that element, with this definition usually known as the *betweenness centrality*. In this way, the betweenness centrality measures how important is a given node or link in terms of the information flow. For example, if there is only one link connecting two otherwise disconnected parts of the network, all shortest paths between the parts must go through that link giving it a high value of centrality. Another important notion that affects information flow in graphs is that of **clustering**, which refers to the density of links in the neighborhood of a given node. Basically, if the neighbors of node i are all connected between themselves, then node i has a clustering coefficient of $C_i = 1$. An easier way to interpret this notion is geometrically, counting the number of closed triangles in which node i is a member of. The clustering coefficient then becomes this number, T_i, over the total possible of triangles that the node i could be a member of based on its degree k_i:

$$C_i = \frac{T_i}{k_i(k_i-1)/2} \tag{2.4}$$

To characterize the macro-scale properties of the network, it is usual to talk about the averages of the previous quantities. On one hand, knowing the size of the network N, the average connectivity of the network $\langle k \rangle$ gives you information on how connected the network is, while the average clustering coefficient $\langle C \rangle$ gives an overall idea of how densely connected are the nodes locally. On the other hand, the average shortest path length $\langle \ell \rangle$ tells about how close the nodes are and how fast the information can diffuse in the network.

Attending now to network topology, in function of how the network is formed, the shape of the connectivity distribution $p(k)$ may differ completely (this is, the probability of randomly choosing in the network a node with degree k). In order to explain and classify the different topologies observed in real networks, the following models were proposed and studied in time over the evolution of the field.

- **Regular networks**. Here the connectivity is homogeneous and every node has the same number of connections. Regarding structure, here we can find nearest neighbor connections in the form of rings, grids or lattices but also fully connected graphs, where each node is connected to all the others.

- **Erdos-Renyi networks (ER)** [Erdös and Renyi, 1959]. This model starts with a set of N isolated nodes, and for each possible pair, there is a binomial probability p that they are

connected. In this way one obtains a **fully random** network.

- **Watts-Strogatz networks (WS)** [Watts and Strogatz, 1998], lie between order and randomness. This model starts also with a set of N nodes connected with their k nearest-neighbors in a ring topology. Afterwards, for each link there is a probability p_r of being rewired to a random node of the network creating a *shortcut*. This model corresponds therefore to an intermediate stance between the previous two and holds two features usually found in social networks: most ties being local (high clustering) but overall short distances between any two nodes given by the shortcuts. Think for example about your circles of close friends, family and coworkers. In each circle they all know each other (so the clustering is high) but there might be no connection at all between the different circles. However, you are central in connecting the three groups in a distance of just two links of separation.

- **Scale-free networks (SF)** are characterized by a power-law in the connectivity distribution $p(k) = Ck^{-\gamma}$, with γ being a real number between $2 \leq \gamma \leq 3$ and C a scaling constant. For these values, while there is a vast majority of low-connectivity nodes, there exists a few number of nodes at the tail of the distribution that possess a large amount of links. These latter nodes are termed *hubs* and are highly central to the network. The original understanding of this topology came from the Barabasi-Albert model [Barabási and Albert, 1999], who proposed that large networks self-organize into this scale-free state by means of growth and preferential attachment. This is, new nodes that are incorporated to the network do not do it randomly but looking for nodes that already have a high connectivity. That most real networks seem to arrange into this scale-free distribution [Albert and Barabási, 2002], was the discovery that fueled the emergence of the field as we described it above.

In Figure 1.4 of the Introduction we had already teased these four type of topologies drawing representative examples. Here we show in Figure 2.1 the connectivity distributions for each one, this is, the probability $p(k)$ of randomly picking a node which has connectivity k. Note that for the SF, we show the cumulative probability distribution in logarithmic scale for visualization purposes. From here, we can grasp that both ER and WS topologies have clearly defined first and secord order moments of the connectivity, this is, the mean $\langle k \rangle$ and variance $\langle k^2 \rangle$. This does not occur for the SF, where the average connectivity is measurable but it does not tells us much about how the connectivity is distributed. Here, we see how low connectivity nodes form the majority as they have the highest probability to be randomly picked, while high connectivity nodes, the hubs, have an extremely low frequency. Furthermore, if the power-law exponent γ of the distribution is found between 2 and 3, the second order moment $\langle k^2 \rangle$ diverges [Barabási and Pósfai, 2016a]. Therefore computing this exponent is a rather proper measure to characterize the distribution, which can be easily done by applying logarithms to the expression and then performing a linear fit to the data. This gives you the γ exponent of the scale-free distribution as the slope of the fit (see the red line in Figure 2.1).

$$\log(p(k)) = \log(C) - \gamma log(k) \tag{2.5}$$

USC DE COMPOSTELA

These are just the simplest configurations for each type of topology, but in the literature one can find a myriad of network building models, each one more sophisticated than the last. In general, using regular networks is of high interest when the focus is to deeply comprehend the

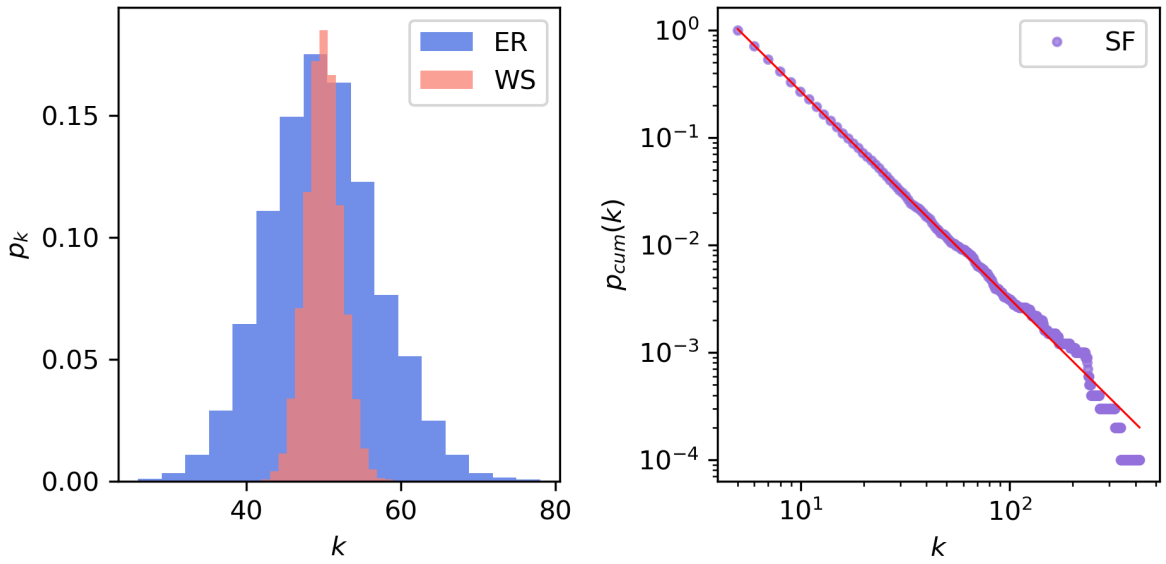


Figure 2.1: Network connectivity distributions for the Erdos-Renyi (ER), Watts-Strogatz(WS) and Scale-free (SF). We do not show the regular network as it would show a unique bar of probability 1 at a given value k, as all nodes have the same connectivity.

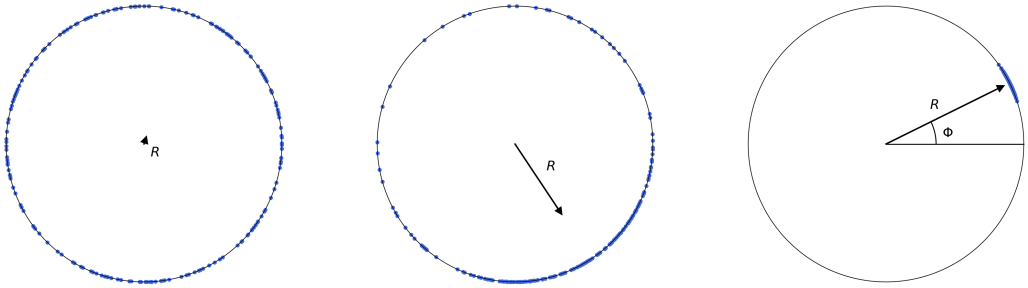
complexity of the nonlinear dynamics of a large set of coupled nodes. In this sense, the fully connected network is a common approach when first approaching the problem or testing new features of a model as it reduces any possible heterogeneity induced by the network. Once the effect of coupling multiple dynamic units is understood, one is ready to consider more complex architectures and a good start is the opposite case: a fully random structure. From there the Watts-Strogatz model offers a suitable modelling approach to test all the scenarios in between. Finally, using scale-free networks is the most complex case considered here, where the hubs act as super-spreaders of information and the divergence of the second order moment affect significantly the critical transitions. Regarding the network construction for our investigations, we will use the open source `Python` library `networkx` which contains efficient algorithms to generate from scratch adjacency matrices of arbitrarily size N according to each network model.

Within the scope of network theory it is also important to understand degree correlations, network robustness and the presence of modularity and communities within the network. These topics are thoroughly covered in the books and reviews mentioned already ([Boccaletti et al., 2006],[Barabási and Pósfai, 2016b]) and since we have not considered them in our thesis we will not delve into them now, although we encourage the network enthusiast to carefully check them out.

2.2 The Kuramoto model for synchronization phenomena

The study of collective dynamics of periodic oscillators will be the main focus for the first part of this thesis. Therefore, we review here for the unfamiliar reader in the topic, the basic results derived from the classical Kuramoto model, the paradigm of synchronization phenomena. Let us start by considering a population of N phase-coupled oscillators whose

USC UNIVERSIDADE DE SANTIAGO DE COMPOSTELA



(a) $K = 0$ **(b)** $K = 0.5$ **(c)** $K = 10$

Figure 2.2: Geometric interpretation of the order parameter (eq. 2.7) and the global phase Φ for increasing levels of the coupling K.

phase $\theta_i(t)$ evolves in time as:

$$\dot{\theta}_i = \omega_i + \frac{K}{N}\sum_{j=1}^{N}\sin(\theta_j - \theta_i) \quad i = 1,...,N \tag{2.6}$$

with ω_i being the natural frequency of each oscillator, distributed accordingly to a given probability density $g(\omega)$. The functional form of $g(\omega)$ affects considerably the behavior of the model, so for now we will assume it to be symmetric around zero and unimodal. To keep it simple, the coupling between any two oscillators i and j of the network is considered to be purely sinusoidal and the system is arranged in a regular, all-to-all network with equal weights K between the oscillators. This means that each oscillator in the system interacts with all the others and with the same strength, but note that one can consider any other type of interaction functions, different weights and network configurations. In the absence of coupling, each oscillator will evolve independently at its own rhythm given by their internal frequency $\dot{\theta}_i = \omega_i$. On the other hand, once the coupling is turned on, the oscillators will experience an attractive force that will pull them together once a threshold in the coupling strength is overcome.

Now, because of the rotational symmetry in the model, we can consider a suitable change of variable to a rotating frame at frequency ω_c, $\theta_i \to \theta_i - \omega_c t$ and set $\omega_c = 0$ to be the mean frequency of the system. This transforms eq. 2.6 to an equivalent system where the ω_i denotes deviations from the mean frequency. In this sense, we can visualize the dynamics of the phases as a set of points drifting across the unit circle in the complex plane, as pictured in Figure 2.2 (a).

To measure the level of synchronization of the whole population, Kuramoto proposed the following macroscopic order parameter,

$$R(t)e^{i\Phi(t)} = \frac{1}{N}\sum_{j=1}^{N} e^{i\theta_j(t)} \tag{2.7}$$

where $\Phi(t)$ is the average phase of the synchronized cluster and the modulus $R(t)$ is a value between 0 and 1 that tells the degree of coherence in the system in time. Therefore, the time averaged $\langle R(t)\rangle$ it is usually referred to as the Kuramoto order parameter. Following the geometric representation in the complex plane, the modulus and direction of $\vec{R}$ indicates the degree and average position of the synchronized cluster, and Φ its phase (see Figure 2.2 (c)). If

USC SANTIAGO

the oscillations are scattered around the circle, then $R \simeq 0$, since the average of the individual oscillations is incoherent. On the other hand, if all oscillators are phase-locked, they act, in the words of Kuramoto, as a ´´single giant oscillator" with phase Φ and thus $\|\vec{R}\| = 1$.

Using this quantity, one can derive a mean-field expression of equation 2.6 multiplying by $e^{-i\theta_i}$ both sides and equating the imaginary parts:

$$\Im\left(Re^{i(\Phi-\theta_i)}\right) = \Im\left(\frac{1}{N}\sum_{j=1}^{N} e^{i(\theta_j-\theta_i)}\right) \tag{2.8}$$

obtaining,

$$R\sin(\Phi-\theta_i) = \frac{1}{N}\sum_{j=1}^{N}\sin(\theta_j-\theta_i) \tag{2.9}$$

which we can insert in 2.7 to give

$$\dot{\theta}_i = \omega_i + KR\sin(\Phi-\theta_i) \qquad i = 1,...,N \tag{2.10}$$

In this form, each oscillator interacts with all the others through the mean field variables R and Φ, establishing a positive feedback loop with the collective dynamics. Now, the phase of θ_i is pulled toward the mean phase Φ of the system instead of the phase of other oscillators, and as more oscillators are synchronized, the strength of the coupling increases proportionally to R. But how does R evolve in time and with the coupling parameter K? For illustration, let us suppose that we fix the natural frequency distribution of $g(\omega)$ to be a Gaussian with very long tails, and vary the coupling K. We see from simulations (Figure 2.3) that when this coupling is below the critical one K_c, the oscillators act incoherently and $R(t)$ decays to a value of $\simeq N^{-1/2}$. However, for $K \geq K_c$, the incoherent state becomes unstable and $R(t)$ grows exponentially. This is the result of the formation of a small cluster of oscillators near the center of the frequency distribution, that lock together at the mean frequency ω_c generating the collective oscillation. Oscillators in the tails of the distribution however, are still too far away to adapt their internal rhythm and so, they run near their natural frequency drifting apart from the synchronized cluster. This state is usually referred to as the partial synchronized state, whose level of synchronization grows with increasing values of K as shown in Figure 2.3. But why does this happen? The main feat of the Kuramoto model was that it allowed to understand these numerical results by solving analytically the system. In this way, we can fully characterize the order parameter $R(K)$ in function of the coupling K and calculate the critical coupling K_c at which the onset of synchronization begins.

In a steady solution, we can assume that the mean field variables $R(t)$ and $\Phi(t)$ are constant, the first one denoting a given value of synchronicity and the second one the phase of the global cluster rotating uniformly at frequency Ω. Because of this rotating frame, we can set $\Phi = 0$ without loss of generality and write eq. 2.10 as

$$\dot{\theta}_i = \omega_i - KR\sin(\theta) \qquad i = 1,...,N \tag{2.11}$$

To solve this equation for the resulting motion of all the oscillators we will apply the strategy called as the *self-consistent approach*, since R is now both a parameter and a result of the collective dynamics. Depending on the size of $\|\omega_i\|$ relative to KR, we can now distinguish two types of long term behaviors. On one hand, the phase-locked oscillators at frequency $\Omega = 0$

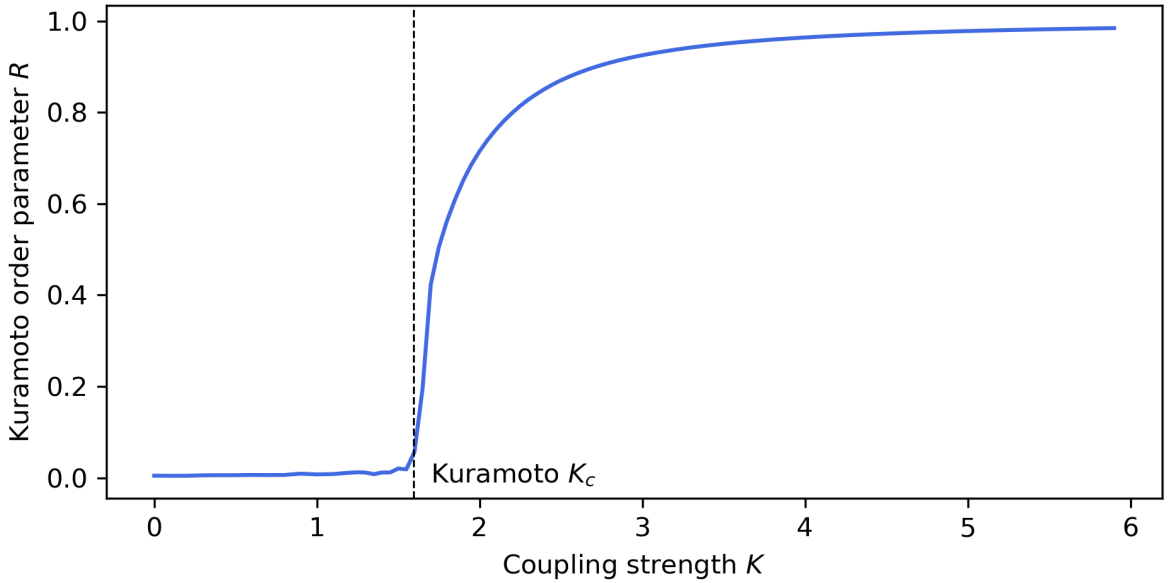


Figure 2.3: Numerical simulations of the Kuramoto order parameter R versus the coupling strength K for a network of $N = 5 \cdot 10^4$ oscillators. The transition to the full-synchronization regime is of second-order type, characterized by a critical coupling K_c at which the order parameter starts to grow continuosly but exponentially. The black dashed line represents the critical value predicted by eq. 2.15 in the thermodinamic limit, which agrees quite well with our numerical results.

must satisfy then $\dot{\theta}_i = \Omega = 0$ and therefore we obtain that $\omega_i = KR\sin(\theta_i)$, which is itself a stable fixed point of the system (see the next section for the study of stability of fixed points). This condition will be satisfied by all those oscillators whose frequency $\|\omega_i\| \leq KR$, which will adapt their rhythm to the collective one. On the other hand, those that have $\|\omega_i\| > KR$ will be drifting around the circle at different velocities and accelerating near some phases and decelerating at others. As was advanced previously, the locked oscillators are the ones that correspond to the center of $g(\omega)$ while the drifting ones correspond to the tails. Increasing K therefore allows for a wider range of frequencies within the phase-locking condition, until all the population is absorbed into the single giant oscillator.

The existence of the drifting oscillators could seem to contradict the original assumption that our mean field variables R and Φ were constant, but this problem is actually solved if we demand that the drifting oscillators form a stationary distribution around the circle. In this way, individual contributions of oscillators that continue to move cancel each other and the centroid stays fixed. Imposing these conditions and deriving the contribution to the order parameter of each group [Strogatz, 2000], one finds that the contribution given by the drifting oscillators $\langle e^{i\theta}\rangle_{\text{drift}}$ actually vanishes, leaving only the contribution of the locked oscillators in the form of the following self-consistent equation for R:

$$Re^{i\phi} = R = \int_{-KR}^{KR} \cos(\theta) g(\omega) d\omega = KR \int_{-\pi/2}^{\pi/2} \cos^2(\theta) g(KR\sin(\theta) d\theta \tag{2.12}$$

where we used the previous condition that $\omega = KR\sin(\theta)$. The trivial solution $R = 0$ for any value of K corresponds to a completely incoherent state. A second branch of solutions corresponding to partially synchronized states is given by

USC DE COMPOSTELA

$$1 = K \int_{-\pi/2}^{\pi/2} \cos^2(\theta) g(KR\sin(\theta) d\theta \tag{2.13}$$

which bifurcates continuously from $R = 0$ at a value $K = K_c$ obtained by letting R approach to zero from the right, $R \to 0^+$. In this way, we can solve the integral as,

$$1 = K_c g(0) \int_{-\pi/2}^{\pi/2} \cos^2(\theta) d\theta = K_c g(0) \frac{\pi}{2} \tag{2.14}$$

obtaining the mean field expression for the critical coupling at the onset of synchronization,

$$K_c = \frac{2}{\pi g(0)} \tag{2.15}$$

beyond which $R > 0$. If we consider a Gaussian distribution centered at zero for the natural frequencies, then we can obtain $g(0)$ as

$$g(0) = \frac{1}{\sqrt{2\pi}\sigma}$$

with σ the standard deviation of the distribution. For the simulations shown in Figure 2.3, the predicted critical threshold given by eq. 2.15 is $K_c = 1.6$, marked by the vertical dashed line. We can see then that the numerical simulations clearly verify this prediction. Besides, near the onset, it can also be computed that the order parameter obeys the usual square-root scaling for mean field models with a power law equal to $1/2$:

$$r \sim (K - K_c)^{1/2} \tag{2.16}$$

Because of the good agreement between numerical simulations and theoretical predictions, the Kuramoto model became a breakthrough for understanding the synchronization in large populations of oscillators. This quickly gave raise to hundreds of papers in the field, exploring many different configurations. Between these, an important general result that will be considered later in Chapter 3 relates to the presence of higher order armonics in the interaction function Γ_{ij} that connects any two oscillators i, j. It was observed that when Γ_{ij} has at least two harmonics, this leads naturally to the emergence of clustering states [Hansel et al., 1993, Okuda, 1993, Komarov and Pikovsky, 2014], this is, that the ensemble of phase oscillators split into two groups, usually equally populated and located in phase opposition.

Another increase in complexity comes from considering that the phase oscillators are not coupled in a regular all-to-all configuration but in a more complex network architecture as the ones seen in the previous section. There the coupling between two connected oscillators i, j becomes $\sigma_{ij} = K/k_i$, with k_i being the degree of node i. In complex systems science, understanding the deep relationship between function and structure is one of the main challenges, where investigating synchronization dynamics is of high interest as it bridges both elements. In brain networks, for example, synchronization represents a fundamental dynamical feature that increases the effectiveness of interactions between brain regions, modulating the cortical interactions and being in overall of great importance for the brain's cognitive function [Fries, 2005]. Between other things, through synchronization studies it has been

revealed that at a cortical level the network functioning displays highly clustered organization [Hilgetag and Kaiser, 2004, Zemanová et al., 2006], while abnormal high synchronous activity of large neuronal ensembles is related to pathological situations like epileptic seizures [Lehnertz and Elger, 1998, Elger and Lehnertz, 1998, Kudela et al., 2003].

In [Arenas et al., 2008], they do an extensive review on the interplay between network topology and synchronization dynamics, from which here we will just highlight a couple of points to give some context. As we mentioned, the Kuramoto model can be easily extrapolated to heterogeneous networks as:

$$\dot{\theta}_i = \omega_i + \sum_J^N \sigma_{ij} A_{ij} \sin(\theta_j - \theta_i) \qquad i = 1, ..., N \tag{2.17}$$

where A_{ij} is the adjacency matrix as defined in eq. 2.1. One important result that can be derived from the mean field analysis to this equation shows that in the thermodynamic limit, the critical coupling at which the onset of synchronization starts strongly depends on the topology of the graph as [Arenas et al., 2008]:

$$\sigma_c = \frac{2}{\pi g(0)} \frac{\langle k \rangle}{\langle k^2 \rangle} = K_c \frac{\langle k \rangle}{\langle k^2 \rangle} \tag{2.18}$$

revealing that given a fixed mean connectivity, increasing the heterogeneity of the graph results in smaller values of σ_c, making easier the onset of synchronization. Furthermore, this result tells us that for scale-free networks with exponent $2 \leq \gamma \leq 3$, where the second order moment $\langle k^2 \rangle$ diverges, the critical coupling should vanish. This means that in scale-free networks, at least some minimal levels of synchronization appears instantaneously for any finite value of the coupling K. Another qualitative difference can be found in the synchronization patterns and the path to the fully synchronized state [Gómez-Gardeñes et al., 2007]. In a random Erdos-Renyi network, as the coupling σ is increased, a huge number of oscillators that are originally spread over the network become synchronized by pairs and small groups. Eventually, as the coupling is increased more, they drastically merge together forming a giant synchronized cluster. On the other hand, in a scale-free network, a giant synchronized component is formed quickly because of the hubs and single oscillators are continuously added with the increase of σ.

Finally, a further leap in complexity comes from considering group interactions as we introduced them in Figure 1.3. What happens now if instead of just interacting in pairs, the oscillators could interact in triads? In Chapter 3, the first with original results of this thesis, we embark on the journey of synchronization by considering an extension of this classical Kuramoto model to higher order interactions. We will explore in detail how the monotonous transition from the asynchronous state to the fully synchronous one (shown in Figure 2.3) abruptly changes with the inclusion of the three-body interactions. Coexistence of dynamical states, multi-stability and the emergence of several cluster states will be also found and explored, revealing all the complexity that is hidden in just one differential equation.

2.3 The Belousov-Zhabotinsky reaction

USC DE COMPOSTELA

Since its discovery between the 1950s and the 1960s, the Belousov-Zhabotinsky chemical reation has motivated a plethora of works with different recipes and setups because of its spatio-temporal properties in the form of waves and oscillations. Its complex non-linear

behavior has served as an experimental bedtest for periodic oscillator, birth of spiral waves, pattern formation, deterministic chaos and our main interest here: synchronization [Field and Burger, 1985, Epstein et al., 1998, Taylor et al., 2009]. Despite all its history of fruitful works and a Lenin prize in 1980, a harsh truth is that its discovery was originally not well received by the scientific community, and the father of the reaction died without knowing the importance of his creation.

This was in the 1950s, while the biophysicist Boris Pavlovich Belousov was trying to obtain an in vitro model of the Krebs cycle, he observed periodic oscillations of color between the oxidation states of the cerium (Ce^{4+} and Ce^{3+}) in a solution composed of sulfuric acid (H_2SO_4), bromate BrO_3^- and citric acid ($C_6H_8O_7$) as the organic substrate [Winfree, 1984]. However, closed homogeneous chemical systems should always evolve monotonously towards equilibrium and and so his reviewers demanded a more detailed explanation, stating that such sustained oscillations were *impossible*. After a second rejection years later, he resolved to withdrew his research on the reaction. His recipe however, circulated aimlessly around the university for several years until A. M. Zhabotinsky started to experiment with it. Zhabotinsky improved it changing some of its reactants and after profound investigations, he developed a much more detailed description of its mechanisms, setting the foundations for the nowadays well-known Belousov-Zhabotinsky reaction (BZ) [Zhabotinskii, 1964]. The thing was, that chemical oscillations are possible if one is far from thermodynamical equilibrium, as I. Prigogine had theorized some years before [Prigogine and Balescu, 1956].

The first kinetic model of the reaction appeared some years later in 1972 with the FKN model (Field, Köros and Noyes), who gave a detailed description of the chemical species and their interactions that are responsible for the cycles in the BZ reaction [Field et al., 1972]. The key processes however, can be summarized in the following three steps:

I The autocatalytic production of the bromous acid $HBrO_2$ by bromate BrO_3^- induces the oxidation of the metal-ion catalyst.

II Reduction of the metal-ion catalyst by the oxidation of the bromo-malonic acid BrMA plus bromide ion production Br^-.

III The bromous acid $HBrO_2$ reacts with the bromide to produce hypobromous acid HBrO. At this step, the autocatalytic oxidation is completely inhibited.

Steps I and II are therefore the ones responsible for the oscillations, while step III inhibits the process leaving the reaction in a refractory state, while the bromide does not decrease over a critical value that allows step I to happen again. The change in color of the reaction comes from the metal ion oxidizing from the lower to the higher state. Depending on the catalyst used, the observed color is different. For example, the color change between reddish and blue for the ferroin Fe^{2+} or between orange and transparent for the ruthenium Ru^{2+}. Besides, that the reaction allows different catalysts is so interesting since in this latter case, the ruthenium complex is photosensitive and can be excited by photons in the range of 450 nm. This means that tuning the intensity of light you can affect the dynamical rates of the reaction [Gáşpár et al., 1983], which in other words, means that you can control the oscillation period of your reactor.

Some years later, Field and Noyes reduced their highly complicated model so they could numerically and theoretically study the dynamics of the BZ reaction [Field and Noyes, 1974].

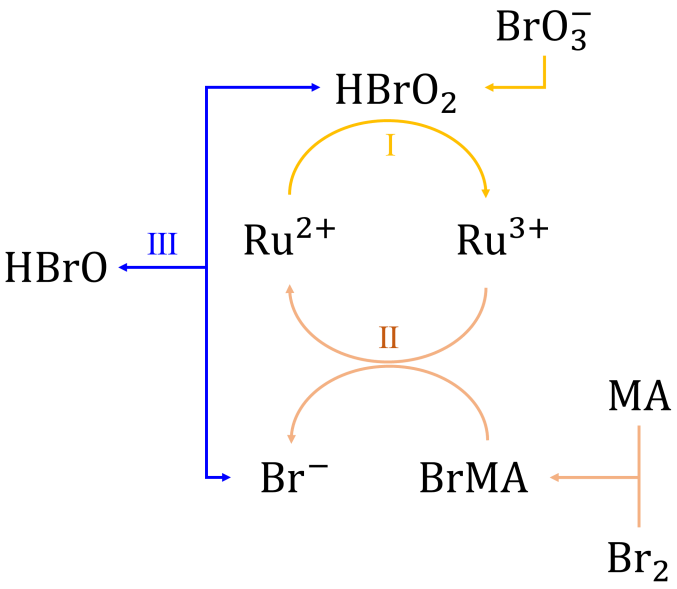


Figure 2.4: Schematic diagram of the key processes involved in the BZ reation. The bromous acid $HBrO_2$ is produced autocatalitically in step I, oxidizing the Ruthenium catalyst in the process. Then, the catalyst is reduced in step II because of the action of the bromo-malonic acid. Finally, the reaction between Br^- and $HBrO_2$ inhibits the autocatalytic oxidation of step I. This cycle repeats again when the concentration of Br^- decreases enough, and so the autocatalytic oxidation starts again.

This new model, named the *oregonator*, consisted just in three main dynamical variables: the activator X, corresponding to the concentration of $HBrO_2$, the inhibitor Y, Br^- and the catalyst Z. With this, the FKN was reduced to the following five steps:

$$A + Y \xrightarrow{k_1} X + P \qquad \text{activator production}$$
$$X + Y \xrightarrow{k_2} 2P \qquad \text{inhibition of the activator}$$
$$A + X \xrightarrow{k_3} 2X + 2Z \qquad \text{autocatalyst production of the activator}$$
$$2X \xrightarrow{k_4} A + P \qquad \text{decay of the activator}$$
$$B + Z \xrightarrow{k_5} fY \qquad \text{inhibitor production}$$

where A and B are the reactants BrO_3^- and MA (this is also the organic sustrate), which are considered to be in large excess and therefore changing very slowly in contrast to the dynamic variables. Plus, the parameter f is an adjustable stoichiometric factor to modulate the reaction dynamics. With all this, we obtain the kinetic equations that correspond to the following three

USC UNIVERSIDADE DE SANTIAGO DE COMPOSTELA

nonlinear diferential equations of the *oregonator* model:

$$\begin{cases} \frac{dX}{dt} = k_1AY - k_2XY + k_3AX - 2k_4X^2 \\ \frac{dY}{dt} = -k_1AY - k_2XY + \frac{f}{2}k_5BZ \\ \frac{dZ}{dt} = 2k_3AX - k_5BZ \end{cases} \tag{2.19}$$

These equations can be further simplified by considering the dimensionless transformation of [Tyson, 1979] which consists in

$$X_0 = \frac{k_3A}{2k_4}, \qquad Y_0 = \frac{k_3A}{k_2}, \qquad Z_0 = \frac{(k_3A)^2}{k_4k_5B}, \qquad T = \frac{1}{k_5B}$$

and taking the parameters

$$\varepsilon = \frac{k_5B}{k_3A}, \qquad \delta = \frac{2k_4k_5B}{k_2k_3A}, \qquad q = \frac{2k_1k_4}{k_2k_3}, \qquad f$$

we recover the following dimensionless variables

$$x = \frac{X}{X_0}, \qquad y = \frac{Y}{Y_0}, \qquad z = \frac{Z}{Z_0}, \qquad \tau = \frac{t}{T}$$

that transform equations 2.19 into:

$$\begin{cases} \frac{dx}{dt} = qx - xy + x - x^2 \\ \frac{dy}{dt} = -qy - xy + fz \\ \frac{dz}{dt} = x - z \end{cases} \tag{2.20}$$

With this differential equations, we can recover the oscillatory dynamics of the BZ reaction as shown in Figure 2.5(a), with the corresponding stable limit-cycle drawn in panel (b). The basic mechanisms explained by the FKN model and the dimensionless oregonator model will be our cornerstones for studying the synchronization of chemical oscillators. More in particular, in Chapter 4, we will transform equations into a spatially extended setup where a population of N chemical oscillators can flow and interact with each other through the surrounding chemical solution.

2.3.1 Photosensitive variant of the BZ reaction

On the other hand, in Chapter 5 we will focus on the influence of light on the Belousov-Zhabotinsky reaction. As we advanced earlier, several works with the Ruthenium complex as catalyst of the reaction reported both photoinhibition and photoinduction of oscillations when exposed to visible and ultraviolet light (see e.g. [Gáspár et al., 1983, Reddy et al., 1994, Hanazaki et al., 1995, Muñuzuri et al., 1996, Kádár et al., 1997]). In function of the illumination intensity ϕ that reaches the reaction, its dynamical properties change considerably. We illustrate this in Figure 2.6. For low intensities, the reaction shows the regular oscillatory dynamics. As the light intensity is increased (see red dashed line), the periods of oscillations also increase until a certain value, where oscillations cease as the medium becomes excitable . Here, the propagation of waves can still occur but only if they are originated

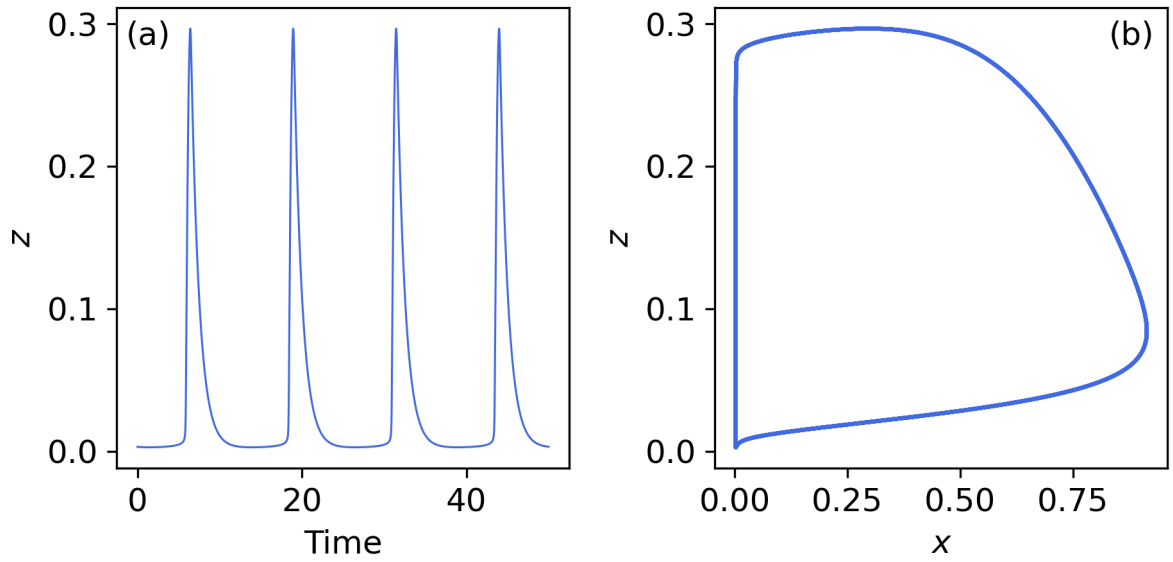


Figure 2.5: Simulated dynamics of the Belousov-Zhabotinsky reaction with the oregonator model. IN (a), oscillations in the concentration of the catalyst z (a), and in (b), the limit-cycle in the phase space of (x, z).

elsewhere, such as in a shadowed region with less light intensity. Finally, if light is increased sufficiently, the wave propagation can be inhibited completely.

The mechanism behind either photoinduction or photoinhibition has been explained by [Kádár et al., 1997], and both start with the absorption of photons by the Ruthenium complex $Ru(bpy)_3^{+2}$:

$$\text{Ru(II)} + h\nu \rightarrow \text{Ru(II)}^* \tag{2.21}$$

with h the Planck constant and ν the photon's frequency. After the photoactivation of the ruthenium, in function of the light intensity and the initial concentrations of the BZ reactants, we can observe two mechanisms,

I $\text{Ru(II)}^* + \text{BrMA} \rightarrow \text{Ru(III)} + \text{Br}^- + \text{products}$

II $\text{Ru(II)}^* + \text{Ru(II)} + + \text{BrO}_3^- + 3\text{H}^+ \rightarrow 2\text{Ru(III)} + \text{HBrO}_2 + \text{H}_2\text{O}$

The first one is the inhibitive channel, observed at high level of light intensity where the excited catalyst is oxidized by the bromomalonic acid (BrMA) producing free bromide ions. At the same time, as we saw in the diagram of Figure 2.4, the oxidized catalyst Ru(III) also reacts with BrMA to produce more free bromide ions. The higher concentration of bromide ions increase the time needed to reach the critical threshold where the autocatalytic production of bromous acid $HBrO_2$ is allowed and thus, increasing the oscillation period. In the second process, for low levels of light intensity, the excited catalyst interacts with the bromate ions to produce the autocatalytic species $HBrO_2$. This additional bromous acid consume bromide ions helping to reach the critical threshold at a faster rate and thus, making the oscillator to fire earlier.

In this way, we can alter the oscillators using short pulses of light at different intensities, either reducing it suddenly to excitate the oscillators or increasing it to estimulate the production of bromide ions and delaying the firing. In Chapter 5, using this procedure, we shall focus on a experimental setup that attempts to build a network of adaptive photo-chemical oscillators

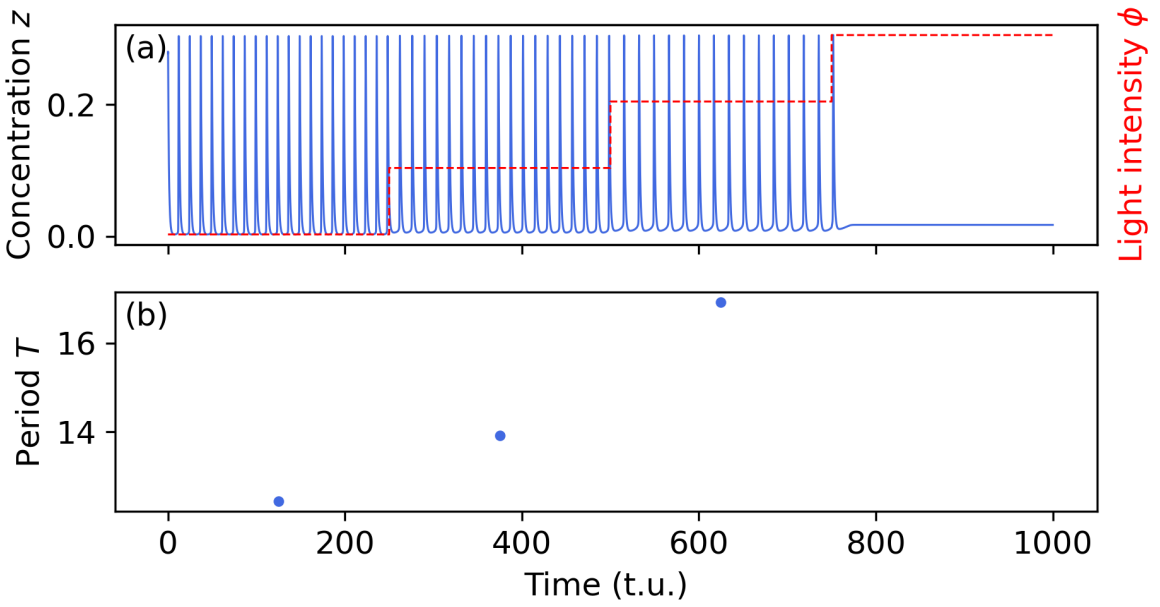


Figure 2.6: (a) Effects of the light intensity (red dashed line) in the dynamics of the Belousov-Zhabotinsky reaction simulated with a variation of the oregonator model. The increasing oscillation period with the light intensity is shown in panel (b).

coupled by light impulses, using the ruthenium as the metal-ion catalyst of each individual oscillator.

USC
UNIVERSIDADE DE SANTIAGO DE COMPOSTELA

2.4 Linear stability analysis. Equilibrium points and growth factors

In the later chapters of this thesis (namely 6 and 7), we will analyze how perturbations to the equilibrium state evolve in function of the network structure. This is especially useful for determining Turing patterns since it will explicitly give the conditions under which the instability occurs.

Let us start proposing the following two variable reaction-diffusion model in a spatially extended system:

$$\begin{cases} \frac{\partial u}{\partial t} & = f(u,v) + D_u \nabla^2 u \\ \frac{\partial v}{\partial t} & = g(u,v) + D_v \nabla^2 v \end{cases} \tag{2.22}$$

where D_u, D_v are the simple diffusion coefficients and ∇ is the Laplacian operator that accounts for second order partial derivatives in u and v. In absence of diffusion, the fixed points of the system will be determined by,

$$\begin{cases} f(u^*,v^*) & = 0 \\ g(u^*,v^*) & = 0 \end{cases} \tag{2.23}$$

where there can be one or more solutions depending on the system. If the trajectories of the dynamics converge to a certain fixed point, then that fixed point is said to be stable. We can assess this stability by introducing a perturbation $(\delta u, \delta v)$ and studying the flow of the dynamics in its vecinity through the system's Jacobian evaluated at the fixed point,

$$J\big|_{(u^*,v^*)} \equiv J^* = \begin{pmatrix} f_u & f_v \\ g_u & g_v \end{pmatrix}\Bigg|_{(u^*,v^*)} \tag{2.24}$$

If the perturbation grows, then the fixed point is not stable and viceversa. The exact conditions for stability are given by [Strogatz, 2015]:

$$\tau(J^*) = f_u^* + g_v^* < 0 \tag{2.25}$$

$$\Delta(J^*) = f_u^* g_v^* - f_v^* g_u^* > 0) \tag{2.26}$$

where τ is the trace, Δ the determinant and the superindex * indicates that those functions are evaluated at the fixed point. Note that since the functions $f(u,v)$ and $g(u,v)$ also depend on the system's parameters, it is common that through variations in the parameters the fixed points suddenly lose their stability, usually in favor of another fixed point. In this case, we will talk about a phase transition occurring via a local bifurcation, where the system undergoes a significant qualitative change in its behavior. This is of key importance in this work, since in many of the following chapters we will explore the phase space of the models in function of the control parameters. Every time we will encounter a phase transition from one dynamical regime to the next, it will imply that there was an interchange of stability between the system's solutions. There are several types of bifurcations, depending on how this stability is lost or which is the new stable state. For example, we will encounter the so-called *transcritical* bifurcation, where a fixed point interchanges its stability with another at a critical value. This would be the case for the transition from the asynchronous to the synchronous regime in the Kuramoto model that we just recently discussed. Another common bifurcation is the

USC DE SANTIAGO

saddle-node, where a pair of fixed points with opposite stability annihilate each other at the critical value. We will also encounter the *Hopf* bifurcation, where the system interchanges its stability from a fixed point to an oscillating solution in the form of a limit cycle. This is the responsible (for example) for the emergence of oscillations in the oregonator model.

Going back to the reaction-diffusion dynamics, let us assume that we have found the fixed point (u^*, v^*) and determined that it is indeed stable. We are interested now in studying if its stability changes because of the introduction of diffusion instead of a change int the parameters. Again, analyze this by introducing a small perturbation to the equilibrium point,

$$\delta \mathbf{x} = \begin{pmatrix} \delta u \\ \delta v \end{pmatrix} = \begin{pmatrix} u - u^* \\ v - v^* \end{pmatrix} \tag{2.27}$$

substituting this perturbation in eqs.2.22 and linearizing the system around the fixed point we obtain,

$$\begin{cases} \frac{\partial \delta u}{\partial t} & = f_u^* \delta u + D_u \nabla^2 \delta u \\ \frac{\partial \delta v}{\partial t} & = g_v^* \delta v + D_v \nabla^2 \delta v \end{cases} \tag{2.28}$$

which in vector notation can be rewritten simply as:

$$\frac{d\delta \mathbf{x}}{dt} = J^* \delta \mathbf{x} + \mathscr{D} \nabla^2 \delta \mathbf{x} \tag{2.29}$$

with $\mathscr{D}$ being the diffusion matrix

$$\mathscr{D} = \begin{pmatrix} D_u & 0 \\ 0 & D_v \end{pmatrix}$$

A possible solution to this system is the following decomposition in plane waves,

$$\delta \mathbf{x}(t) = \sum_k c_k e^{\lambda(k)t} \phi_k \tag{2.30}$$

where $\lambda(k)$ defines the dispersion relation of the waves and the autovectors ϕ_k must satisfy that

$$\nabla^2 \phi_k(\mathbf{r}) = -k^2 \phi_k \tag{2.31}$$

Substituting this solution in 2.38, we obtain

$$\frac{\partial}{\partial t}\left(\sum_k c_k e^{\lambda(k)t} \phi_k\right) = J^* \sum_k c_k e^{\lambda(k)t} \phi_k + \mathscr{D} \nabla^2 \sum_k c_k e^{\lambda(k)t} \phi_k \tag{2.32}$$

Operating both sides,

$$\sum_k c_k \lambda(k) e^{\lambda(k)t} \phi_k = J^* \sum_k c_k e^{\lambda(k)t} \phi_k + \mathscr{D} \sum_k c_k e^{\lambda(k)t} \nabla^2 \phi_k \tag{2.33}$$

and now using 2.31 on the right hand side,

$$\sum_k c_k \lambda(k) e^{\lambda(k)t} \phi_k = J^* \sum_k c_k e^{\lambda(k)t} \phi_k + \mathscr{D} \sum_k c_k e^{\lambda(k)t} (-k^2 \phi_k) \tag{2.34}$$

USC UNIVERSIDADE DE SANTIAGO DE COMPOSTELA

we obtain, for each k,

$$\cancel{c_k e^{\lambda(k)t}}\lambda(k)\phi_k = \cancel{c_k e^{\lambda(k)t}}\left(J^*\phi_k - \mathscr{D}k^2\phi_k\right) \tag{2.35}$$

$$\lambda(k)\phi_k = J^*\phi_k - \mathscr{D}k^2\phi_k \tag{2.36}$$

Grouping all the terms together, we finally end up with the following linear system of equations,

$$\left(J - \mathscr{D}k^2 - \lambda(k)I\right) = 0 \tag{2.37}$$

with I the identity matrix. From here, we need to compute the dispersion relations $\lambda(k)$ by solving the determinant of the system. Since the sign of $\lambda(k)$ indicates whether the perturbations will grow exponentially or not, we can say that the diffusion induces an instability if $\mathrm{Re}(\lambda(k)) > 0)$ for any k. This means that a perturbation with that particular wavelength may exponentially grow until reaching a different stability regime, which will eventually result in a Turing structure. Therefore, to locate the region of the parameter space where the Turing instability occurs, we just need to solve the previous system of equations for each model.

On the other side of things, networks are not spatially extended systems however, so we need to reformulate slightly the problem. Here we have discrete nodes where the reaction dynamics take place and the variables diffuse to the other nodes across the links of the network. This is not much of an issue since the Laplacian operator ∇^2 can be easily discretized through the network Laplacian matrix, $L_{ij} = A_{ij} - \delta_{ij}k_i$, where δ_{ij} is the Kronecker delta. In this way, the problem can be adapted straightforwardly, transforming equations 2.22 into

$$\begin{cases} \frac{du_i}{dt} &= f(u_i, v_i) + D_u \sum_j^N L_{ij}u_j \\ \frac{dv_i}{dt} &= g(u_i, v_i) + D_v \sum_j^N L_{ij}u_j \end{cases} \tag{2.38}$$

for each node i, with $i = 1, ..., N$. Note that from the definition of the Laplacian matrix, we have the following identity $\sum_j^N L_{ij}u_j = \sum_j^N A_{ij}(u_j - u_i)$ which is nothing less but the Fick's law of diffusion across the links of the network.

Let us consider again a perturbation $\delta\mathbf{x} = (\delta u_i, \delta v_i)$ to the equilibrium point. In networks, the role of plane waves and wave numbers is played by the eigenvectors $\Phi_i^{(\alpha)} = (\phi_1^{(\alpha)}, ..., \phi_N^{(\alpha)})$ and eigenvalues Δ_α $(\alpha = 1, ..., N)$ of the Laplacian matrix [Othmer and Scriven, 1971, Nakao and Mikhailov, 2010], which are determined by the eigenvalue problem

$$\sum_j^N L_{ij}\phi_j^{(\alpha)} = \Lambda^\alpha \phi_i^{(\alpha)}, \text{ with } \alpha = 1, ..., N \tag{2.39}$$

Since L_{ij} has the property of zero-row sum and the diagonal elements are given by $-k_i$, all eigenvalues are real and non-positive. On the other hand, the modes (α) are sorted in decreasing order, so

$$0 = \Lambda_1 \geq \Lambda_2 \geq ... \geq \Lambda_N$$

Following eq. 2.30, we can propose then as the system's solution the following decomposition in terms of the Laplacian eigenvectors:

$$\delta u_i(t) = \sum_\alpha^N B_\alpha e^{\lambda_\alpha t}\phi_i^{(\alpha)} \qquad \delta v_i(t) = \sum_\alpha^N C_\alpha e^{\lambda_\alpha t}\phi_i^{(\alpha)} \tag{2.40}$$

USC UNIVERSIDADE DE SANTIAGO DE COMPOSTELA

Following the same approach as in eqs.2.32 to 2.35, this is, inserting these solutions in the linearized equations for the perturbations and operating each term, we eventually recover a similar linear system for the exponents λ_α, obtaining for each mode α

$$\lambda_\alpha = \begin{pmatrix} f_u^* + D_u\Lambda_\alpha & f_v^* \\ g_u^* & g_v^* + D_v\Lambda_\alpha \end{pmatrix} = J^* + \Lambda_\alpha \mathscr{D} \tag{2.41}$$

Likewise, to determine the stability of the fixed point we must compute the exponents λ_α by solving the determinant of

$$\det\left(J^* + \Lambda_\alpha \mathscr{D} - \lambda_\alpha I\right) = 0 \tag{2.42}$$

which leads to,

$$0 = (f_u^* + D_u\Lambda_\alpha - \lambda_\alpha)(g_v + D_v\Lambda_\alpha - \lambda_\alpha) - f_v g_u \tag{2.43}$$

$$f_u g_v - f_v g_u + (f_u D_v + g_v D_u)\Lambda_\alpha + D_u D_v \Lambda_\alpha^2 - (f_u + g_v + (D_u + D_v)\Lambda_\alpha)\,\lambda_\alpha + \lambda_\alpha^2 \tag{2.44}$$

where we have already grouped the terms in the second line attending to their order in λ_α. We can identify most of these terms with the trace and determinant of the Jacobian J^* evaluated at the fixed point and the diffusion matrix $\mathscr{D}$. The term $(f_u D_v + g_v D_u)$ is more tricky but it can be written as the sum over the element wise multiplication (the Hadamard product) of J^* by the adjugate of $\mathscr{D}$, $\mathrm{adj}(\mathscr{D})$. This is, $\sum_{ij} J_{ij}^* \mathrm{adj}(\mathscr{D})_{ij}$:

$$0 = \det(J^*) + \left(\sum_{ij} J_{ij}^* \mathrm{adj}(\mathscr{D})_{ij}\right)\Lambda_\alpha + \det(\mathscr{D})\Lambda_\alpha^2 - (\tau(J^*) + \tau(\mathscr{D})\Lambda_\alpha)\lambda_\alpha + \lambda_\alpha^2 \tag{2.45}$$

The second term can be identified with the sum over the element wise multiplication of J^* by the adjugate of $\mathscr{D}$, $\mathrm{adj}(\mathscr{D})$. This is, the sum over the Hadamard product $\sum_{ij} J_{ij}^* \mathrm{adj}(\mathscr{D})_{ij}$. Solving the quadratic equation for λ_α, we obtain,

$$\begin{aligned} \lambda_\alpha(\Lambda_\alpha) = \frac{1}{2}\Bigg(\tau(J^*) + \tau(\mathscr{D})\Lambda_\alpha \pm \Bigg[(\tau(J^*) + \tau(\mathscr{D}))^2 - \\ -4(\det(J^*) + \left(\sum_{ij} J_{ij}^* \mathrm{adj}(\mathscr{D})_{ij}\right)\Lambda_\alpha + \det(\mathscr{D})\Lambda_\alpha^2 \Bigg]^{\frac{1}{2}} \Bigg) \end{aligned} \tag{2.46}$$

We note that this expression is general and holds also for diffusive matrices with elements outside the diagonal, as the extra terms are included either in the determinant of $\mathscr{D}$ or in the Hamadart product term.

We will denote λ_α as the **growth factors** or **growth rates** of the system since they will tell us that the αth mode is unstable if $\mathrm{Re}(\lambda_\alpha)$ is positive. Studying the dispersion relations $\lambda_\alpha(\Lambda_\alpha)$ for different values of the parameters, we can trace the emergence of the instabilities and find which are the modes that trigger them. Considering also different types of networks, we can better understand how the structural properties of the network's topology affect the instabilities and, mainly, which topology structure is more likely to induce them [Mimar et al., 2019]. In Figure 2.7 we have drawn three examples of the dispersion relation $\lambda_\alpha(\Lambda_\alpha)$ obtained from eq. 2.46 for different diffusive parameter values. Depending on the Laplacian eigenvalues of each

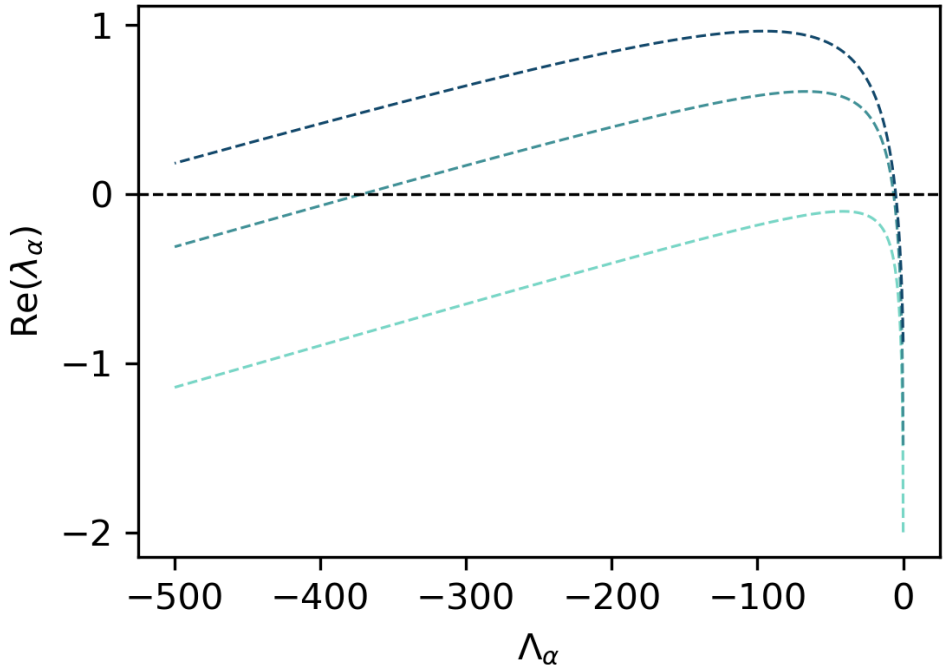


Figure 2.7: Three dispersion relation curves $\lambda_\alpha(\Lambda_\alpha)$ obtained from eq. 2.46 for different values of the model parameters. Those modes with $\mathrm{Re}(\lambda_\alpha > 0)$ will trigger an instability changing the system to another dynamical state.

network, we will see that the growth factors accommodate somewhere along those curves. We are showing in this case three possible outcomes: in the lower one, the curve does not intersect with 0, so it is impossible to trigger the instability independently of the network chosen. In the middle one, there are two points of intersection so the area where $\lambda_\alpha(\Lambda_\alpha) > 0$ is bounded. This means that depending on the distribution of the eigenvalues, we could see the instability or not. Finally, in the upper case there is only one intersection, so if there is at least one eigenvalue higher than the critical one, $\Lambda_\alpha > \Lambda_c$, we will find the instability. This will be the purpose of Chapter 6 in the context of polarization in opinion formation. Furthermore, as we will also see in Chapter 7, we can also use the quantitative values of the growth rates to extract relevant information about the evolution of the dynamics.

As a final note, we must mention here that this type of stability study closely resembles those used also for the *synchronizability* of networks, this is, the study of the stability of the synchronized state in function of the network topology [Arenas et al., 2008]. There, the eigenvalues of the network's Laplacian matrix are also considered in order to define an objective criterion: the Master Stability Function (MSF) [Pecora and Carroll, 1998], which is qualitatively identical to our dispersion relation. Similarly as in Figure 2.7, the shape of the MSF in function of the Laplacian's eigenvalues and the coupling parameter K characterizes the stability of the synchronous state, informing on the location of the critical values of the coupling parameter K.

USC
UNIVERSIDADE DE SANTIAGO DE COMPOSTELA

USC
UNIVERSIDADE
DE SANTIAGO
DE COMPOSTELA

Part I

Collective behavior in periodic oscillators: Synchronization and applications.

USC
UNIVERSIDADE DE SANTIAGO DE COMPOSTELA

USC
UNIVERSIDADE
DE SANTIAGO
DE COMPOSTELA

Motivation and specific objectives

Synchronization processes between elements of the same population are one of the many ways in which Nature shows self-organization giving rise to collective and complex behaviors. They seem to be ubiquitous in every complex system where periodic behavior and oscillations are present [Strogatz, 2003]. In the introduction, we have already presented plenty of examples composed of both living (neurons, pacemaker cells, insects and even humans) and inanimate objects (lasers, electrical circuits or chemical oscillators) and commented that from simple mathematical abstractions we can bridge the difference between them creating an unifying theory that describes them all.

Motivated by these ideas, in the following chapters we aim to deepen in the fundamental study of the mechanisms behind theses processes and the necessary conditions that give rise to its emergence. For that purpose, we focus on two of the paradigms for synchronization phenomena. First, Chapter 3 is directly related to the Kuramoto model, the simplest model for periodic oscillators, and considers the incorporation of higher order interactions in the network substrate that connect the phase oscillators. In the recent years, an increasing amount of evidence is showing that taking into account higher-order structures beyond pairwise interaction enhance the modeling capacities, helping to better understand and predict the dynamical behavior of very high complex systems as the brain [Battiston et al., 2020]. Thus, carefully understanding first the effect of these structures in the mathematical abstraction of the Kuramoto model can give us new insights that can be applied not only to spiking neurons but to any other periodic system.

On the other hand, the dynamics of the Belousov-Zhabotinsky (BZ) reaction allows the numerical and experimental study of synchronization with a system of large population of catalyst-loaded particles immersed in a catalyst-free solution. This configuration allows to exploit the excitable and oscillating properties of the BZ to build a framework of periodic oscillators where synchronization can be studied in function of several variables, from the size of the population to the coupling strength. In Chapter 4, we simulate a two-dimensional reactor where we study the dynamics of the non-linear chemical oscillators in conditions of low-mixing and focusing on local interactions between the particles, instead considering the solution as a mean field coupling. On the other side, in Chapter 5 we present a experimental setup where we can study large arrays of these chemical oscillators but where the coupling now is controlled via light pulses.

In summary, one transversal objective of this part is to stress the importance of the interactions in a complex system in regards to the emerging phenomena derived from the collective behavior, proposing thus in each chapter new ways of either connecting the elements or increasing their complexity. For each case, we will see new dynamical regimes and important changes in the phase transitions between them.

USC
UNIVERSIDADE DE SANTIAGO DE COMPOSTELA

USC
UNIVERSIDADE
DE SANTIAGO
DE COMPOSTELA

Chapter 3

The Kuramoto model with higher order interactions

Part of the text and figures for this chapter are reproduced from

* Carballosa A.[1,2], Muñuzuri A.P.[1,2], Boccaletti S.[3], Torcini A.[4,3,5] & Olmi S.[3,5] *"Cluster states and the π-transition in the Kuramoto model with higher order interactions"* arXiv (2023), https://doi.org/10.48550/arXiv.2308.05406 (in press, Chaos Solitons & Fractals)

[1] Group of Nonlinear Physics, Faculty of Physics, University of Santiago de Compostela, 15782 Santiago de Compostela, Spain
[2] Galician Centre for Mathematical Research (CITMAGa), University of Santiago de Compostela, 15782 Santiago de Compostela, Spain
[3] CNR, Consiglio Nazionale delle Ricerche, Istituto dei Sistemi Complessi, 50019, Sesto Fiorentino, Italy
[4] Laboratoire de Physique Théorique et Modélisation, UMR 8089, CY Cergy Paris Université, CNRS, 95302 Cergy-Pontoise, France
[5] INFN, Sezione di Firenze, Via Sansone 1, I-50019 Sesto Fiorentino (FI), Italy

3.1 Introduction

We start our study on synchronization with one of the roots and core topics of the field. In the Methods section. we have seen the main features of the classical Kuramoto model for a population of N phase oscillators connected in an all-to-all network of pair-wise interactions. Here we will go beyond networks, considering many body interactions in the form of simplicial complexes and introducing them directly into the Kuramoto model. Mainly, this adds new source of nonlinearity into the system, with the oscillators now experiencing a stronger pull that will try to synchronize the group. As we briefly commented in the Introduction, a simplicial complex of dimension 2 represents the triangle's faces formed by a closed loop of 3 nodes. This increase in the complexity of the network structure changes the nature of the synchronization transitions, that pass from being continuous and of second order to become abrupt and explosive [Skardal and Arenas, 2019, Skardal and Arenas, 2020].

Furthermore, the higher order term induces a bi-harmonic interaction in the mean field experienced by the oscillators, which as we mentioned earlier this allow

USC UNIVERSIDADE DE SANTIAGO DE COMPOSTELA

the existence of two-cluster states [Skardal and Arenas, 2019, Tanaka and Aoyagi, 2011, Komarov and Pikovsky, 2015]. Coexisting stable states and multi-stability seems to be also a general trend when introducing higher order interactions [Skardal and Arenas, 2019, Tanaka and Aoyagi, 2011, Xu et al., 2020a], with the bi-clusters usually coexisting with the asynchronous regime. Furthermore, if considering both pairwise and triadic interactions in the system, another striking feature is that higher order interactions can stabilize strongly synchronized states for repulsive (negative) values of the pair-wise coupling [Skardal and Arenas, 2020][Dai et al., 2021], a situation prohibited in the classical Kuramoto model. In fact, even with both pair-wise and triadic couplings being repulsive, it has been found that the two-cluster state can still emerge when the triadic strength is large enough [Kovalenko et al., 2021]. In social terms, this would mean that despite all the individuals being contrarians to the mainstream, there can still exist some levels of agreement in the network.

On the one hand, the work presented in this chapter expands the findings of [Kovalenko et al., 2021] carried out with the higher order model and unimodal distributions of natural frequencies, to the general case of bimodal distributions. The introduction of the latter in the classic Kuramoto model gives raise to more complex, time dependent states and also hysteretic transitions [Crawford, 1994, Pazó and Montbrió, 2009, Bi et al., 2016]. What's more, the phase diagram of the Kuramoto model for bimodal Lorentzian distributions has been analytically resolved in [Martens et al., 2009], showing also the emergence of multi-stability and a limit-cycle solution of the order parameter termed standing waves (SW). This is a synchronous state characterized by two counter-rotating clusters with opposing angular velocity. With all these in mind, we aim to further characterize the novel phenomena introduced by the higher order interactions, investigating how the higher order interactions affect the standing waves on one side, and on the other how the bimodal distributions affect the bi-clusters already found in the higher order model.

3.2 Methods

3.2.1 Model

The model that we use here is a direct extension of the Kuramoto model (see eq. 2.6), where we consider both pair-wise and triadic interactions with different coupling weights, λ_1 and λ_2. As in the original Kuramoto model, we consider a regular all-to-all network where all possible pairs and triangles are formed:

$$\dot{\theta}_i = \omega_i + \frac{\lambda_1}{N}\sum_{j}^{N}\sin(\theta_j - \theta_i) + \frac{\lambda_2}{2N^2}\sum_{j}^{N}\sum_{k}^{N}\sin(\theta_j + \theta_k - 2\theta_i) \tag{3.1}$$

Here, oscillator i will not only adjust its phase accordingly to all of its neighbors j, but will be affected too by the phases of neighbors j and k simultaneously. For the natural frequencies, we have considered a bimodal distribution of frequencies $g_B(\omega)$, given by the superposition of two Gaussian functions with centers $\pm\omega_0$ and a standard deviation Δ:

$$g_B(\omega) = \frac{1}{2\sqrt{2\pi\Delta^2}}\left(e^{\frac{-(\omega+\omega_0)^2}{2\Delta^2}} + e^{\frac{-(\omega-\omega_0)^2}{2\Delta^2}}\right) \tag{3.2}$$

USC UNIVERSIDADE DE SANTIAGO DE COMPOSTELA

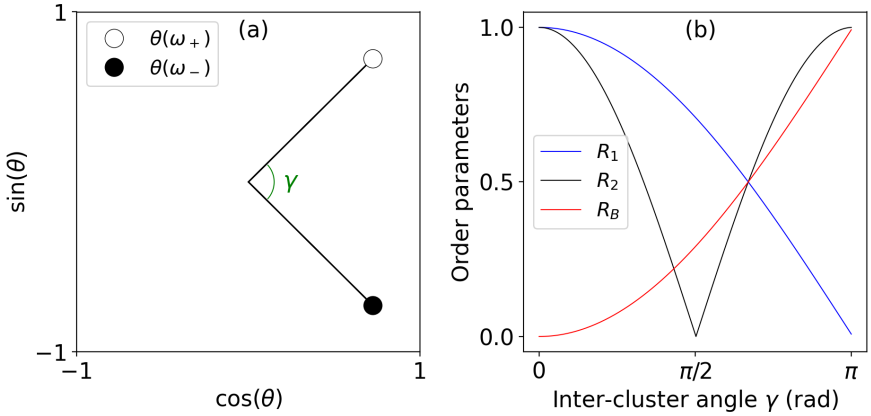


Figure 3.1: Order parameters (b) against the inter-cluster angle α (a). R_1 is the global Kuramoto order parameter, R_D is the Daido-Kuramoto order parameter and R_B is our clustering order parameter defined in eq. 3.3

.

Note that through this formula we can recover the unimodal distribution by choosing $\omega_0 = 0$.

3.2.2 Coherence indicators

To characterize the collective states present in the model 3.1, we will use Kuramoto order parameter R_1 seen in the Methods for the global synchronization of the system, while we define as well the a new indicator R_B that will be particularly suited to reveal the presence of the two-cluster states:

$$R_1 = \frac{1}{N}\sum_{j}^{N} e^{i\theta_j} \qquad\qquad R_B = \frac{R_+ + R_-}{2} - R \tag{3.3}$$

Here, R_+ represents the order parameter R_1 of the oscillators with positive natural frequencies, centered at ω_0, wile R_- the counterpart for those with negative natural frequencies centered at $-\omega_0$. This measure will be very suitable since, as we will describe soon, one of the two-cluster states is formed with the oscillators splitting according to their frequency sign. Thus, R_B will be 0 when either the oscillators are decoupled or fully synchronized, and 1 when these two clusters are anti-symmetrical with an angle $\gamma = \pi$ and there is strong synchronicity within the clusters. At this point, we must mention that for measuring cluster synchronicity the usual approach is to employ the Daido-Kuramoto second order parameter [Daido, 1996], $R_2 = \frac{1}{N}\sum_j^N e^{i2\theta_j}$. However, for our particular case where our clusters are not located at phase oposition but at an intermediate angle γ between 0 and π, we have seen that R_2 shows a non monotonic dependence with the angle that could lead us to wrong measures (see Figure 3.1).

3.2.3 Simulation protocols

As the system shows many complex, multistable behaviors, we have examined the system evolution from many different initial conditions. For that purpose, we introduce the variable η as the percentage of initially phase-locked oscillators and define the following two simulation protocols: protocol (I) refers to simulations started from $\eta = 0$, with all the oscillators being

decoupled with random initial phases; protocol (II) refers to the opposite case, simulations started from $\eta = 1$ where all oscillators were phase-locked. Furthermore, if the label "A" is added to the simulation protocol (IA, IIA), it refers to simulations where one of the coupling parameters was varied adiabatically between the values shown.

On the other hand, the frequency distributions $g(\omega,\Delta)$ are generated randomly from the bimodal distribution of eq.3.2, ensuring that each mode is equally populated. For the numerical integration of the model, we will use a 4th order Runge-Kutta scheme with either a fixed time step with $dt = 10^{-2} - 10^{-3}$ or with an adaptive time-step scheme coupled with a Runge-Kutta-Fehlberg scheme (see Appendix B).

3.2.4 Mean field analysis

Analogously as we did with the Kuramoto model, we are interested in writing eq. 3.1 in terms of the macroscopical mean-field quantities R_1 and the global phase $\Phi = \omega_c t$. The first term can be derived identically as we did in to obtain $R_1 \sin(\phi - \theta_i)$, while for the higher order term we need to elevate the identity of eq. 2.8 to the power of 2, as follows:

$$\left(R_1 e^{i(\Phi-\theta_i)}\right)^2 = \left(\frac{1}{N}\sum_{j=1}^{N} e^{i(\theta_j-\theta_i)}\right)^2 \tag{3.4}$$

If we derive the right hand side of this equation we get,

$$\begin{aligned}
\left(\frac{1}{N}\sum_{j=1}^{N} e^{i(\theta_j-\theta_i)}\right)^2 &= \frac{1}{N^2} e^{-2i\theta_i} \sum_{j}^{N}\sum_{k}^{N} e^{i(\theta_j+\theta_k)} \\
&= \frac{1}{N^2}(\cos 2\theta_i - i\sin 2\theta_i)\sum_{j}^{N}\sum_{k}^{N}\big(\cos(\theta_j+\theta_k) + i\sin(\theta_j+\theta_k)\big) \\
&= \frac{1}{N^2}\left(\sum_{j}^{N}\sum_{k}^{N}\cos(\theta_j+\theta_k)\cos 2\theta_i + \sum_{j}^{N}\sum_{k}^{N}\sin(\theta_j+\theta_k)\sin 2\theta_i\right) + \\
&\quad + \frac{i}{N^2}\left(\sum_{j}^{N}\sum_{k}^{N}\sin(\theta_j+\theta_k)\cos 2\theta_i - \sum_{j}^{N}\sum_{k}^{N}\cos(\theta_j+\theta_k)\sin 2\theta_i\right)
\end{aligned} \tag{3.5}$$

Equating now the imaginary parts of both sides of eq. 3.4. we obtain

$$R_1^2 \sin(2\Phi - 2\theta_i) = \frac{1}{N^2}\left(\sum_{j}^{N}\sum_{k}^{N}\sin(\theta_j+\theta_k)\cos 2\theta_i - \sum_{j}^{N}\sum_{k}^{N}\cos(\theta_j+\theta_k)\sin 2\theta_i\right) \tag{3.6}$$

Using the definition of the sinus of an angle difference, namely $\sin(x-y) = \sin x\cos y - \cos x\sin y$, it follows that

$$R_1^2 \sin(2\Phi - 2\theta_i) = \frac{1}{N^2}\left(\sum_{j}^{N}\sum_{k}^{N}\sin(\theta_j+\theta_k-2\theta_i)\right) \tag{3.7}$$

USC UNIVERSIDADE DE SANTIAGO DE COMPOSTELA

which is our three-body interaction term. Using this identity, we can rewrite eq. 3.1 as

$$\dot{\theta}_i = \omega_i + \lambda_1 R_1 \sin(\Phi - \theta_i) + \frac{\lambda_2}{2} R_1^2 \sin(2\Phi - 2\theta_i) \qquad i = 1, ..., N \tag{3.8}$$

In this way, the second harmonic interaction due to the three-body interactions is made obvious. Furthermore, as we have removed the summations, using this equation will result in way easier numerical computations while also allowing us pursuing farther analytical treatment in the form of a self-consistent approach. If we consider now the rescaled phase $\phi = \theta - \Phi \in [-\pi : \pi]$, the frequency $\Omega_i = \omega_i - \omega_c$, where ω_c is the frequency of the synchronous cluster, we can rewrite eq. 3.8 as

$$\dot{\phi}_i = \Omega_i - \lambda_1 R_1 \sin(\phi) - \frac{\lambda_2}{2} R_1^2 \sin 2\phi) \qquad i = 1, ..., N \tag{3.9}$$

where we have also assumed that $\Phi = 0$ in the synchronous case. This equation can be interpreted as the dynamical equation for an overdamped oscillator subject to a potential well given by

$$V(\phi) = \ddot{\phi} = -\Omega\phi - \lambda_1 R_1 \cos(\phi) - \frac{\lambda_2 R_1^2}{2} \cos(2\phi) + C \tag{3.10}$$

with C the integration constant. The minima of this potential will tell us a lot about the stability of the solutions of R_1, as we shall see later. For even frequency distributions and in the synchronous case, we can assume that $\Omega = 0$. In such a case V is symmetrical to a change of phase sign, $V(\phi) = V(-\phi)$, so its shape will be mainly dependent on the sign of λ_2. As we see from Figure 3.2, the shape of V for different values of (λ_1, λ_2) in general presents two minima.

Following [Komarov and Pikovsky, 2014], we can affirm that the potential will always reveal two coexisting minima whenever

$$|u| = \left| \frac{\lambda_1}{\lambda_2 R_1} \right| < 1, \tag{3.11}$$

otherwise, it displays a single minimum analogously to the usual Kuramoto model. We will focus mostly on the region where the two minima coexist, by analysing separately the cases for positive and negative λ_2-values. For $|u| < 1$ the potential presents three extrema located at

$$\phi = 0, \qquad \phi = \pm\pi, \qquad \phi = \pm\bar{\phi} = \pm \arccos(-u), \tag{3.12}$$

since the phases $\pm\pi$ coincide.

As shown in Figure 3.2 (a-b), for $\lambda_2 > 0$, the potential displays two minima of different heights in $\phi = 0$ and $\phi = \pm\pi$, and two maxima in $\pm\bar{\phi}$. Therefore, depending on the initial conditions and on the protocol used for the simulations, one or two clusters may emerge in the system. In particular we notice that, for increasingly larger positive values of λ_1, the minimum corresponding to the cluster in $\phi = 0$ becomes deeper and therefore more stable, as evident when looking at $V(\phi)$ (black solid lines) reported in Figure 3.2 (a). Furthermore, for $\lambda_1 \leq -\lambda_2 R_1$ the minimum in $\phi = 0$ ($\phi = \pm\pi$) disappears and the potential shows an unique minimum. Exactly the opposite happens for negative values of λ_1 (see panel (b)) but regarding the other minimum in $\phi = \pm\pi$, which eventually disappears for $\lambda_1 \geq \lambda_2 R_1$ On the other hand, for a negative λ_2 values the potential presents two maxima at $\phi = 0$ and $\pm\pi$ and two symmetric minima of same

USC DE COMPOSTELA

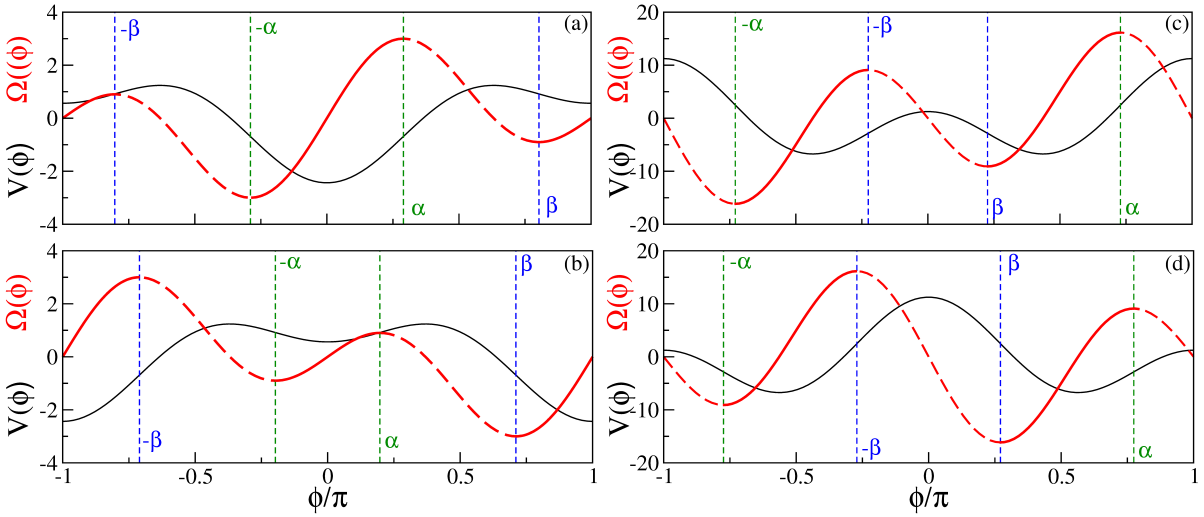


Figure 3.2: Potential $V(\phi)$ 3.12(in black) and frequencies $\Omega(\phi)$ 3.13 (red) versus the phase ϕ for positive $\lambda_2 = 15$ (a-b) and negative $\lambda_2 = -100$ (c-d). Panels (a,b) refers to $\lambda_1 = 3, \lambda_1 = -3$ respectively, while panels (c,d) to $\lambda_1 = 10$ and $\lambda_1 = -10$. The red solid curves identify the stable branches associated to phases locked oscillators, while the dashed lines the unstable ones. The dashed green (blue) vertical lines denote the angles $\pm\alpha$ ($\pm\beta$) demarking the stable/unstable regions. For all panels, $R_1 = 0.5$ and $\Omega = 0$.

height at $\pm\bar{\phi}$, as shown in Figure 3.2 (c) and (d) (black solid lines).

The locked phases correspond to stationary solutions of (3.9) given by

$$\Omega = \lambda_1 R_1 \sin(\phi) + \frac{\lambda_2}{2} R_1^2 \sin(2\phi) = Y(\phi, R_1) \quad . \tag{3.13}$$

These solutions will be stable whenever $\partial Y/\partial\phi = V^{"}(\phi) > 0$, this is, when the potential is concave in proximity of some minimum. The curves $\Omega = Y(\phi, R_1)$ are shown in Figure 3.2 as solid (dashed) red lines denoting the stable (unstable) regions. There, we can see that function $\Omega = Y(\phi, R_1)$ presents also four extrema in correspondence to the angles

$$\pm\alpha = \pm \arccos \frac{-u + \sqrt{u^2 + 8}}{4} \tag{3.14}$$

and

$$\pm\beta = \pm \arccos \frac{-u - \sqrt{u^2 + 8}}{4} \quad . \tag{3.15}$$

At each extrema, we have denoted the absolute value of the natural frequencies as $\Omega_1 = |\Omega(\pm\alpha)|$ and $\Omega_2 = |\Omega(\pm\beta)|$, with the minimal frequency among the two as Ω_{min}.

Looking at the curves $\Omega = Y(\phi, R_1)$ shown in Figure 3.2 for $|u| < 1$, it is evident that the system will always display two stable branches, which can be identified as follows:

- For $\lambda_2 > 0$ (panels a,b): the first branch corresponds to phases in the interval $\Phi_1 \in [-\alpha : \alpha]$ with associated frequencies $[-\Omega_1 : \Omega_1]$, while the second one corresponds to phases in the interval $\Phi_2 \in [-\pi : -\beta] \cup [\beta : \pi]$ with frequencies $[-\Omega_2 : \Omega_2]$.
- For $\lambda_2 < 0$ (panels c,d) : the first branch corresponds to phases in the interval $\Phi_1 \in [-\alpha : -\beta]$ with frequencies $[-\Omega_1 : \Omega_2]$, while the second one to phases in the interval $\Phi_2 \in [\beta : \alpha]$, with $[-\Omega_2 : \Omega_1]$.

It is worth noticing that there is a region of coexistence between the two stable branches for $-\Omega_{min} \leq \Omega \leq \Omega_{min}$, where oscillators with the same frequency Ω can be locked to 2 different phases (see red solid curves in Figure 3.2). This will be an important thing to consider when we integrate over the frequencies later on.

Now, the self-consistent equation for the order parameter R_1 in the thermodynamic limit is analogous to the one for the Kuramoto model reviewed in Methods (see 2.2) and it can be written as

$$R_1 e^{j\Phi} = e^{j\Phi} \int\int d\phi d\Omega \rho(\phi|\Omega) e^{j\phi} g(\Omega) \tag{3.16}$$

where $g(\Omega)$ is the distribution of the natural frequencies and $\rho(\phi|\Omega)$ the conditional probability distribution function characterizing the oscillator population. The oscillators can be divided in drifting or locked depending on their natural frequency.

Following [Komarov and Pikovsky, 2015], we denote with Y_{max}, Y_{min} the maximum and the minimum of the function $Y(\phi, R_1)$ 3.13. According to this notation, the locked oscillators will have $Y_{min} \leq \Omega \leq Y_{max}$ while drifting oscillators, $\Omega > Y_{max}$ and $\Omega < Y_{min}$. On one hand, the probability distribution ρ_d for the drifting oscillators is proportional to the inverse of their phase velocity [Kuramoto, 1984]:

$$\rho_d(\phi|\Omega) = \frac{C}{|\Omega - Y(\phi, R_1)|}, \quad C = \frac{1}{\int_{-\pi}^{\pi} d\phi |\Omega - Y|} \ . \tag{3.17}$$

On the other hand, the distribution ρ_l of the locked oscillators in the region of coexistence can be written as

$$\rho_l(\phi|\Omega) = \sigma\delta(\phi - \Phi_1(\Omega)) + (1-\sigma)\delta(\phi - \Phi_2(\Omega)) \ ; \tag{3.18}$$

where $0 \leq \sigma \leq 1$ is the redistribution factor of the oscillators among the two stable branches. Outside the coexistence region the distribution ρ_l is simply given by

$$\rho_l(\phi|\Omega) = \delta(\phi - \Phi_x(\Omega)) \quad , \ x = 1, 2 \ , \tag{3.19}$$

depending if the oscillator characterized by the phase ϕ is locked to the first or second branch.

For $\lambda_2 > 0$, by assuming the frequency distribution to be even ($g(\Omega) = g(-\Omega)$) and by taking into account the symmetry of the integrand, the expression for the Kuramoto order parameter takes the form

$$\begin{aligned} R_1 &= 2\left[\int_0^{\alpha} dY(\phi) S_1(Y(\phi)) g(Y(\phi)) \cos(\phi) \right. \\ &+ \left. \int_{\beta}^{\pi} dY(\phi) S_2(Y(\phi)) g(Y(\phi)) \cos(\phi)\right] \\ &+ \int_U \int_{-\pi}^{\pi} d\Omega d\phi \frac{C g(\Omega) \cos(\phi)}{|\Omega - Y(\phi, R_1)|} \ , \end{aligned} \tag{3.20}$$

where $S_1 = \sigma$ and $S_2 = 1 - \sigma$ in the coexistence regions, $S_1 = S_2 = 1$ outside the coexistence region and

$$dY(\phi) = [\lambda_1 R_1 \cos(\phi) + \lambda_2 R_1^2 \cos(2\phi)] d\phi \ . \tag{3.21}$$

The integration region $U = (-\infty, Y_{min}) \cup (Y_{max}, +\infty)$ that appears in the third integral in (3.20), is the frequency domain where the oscillators are drifting.

For $\lambda_2 < 0$ the expression for R_1 becomes

$$\begin{aligned} R_1 &= \left[\int_{-\beta}^{-\alpha} dY(\phi) S_1(Y(\phi)) g(Y(\phi)) \cos(\phi) \right. \\ &+ \left. \int_{\beta}^{\alpha} dY(\phi) S_2(Y(\phi)) g(Y(\phi)) \cos(\phi)\right] \\ &+ \int_U \int_{-\pi}^{\pi} d\Omega d\phi \frac{C g(\Omega)\cos(\phi)}{|\Omega - Y(\phi, R_1)|} \ ; \end{aligned} \tag{3.22}$$

in this case due to the symmetry of the potential wells (see Figure 3.2 (c-d)) the value of R_1 does not depend on the value of the redistribution factor σ, as we have verified. Therefore we can set $S_1 = S_2 = 1/2$ inside the coexistence region and $S_1 = S_2 = 1$ outside, without any loss of generality. It should be noted that, for the parameter values considered in this paper, the contribution of the drifting oscillators to (3.20) and (3.22) is usually negligible.

The self-consistent approach will allow us to find coherent solutions of the system in the thermodynamic limit ($N \to \infty$) corresponding to finite values of the Kuramoto order parameter, but note that it will not determine their stability properties.

3.3 Results

3.3.1 Dynamical regimes

Integrating equation 3.8 for a wide range of values of the coupling parameters (λ_1, λ_2) and measuring the global order parameter R_1, we obtain the dynamical landscape presented in Figure 3.3, for the unimodal distribution and two configurations of the bimodal distribution, namely $\omega_0 = 0, \pm 1, \pm 3$. For every configuration, we considered a fixed standard deviation of $\sigma = 0.25$ so we satisfy the criterion of [Martens et al., 2009] that discriminates unimodal from bimodal distributions if $\omega_0 > \Delta/\sqrt{3}$. The upper row of the figure corresponds to simulations done accordingly to simulation protocol (I), this is, with a random initial condition for the oscillator phases ($\eta = 0$) while the lower row corresponds to simulation protocol (II), and thus all oscillators initially phase-locked at $\theta_i = 0$ ($\eta = 1$). Note that for each pixel the initial condition has been reset, so this phase diagrams do not show adiabatical simulations. The labels written in the panels correspond to the following dynamical states, represented in detail in Figure 3.4:

- *Asynchronous State* (AS): as shown in panel 3.4(a), in this state the phase oscillators are completely spread around the circles as they move asynchonously driven by their natural frequencies (e). Because of this, the order parameters R_1 and R_B are essentially zero, as shown in panel (i).
- *Standing Waves* (SWs): these solutions are characteristic of a bimodal distribution of natural frequencies and correspond to two counter-rotating clusters of oscillators (see panels 3.4(b,f,j)) that move with the same angular velocity but of different sign, thus inducing ocillations in the order parameters.
- *Bimodal Clusters* (BCs): these correspond to panels 3.4(c,g,k) and are made of two groups of oscillators located in correspondence of the two peaks of the bimodal

USC DE COMPOSTELA

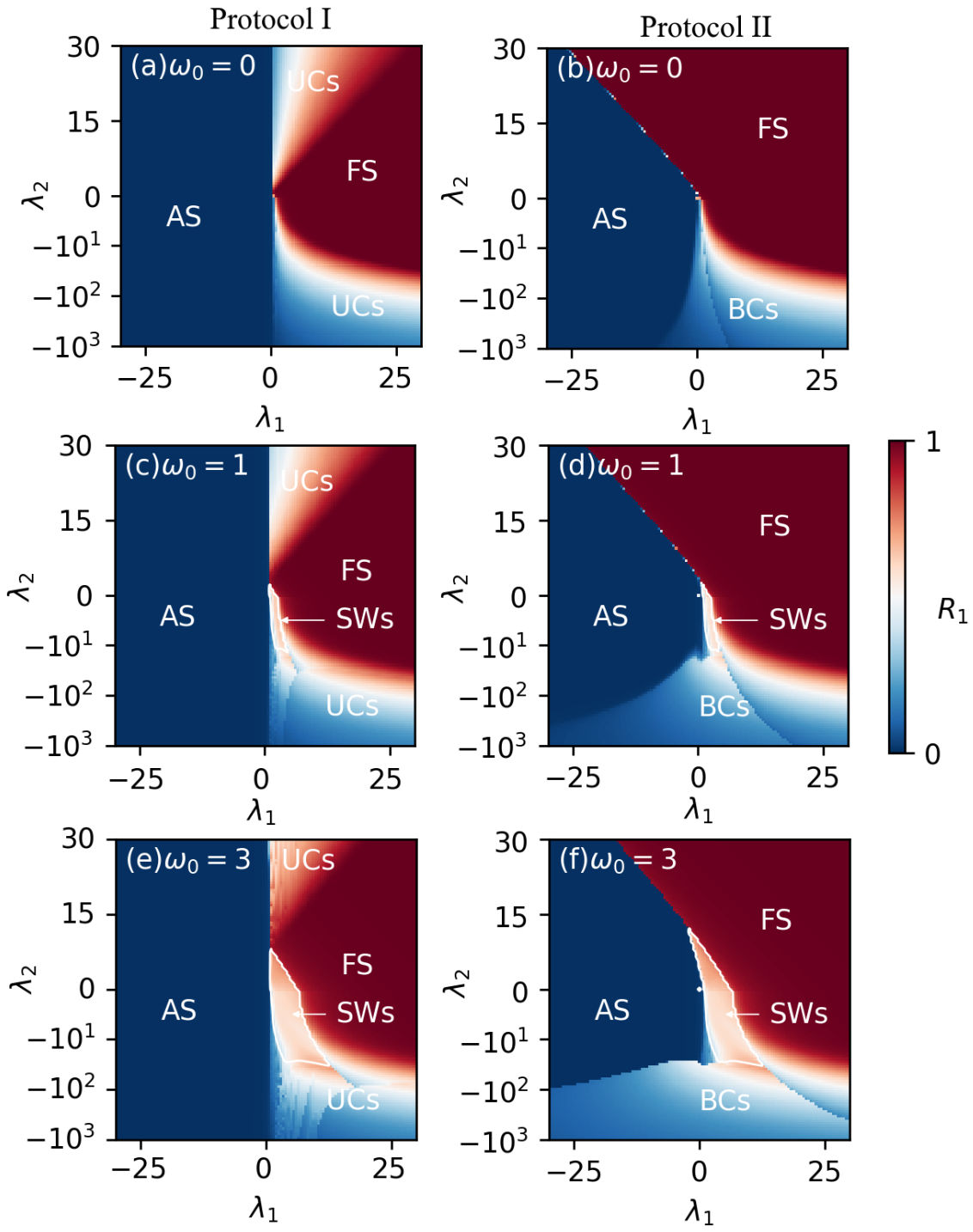


Figure 3.3: Numerical simulations from eq.3.8 of the order parameter R_1 as a function of the coupling parameters λ_1 and λ_2, for different frequency distributions. Namely, (a,b) unimodal Gaussian distribution centered at $\omega_0 = 0$ with a dispersion of $\Delta = 0.25$; (c,d,e,f) bimodal distributions centered at $\omega_0 = 1$ and $\omega_0 = 3$ respectively, both with $\Delta = 0.25$. Within the figures, the abbreviations distinguish the possible states of the system, namely the asynchronous state (AS), the fully-synchronous state (FS), the standing waves (SWs) and the bi-cluster states (BCs) and (UCs), depending on their phase distribution. Panels (a,c,e) correspond to simulations according to protocol (I) while panels (b,d,f) to simulations with protocol (II). For each point, the initial conditions are reset. The total number of oscillators is set to $N = 5000$.

USC
UNIVERSIDADE DE SANTIAGO DE COMPOSTELA

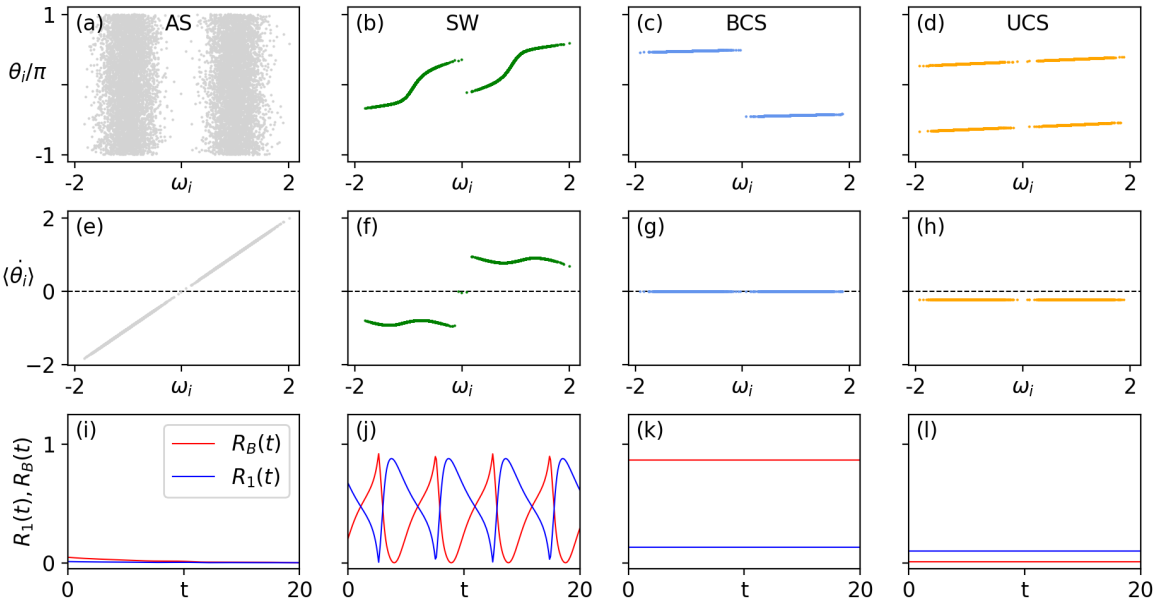


Figure 3.4: Microscopical details of the dynamical states: asynchronous (AS) with (λ_1,λ_2)=(-10,-10), standing wave (SW) with (λ_1,λ_2)=(3,-5), clustering state (CS) (λ_1,λ_2)=(10,-1000) and travelling wave (TW) also with (λ_1,λ_2)=(10,-1000). Row-wise, instantaneous phase (a-d) and time-averaged velocity (e-h) against the natural frequencies of the oscillators, and time evolution of the order parameters (i-l), for each dynamical state. CS is obtained from simulation protocol (II) while TW is obtained from simulation protocol (I). For all cases, $N = 10000$, $\omega_0 = 1.0$ and $\Delta = 0.25$.

distribution, with each cluster locked to a different phase value (see panel (c)). They are also frequency locked at the same angular velocity, that for symmetrically populated clusters is zero. However, as indicated in Figure 3.3 (a), note that this state can also appear for unimodal distributions where finite size effects involve asymmetries in the cluster population and induce a finite value for the angular velocity. The value of R_1 is small but not zero, as the two clusters are not located in phase opposition, while R_B has a finite value depending on the phase-shift γ between the clusters (k). This state emerges only when the initial condition is fully synchronized, i.e $\eta = 1$.

- *Uniform Clusters* (UCs) are also constituted by two groups of oscillators phase locked at two different phases, but the oscillators of each cluster can have positive or negative natural frequencies (see panel 3.4(d)). In this case, the two clusters are usually not equally populated which again gives rise to a finite common angular velocity (h). Besides, R_B is essentially zero, since now is not possible to identify two clusters on the basis of their natural frequencies, while R_1 is again small but not zero since the angle γ between the clusters is tipically not π (l).

Going back to the phase diagrams of Figure 3.3, we see that the asynchronous regime (AS) occupies most part of the negative semiplane of λ_1, where coexistence with other states is revealed comparing the simulations from both protocols. For positive λ_2 on one hand, the AS obtained with an asynchronous initial condition ($\eta = 0$, protocol I), coexists with the fully-synchronous regime (FS) that remains from a synchronous initial condition ($\eta = 1$, protocol II). Here we see that for a certain critical value, the FS regime becomes unstable and abruptly de-synchronize to $R_1 \simeq 0$. For considerably large negative λ_2 and specially for bimodal

configurations, we see that the AS coexists with the bimodal cluster states (BCs). Because of the nature of this latter state, the value of R_1 is small as the clusters are equally populated and almost at phase opposition, but still, we can grasp from these panels that the de-synchronization transition to AS is also quite abrupt. This is made more clear in panel 3.3(f) with the bimodal center at $\omega_0 = \pm 3$, where we can also see that the existence of BCs has been enlarged to occupy all the range of values considered for λ_1, and within a wide region of values of λ_2 that go from $\lambda_2 = -100$ to $\lambda_2 = -1000$.

On the other hand, attending to simulations run from protocol I ($\eta = 0$, top panels), we see a transition from the AS towards the FS that starts at a critical value of $\lambda_1^{AS} = \frac{2}{\pi g(0)}$ corresponding to that of the classical Kuramoto model (see eq. 2.15 in the Methods). This transition seems to be more continuous on R_1 and is generally mediated by intermediate states in the form of clusters. For the unimodal frequency distribution (panel (a)), we see that the uniform clusters (UCs) emerge for both positive and negative values of λ_2. However, we must note that these two UCs are slightly different, in the sense that the ones that emerge for positive λ_2, are not equally populated and this asymmetry is increased with λ_1. In other words, as we increase λ_1, one of the clusters starts to absorb oscillators from the other until there is only one giant cluster that conforms the FS state. We can understood this in terms of the potential $V(\phi)$ shown in Figure 3.2 (a), where the central minima increases with λ_1 while the external at $\phi \pm \pi$ becomes flat. In contrast, for negative λ_2, the two minima of the potential are symmetric around zero and have the same depth. Thus, in this region the UCs are always equally populated and the increase in R_1 comes from the two clusters slowly approaching each other until they merge into one. This scenario is very similar for the bimodal frequency distribution, with the novelty that a new dynamical state emerges for very small positive λ_1 and not too negative values of λ_2. These are the standing waves, SWs, that as we stated before, it is a state conformed by two clusters with opposite angular velocity. This state appears independently of the simulation protocol, but we can see that increasing the distance between the bimodal centers $\pm\omega_0$ leads to a wider region in their parameter space, as was already expected from [Crawford, 1994, Martens et al., 2009]. In particular, we see that for $\omega_0 = \pm 1$ they emerge for $\lambda_2 \in (-12, 2)$ and $\lambda_1 \in (1, 5)$ while for $\omega_0 = \pm 3$, the region extends to $(-30, 8)$ in λ_2 and $(1, 13)$ in λ_1.

3.3.2 Transitions to the coherent state

We will now characterize in detail the transitions previously described, contrasting the previous numerical results with the solutions given by the mean-field analysis reported in the Methods. In order to make the section clearer, we will distinguish four situations depending on the sign of λ_2 and the two type of distributions considered for the natural frequencies. For this purpose, we will fix λ_2 and then we will carefully follow the transitions by varying quasi-adiabatically λ_1 accordingly to simulation protocols (IA) and (IIA), depending on the initial condition.

Unimodal distribution of the natural frequencies, $\lambda_2 > 0$

We start then by considering the case of unimodal Gaussian distributions accordingly to $g_U(\omega)$ with $\Delta = 0.25$, in correspondence to the phase diagram of Figure 3.3(a). For positive $\lambda_2 = 15$, we recover the phase transitions shown in Figure 3.5 (a). For protocol (I A) (see blue dots), a partially synchronized state emerges for $\lambda_1^{AS} \simeq \frac{2}{\pi g(0)} \simeq 0.4$ corresponding to the

USC UNIVERSIDADE DE SANTIAGO DE COMPOSTELA

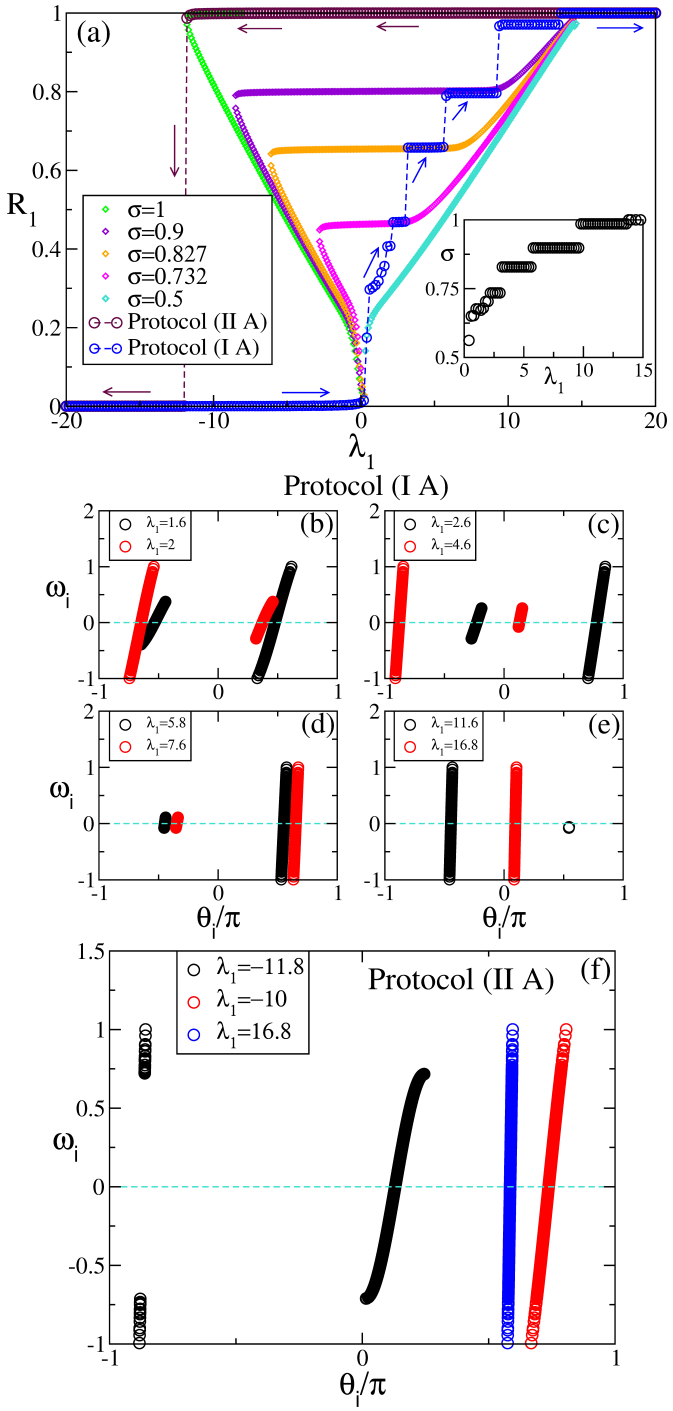


Figure 3.5: Phase transitions for the unimodal Gaussian distribution of natural frequencies and positive $\lambda_2 = 15$. (a) R_1 versus λ_1 : the blue and maroon circles refer to simulations performed by following protocols (I A) and (II A), respectively. The value reported for R_1 represents the average in time over a simulation time T_s. The diamonds of different colours denote the self consistent evaluation of the order parameter R_1, for different σ values, obtained by employing eq. (3.20). In the inset it is shown σ versus λ_1 as estimated by following protocol (I A). In panels (b-e) are reported snapshots of the natural frequencies ω_i versus their phases θ_i for different values of λ_1 obtained by following protocol (I A). Analogous snapshots are shown in (f) for simulations done by following protocol (II A). When necessary, the snapshots are arbitrarly shifted along the x-axis to improve readability. The displayed results refer to $\Delta = 0.25$ for $g_U(\omega)$, $\Delta\lambda_1 = 0.2$, $T_t = 10$, $T_s = 200$, integration step $dt = 0.001$ for the adiabatic simulations, and a network size $N = 10000$.

usual critical value predicted by the Kuramoto model. This is expected since the stability of the incoherent regime is usually analysed in the proximity of the transition to coherence via an expansion of the model at first order in R_1. As the the higher order interactions are proportional to R_1^2 (as shown in eq. 3.9), in this case they do not affect the stability. The approach to the fully synchronous regime (FS) occurs via a series of plateaus with increasing levels of synchronization, where R_1 remains constant when varying λ_1, until the system becomes fully synchronized ($R_1 = 1$) at $\lambda_1 \simeq 13.7$. As we mentioned earlier, these plateaus are actually formed by two phase-locked clusters that are differently populated with oscillators from both positive and negative frequencies (the UCs), that we now show in detail in panels (b-e) of Figure 3.5, for different values of λ_1. Here it is better grasped how the main cluster, that corresponded to the principal minimum of the potential $V(\phi)$, becomes more and more populated at the expenses of the secondary cluster, until only one remains. This can be clearly appreciated by measuring the redistribution factor σ directly from the simulations, where σ corresponds to the fraction of the oscillator in the larger minimum located at $\phi = 0$ (see the inset of Figure 3.5 (a)). In particular we observe that $\sigma \geq 0.5$ always, meaning that the cluster at $\phi = 0$ is always more populated than that at $\phi = \pm\pi$.

For protocol (II A), we remember that the system is initialized with all the phases equal to $\theta_i = 0$. Therefore, the oscillators are all located in the minimum $\phi = 0$ of the potential and they remain fully synchronized until $\lambda_1^{(PS)}(\sigma = 1) \equiv \lambda_1^{(FS)} \simeq -11.8$, where they abruptly de-synchronize. In particular, $\lambda_1^{(PS)}(\sigma)$ indicates the critical value at which the coherent regime characterized by σN oscillators in the minimum $\phi = 0$ ($(1-\sigma)N$ in the other minimum $\phi = \pm\pi$), looses stability.

To get some more understanding we estimated the self-consistent solutions (3.20) for different σ-values, obtaining thus the evolution of R_1 as a function of λ_1, shown in Figure 3.5 (a) for a few σ-values denoted by colored diamonds. We see that these curves for $\sigma > 0.5$ have all a similar shape. The partially synchronized state emerges abruptly via a bifurcation, that we can identify as a saddle-node, at a value $\lambda_1^{(PS)}(\sigma) < 0$, with a finite order parameter value,

$$R_1(\sigma) = 2\sigma - 1$$

corresponding to a two-cluster state with σN oscillators in $\phi = 0$ and $(1-\sigma)N$ oscillators in $\phi = \pm\pi$. The critical value $\lambda_1^{(PS)}(\sigma)$ should be larger than $\lambda_1 = -\lambda_2 R_1(\sigma)$, this is, where the minimum at $\phi = 0$ in $V(\phi)$ emerges. By increasing λ_1, the value of the order parameter remains equal to $R_1(\sigma)$ within a certain interval, giving rise to a plateau, and finally it approaches $R_1 = 1$ for $\lambda_1 = \lambda_2$, corresponding to the value where the smaller minimum in $V(\phi)$ at $\phi = \pm\pi$ disappears. Here, all the oscillators are fully synchronized at $\phi = 0$. We have estimated a few self-consistent curves corresponding to different σ-values measured during the finite size quasi-adiabatic simulation. The plateaus observed during the simulation performed via protocol (I A) coincide with those obtained by the self-consistent approach for the corresponding σ-value, as is clearly evident in Figure 3.5 (a). Furthermore, the self-consistent results for $\sigma = 1$ perfectly coincide with the simulations obtained with protocol (II A) and the de-synchronization transition occurs exactly at $\lambda_1^{(FS)} = -11.8$ as in the finite size simulations.

For the case $\sigma = 0.5$, corresponding to equally populated clusters, the self-consistent approach reveals that this state emerges at $\lambda_1^{(PS)}(\sigma = 0.5) \simeq 0.25$ with an order parameter value that is quite small ($R_1 \simeq 0.04$). Moreover, according to the self-consistent approach for $\sigma = 0.5$, no plateau is observable (see the cyan line in Figure 3.5 (a)). Similar results have been found

UC DE SANTIAGO

for $\sigma < 0.5$ with curves $R_1 = R_1(\lambda_1)$ lying slightly below the one obtained for $\sigma = 0.5$.

Note that we would expect the incoherent regime to become unstable at $\lambda_1^{AS} = \frac{2}{\pi g(0)} \simeq 0.4$ in the thermodynamic limit, as it is the theoretical prediction from the model. However there seems to be a wide region of multistability in the interval $\lambda_1 \in [\lambda_1^{(FS)}; \lambda_2] = [-11.8; 15]$, where the two cluster state solutions coexist, populated with a different percentage σ of oscillators. Therefore we expect the synchronization transition to be generically hysteretic, in a scenario somehow similar to that already observed for the Kuramoto model with inertia [Olmi et al., 2014]. The hysteretic nature of the transition is evident by considering the simulation performed by employing protocol (II A).

Unimodal distribution of the natural frequencies, $\lambda_2 < 0$

Attending now to negative $\lambda_2 = -100$ (panel (d) of Figure 3.3), we see that following protocol (IA), the asynchronous regime looses its stability again via a continuous transition in the proximity of $\lambda_1^{AS} = \frac{2}{\pi g(0)}$, as we show in the blue dots of Figure 3.6 (a). In the newly formed partial synchronized regime, two almost equally populated clusters emerge with uniformly distributed frequencies (the UCs), which are always present as shown in Figure 3.6 (b). Increasing λ_1 makes the synchronization within the clusters stronger, and so we see that the oscillators have their phases more vertically aligned. This behavior was expected from the shape of the potential $V(\phi)$, that in this case presents two minima of equal heights as shown in Figure 3.2(c).

For simulation protocol (II A) (see purple dots), we noticed that by decreasing λ_1, the order parameter R_1 decreases monotonically at first, but then, at $\lambda_1^{\pi} \simeq 3$, it shows an abrupt jump to a higher value. Afterwards, it continues to decrease towards zero until the asynchronous regime is smoothly achieved for $\lambda_1 \simeq -2.1$. This discontinuity has been previously reported in [Bi et al., 2016, Kovalenko et al., 2021], but its origin is still unclear. From the phase diagrams in Figure 3.3, we can see that this discontinuity crosses the whole negative semiplane and that the value λ_1^{π} increases with further negative values $-\lambda_2$. An important aspect to notice is that the two-cluster state is slightly modified at the discontinuity, as we report in panel 3.6(c): before the jump the oscillators are organised in two equally populated clusters separated by either positive or negative natural frequencies (the BCs), while after the jump the two clusters present mainly either positive or negative natural frequencies, but with a small group of oscillators of the opposite sign that have switched sides (as visible in 3.6(c) for $\lambda_1 = 2.2$).

Up to the discontinuity, we can shed some light in the emergence of the coexisting UCs and BCs from looking at the potential $V(\phi)$ in Figure 3.2(c). Since for protocol (IA) the oscillators' phases are distributed randomly across the circle, it is natural to see that depending on their initial phase the oscillators end up in the nearest minima independently of their natural frequency. On the other hand, for protocol (II), the oscillators are all initialized with the same phase $\phi = 0$, that corresponds to a local maximum of the potential. In this way, depending on the sign of their natural frequencies the oscillators migrate towards the minimum of $V(\phi)$ located in correspondence to the positive or the negative phase, splitting into two clusters where the oscillators have all the same sign of ω_i.

Also in the present case we can estimate the possible values attained by R_1 as a function of λ_1 in the mean field limit corresponding to protocol (I A), by solving the self-consistent equation eq. (3.22). As already mentioned, in this case, due to the symmetries of the potential $V(\phi)$, we do not observe any dependence on σ, therefore we set $\sigma = 0.5$ in eq. (3.22). The

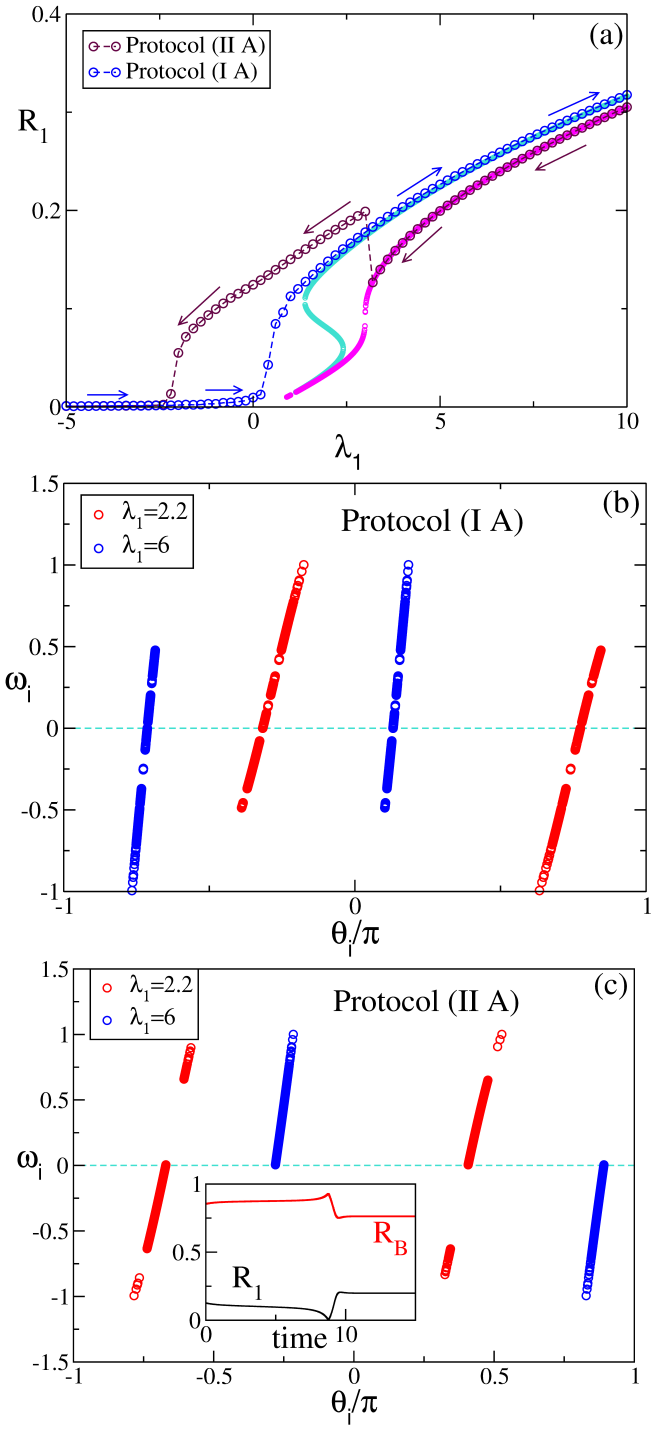


Figure 3.6: Phase transitions for the unimodal Gaussian distribution of natural frequencies and negative $\lambda_2 = -100$. (a) R_1 versus λ_1 : the blue and maroon circles refer to simulations performed by following protocols (I A) and (II A), respectively. The cyan (magenta) line refers to the self consistent evaluation of the order parameter R_1 by employing eq. (3.22) estimated in the whole range of frequencies (restriced to positive frequencies). In panels (b) and (c) are reported snapshots of the natural frequencies ω_i versus their phases θ_i for different values of λ_1 for simulations obtained by following protocols (I A) and (II A), respectively. In the inset of panel (c) we report the instantaneous values of $R_1(t)$ (black curve) and $R_B(t)$ (red curve) versus time for $\lambda_1 = 3$ obtained by following protocol (II A). The displayed results refer to $\Delta = 0.25$ for $g_U(\omega)$, $\Delta\lambda_1 = 0.2$ for the adiabatic simulations, and a network size $N = 10000$.

USC DE COMPOSTELA

results are shown as a cyan line in Figure 3.6 (a): the self-consistent solution for R_1 reveals two successive saddle-node bifurcations at $\lambda_1 \simeq 2.41$ and $\lambda_2 \simeq 1.38$. However a good agreement with the numerical data is observable for $\lambda_1 \geq 2.0$ only. This is due to the fact that the phase clusters emerge only above $\lambda_1 \geq 2.0$ while, below such a value, the system do not reveal any clear cluster.

To estimate the results corresponding to protocol (II A) via the self-consistent approach, we solved eq. (3.22) by integrating only either on positive or negative natural frequencies, depending if the oscillators are in the cluster with positive or negative phases. Once more, the agreement with the simulations is quite good from large λ_1 values down to the discontinuous transition value $\lambda_1^{(\pi)}$. The self-consistent solution (magenta line in Figure 3.6 (a)) reveals a sharp transition at $\lambda_1^{(\pi)} \simeq 3.0$, that we have termed the π-transition for reasons that will become evident in the following. Since we have no information about the stability of the solutions themselves, we can argue that the solution is stable for $\lambda_1 > \lambda_1^{(\pi)}$, and unstable for $\lambda_1 < \lambda_1^{(\pi)}$; with the 2 solutions annihilating in a saddle-node bifurcation at $\lambda_1^{(\pi)}$. The destabilization of the phase cluster states characterized by either positive or negative ω_i can be understood by following the evolution in time of the order parameters R_1 and R_B at $\lambda_1 = 3.0$, as shown in the inset of Figure 3.6 (c). There, both values of R_1 and R_B are initially constant until some time around $t \simeq 9$, where R_1 abruptly vanishes and R_B reaches one. Right afterwards, the value of R_1 becomes larger than the one it had initially, and R_B becomes smaller. Attending to the location of the clusters in the simulations, this behaviour can be interpreted as follows: the two cluster states are initially separated by an angle $\gamma < \pi$, then, they suddenly recede and γ reaches exactly π, corresponding to an anti-phase situation. The vanishing of R_1 implies a vanishing of the potential $V(\phi)$, therefore the 2 clusters destabilize and reform with a smaller angle γ between them. Moreover they reform with a different composition inside each cluster, which now includes oscillators with positive and negative natural frequencies.

Bimodal distribution of the natural frequencies, $\lambda_2 > 0$

Now we examine the transitions in the bimodal case, where the natural frequencies are distributed according to eq. 3.2 as $g_B(\omega_0 = 1, \Delta = 0.25)$, in correspondence to panel (b) and (e) of Figure 3.3. As we did before, we distinguish between positive and negative λ_2 and contrast the numerical results with those obtained from the self-consistent approach.

In this situation, due to the bimodal distribution of frequencies, in the asynchronous regime we have two groups of oscillators rotating with opposite frequencies that at some critical value λ_1^{AS} start to become synchronous at a common frequency $\Omega = 0$. In contrast to the unimodal case, here the effort done by oscillators of opposing frequencies to synchronize is considerably higher, with this effort being higher the larger the distance between bimodal centers ω_0. As a consequence, it is expected that the transition to the partially synchronous regime will be discontinuous and at a larger critical value than in the unimodal case [Pazó and Montbrió, 2009], which is what we see from Figure 3.7. Here we considered again $\lambda_2 = 15$, and for numerical simulations with protocol (IA) we found the critical point at $\lambda_1^{AS} \simeq 0.7$ (see the blue dots). The 2 cluster states formed after the transition find themselves at a distance π, as in the unimodal case. However they are now quite asymmetric, as evident from the value of σ, measured during the simulations and shown in the inset of Figure 3.7 (a). By increasing λ_1 the main cluster at $\phi = 0$ becomes more and more populated and, for $\lambda_1 \geq \lambda_2 = 15$, all the oscillators reside in such a cluster (see Figure 3.7 (b-e)). Therefore, once

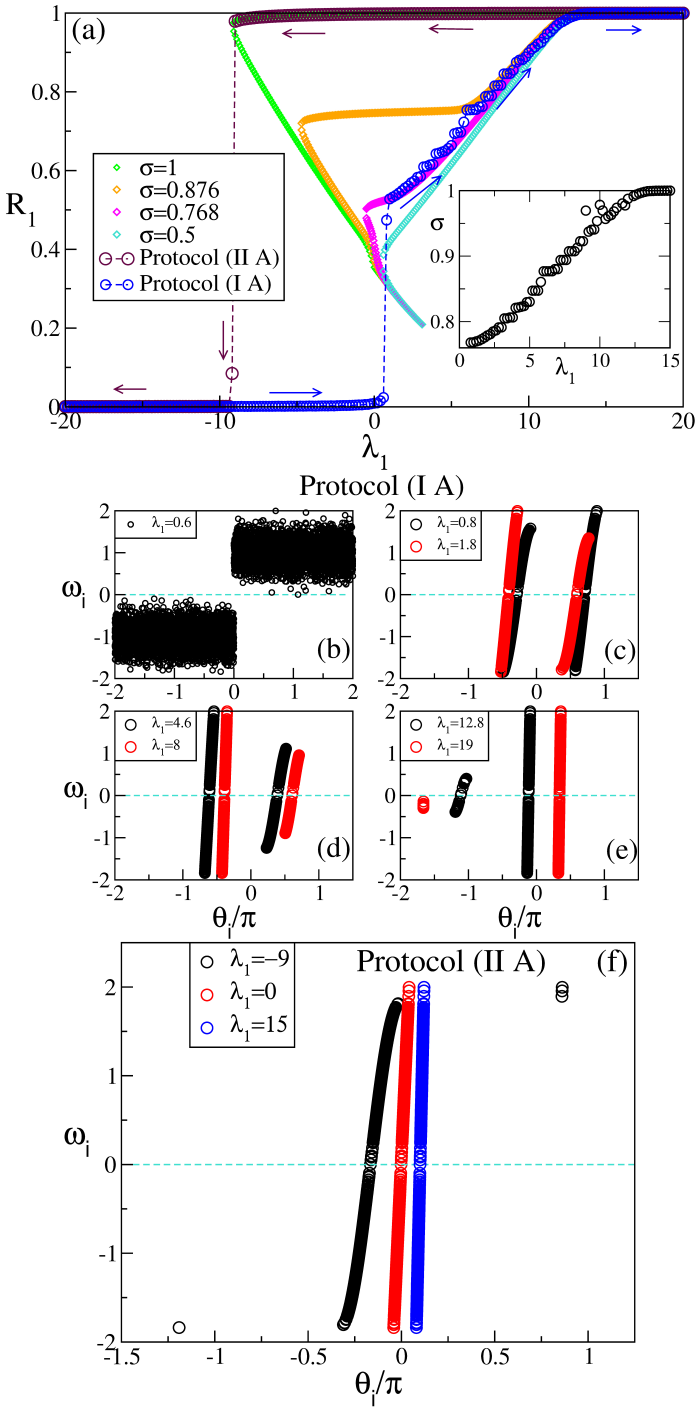


Figure 3.7: Phase transitions for the bimodal Gaussian distribution of natural frequencies with positive $\lambda_2 = 15$. (a) R_1 versus λ_1 : the blue and maroon circles refer to simulations performed by following protocols (I A) and (II A), respectively. The diamonds of different colours denote the self consistent evaluation of the order parameter R_1, for different σ values, obtained by employing eq. (3.20). In the inset it is shown σ versus λ_1 as estimated by following protocol (I A). In panels (b-e) are reported snapshots of the natural frequencies ω_i versus their phases θ_i for different values of λ_1 for simulations obtained by following protocol (I A). Analogous snapshots are shown in (f) for simulations done by following protocol (II A). The displayed results refer to $\omega_0 = 1$ and $\Delta = 0.25$ for $g_B(\omega)$, $\Delta\lambda_1 = 0.2$ for the adiabatic simulations, and a network size $N = 10000$.

USC UNIVERSIDADE DE SANTIAGO DE COMPOSTELA

the partially synchronized regime is emerged, the scenario turns out to be quite similar to that observed for the unimodal frequency distribution with $\lambda_2 > 0$. Indeed, also in this case a small plateau is observable for $\sigma = 0.876$.

The self-consistent approach estimated by employing eq. (3.20) for $\sigma > 0.5$ reveals, in complete analogy with the unimodal case, that a partially synchronized regime emerges via a saddle-node bifurcation at $\lambda_1^{(PS)}(\sigma)$, characterized by a finite value of the order parameter $R_1(\sigma) = 2\sigma - 1$. In this regard we have reported a few of these curves in Figure 3.7 (a). The solution shown as magenta diamonds, corresponds to $\sigma = 0.768$, which is the minimal σ value measured via the simulations in the PS regime. The magenta solution reproduces quite well the numerical simulations for $\lambda_1 > 0.7$ up to the complete synchronization, apart for the plateau, which is instead captured by the self-consistent solution for $\sigma = 0.876$ (orange symbols). Finally, the curve for $\sigma = 1$ (green symbols) perfectly reproduces the simulations obtained by following protocol (II A) (maroon circles) at the de-synchronization transition. At $\lambda_1 \simeq -9$ the evaporation of few oscillators towards the second minimum results in the reduction of R_1, with a consequent abrupt system de-synchronization, as shown in Figure 3.7 (e).

On the other hand, the self-consistent solution for $\sigma = 0.5$ (cyan symbols) shows the formation of a partially synchronous (PS) state via a saddle-node bifurcation for $\lambda_1 > \lambda_1^{(PS)}(\sigma = 0.5) \simeq 0.6$ with a finite value of the order parameter $R_1 \simeq 0.36$. The value $\lambda_1^{(PS)}(\sigma = 0.5)$ can represent a reasonable approximation of the numerically observed transition. As in the unimodal case, we have a wide interval of λ_1-values where we can have coexistence of incoherent and partially synchronized states. Moreover, also in this case, hysteretic synchronization transitions are observable. From the analysis reported in [Martens et al., 2009], one expects the transition from the asynchronous to the partially synchronous regime to be mediated by the emergence of SWs. However, for the present choice of parameters, we do not observe stable SWs. Indeed for $\omega_0 = \pm 1$ and $\Delta = 0.25$, SWs are observable only in the range $\lambda_2 \in [-11.7; 2]$, as we will discuss in the following.

Bimodal distribution of the natural frequencies, $\lambda_2 < 0$

Now, for negative $\lambda_2 = -100$, we observe for protocol (IA) that the transition to the partially synchronized case is also slightly discontinuous, with a critical coupling at $\lambda_1^{AS} \simeq 0.6$ (cyan lines of Figure 3.8(a)). The self-consistent estimation of the order parameter R_1 is obtained by solving eq. (3.22). Analogously to the unimodal case we observe that, due to the symmetric shape of the potential, the integral in eq. (3.22) does not depend on σ and therefore we can fix $\sigma = 0.5$. From the numerical simulations, the PS emerges at $\lambda_1^{(PS)} \simeq 3.8$, with the two cluster state being already observable immediately after the transition. However, the mean-field results and numerical simulations are in reasonable agreement only for $\lambda_1 > 5$, as shown in Figure 3.8 (b).

On the other hand, the analysis of the network simulations performed following protocol (II A), reveals that we recover again the BCs state where the oscillators are in two clusters characterized by only positive or negative natural frequencies, as is shown in panel (c). Following the same approach for the self-consistent analysis as in the unimodal case , we obtain two branches of solutions that merge in a saddle-node bifurcation at $\lambda_1^{(\pi)} \simeq 8.80$ (the magenta lines in Figure 3.8 (b)). Likewise, here we observe a very good agreement between the numerical values and the mean-field up to the discontinuity, where R_1 should drop to zero. In the inset of Figure 3.8 (c), we show again the time-evolution of both order parameters R_1

and R_B right at the discontinuity with $\lambda_1 = 8.8$, where we can observe something similar: at the transition point, R_1 reaches 0 while simultaneously R_B reaches 1, meaning that both clusters have reached phase opposition (with an intercluster angle $\gamma = 1$). Inmediately after, they quickly rearrange at a different angle $\gamma < \pi$ but now each cluster is still populated by oscillators with all positive or all negative natural frequencies. In this case, after the $\pi-$transition, what occurs is that the two clusters are much closer in distance, which results in the abruptly increase of the global order parameter R_1. By further decreasing λ_1, R_1 continues to decrease as the system becomes less and less synchronous until it becomes completely asynchronous at $\lambda_1^{PS} = -12$. In contrast to the unimodal case, the modified BCs state with a few oscillators switching sides that appeared after the SN bifurcation (seen in Figure 3.6), here it is only observed for small negative values of $\lambda_2 \leq -35$.

It seems then that at the discontinuity, there is an effort from the system to increase the global synchronization somehow, so in order to compensate for not being able to switch sides it seems that the two clusters approach together to obtain the increase of R_1. Let us now re-examine the transition obtained with protocol (II) from the point of view of our clustering order parameter R_B and the inter-cluster angle γ. In Figure 3.9(a), we report the phase diagram for $\omega_0 = 1.0$ (note that this is the one previously shown in Figure 3.3(e)) but showing now R_B). We can see from this panel that in the negative semiplane of λ_2, there is indeed a very strong level of cluster-synchronicity composed in this case of BC states, and that this state remains very well-defined after the discontinuity that can still be seen in the positive region of λ_1. In panels (b) and (c) we show the de-synchronization transitions from FS to BCs, to AS; and BCs to AS respectively, which correspond to the white arrows outlined in panel (a). The first one corresponds to $\lambda_2 = -30$, where we observe that for decreasing λ_1, while R_1 decreases accordingly, R_B and γ increase, indicating that the fully synchronous state splits smoothly into the two the clusters that progressively separate (note that this could not be appreciated from panel (a) of Figure 3.8, where we examined $\lambda_2 = -100$). This continues until the discontinuity is reached at λ_1^{π}, where the clusters suddenly approach the phase opposition at $\gamma = 1$, cross to the other quadrant and stabilize at an angle γ smaller. This results in the sudden increase of R_1 and therefore the decrease in R_2, as the latter is a function of the former. By further decreasing λ_1, the clusters begin to separate again and before reaching phase opposition, the BC state is destroyed abruptly at some negative λ_1^{PS}, recover the asynchronous state. This latter transition occurs similarly from the point of view of increasing adiabatically λ_2 and fixing λ_1, as it can be grasped from panel (c). Here we see that R_B is close to 1 for a wide range of the higher order coupling. Around $\lambda_2 \simeq -500$, the clusters slowly begin to de-synchronize until a certain critical value is reached and the clusters abruptly dissapear. In this case however, notice that the decrease of R_2 is not caused by the clusters approaching each other (R_1 is not increasing), but because the oscillators with the natural frequencies furthest from the centers of the distribution begin to drop out of the clusters. Panels (d) and (e) show evidence of this disintegration by plotting snapshots of the oscillator phases and time-averaged velocities against their natural frequencies, for the circled points drawn in panel (c). From these panels it is clear that only the oscillators with natural frequencies in proximity of $\Omega = 0$ are synchronized and their number decrease by approaching the transition towards the incoherent state.

USC
UNIVERSIDADE DE SANTIAGO DE COMPOSTELA

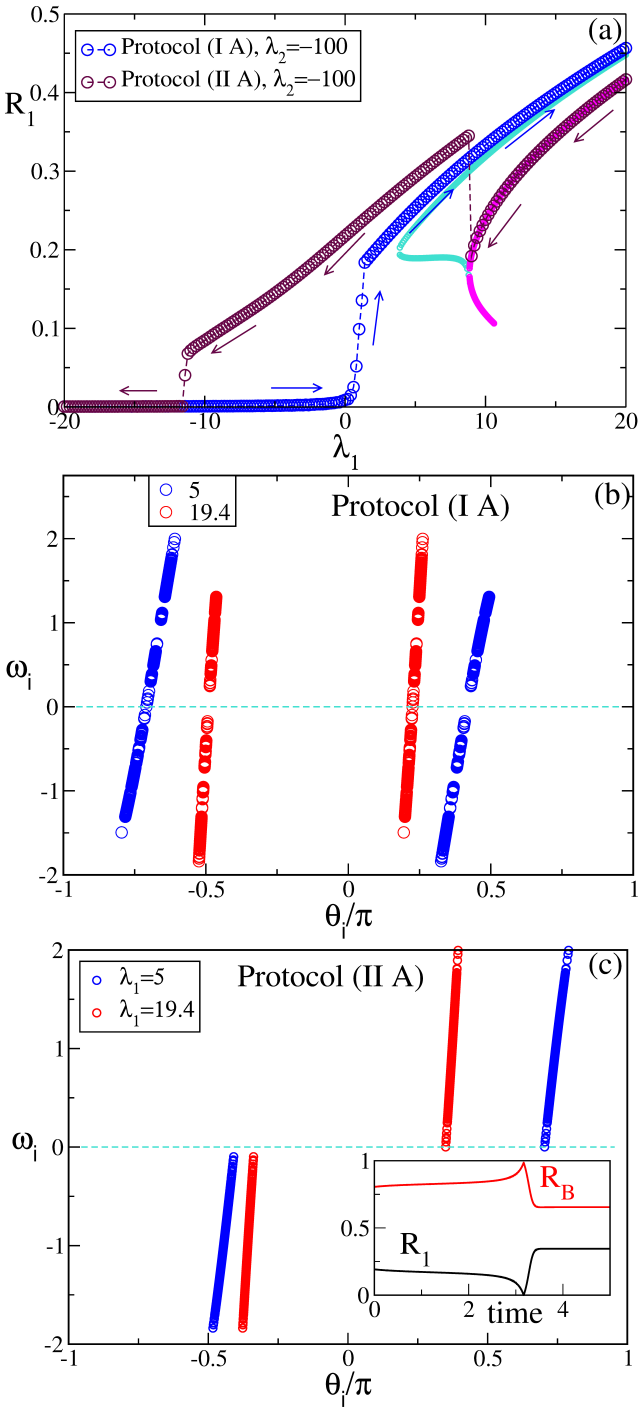


Figure 3.8: Phase transitions for the bimodal Gaussian distribution of natural frequencies and negative $\lambda_2 = -100$. (a) R_1 versus λ_1 : the blue and maroon circles refer to simulations performed by following protocols (I A) and (II A), respectively. The cyan (magenta) line refers to the self consistent evaluation of the order parameter R_1 by employing eq. (3.22) estimated in the whole range of frequencies (restriced to positive frequencies). In panels (b) and (c) are reported snapshots of the natural frequencies ω_i versus their phases θ_i for different values of λ_1 for simulations obtained by following protocols (I A) and (II A), respectively. In the inset of panel (c) we report the instantaneous values of $R_1(t)$ (black curve) and $R_B(t)$ (red curve) versus time for $\lambda_1 = 8.8$ obtained by following protocol (II A). The displayed results refer to $\omega_0 = 1$ and $\Delta = 0.25$ for $g_B(\omega)$, $\Delta\lambda_1 = 0.2$ for the adiabatic simulations, and a network size $N = 10000$.

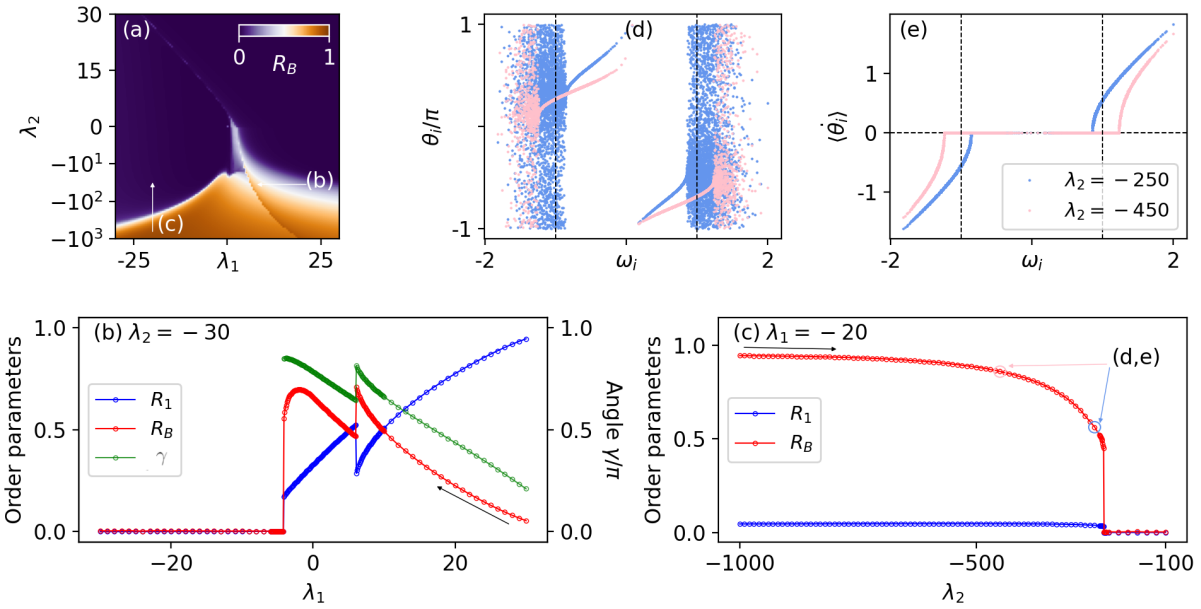


Figure 3.9: Numerical analysis of BC state. In (a), the order parameter R_B is a function of the coupling strengths λ_1 and λ_2, only for the simulation protocol (II A). The white arrows give the sense and direction to the de-synchronization transitions shown in panels (b) and (c), obtained by varying quasi-adiabatically the coupling parameters. For (b) $\lambda_2 = -30$, while for (c) $\lambda_1 = -20$. The pink and blue circles highlighted in panel (c) refer to (λ_1,λ_2)=(-20,-450) and (λ_1,λ_2)=(-20,-250) respectively. Using the same colorcode (pink and blue), these states are analyzed in panels (d,e) in terms of their instantaneous phases and averaged velocities. The snapshot presented in (d) is related to the instantaneous phases against their natural frequencies. In (e) the time-averaged velocity of each oscillator is reported against its natural frequency. For all panels, the bimodal parameters were fixed at $\omega_0 = 1$ and $\Delta = 0.25$.

USC UNIVERSIDADE DE SANTIAGO DE COMPOSTELA

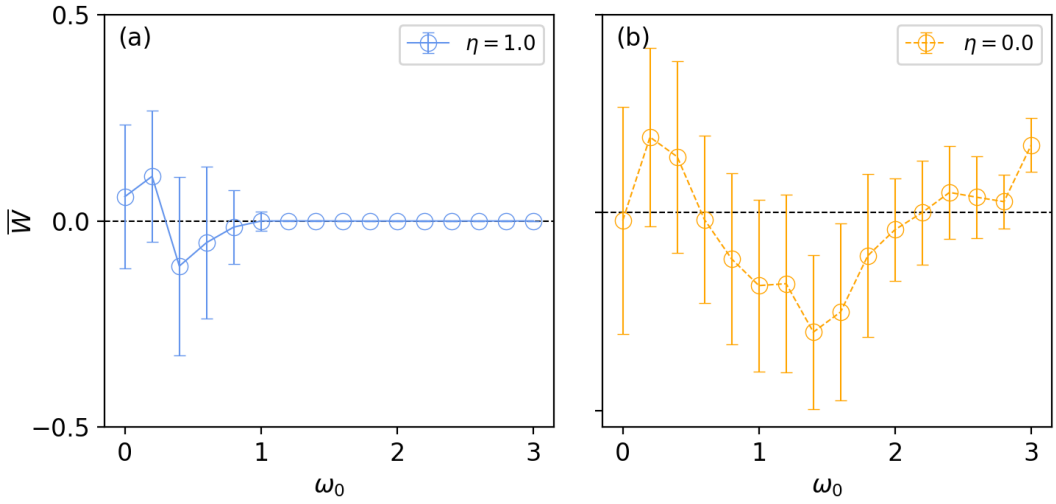


Figure 3.10: Time averaged velocity of the ensemble $W = \frac{1}{N}\sum_j^N \langle \dot{\theta}_j \rangle$ versus the center of the symmetric bimodal peaks. The error bars denote an average over a significant number of system realizations to state the effects of different realizations of the natural frequencies. Panel (a) correspond to simulations started from synchronous initial conditions ($\eta = 1$), while the orange points correspond to simulations started from asynchronous ones ($\eta = 0$). For each point $(\lambda_1, \lambda_2) = (10, -1000), \Delta = 0.25, N = 5000$ and $n_{sim} = 100$.

3.3.3 Multistability and clustered regimes

Finally, to end this chapter's results we pay some attention to the system's multistability, especially between the bimodal and uniform cluster states.

We start by examining the dependence of the average angular velocity $W = \frac{1}{N}\sum_j^N \langle \dot{\theta}_j \rangle$ on the distance between the bimodal centers ω_0 of the frequency distribution. For the case of the bimodal clusters (BCs), we observe that W becomes zero from $\omega_0 \geq 1$, which is the distance at which essentially the two modes are sufficiently separated and neither of the two cross zero. On the other hand, for the uniformly distributed clusters (UCs), W exhibits large oscillations depending on the initial conditions and remains finite even for large $\omega_0 \simeq 6x\Delta$. This is shown in panels (a) and (b) of Figure 3.10, where the error bars represent the standard deviations from multiple simulations with different initial conditions. This result can be easily understood in terms of the population symmetry: for the BCs, if $\omega_0 \geq 1$ one observes that the two clusters emerge being equally populated, while if the two modes of the distribution are closer to zero and have both positive and negative frequencies, then some asymmetries may appear which induce the finite average velocity. On the other hand, starting from initially random phases and obtaining the UCs, each oscillator has a random chance to jump to one of the two clusters and therefore because of finite size sampling there are always some asymmetries in the cluster populations. Nevertheless, a remarkable feature of both cluster states is that all the oscillators are frequency locked, so these two situations, either if all the oscillators move coherently around the circle or they are all at rest, can be considered identical when examined in a comoving reference frame moving with velocity W.

We move on now to analyzing the dependence of the cluster states on the initial conditions and measured their synchronicity using R_B. So far we have only examined what happened when either all oscillators where initially phase-locked ($\eta = 1$) or were totally incoherent ($\eta = 0$), generally obtaining the BCs with $R_B = 1$ and the UCs with $R_B = 0$ respectively (this was specially true for sufficiently negative λ_2 and positive λ_1). By sweeping η from 0 to 1 with

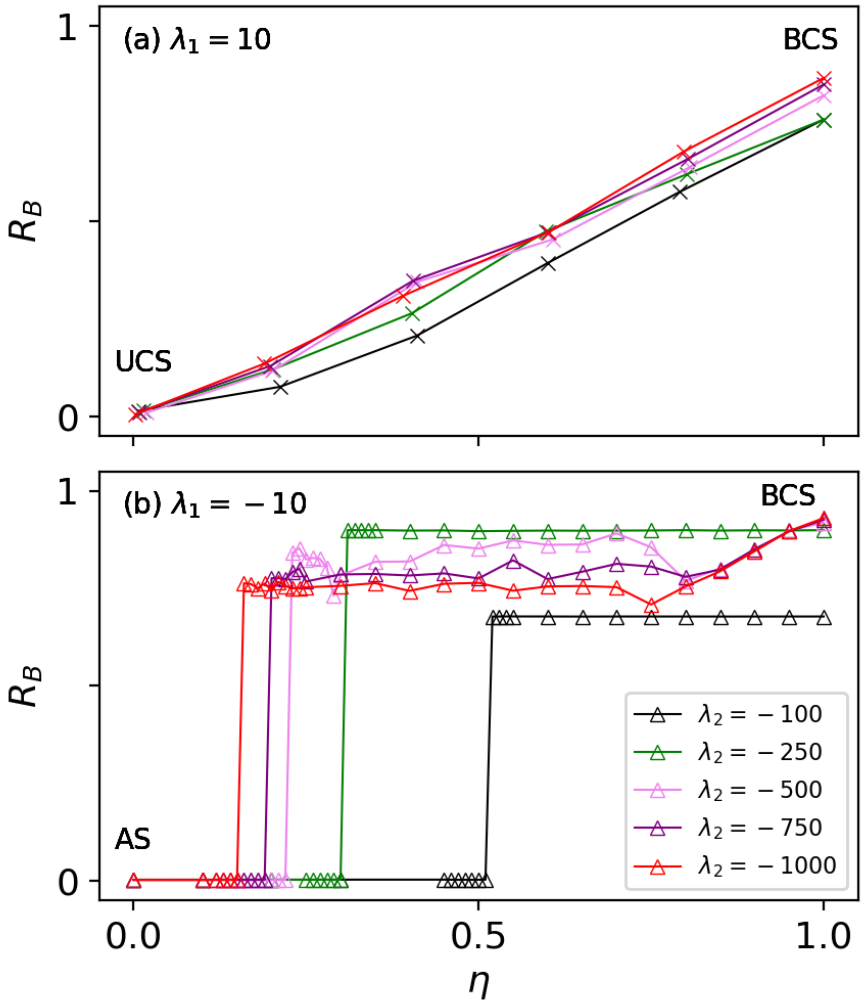


Figure 3.11: Clustering order parameter R_B for increasing values of the initial degree of phase-locking η, and different values of the higher order coupling λ_2. In (a), with $\lambda_1 = 10$, the labelled points correspond to panels (c) and (d) of Figure 3.4, and in the middle we can see all the intermediate steps from one state to the other. In (b), with $\lambda_1 = -10$, we see tje transition from the asynchronous state AS to the bimodal cluster state BCS at different critical points in function of the value of λ_2. For every point, $\omega_0 = 1.0, \Delta = 0.25, N = 5000$.

$\lambda_1 = 10$ and several values of λ_2, we found a stable cluster state for each value of η, observing that R_B increased accordingly to η and independently of λ_2 (see Figure 3.11(a)). Thus, it seems that we pass smoothly from a situation where the phase clusters are not associated to the frequency distribution of ω_i (as in Figure 3.4(d)), to one where each cluster involves only oscillators with positive/negative ω_i (Figure 3.4(c)). We have also considered the case where there is multistability between the BCs and the asynchronous state (AS) (see Figure 3.11(b)). In this situation, for $\lambda_1 = -10$, by varying η we find that there exists a myriad of abrupt transitions depending on the value of λ_2. The more large is $\|\lambda_2\|$, the sooner appears the critical value η_c at which the cluster state emerges. In this sense, very large negative higher order interactions seem to have a strong destabilizing impact on the asynchronous regime and therefore favoring a synchronized one. This could also be related to the fact that the depth of the two symmetric minima in the potential $V(\phi)$ increased with $\|\lambda_2\|$, as we saw in Figure 3.2(b).

USC
UNIVERSIDADE DE SANTIAGO DE COMPOSTELA

3.4 Summary and conclussions

In this chapter, we have considered a strong increase in the complexity of the Kuramoto model by combining the usual pair-wise first harmonic interaction term with the addition of a symmetric three body interaction. We have characterized the phase space of the model attending to the different coupling strengths, λ_1 and λ_2 and for both unimodal and bimodal Gaussian distributions of the natural frequencies. For each case, we carefully examined the transitions between the dynamical regimes with the help of the self-consistent approach.

To better understand the origin of these transitions at the mean-field level, we have analyzed the dynamics of a reference oscillator with that of an overdamped particle moving in a potential well $V(\phi)$ (see eq.3.12), with this potential being very insightful to explain the coexistence between the dynamical states presented in Figure 3.4. Depending on the sign of the higher order interactions λ_2, $V(\phi)$ showed different characteristics: for example, for positive λ_2, the potential presented two minima with different depths controlled by λ_1 that corresponded to two clusters slowly merging into the one with increasing depth (which eventually led to the fully-synchronous state (FS)). On the other hand, for negative λ_2, the potential showed two symmetric minima around zero of equal depth that depending on the initial condition of the phases, it gave raise to two qualitatively different cluster states, the BCs and the UCs. While in the first one there exists a clear correlation between the sign of the oscillators' natural frequencies and the cluster they occupy, in the second one there is not any sign of this correlation. Guided by the potential, we believe that this occurs because as the oscillators start being totally synchronous, the sign of their natural frequency leads them to fall into the respective minima of the potential; while if they have an initial random phase, they fall indistinctly in any of them.

We have paid special interest to these clustering regimes, since the introduction of the bimodal frequency distribution seems to destabilize the asynchronous regime in favor of the BCs, allowing for a considerably wide region of the parameter space where a synchronous state can emerge even with both interaction couplings being negative. This striking feature was first discovered by [Dai et al., 2021] for the unimodal frequency distribution, and it must be noted that it is a pure effect of the higher-order contribution, as this is totally prohibited in the pair-wise Kuramoto model. Here we showed through Figure 3.3 that the presence of a bimodal frequency distribution even makes this state more accessible, considerably enlarging their area of emergence in the parameter space for increasing distances of the bimodal peaks $\|\omega_0\|$.

We have also analyzed here the origin of the discontinuity in the order parameter observable across the whole seminegative plane in λ_2 for protocol (II) (see panels (d-f) of Figure 3.3). In particular, we have seen that for sufficiently negative λ_2, decreasing λ_1 from the fully synchronous state (FS) results in the smooth formation of the two bimodal clusters (BCs) that slowly separate from each other until they reach discontinuity λ_1^{π}. Here, the self-consistent approach predicts that the system should de-synchronize in terms of R_1, but what we see from simulations is that although R_1 becomes zero for an instant (because of the 2-clusters reaching phase-opposition with $\gamma = \pi$), right after the transition the clusters rearrange at a different angular distance γ smaller than before. Besides, for unimodal configurations (and also for smaller values of λ_2 in the bimodals), this is new state is also characterized by oscillators that have switched clusters. All this leads to the abrupt jump in R_1 observed in the phase diagrams.

As an ending note, the notions and dynamical regimes presented in this chapter summarize well the phenomena expected when dealing with synchronization problems and the

USC DE COMPOSTELA

methodology used to tackle them: building the phase portrait, examining the synchronization transitions and carefully looking at the micro features of the states as the phases and angular velocities. We will use this similar methodology in the following chapters where we will deal with more complex oscillators in which besides the phase one must also have to pay attention to other features as the oscillation's amplitudes and periods. There we will also look for clustering regimes and under which conditions they emerge.

USC
UNIVERSIDADE
DE SANTIAGO
DE COMPOSTELA

USC
UNIVERSIDADE
DE SANTIAGO
DE COMPOSTELA

Chapter 4

Intermittency regimes in chemical oscillators with local interactions

In the previous chapter, we examined the synchronization of periodic phase-oscillators, arguably the simplest kind of oscillating elements and yet so filled of complex behaviors. Here, we study another type of oscillator obtained from the chemical dynamics of the Belousov-Zhabotinsky reaction, thus reducing the abstraction and getting one step closer to realism. Now, besides the phase variable, these oscillators present different amplitudes and frequencies that vary with the coupling parameters, with abrupt changes from one dynamical regime to the next. Here we also enhance the complexity by leaving behind the mean-field and the all-to-all configuration in favor of nearest neighbor interactions. In this way, here we simulate a two-dimensional pool of these chemical oscillators that interact only locally with those oscillators in its neighborhood and its surrounding fluid parcel, studying how different mixing rates affect the overall dynamical landscape.

Part of the text and figures for this chapter are reproduced from

* Carballosa, A.[1,2] & Muñuzuri, A.P[1,2], *"Intermittency regimes of poorly-mixed chemical oscillators"*, Chaos, Solitons & Fractals, Volume 157, 111920 (2022), `https://doi.org/10.1016/j.chaos.2022.111920`.

[1] Group of Nonlinear Physics, Faculty of Physics, University of Santiago de Compostela
[2] Galician Centre for Mathematical Research (CITMAGa), University of Santiago de Compostela

4.1 Introduction

Large populations of catalyst-loaded oscillatory beads immersed in a catalyst-free BZ reaction represent an experimental paradigm of synchronization phenomena, with a huge range of different experimental set ups in which can be arranged and with the corresponding numerical schemes that are able to recover the main features of the system [Field, 2000]. To give some context, one basic setup consists in a continuously stirred tank reactor (CSTR) where the oscillating chemical reaction is taking place in the surface of the catalyst loaded particles and the system is stirred at different rates. The stirring rates acts then as a control parameter that is equivalent to the coupling K of the Kuramoto model. Thus the higher the stirring rate, the higher the chemical exchange between particles and solution. This accelerates the dynamics of

the reaction and therefore the periods of the oscillations, or in other words making the oscillators closer in frequency. Eventually, and as we saw from the insights of the Kuramoto model, when the oscillators have sufficiently close frequencies they start to group up into a synchronous cluster. In this setup, the level of synchronization can be experimentally measured from the global electrochemical signal, which is noisy on the start, but becomes ordered as more and more oscillators group together. In contrast to the plain phase oscillators, here the number of oscillators have an important role too on synchronization. Having more of them in the tank implies more chemical concentration of the catalyst and this modifies too the dynamics of the reaction. This is, with the chemical oscillators there are at least two different routes toward synchronization, with different corresponding phase transitions [Taylor et al., 2009]. At low values of the stirring rates, for low values of the bead density the situation is completely asynchronous, with each particle oscillating at its natural frequency. However, there is a critical density at which small amplitude oscillations appear in the electro-chemical global signal, and with increasing densities the signal becomes totally clear as all the oscillators oxidize simultaneously . This phase transitions corresponds almost exactly with the partial synchronization one of the classical Kuramoto model. In this case, the solution acts as the mean-field coupling all the oscillators together. Here there is also a feedback loop between the degree of synchronization in the system and the influence that the mean-field exerts on the individual particles. When the cluster oscillates, there is a sudden change in the concentrations of the solution that reaches the uncoupled oscillators. In this case, because of the excitable features of the BZ reaction, if the conditions are propitious then when the uncoupled oscillators receives this signal from the mean field, it fires in advance and in synchrony with the rest of the cluster. For higher values of the stirring rates however, the transition to synchronization is explosive at the critical value, as more complex dynamics between the chemical concentrations prohibit oscillations for low density values. This latter state is usually termed as a quiescent state or oscillation death and is very characteristic of this type of oscillators.

More complex collective states have been also reported with variations of this experimental setup, such as phase-clusters [Tinsley et al., 2009, Mersing et al., 2021], chimera states [Tinsley et al., 2009, Totz et al., 2018], spatio temporal waves [Tinsley et al., 2010, Tinsley et al., 2012] and a special type of full phase synchronization between the beads and the surrounding solution, termed as super-synchronization or mobbing state [Ghoshal et al., 2016]. This latter state introduced a new perspective into the usual approaches, where the surrounding solution was considered to act just as the mean field that coupled the bead's population, but ignoring its potentiality as an oscillator itself [García-Selfa et al., 2021]. Besides, in this way, non-homogeneous mixing in the reactor and spatial heterogeneities are usually left aside, along with possible states of partial synchronization due to local density variations or swarming-like behaviors induced by the movement of the oscillators, as occurs with swarming insects or flocking birds [O'Keeffe et al., 2017]. In this sense, it has been pointed out by [Garaboa-Paz et al., 2016] that non-perfect mixing with the surrounding solution modelled as a turbulent chaotic flow leads to spatial patches of synchronized regions within the domain.

Following the latter ideas, we discretized the surrounding solution as another set of potentially-oscillating particles and only allowed interactions and chemical exhange between the particles within a given radius. Assuming a two dimensional reactor that is being subject to a uniform external vibration, we consider that all particles move randomly across the reactor and at different velocities, simulating a spatially extended CSTR (continuously stirred tank reactor). With this approach we were able to recover the dynamical states already reported in the

literature for this type of setup, including the super synchronization state, but in contrast to the smoot phase transitions previously found on [Ghoshal et al., 2016], we found an intermittence between the dynamical states that lingered persistently in the vicinity of the transitions. This occurred mainly in conditions of non-perfect mixing due to low velocities of the particles, when chemical exchange between same neighbors occurred for prolonged periods in time.

4.2 Methods

4.2.1 Model

The oregonator model introduced in eq. 2.3 can be adapted straightforwardly to the dynamics of each oscillating bead i. Here, the concentration values for $HBrO_2$, Br^- and catalyst are denoted by u_i, v_i and w_i respectively. The coupling parameter of the system is given by K_{ex}, which represents the chemical exchange rate between the beads and the catalyst-free solution, that here will be also discretized as fluid particles. The equations of our model are, for the particles representing the beads,

$$\begin{cases} \dot{u}_i^B = \frac{1}{\varepsilon}\left(u_i^B(1-u_i^B) + v_i^B(q-u_i^B) - K_{ex}\left(\frac{1}{N_B+N_S}\sum_k^{N_B}(u_i^B-u_k^B) + \frac{1}{N_B+N_S}\sum_{S\,k}^{N}(u_i^B-u_k^S)\right)\right) \\ \dot{v}_i^B = \frac{1}{\varepsilon'}\left(2hw_i^B - v_i^B(q+u_i^B) - K_{ex}\left(\frac{1}{N_B+N_S}\sum_k^{N_B}(v_i^B-v_k^B) + \frac{1}{N_B+N_S}\sum_k^{N_S}(v_i^B-v_k^S)\right)\right) \\ \dot{w}_i^B = u_i^B - w_i^B \end{cases} \tag{4.1}$$

where the super-index B refers to variables representing the beads and super-index S refers to the particles representing the catalyst-free solution where the beads are immersed. The equations governing the chemical state of such particles are given by,

$$\begin{cases} \dot{u}_i^S = \frac{1}{\varepsilon}\left(u_i^S(1-u_i^S) + v_i^S(q-u_i^S) - K_{ex}\left(\frac{1}{N_B+N_S}\sum_k^{N_S}(u_i^S-u_k^S) + \frac{1}{N_B+N_S}\sum_k^{N_B}(u_i^S-u_k^B)\right)\right) \\ \dot{v}_i^S = \frac{1}{\varepsilon'}\left(-v_i^S(q+u_i^S) - K_{ex}\left(\frac{1}{N_B+N_S}\sum_k^{N_S}(v_i^S-v_k^S) + \frac{1}{N_B+N_S}\sum_k^{N_B}(v_i^S-v_k^B)\right)\right) \end{cases} \tag{4.2}$$

q,h,ε and ε' are parameters of the model regarding the chemical kinetic rates and initial concentrations. On the other hand, the summations take into account only those N_B beads and N_S solution particles with whom the particle i chemically interacts. In other words, those particles that fall within a distance less than R_0 from the particle i. From here on, we will refer to this quantity as the interaction radius of particle i. This interacting radius can be interpreted from the point of view of networks as a temporal adjacency matrix for each node, with node i connected to all those nearest neighbors given by the radius. In fact, in order to carry the simulations we define a squared adjacency matrix of size N_B+N_S whose elements a_{ij} are 1 if particle j falls within the radio of i and 0 otherwise. This adjacency matrix is updated at each time step, with the corresponding connectivity distribution being Poissoninan shaped as the total number of oscillators that fall within the radius is random in nature. Now, notice that each sum is weighted over the total number of particles within that radius in order to account for

USC DE SANTIAGO

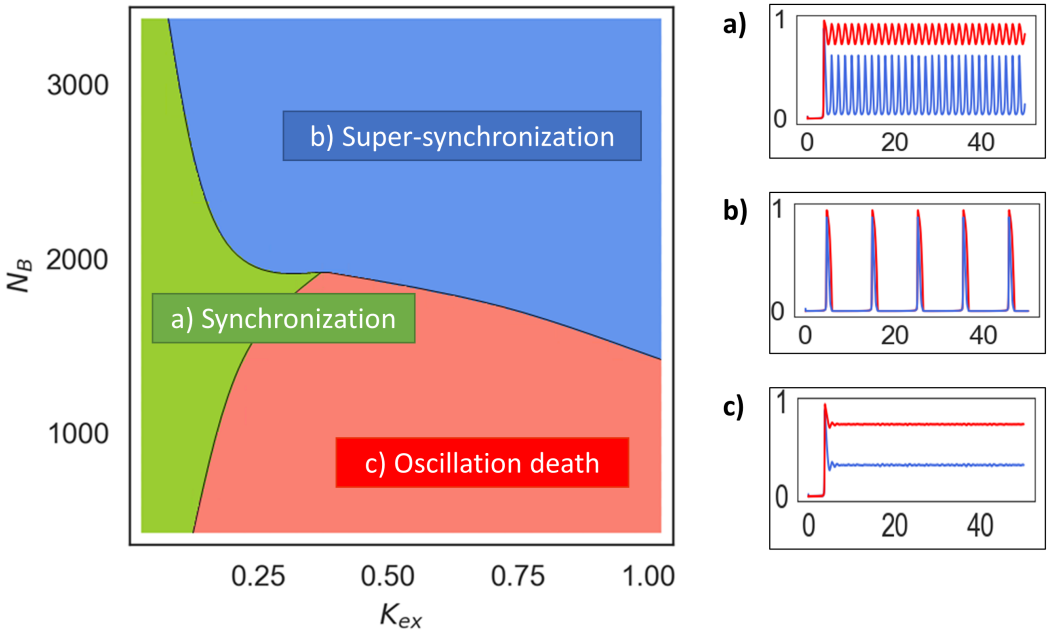


Figure 4.1: Phase diagram of the model with high mixing rate, $r > 0.01$, $N_s = 2000$ fluid particles and an interaction radius $R_0 = 0.01$. In the right panels, the blue line represents the average concentration u of the bead ensemble while the red line is the average concentration u_S of the solution particles

the particle density, one of our control parameter. As we will leave the total number of solution particles N_S fixed, the density of the system will be given by the total number of bead particles N_B. The other control parameter in our simulations will be the coupling constant, K_{ex}. The dynamical landscape given by the phase space of these two parameters is represented in Figure 4.1. For low values of K_{ex}, we recover the synchronization regime, where all the beads in the reaction have synchronized their phase and oscillate with high frequency and small amplitude. For high values of K_{ex} and low density of bead particles N_B, the system is found on oscillation death, where the oscillations have vanished and the chemical activity remains quiescent.

Finally, for higher values of K_{ex} and very high density we reach the super-synchronization state, where the bead population is not only synchronized between themselves but also with the solution population. Another important difference between both synchronization regimes is that the latter exhibits oscillations of significantly larger period and amplitude. There is also present the asynchronous regime, but with the kinetic parameters considered it is found only in a very small window of parameter space for really low values of the coupling strength, not considered here.

As we commented earlier, the particles are allowed to move with random jumps in any possible direction inside a simulation square box of size L as the one in Figure 4.2, with reflective boundary conditions. Each jump has a random uniformly distributed distance between 0 and r. The maximum jump distance r is left as a free parameter that will account for the mixing rate of the system. The higher this value, the higher the average velocity of the particles inside the reactor and thus the higher the mixing of the system. We can consider that proper mixing rates are achieved when r is equal or larger than 10% of the box size L, as it is the value at which we recover the phase-space for the mean-field model shown in Figure 4.1. An example of the

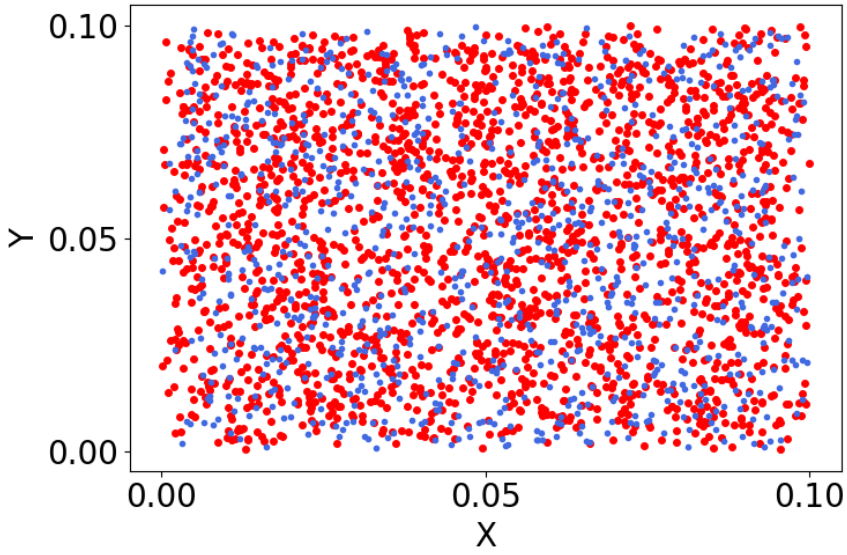


Figure 4.2: Random spatial distribution of the solution (red) and bead (blue) particles in a simulation box of size $L = 0.1$, $N_B = 1000$ and $N_S = 2000$.

simulation box for $L = 0.1$, $N_B = 1000$ and $N_S = 2000$ is represented in Figure 4.2. In order to characterize the system at different levels of mixing rate, notice that we can tune either the maximum particle distance r or the interaction radius R_0. On one hand, decreasing R_0 limits the number of particle interactions and therefore the chemical exchange, while increasing it over the size of the box recovers the mean field approach. On the other hand, decreasing r to zero is equivalent to all particles being static, while large values of r make the particles so fast that each new interaction between two particles i, j is completely random. Thus, both parameters affect significantly the mixing and we have observed that the outcome is quite analogous. So, we have fixed $R_0 = L/10 = 0.01$ and chose r as the control parameter for our simulations as it is a variable easier to reproduce in a controlled laboratory experiment.

Finally, the synchronization among the beads is measured through the Kuramoto order parameter R,

$$R = \left\langle \frac{1}{N} \sum_{j}^{N} e^{i\phi_j} \right\rangle \tag{4.3}$$

where ϕ_j is the phase of the jth oscillator and the brackets account for average in time. The phase of each oscillator is estimated from the concentration u_j by means of a Hilbert transform. As in the Kuramoto model, this order parameter measures coherence in ranges from 0 to 1, with zero being completely asynchronous and 1 total synchronization.

4.2.2 Numerical details

The kinetic parameters of equation 4.1 are fixed to $q = 0.002$,$h = 0.70.03$,$\varepsilon = \varepsilon' = 0.01$ to ensure oscillating dynamics. Besides, some Gaussian noise is added in the h value to induce heterogeneity in the oscillators' natural periods and to simulate experimental conditions. With this parameters, Figure 4.3 shows the distribution of natural periods and phases for the uncoupled case, $K_{ex} = 0$. For the simulation box, we leave $L = 0.1$ and $N_S = 2000$, as

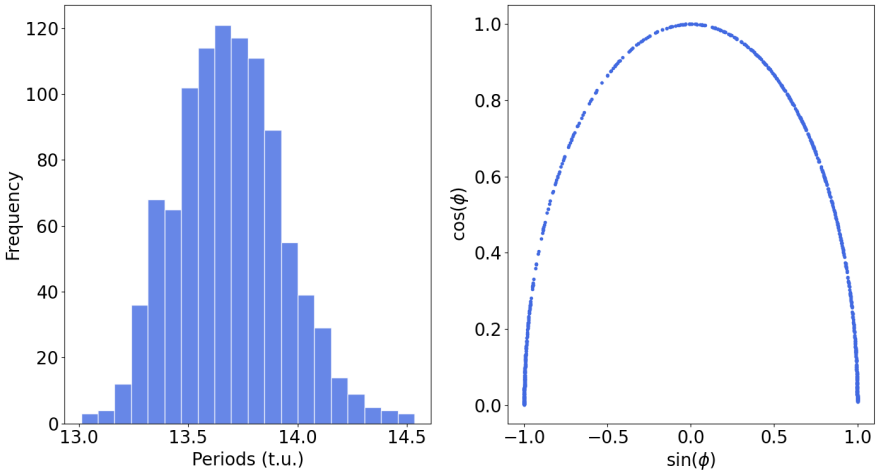


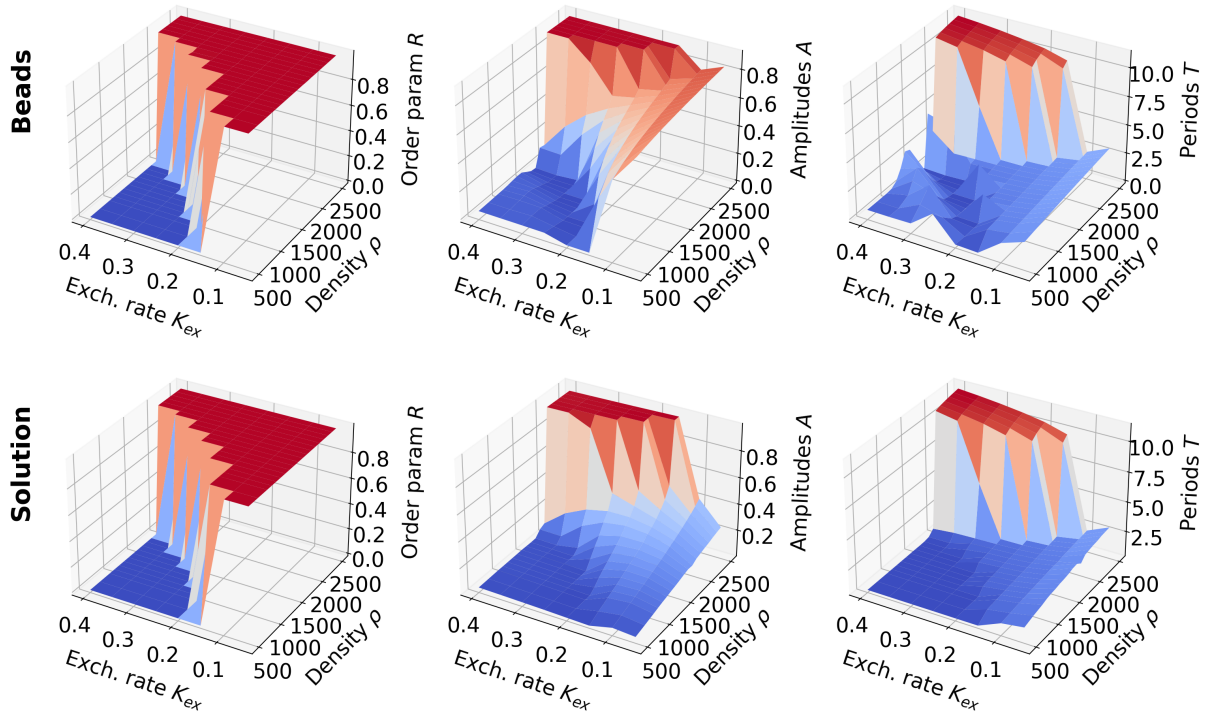
Figure 4.3: Distribution of bead periods and phases for the parameter values considered. In this case, $K_{ex} = 0$ and $N_B = 1000$.

this combination of parameters resulted in a reasonable amount to discretize the fluid in the box domain. Notice that increasing N_S, as we shall see later, increases exponentially the computational cost needed to run the simulation. Regarding the numerical integration of the system, a 4th order Runge-Kutta with $dt = 0.002$ was employed (see Appendix B for details on the numerical scheme).

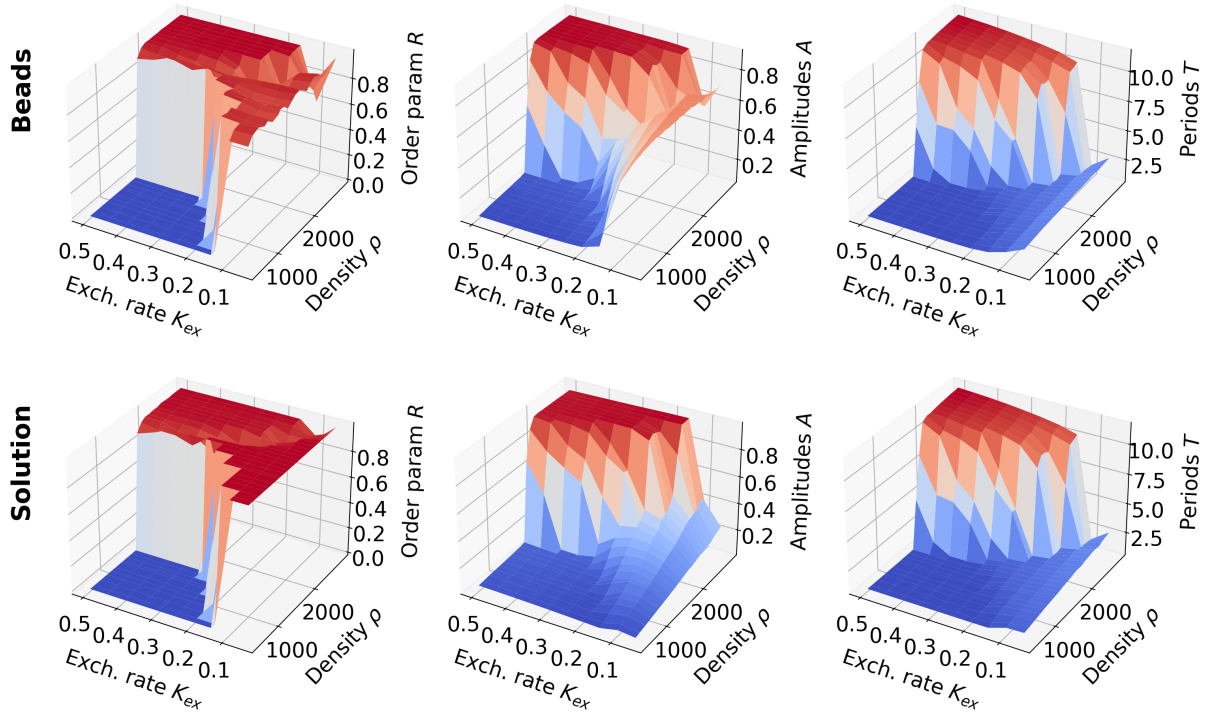
4.3 Results

We have simulated extensively the model in eqs. 4.1 and 4.2, recovering the phase space of solutions in terms of the parameters (K_{ex}, N_B) for several values of the mixing rate r. For each simulation, we have measured the order parameter R, the oscillation amplitude A and the synchronized period T. In Figure 4.4 we have summarized all this information for two values of r, namely the well-mixed case with $r = 0.1$ (see panel (a)) which corresponds to the phase diagram shown in Figure 4.1, and for a low mixing rate $r = 0.005$ (see panel (b)).

Let us start by analyzing the information given by the beads' panels of subfigure (a). On one hand, the Kuramoto parameter informs us about the character of the transition from the oscillation death (OD from here on) to the synchronous regime (FS from here on) which is clearly abrupt and discontinuous. This is the "quorum sensing" transition explained in the introduction and experimentally reported in [Taylor et al., 2009]. On the other hand, from the other two panels we can see that the chemical exchange rate K_{ex} has an important effect on the amplitudes and periods of the synchronized regime. Starting at low values for both K_{ex} and N_B and increasing the chemical exchange, we range from large amplitude oscillations ($A \sim 0.7$) with short periods ($T \sim 5$) to increasingly faster oscillations with both smaller period and amplitude. This occurs monotonically until the synchronous oscillators disappear abruptly. On the other side, for large density values, the oscillations initially decrease in amplitude but at some point around $K_{ex} = 0.2$ both the amplitude and period abruptly jump to the red plateau conformed by the super-synchronous regime. Looking now at the lower panels, we can see also how the fluid particles are acting as a giant synchronized oscillator of very small amplitude ($A \sim 0.2$) but same periods as the bead particles. At the super-synchronous region, all



(a) $r = 0.01$



(b) $r = 0.001$

Figure 4.4: Numerical results obtained with our simulations for a low value of the interaction radius $R_0 = 0.01$ and two different mixing rates (a) r=0.1 and (b) r=0.001. In each subfigure, top panels account for bead particles while the bottom panels for solution particles. The simulations presented here were carried out with a total number of N_S=2000 fluid particles. The quantities shown represent the Kuramoto order parameter, the oscillating amplitudes and the synchronized periods of the particles. In the oscillation death region, the Kuramoto parameter is set to zero as it loses its physical meaning.

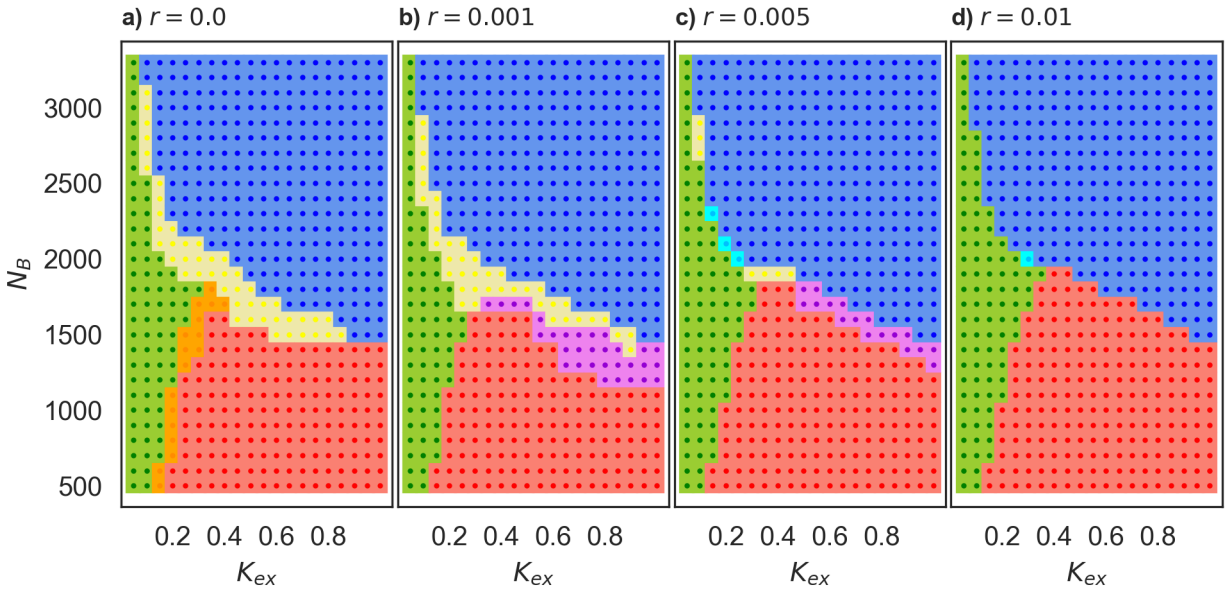


Figure 4.5: Phase diagrams of the model for increasing values of the mixing rate r. The (red,green,blue) color scheme follows the meaning of Figure 4.1, while the yellowed region represents the parameter space where irregular behavior and de-synchronization was found. The orange region represents a regime of oscillating beads coexisting with beads in oscillation death, the violet one denotes synchronized intermittence between oscillation death and super-synchronization and cyan colored points represent the synchronized intermittent state between synchronization and super-synchronization.

particles become remarkably undistinguishable. Looking now at the panels with lower mixing rate, $r = 0.001$, we can see that the main difference stems from the Kuramoto order parameter. Where there was a solid plane at $R = 1$, now we can see a cavity just before the transition to the super-synchronous regime. This de-synchronization can be observed also in the solution particles, revealing the strong interdependence between the two.

In order to better examine what is going on at this transition for lower mixing rates, we focus now on two dimensional cuts of the phase space $(K_{ex}, N_B$ for decreasing values of r. What we see is that when we start to decrease the mixing rate, the transition between the states become blurred as certain degree of intermittence emerges in the form of irregular or synchronized aperiodic behavior. We mapped this intermittent transition for decreasing levels of mixing rates, with the parameter space of each configuration color coded and represented in Figure 4.5

Within our simulations, the phase transitions obtained in Figure 4.1 are perfectly smooth as long as we maintain either a high-rate mixing in the system or a large interaction radius. When we start to decrease one of these control parameters, namely r and R_0, a certain degree of intermittence invades the system and new irregular and aperiodic behaviors arise. This intermittent transition was mapped for decreasing levels of mixing rates, and the parameter space of each configuration is represented in Figure 4.5.

While the general outcome was an overall loss of synchronization before the transitions (as pointed from the Kuramoto order parameter R), for some regions of the parameter space we found a series of novel synchronized intermittent states that could be of valuable physical interest as they might explain experimental observations. An important result that helps to understand these states is that, the main effect of having introduced a spatial dimension and an interaction radius in our simulations is the appearance of a single synchronization wave

that sweeps the reactor. In the fully synchronized regime, this wave is fast enough to be almost unnoticed, keeping all the beads in sync. In the special case of non-mixing ($r = 0.0$), the wave travels slower across the reactor (with its velocity depending on the radius R_0) and the synchronization occurs therefore time-lagged, making the Kuramoto parameter to decrease from 1. In other words, the period and amplitude of this synchronization wave fully depends on the control parameters.

The yellow-colored points of Figure 4.5 account for this irregular less-ordered behavior that dominates the transition to the super synchronization regime. For small values of K_{ex}, we observed that this synchronization wave broke into several smaller waves that appeared simultaneously in the reactor with different wavefronts, causing irregular oscillating patterns that varied in amplitude and period across the simulation window. This caused the overall synchronization of the system to drastically decrease, until the chemical exchange rate was strong enough to allow for super synchronized oscillations and order re-emerged in the system. For a further small window of parameter space, however, some irregularities were still present and some beads attempted to uncouple from the rest, producing a quick small oscillation right after the one with large amplitude. Further increasing K_{ex} diminished the amplitude of this second peak until the regular super synchronized state was achieved. Panels a) and b) of Figure 4.6 show the time series of this behavior for the static case (r=0) with $N_B = 2100$, and panels c) and d) show snapshots of the spatial visualizations of the simulations where the multiple synchronization waves and the double oscillation peaks can be grasped. Panel e) shows the evolution of the Kuramoto order parameter, the particles' amplitude and periods with K_{ex}, being a direct cut from Figure 4.4(a). As mentioned earlier, the low bead synchronization values seen for $K_{ex} < 0.2$ can be explained taking into account that in the static case the velocity of the synchronization wave is slower and only the oscillators in the wavefront are fully synchronized. Regarding the error bars in panel c), for the order parameter they represent noisy variations in time, while for the amplitudes and periods they represent the dispersion of this quantities along the particle ensemble. The de-synchronization effect can be effectively grasped from these error bars, since we see that in the region of K_{ex} from 0.15 to 0.3 (yellow points) the Kuramoto parameter undergoes a significant average reduction of its value (especially in the solution ensemble) and an increase in its variation in time. Furthermore, the highest dispersion in amplitudes is found for $K_{ex} = 0.2$ (case shown in panel (a)) and in the periods for $K_{ex} = 0.25$ as a result of the double peaks of panel (b). Finally, note that this intermediate yellow regime becomes smaller as the mixing rate is increased. Although we chose to show here the static case, mainly because the single bead oscillations could be distinguished clearer, the behavior in the yellow region for higher-mixing configurations was qualitatively the same.

On the other hand, we found for a small subset of simulations (cyan blue colored points) a synchronized intermittent behavior where the whole system arranges itself to perform a large amplitude oscillation, which is then followed by smaller, quicker oscillations characteristic from the synchronization regime. After a while, bead and solution particles couple their concentrations again to perform another super oscillation, and thus the pattern is repeated in time. The time series of this behavior is represented in panel a) of Figure 4.7, with a small set of spatial snapshots taken at different times of the simulation in panel b). It is remarkable that instead of appearing separated clusters for each regime, features from both dynamical states appear simultaneously and the whole system is synched to this behavior. The time evolution of the Kuramoto parameter in panel c) shows that bead particles retain high levels of synchronization between themselves at almost all times (blue line), as do so the solution

USA

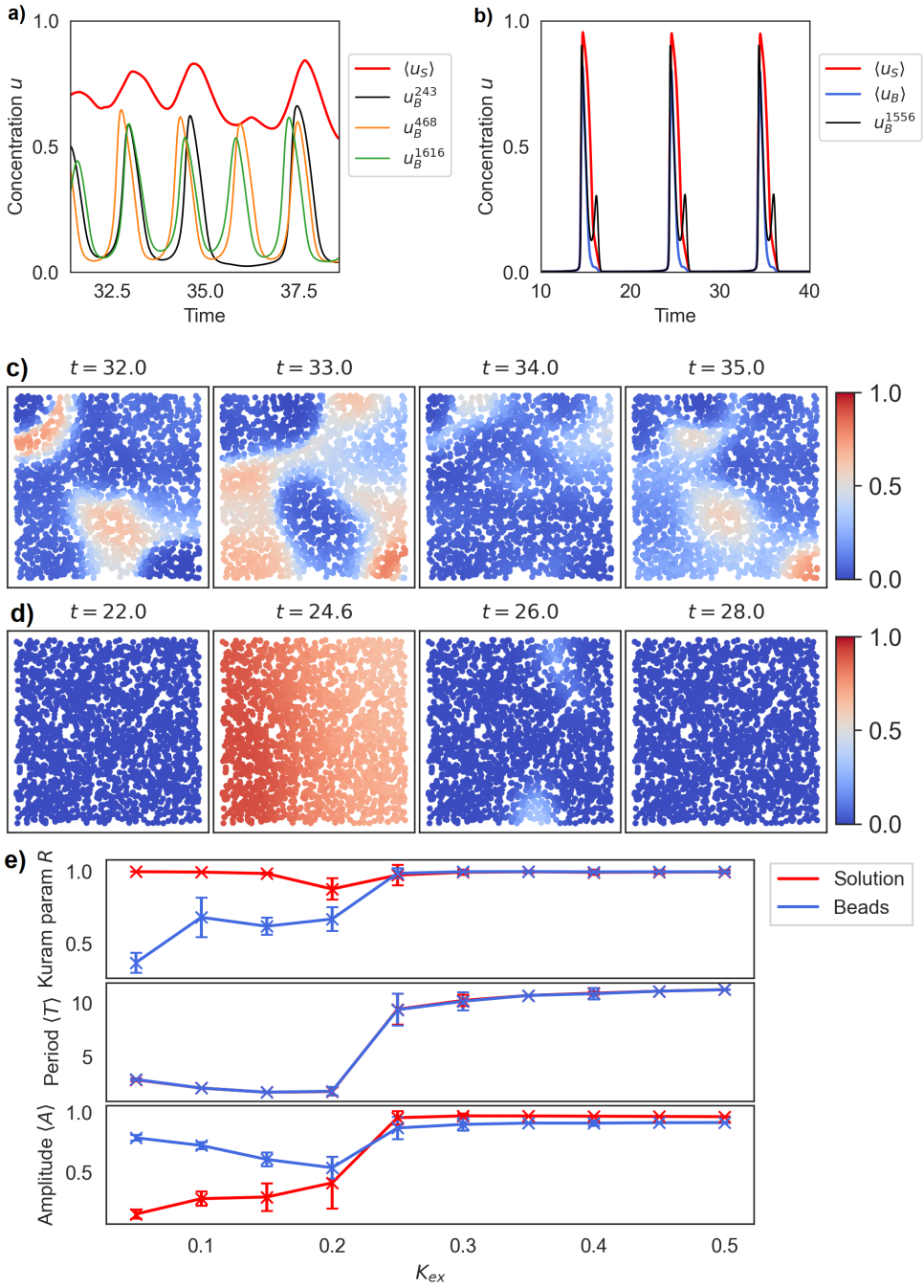


Figure 4.6: Characterization of the transition from synchronization to super-synchronization, corresponding to the ensemble behavior of the yellow region of Figure 4.5. Panel a) shows the de-synchronization with amplitude dispersion and panel b) the double peak oscillation of some particular beads in the close vicinity of super synchronization. Panels c) and d) represent the spatial visualization of the system at different times, showing the presence of multiple auto-waves in the system and the double peak oscillation. Panel e) shows the averaged Kuramoto parameter, period and amplitude of the particle ensembles, extracted from the corresponding cut in Figure 4.4. The number of bead particles is fixed at $N_B = 2100$, panel (a) corresponds to $K_{ex} = 0.2$ and panel (b) to $K_{ex} = 0.25$. In panel a), the solution de-synchronizes by breaking the synchronization waves in the system and the beads show strong dispersions in their amplitude. In panel b), right before super-synchronization is achieved, some particular beads show double peaked oscillations (black curves) in contrast to the overall behavior of the system (blue and red curves).

USC DE COMPOSTELA

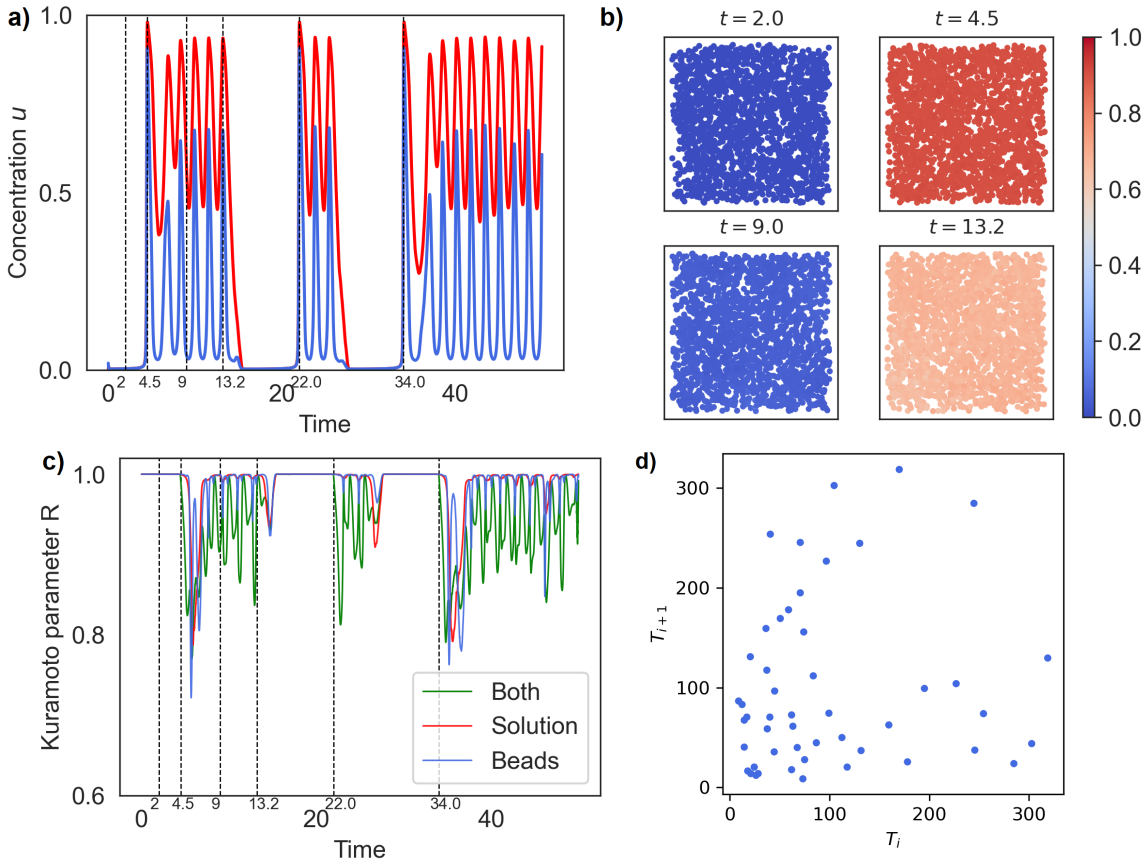


Figure 4.7: Characterization of the synchronized intermittent state between synchronization and super synchronization, corresponding to the ensemble behavior of the cyan region of Figure 4.5. a) Averaged temporal series of the beads' (red line) and solution's (blue line) concentration, namely $\langle u_B \rangle$ and $\langle u_S \rangle$. b) Spatial representation of beads at different times of the particles' behavior using u_B as the coloring. c) Time evolution of the order parameter. d) Return map of the large oscillations of a continued simulation in time, with the time series for this simulation presented below in Figure 4.10(a). The black dashed lines are included to guide the eye for certain moments of the behavior in the different panels. The parameter configuration of these simulations is $N_B = 2100$,$K_{ex=0.2}$ and $r = 0.005$.

particles (red line). Measuring the Kuramoto parameter for the whole set of particles (green line) clearly shows that the de-synchronization of the beads with the solution particles starts right after the large oscillation occurs, and they remain de-synchronized both in phase and amplitude until the concentration jumps back to zero. In the simulation extract shown in panel a), one can see that each set of oscillations is unique and different from the rest, both in the regularity of the small oscillations and in how well the system is synchronized. Analyzing an extended simulation ran for a considerate amount of time, we did not find any specific pattern regarding the number of small oscillations that follow a large one, or the occurrence in time of the large oscillations. We observed that the whole system rearranging itself to perform these oscillations do not follow any periodical pattern nor chaos, suggesting that the nature of this behavior could respond to some random excitabilities of the particle that trigger a cascade effect. Panel d) summarizes this conclusion with the return map of this extended simulation, representing the time that passes between a large oscillation and the next. The time series used for this return map is presented in Figure 4.10(a).

Regarding now the transitions to oscillation death (red points of Figure 4.5), we observed

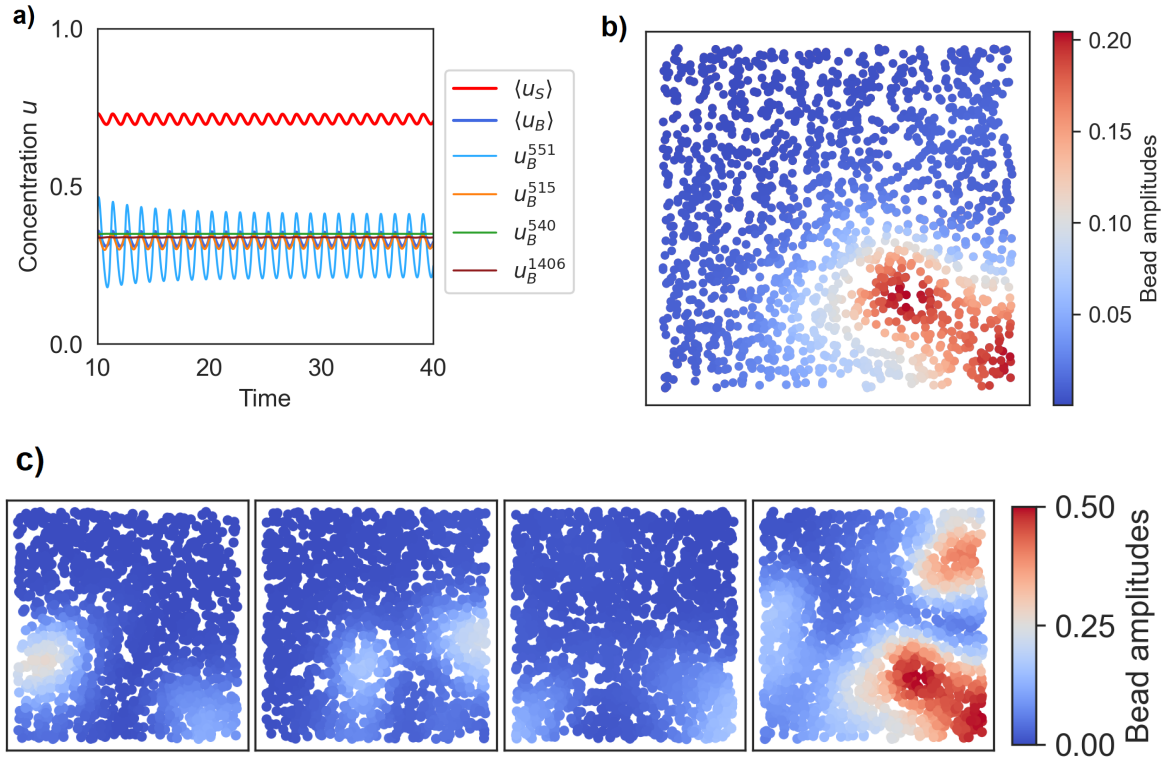


Figure 4.8: Characterization of the transition from synchronization to oscillation death in the static case ($r = 0$), corresponding to the ensemble behavior of the orange region of Figure 4.5(a). In (a), time series for the average ensemble concentrations and three separate particles. (b,c) Spatial representation of the beads' amplitudes, showing that the oscillating particles are localized in a spatial clusters that are likely linked to the initial distribution of particles. For (b), the number of bead particles is $N_B = 1700$ and the interaction exchange is $K_{ex} = 0.4$ while panel (c) shows other oranged points at lower densities.

two relevant states, one for each transition. In the particular case of zero mixing rate, this is, zero particle velocity, we found that during the transition, some particles kept oscillating at different amplitudes while the majority of the particles had ceased their activity. This behavior corresponds to the orange points of Figure 4.5)(a) and it is specifically represented in Figure 4.8(a). Panel (b) show the spatial distribution of the bead amplitudes of (a), while panel (c) shows several other cases where we found this state- From these two-dimensional representations of the beads' amplitudes, we observe that the particles are actually located in spatial clusters distributed along the simulation box. These spatial patches of synchronized activity may conform a single global cluster as in (b), or result in multiple patches as in the ones shown in (c).Since increasing the particle velocity made this behavior vanish, we believe that the origin of this behavior lies mainly in the random differences of local bead density given by the initial condition. This is, if initial the distribution is not-homogeneous and the value of K_{ex} is propitious, then different values on the local density induce the phase transition in the affected beads.

For positive values of the mixing rate, the transition from synchronization to oscillation death was rather smooth and we found that increasing K_{ex} resulted in a continuous decrease of the oscillations' amplitude, to the point where these oscillations started to become noise (see Figure 4.4(a)). Thus, this latter behavior was not categorized as irregular and was colored in red. However, the other new state which we referred to is colored in violet and appears in the

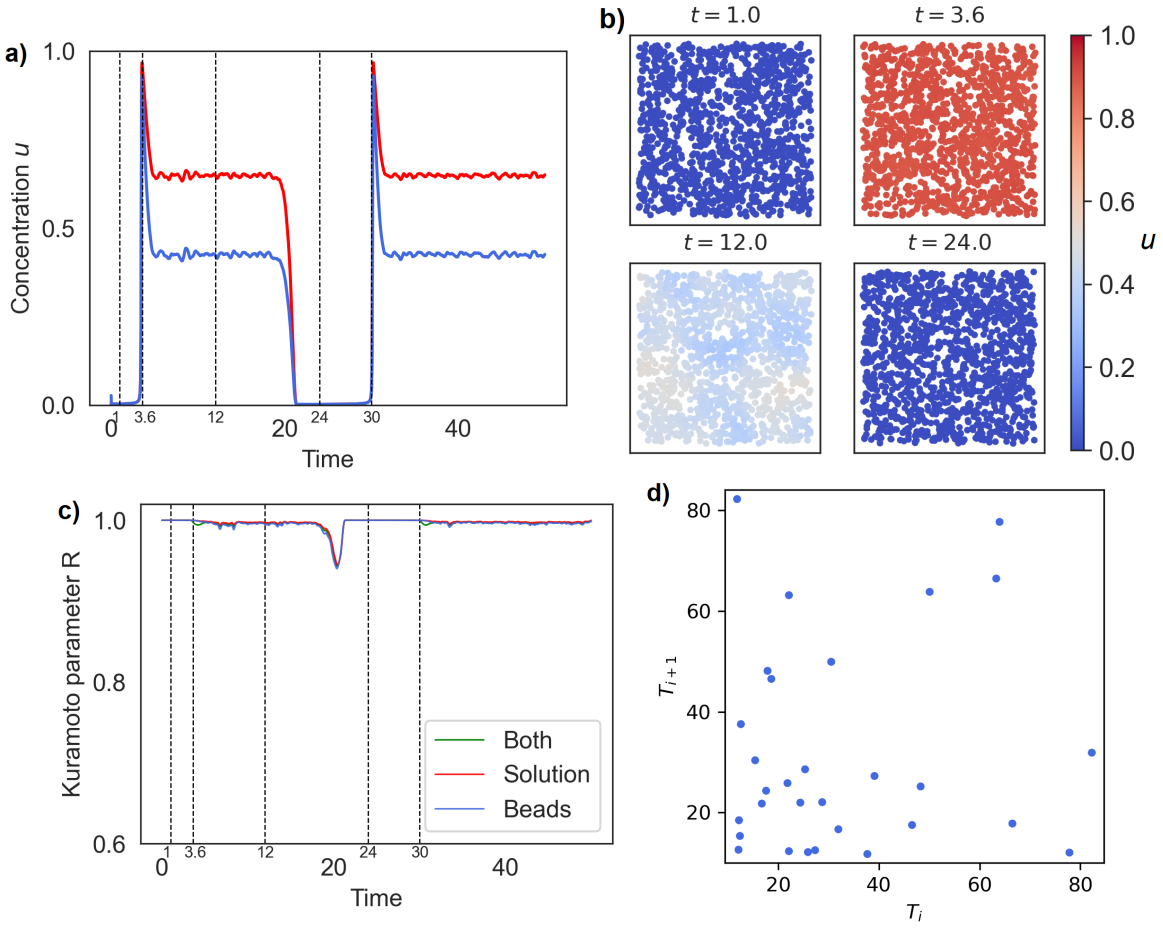


Figure 4.9: Characterization of the synchronized intermittent state between super-synchronization and oscillation death, corresponding to the ensemble behavior of the violet region in Figure 2. a) Averaged temporal series of the beads' (red line) and solution's (blue line) concentration. b) Spatial representation of beads at different times of the particles' behavior using u_B as the coloring. c) Time evolution of the order parameter. d) Return map of the large oscillations of a continued simulation in time, with the time series for this simulation presented below in Figure 4.10(b). The black dashed lines are included to guide the eye for certain moments of the behavior in the different panels. The parameter configuration is $N_B = 1300$,$K_{ex} = 0.75$ and $r = 0.001$.

vicinity with the super synchronization, where again a synchronized intermittency among both regimes appears in a similar fashion to the one presented in Figure 4.7. In this case, as we can grasp from Figure 4.9, the whole system prepares itself to perform a super-synchronized oscillation that is then followed by a low amplitude noise, where particles become quiescent until, again, the whole system reorders itself in a super oscillation. It is in nature very similar to the one described above, since the levels of synchronization given by the Kuramoto order parameter are consistently high and each new large oscillation does not seem to follow any periodic law (panels c) and d) respectively). However, note that here the order parameter loses its previous physical meaning in the oscillation death region, where the phase of the oscillators stops changing periodically. Thus, the relevant information here is the Kuramoto value in the vicinity of the large oscillations, which now does not seem to experience an immediate decrease right after the large oscillation occurs, in contrast to the cyan-colored state.

As a final note, we compare in Figure 4.10 both the intermittent super-synchronized behaviors recorded in the cyan and violet points. Panels (a) and (b) correspond thus to the

long extended time series of the average particle concentrations for each case, where we see that there is no explicit pattern behind the firing of the super oscillation except from all oscillators suddenly decreasing its amplitude to zero. Thus, in panel (a) where we see that there is some intrinsic randomness in the amplitude of the oscillations, this could respond to a sudden reach of a critical value in the inhibitor concentration v_i that makes the oscillators prepare for the synchronized super oscillation. The case of panel (b) is more curious as after the super-oscillation the oscillators became quiescent and, at some random moment, they all prepare to fire again in sync. Furthermore, in Figure 4.11 we also show the transition from the super-synchronized to the synchronized state mediated by the intermittent state, by decreasing the value of K_{ex} in time. Measuring the instantaneous value of the Kuramoto order parameter (panel (d)), we can see how the ensemble remains synchronized almost at all times.

USC
UNIVERSIDADE DE SANTIAGO DE COMPOSTELA

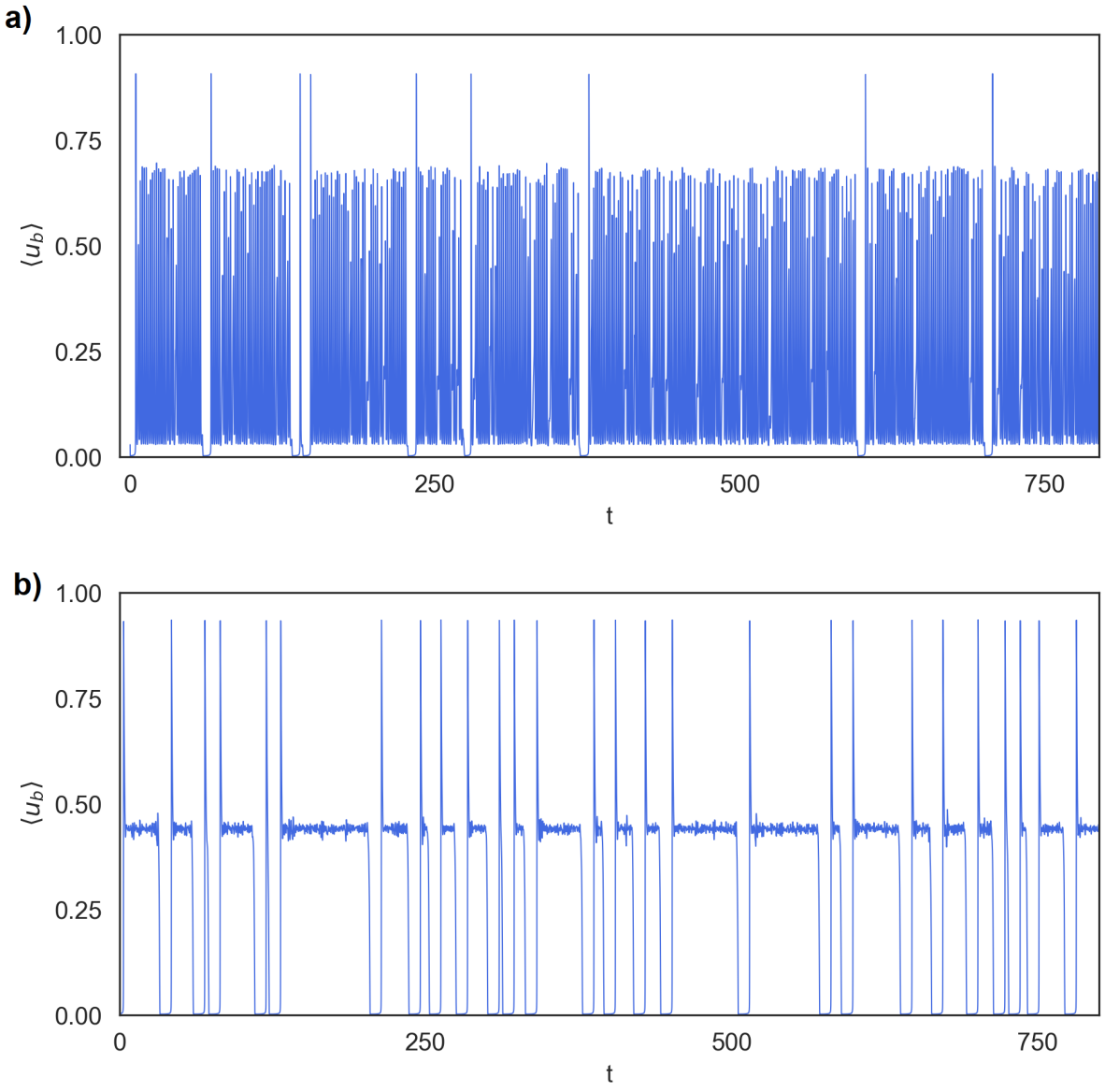


Figure 4.10: Extended time series of the averaged bead concentrations $\langle u_B \rangle$ for the intermittent states presented in Figures 4.7 and 4.9. Panel (a) corresponds to the cyan state with a parameter configuration of $N_B = 2100$, $K_{ex} = 0.2$ and $r = 0.005$, while panel b) corresponds to $N_B = 1300$,$K_{ex} = 0.75$ and $r = 0.001$.

USC
UNIVERSIDADE DE SANTIAGO DE COMPOSTELA

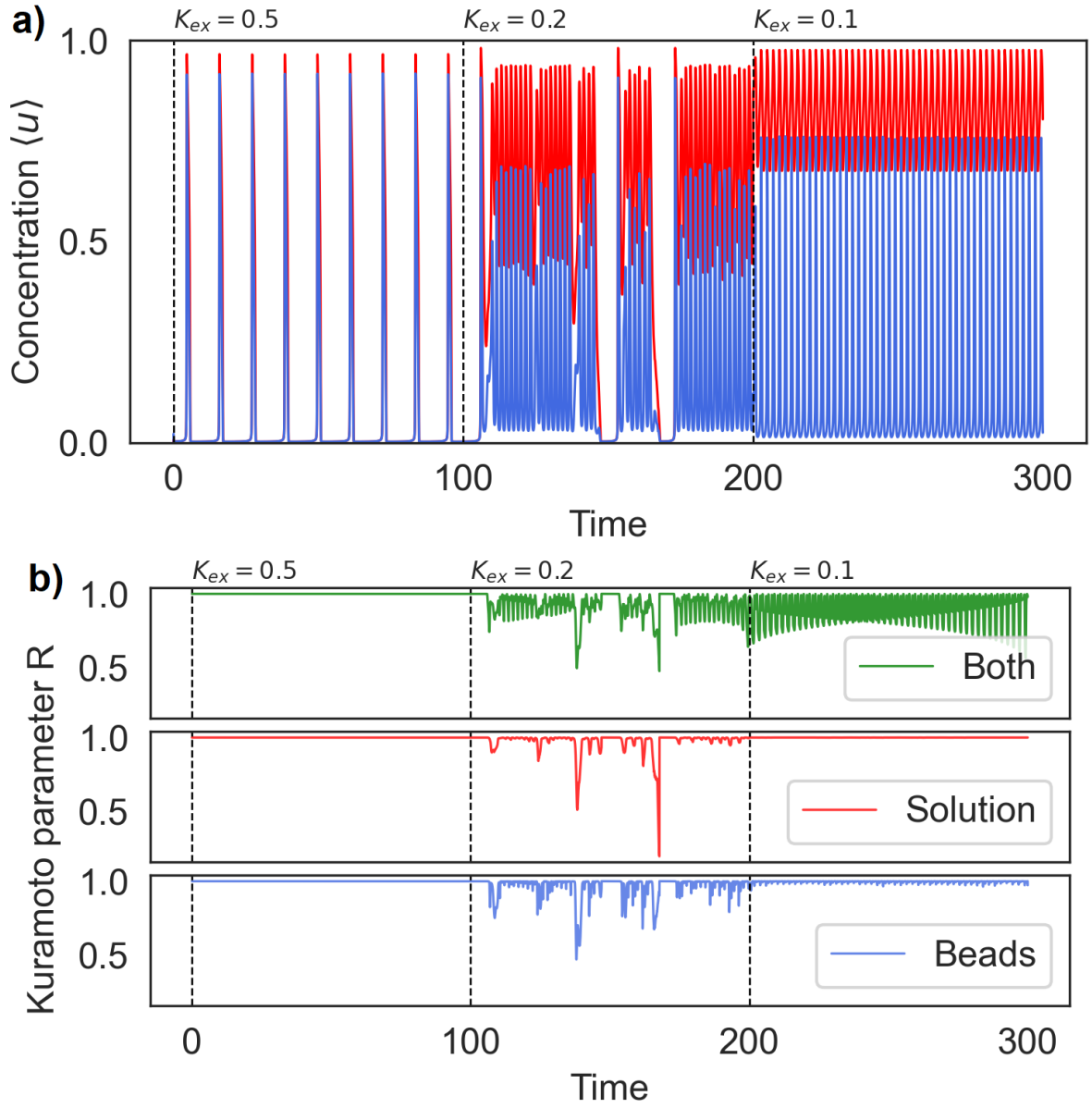


Figure 4.11: (a) Transition from the super synchronized state (with $K_{ex} = 0.5$) to the synchronized state ($K_{ex} = 0.1$) by decreasing K_{ex}, with the intermittent state appearing in between ($K_{ex} = 0.2$). We show the average ensemble concentrations $\langle u \rangle$ for beads (blue) and solution (red), with the associated instantaneous Kuramoto order parameter at each time step (b). The configuration for this simulation corresponds to that of the cyan state in 4.10(a), with $N_B = 2100$, $N_S = 2000$ and $r = 0.005$

USC
UNIVERSIDADE DE SANTIAGO DE COMPOSTELA

4.4 Summary and conclusions

We have developed a numerical model that simulates a two-dimensional chemical reactor where a large population of chemical oscillators are interacting with themselves and the solution particles that surrounds them. We believe that this system is better suited for describing non-perfect mixing conditions that can be reproduced in a laboratory. In perfect mixing conditions, depending on the bead density and the amount of information exchanged between the oscillators, the dynamical regimes correspond to oscillation death, over-all bead synchronization or super-synchronization, a regime where both active solution and beads synchronize their phase and concentration. In our simulation scheme, the oscillators are only allowed to interact with the oscillating particles in its close vicinity instead of considering the active solution as a mean field, introducing thus some degree of spatial heterogeneity. We have seen that this gives rise to new irregular behaviors where either an overall loss of synchronization or a consistent intermittency between dynamical states appear. Besides, from the introduction of the spatial variable and the interaction radius we observed the appearance of travelling synchronization waves that are key in the understanding of the reported numerical results.

In the transition from the synchronization regime to oscillation death, we observed for the static, non mixed case, that not every bead in the reactor ceased its activity but there were a small group of spatially clustered beads that kept oscillating at different amplitudes (see Figure 4.8). Remarkably, the overall synchronization of the clustered oscillating beads was maintained. Although the presence of phase-clusters was observed before in non-locally coupled photochemical oscillators [Tinsley et al., 2012, Mersing et al., 2021], to our extent, the presence of this kind of state with diffusive coupling has yet to be observed experimentally. In this way, our system seems to predict their appearence only in complete absence of mixing and just in the vicinity of the phase transition. When the mixing was activated, this state vanished and a smoother transition to oscillation death was found instead, in which the amplitude of the oscillators decreased to a point where its concentrations were not completely “dead” but rather became a noise of small amplitude (they became quiescent).

On the other hand, in the transition from synchronization to super synchronization, we found that for a significant parameter space the system underwent erratic behavior and disruptions in the order parameter. This decrease in the Kuramoto value occurs because of the synchronization wave breaks into smaller spiral waves that travel simultaneously across the reactor and collide with each other in irregular patterns, as panel c) from Figure 4.6 shows. We note that this spatiotemporal dynamic closely resembles the experimental results of [Tinsley et al., 2010] for diffusive chemical oscillators in unstirred conditions. In our simulations, however, this behavior occurred as well in the poorly-mixed system. In some particular cases for this transition, the system achieved a synchronized intermittent state in which bead particles also synchronized with the surrounding media to perform a large amplitude oscillation and then decoupled to oscillate with lower amplitudes for a while. In the vicinity among the super synchronous state and the oscillation death, a similar intermittency was found. Beads and solutions synchronized in one large oscillation followed by ceased activity with random low amplitude noise.

In general, these irregular states are caused both by low rates of mixing in the system and local spatial effects. Increasing both mixing rate of the system and the interaction radiuses of the particles resulted in the vanishing of this intermittence and the recovery of the

USC DE COMPOSTELA

smooth phase transitions observed in the one dimensional model with mean field chemical interactions. Different sizes for the simulation and number of particles were tested and the presented behaviors were observed each time, although for slightly different variations in the control parameters. The parameter configuration presented here was chosen in order to present a reasonable large enough number of fluid particles while keeping the computational times feasible. All the states described along the manuscript describe poor-mixing configurations that are likely to be experimentally observed as perfect mixing is never truly achieved. The extrapolation of these results to examples in nature also opens new ways to interpret the meaning of these states and might help understanding other collective behaviors in nature.

USC
UNIVERSIDADE DE SANTIAGO DE COMPOSTELA

Chapter 5

Photosensitive control of arrays of chemical oscillators

The experimental studies on synchronization are many and very fruitful, but there is still a lack of literature on those that can consider explicitly complex network architectures. We have seen in the previous chapter the potentiality of the Belousov-Zhabotinsky reaction for studying large populations of oscillators, where the coupling between them consisted in a regular topology with some degrees of stochasticity. With that kind of diffusive coupling, arranging the oscillating beads into more complex topologies is a difficult if not an impossible task. Here we propose a novel experimental setup where this purpose is completely feasible, if one considers the photosensitive version of the reaction.

5.1 Introduction

One of the main goals of understanding the natural mechanisms that govern synchronization processes is to be able to control them. We have already commented how the malfunctioning of biological rhythms in the heart or the brain may cause severe damage in the form of arrhytmias or epileptic seizures, thus being of great importance the ability to counter these anomalous and irregular behaviors. In this sense, the synchronization of non-linear systems became a very important topic in the 90's as it was proved that chaos itself could be controlled and drived by external sources [Pecora and Carroll, 1990, Pecora and Carroll, 1991], with potential applications also to communications. This premise triggered an extensive research in chaos synchronization (see [Boccaletti et al., 2002] for a detailed review), which involved many experimental studies of lasers and circuits with the aim of developing secure communication schemes [Kocarev et al., 1992, Chua et al., 1993, Cuomo and Oppenheim, 1993, Sugawara et al., 1994, VanWiggeren and Roy, 1998]. Later on, this idea of targeting and steering the dynamics of a *slave* system by synchronizing them to the dynamics of a *master* one, was later extrapolated to any type of generic dynamical systems in complex networks [Sorrentino et al., 2007, Gutiérrez et al., 2012, Gutiérrez et al., 2020]. In a more close context, it was also shown that the synchronization of large populations of chemical oscillators loaded with the photosensitive version of the Belousov-Zhabotinsky reaction could be drived and entrained by periodic external light sources [Makki et al., 2014, Muñuzuri and Pérez-Mercader, 2017].

USC DE SANTIAGO DE COMPOSTELA

In this chapter, we aim to contribute to this literature of designing control experiments

by proposing a novel experimental setup where the dynamics of chemical oscillators based on the BZ reaction can be individually controlled through light pulses. A direct application of this setup, as we shall see later, is the possibility to build complex network structures of chemical oscillators. In this sense, there is a similar experiment recently presented by [Mersing et al., 2021], where they use photosensitive catalyst-loaded beads immersed in a BZ solution (like the ones used in [Makki et al., 2014] and [Muñuzuri and Pérez-Mercader, 2017]) to build star network systems of 6 oscillators. A particular consideration of their experiment is that the central/master node has a significantly larger natural period than the peripheral ones, which oscillate much faster. They report that the central oscillator induces phase delays in the peripheral oscillators, leading them to synchronize between themselves in the form of one whole cluster or two clusters of different populations. However, no synchronization is seen between the central and the peripheral oscillators. Considerations about further complexity in their network architecture are not given though. In contrast, our experimental setup is based on the use of silica gels of $\simeq 2$ mm of diameter rather than the resina beads of $\simeq 200\mu$m, in order to have a better spatial resolution where we could include and monitor a larger number of oscillators. Besides, as will be explicited later, we prepare all the oscillators under the similar conditions, so there are not any significant distinctions between them.

5.2 Methods

5.2.1 Experimental setup

The experimental setup is shown in panels (a) to (d) of Figure 5.1 (schematically and in photograph), accompanied by a photograph of the glass reactor empty (b) and a snapshot of the reactor during an ongoing experiment (c). In the setup, we can distinguish between three functional parts. In charge of the illumination we have a Hitachi CP-X300 video projector (1) which was used to illuminate the reaction from below. We opt by this device because it allows us to project illumination fields of different intensity with eight-bit gray scale between 0 and 255 not only varying in space but also in time. The projected image first goes through a collimating lens (2) in order to focus correctly the image on the reflective mirror (3). Before reaching the petri disc that contains the reaction (5), the illumination goes through a diffusor (4). The purpose behind this is on one hand to equalize the spatial inhomogeneities produced by the bulb of the video projector, and in the other to enhance the contrast of the transmitted light monitored through a PixeLink CCD videocamera (6).

The BZ reaction takes place in a Petri disc placed on top of the diffusor (5). For this, we first fill the holes of the glass reactor shown in panel (b) with a silica gel loaded with Ruthenium catalyst [Yamaguchi et al., 1991]. We consider a silica gel for the substrate of our oscillators as they are easy and quick to fabricate, but especially because they allow us to precisely monitorize and control the individual oscillations of many oscillators under the CCD camera angle. In this way, they are not too little nor too large. Besides, it is a setup that has proven to be very efficient in the photosensitive control of waves and other oscillating phenomena in the BZ reaction [Muñuzuri et al., 1996, Muñuzuri and Markus, 1997, Muñuzuri et al., 1997, Sendiña-Nadal et al., 1998]. Loading the metal-ion catalyst in a gel allows to keep it fixed, so the oscillations occur within the surface of the gel, as we can see in panel (c). The holes in the reactor are made using a novel laser technique called SLIPAA [Flores-Arias et al., 2022](Subaquatic indirect Laser-Induced Plasma-Assisted

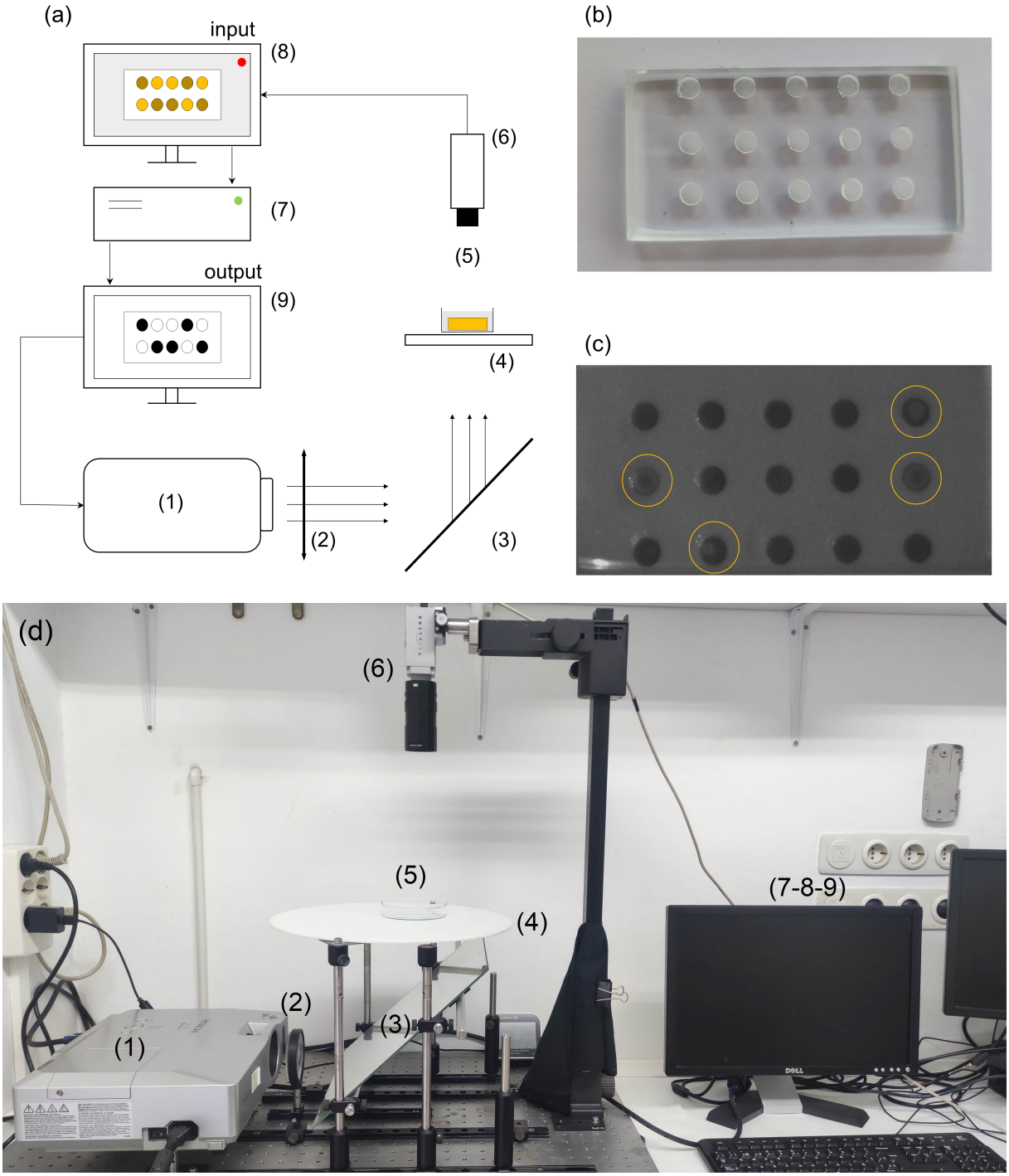


Figure 5.1: (a) Schematic representation of the experimental setup. (1) video projector, (2) collimating lens, (3) reflexive mirror at 45º, (4) light diffusor, (5) Petri disc with the microreactors and BZ solution, (6) CCD camera, (7). (b) glass microreactors fabricated via SLIPAA techniques. (c) snapshot of an ongoing experiment where each dark circle is a BZ oscillating microreactor. The yellow-rounded are showing oscillations.(d) Photograph of the experimental setup.

USC UNIVERSIDADE DE SANTIAGO DE COMPOSTELA

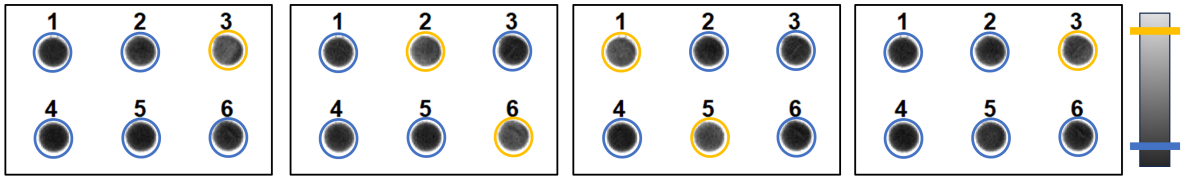


Figure 5.2: Consecutive snapshots of six BZ micro-reactors recorded in an experiment. The oscillations can be seen from the contrast between black and gray. As this contrast can be difficult to graps, we add as a visual aid a yellow circle that means the oscillator is firing, while a blue one means that is resting (see color bar in the side). At $t = 0$, only oscillator 3 is activated. At $t = 8$, oscillators 2 and 6 fire together, while at $t = 24$, it is the turn of oscillators 1 and 5. Finally at $t = 36$, oscillator 3 fires again and the cycle repeats.

Ablation), which allow for accurately polished wells of 2 mm diameter, with a smooth surface, and 2 mm depth. With that small diameter, the oscillation wave in the reactor covers the surface almost instantaneously, avoiding the emergence of multiple wave centers and reducing the possibility of emerging spiral waves. Besides, the micro-reactors are separated within a distance of 3 mm, which is cleaned before initiating the experiment to avoid interactions between neighboring wells. After the reactor is prepared, we place it inside the Petri disc and we cover it with the catalyst-free solution of the BZ reaction until it is completely submerged.

The oscillations in the reactor are recorded through the CCD videocamera (6) and are monitored (7) and recorded in a CPU (8), where we analyze the frames in real time to measure whether an oscillator has just fired or not. Simultaneously, the computer is connected to the projector (1) to send spatio-temporal modulations of the light intensity (9) at the exact positions of the small wells, stablishing a feedback loop that modifies the oscillating period of each reactor. With this setup, we can record up to $N \simeq 100$ oscillating micro-reactors and, through real time monitorization, send pulse of lights that can either excitate or inhibit oscillations in other reactors. In Figure 5.2, we show an example of a series of recorded snapshots where six micro-reactors are firing at different times. The firing of the oscillator can be noticeable in the gray-scale, as the oscillators passes from black to light gray (highlighted with a visual aid in the colorbar).

5.2.2 Preparation of the silica gel and the BZ catalyst free solution

The gelification time is very short, between 1 and 3 minutes, so it requires that everything is prepared beforehand. The recipe for making 5 ml of gel is indicated in table 5.1. In a small beaker with a magnetic stirrer inside, the reactants are added in the same order as listed in the recipe. The sulfuric acid must be the last one and should be treated with care, as it is the one that starts the gelification process. Errors in the pipetting process have to be minimized as small deviations from the listed concentration may cause either instantaneous gelification (in case of less reactant) or no gelification at all (in case of excess of reactant). Right after the preparation and before the gelification takes place, the solution is absorbed with the help of a pipette and injected swiftly in each small well until the desired number of micro-reactors are prepared. After a while, the solution gellifies within each well and the reactor is washed and cleaned with destilled water to remove rests between the micro-reactors.

The solution with the rest of BZ reactants is prepared according to table 5.2 prior to each

Quantity	Compound
3,3 ml	15% $NaSiO_3$
0,62 ml	H_{20}
0,150 ml	22 mM $Ru(bpy)_3^{2+}$
0,93 ml	1M H_2SO_4

Table 5.1: Recipe for the solution of 5 ml of silica gel loaded with Ruthenium catalyst

experiment and after the silica gels are ready. The stock solutions involved here are prepared with distilled water and with reactants commercially available from the SIGMA firm. Namely, we have used, in order of addition: sulfuric acid H_2SO_4, sodium bromide NaBr, malonic acid MA and sodium bromate $NaBrO_3$. As a note, when adding the sodium bromate the solution turns red colored while bromure is liberated from the solution, so it should be prepared within a fume hood. After a while it should become clear again. Once it is ready, the solution is pored onto the Petri disc that contains the reactor, until the latter is smoothly and totally submerged. Thus, the ammount of solution prepared should be enough as to cover the whole reactor.

Quantity	Compound
2,66 ml	H_{20}
3,44 ml	4M H_2SO_4
4,46 ml	1M NaBr
1,67 ml	1M MA
7,77 ml	1M $NaBrO_3$

Table 5.2: Recipe for the solution of 20 ml of catalyst free BZ

5.2.3 Periodic pulses and coupled networks

Our first attempt to control synchronization will consist in stimulating the oscillators with periodic pulses in order to adapt their natural frequencies to the signal. For this purpose, we design a square signal of period P and time duration D like the one drawn in Figure 5.3. The total light intensity ϕ of the signal takes into account the background illumination ϕ_0 and the height or amplitude of the signal I, i.e., $\phi = \phi 0 + I$. Note that this amplitude can be either positive, in order to induce photoinhibition, or negative, to induce photoexcitation of oscillations. A preliminar study of the system under these pulses will allow us on one hand to better characterize the system studying the oscillator's response to light estimulations.

On the other hand, by monitoring in real time the state of each oscillator, we can send the light pulses between the oscillators every time they fire. This is, if we establish a connection between oscillators i and j, every time oscillator i fires the square pulse of intensity I and duration D is sent to oscillator j, and viceversa. In this way, generating an arbitrary adjacency matrix $A_i j$ we could create any kind of network of oscillators.

To measure synchronization, we propose the following estimator in order to compare the observations found within our experiment. Finding the location in time of the oscillator firings, we subdivide the data series into equal fragments given by the average period of oscillations

USC DE SANTIAGO

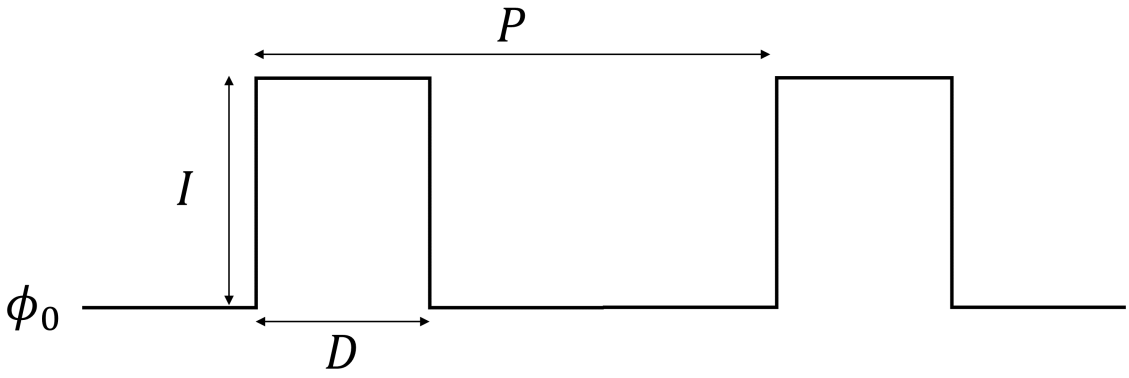


Figure 5.3: Square signal of period P, size D and amplitude I used for the periodic control experiments. Note that this pulse actually results in a total light intensity experienced by the oscillators of $\phi = \phi_0 + I$.

$\langle T \rangle$ and measure the standard deviation σ of the firing times. In this way, if all the oscillations are firing together, $\sigma \simeq 0$, while if they are all asynchronous $\sigma \to \langle T \rangle / 4$, as σ gives us the deviations from the mean at half width maximum and the total width of the measuring window is $\langle T \rangle$. We measure these deviations before and after the control experiment, σ_b and σ_f, so we can define an order parameter ρ as:

$$\rho = 1 - \frac{\sigma_f}{\sigma_b} \tag{5.1}$$

which depends both on the final standard deviation of the firings and on how much the synchronization was improved after the experiment. This serves us as a way to normalize each experiment within its own experimental conditions, while at the same time having an estimator that can range between 0 and 1.

5.3 Results

5.3.1 Characterization of the experimental setup

Small differences in the preparation of the gels may induce small heterogeneities in the oscillators, which are directly related with the concentration of catalyst in each well. This translates in standard deviations of the natural periods of around $\sigma(T) \simeq 2$ seconds in general, that can increase with the light intensity as we show in Figure 5.4. Furthermore, as a photosensitive chemical reaction, other room conditions as the amount of ambient light, humidity and the temperature conditions strongly affect the period of the oscillations. We have seen the effect of light makes the system more excitable and less oscillating, while higher temperatures induce higher frequency of oscillations [Ruoff, 1995, Masia et al., 2001, García-Selfa et al., 2019]. Therefore, we kept the experiments in a dark room with almost non to zero ambient light and tried to maintain room temperature conditions (between 18-22 ºC) with the aid of an AC system.

The first point to characterize is the effect of light illumination in the oscillators. For this purpose, we illuminate the reactor with the video projector with different levels of background intensity ϕ_0, characterized from 0 (total black) to 1 (total white). This is reported in Figure 5.4, with panel (a) showing the recorded pixel values V_i in time for one single oscillator and panel (b) the periods of the ensemble (composed of $N = 20$ oscillators). Starting from $\phi_0 = 0.3$ we

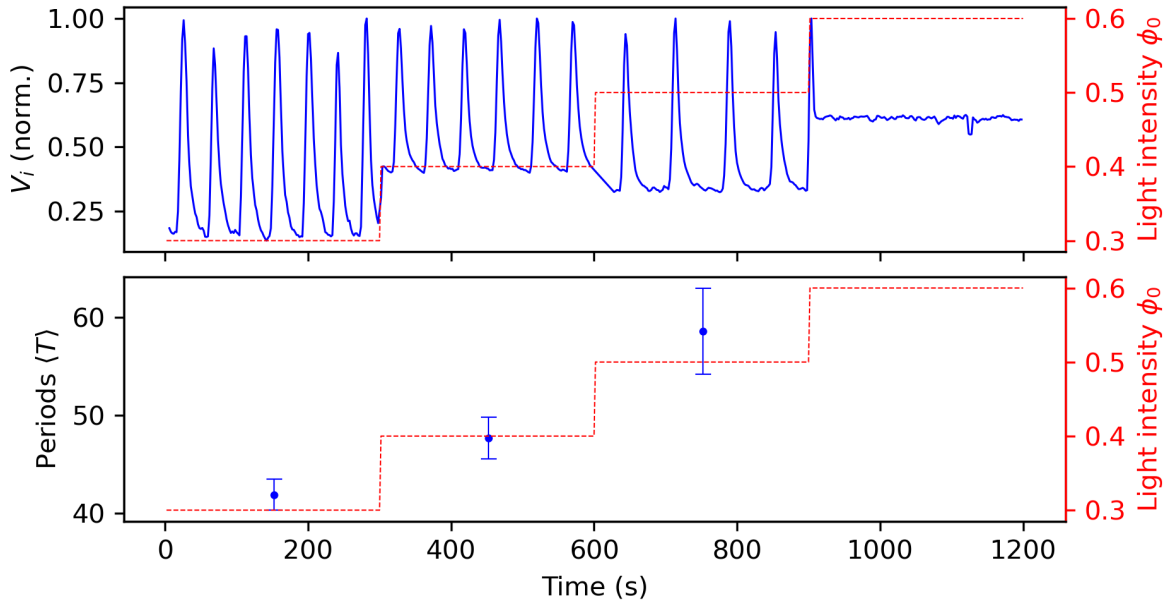


Figure 5.4: Effects of the background light illumination ϕ_0 on the chemical oscillators. Panel (a) reports the recorded pixel value V_i of a single oscillator, showing the oscillations in the metal-ion catalyst, while panel (b) shows the average period and standard deviation of the whole ensemble of $N = 20$ oscillators.

can see that each time we increase the light illumination by $\Delta\phi_0 = 0.1$, there is an increase in the periods of $\Delta\langle T \rangle = 5.8$ from $\phi_0 = 0.3$ to $\phi_0 = 0.4$ and of $\Delta\langle T \rangle = 10.93$ from $\phi_0 = 0.4$ to $\phi_0 = 0.5$. From there on, as we can see in panel (a), the oscillators enter in to the excitatory state and only a few oscillators remain active because of the heterogeneities.

One particularity of this system is that, as the catalyst-loaded gels are quite small (2 mm of diameter at most), the consumption of the metal ion catalyst in each micro-reactor is quite fast and we observe a decay in the periods of around 1-2 seconds every ten minutes. This is reported in Figure 5.5, where we observe a linear decay of the oscillation periods that can be fitted through linear regression to obtain a slope of $m = -0.002s^{-1}$. Depending on the initial period of the oscillations, that can range between 50 and 70 seconds (depending on room humidity and temperature), the mean life of the experiment could run between 2 to 4 hours, until the periods had decayed to $T = 35s$. From this point forward, spirals and other irregular behaviors appeared in the system. Thus we performed our control experiments regularly in the period window between $T \in (40, 60)$ seconds.

5.3.2 Synchronization control by means of periodic pulses

With the periodic square pulses described in the Methods (see Figure 5.3, we have examined the effect of the time duration D and light intensity $\phi = \phi_0 + I$ of the signal in the overall synchronization of the oscillators. Regarding the period of the signals, prior to each experiment we fix it near the current natural period of the oscillators, as the final aim of the experiment is that the signals are sent by the oscillators themselves. Therefore, we focused on entraining the oscillators to periods near their natural ones. For every experiment, the background illumination was also fixed at $\phi_0 = 0.4$ in order to ensure good visibility of the oscillations.

Figure 5.6 show the outcome of two control experiments with different levels of the pulse

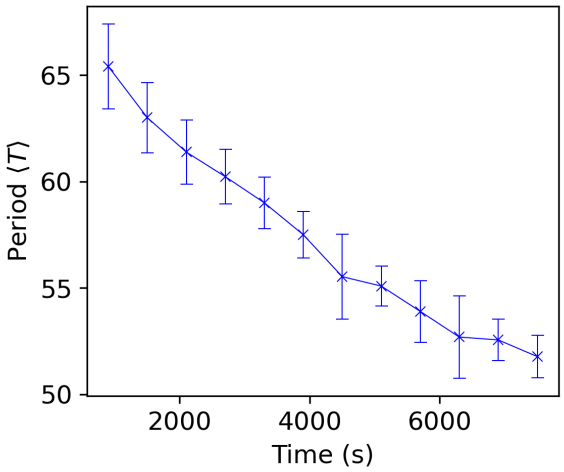


Figure 5.5: Decay of the oscillation periods in time. A linear regresison to this data returns a slope of $m = -0.002s^{-1}$, revealing a decay of $1.2s$ every 10 minutes.

amplitude ϕ, namely $\phi = 0.5$ (panels a-c) and $\phi = 1.0$ (panels (d-e)), and a pulse duration of $D = 10$ seconds. During the control experiments, we let the oscillators run freely for about 5 minutes (300 seconds) and then apply the control strategy for the next 10 minutes. This is highlighted in the figure by the black dashed lines and the broken axis. During this part, recording accurately the oscillations is difficult as very bright square pulses may saturate the CCD camera while also mask the oscillations themselves. Therefore, in order to measure the state of the system after having applied the control procedure, we let the oscillators run free again and record for the next 5 to 10 minutes. Now, panels (a) and (d) show the average recorded pixel values V_i of all the oscillators in the ensemble, shown as a preliminary measure of the system's coherence. Panels (b) and (e), show the individual firings of the oscillators in the form of a raster plot, where each row is a different oscillator and the firings correspond to the colored vertical bars. For the case of $\phi = 0.5$, we can see before the control section that although the oscillators fire somehow next to each other, the overall levels of synchronization are quite low and the averaged signal is noisy. This is confirmed by dispersion in the firings shown in panel (c), where $\sigma \sim 5$ seconds. After the control experiment, we see that this dispersion has not decreased much but at least the oscillators fire closer to each other in a more ordered fashion, as can be grasped from the distorted oscillations in the global averaged signal (panel (a)). In this case, the order parameter ρ computed as in equation 5.1, using the average of the dispersions before and after the experiment, returns a value of $\rho = 0.07$. This low value of the order parameter reflects mainly on the lack of control in the firing dispersions, as the difference between both sides is almost null.

On the contrary, in the experiment of high levels of light intensity with $\phi = 1.0$ (panels d-f) the contrast between the two recorded moments is a lot clearer, with the oscillators firing almost simultaneously and the global averaged signal being well-defined. This is also reflected by the firing dispersions, being now of the order of $\sigma = 1.8$ seconds and the order parameter returning a value of $\rho = 0.67$. One of our choices to define ρ as we did is illustrated from contrasting these two cases. In panel (c), the system is slightly more ordered after the control experiment because it was not that disordered from the beginning. On the other hand, we can see from panel (f) that initial dispersions in the firings can be largely corrected if the pulse is

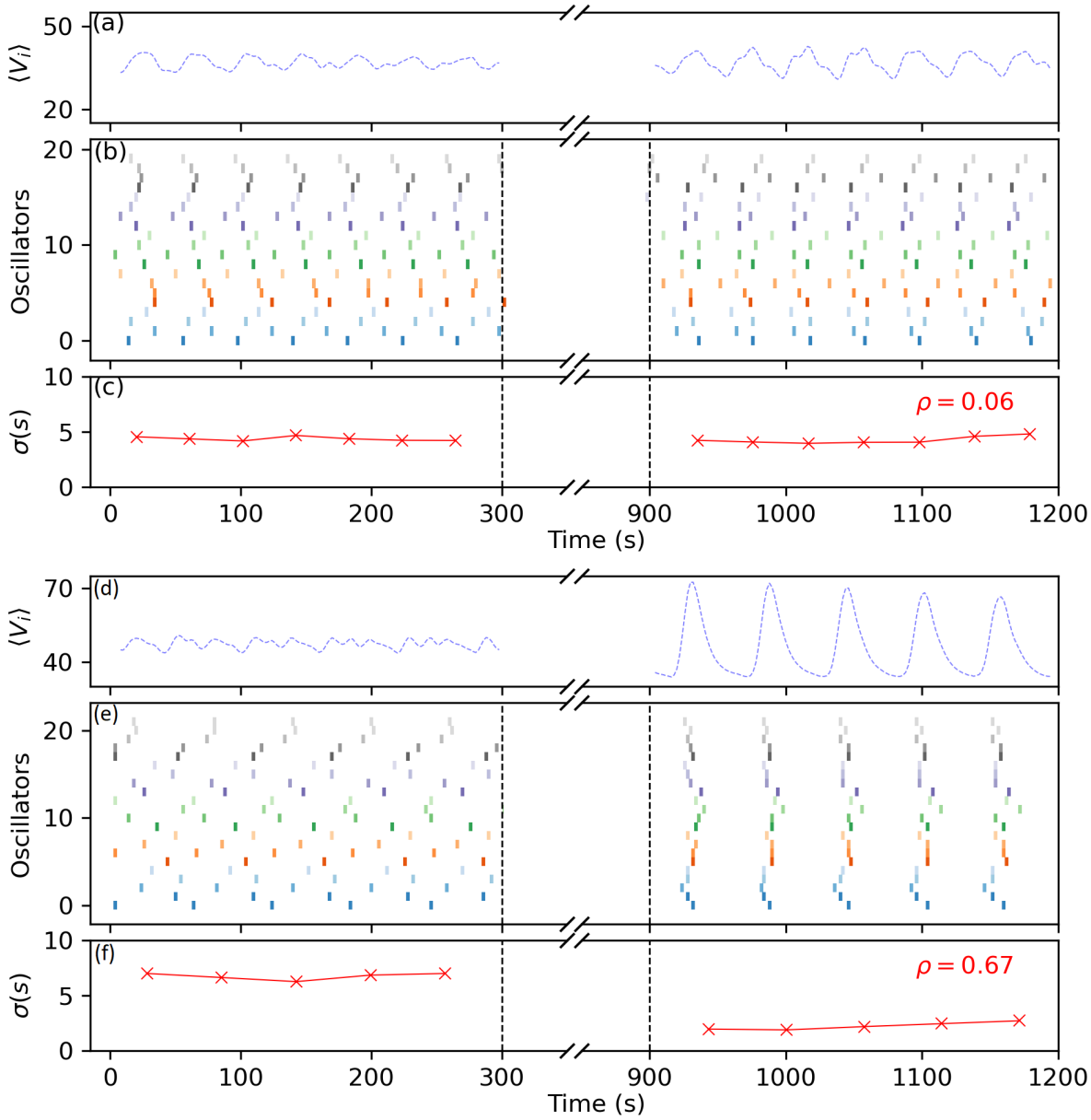


Figure 5.6: Collective oscillations before and after our control experiments with periodic square pulses, for (a,b,c) low pulse intensity $\phi = 0.5$, and (d,e,f) high pulse intensity $\phi = 1.0$. The skipped area in between the black dashed lines represent the control region where we applied the square signal. Panels (a) and (c) correspond to the average values of the pixel intensity of the whole ensemble $\langle V_i \rangle$, while panels (b) and (e) show the firings in time of each oscillator (in colors). Panels (c) and (f) correspond to the standard deviation σ between the firing times of the oscillators, measured in seconds. For both panels, $N = 21$, background intensity is set to $\phi_0 = 0.4$ and pulse duration is set to $D = 10$.

USC UNIVERSIDADE DE SANTIAGO DE COMPOSTELA

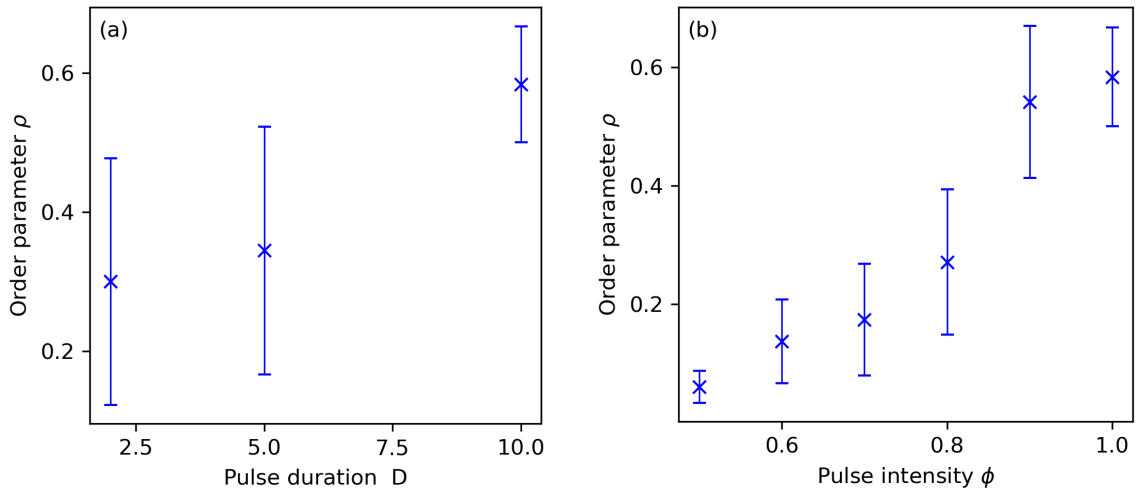


Figure 5.7: (a) Overall levels of synchronization ρ of the control experiments in function of the pulse duration D in seconds, and (b) ρ in function of the pulse intensity ϕ. For panels (a), pulse intensity is fixed at $\phi = 1.0$ while in panel (b) pulse duration is fixed at $D = 10$. In both panels, error bars represent the standard deviation of our synchronization measures between different realizations of the experiment, with at least 5-10 experiments for each point and 20-25 oscillators in each experiment.

strong enough. Therefore, we decided to normalize σ_f over σ_b in order to take into account this feature. Furthermore, in absence of estimuli and as can be grasped from panel (e), oscillators quickly relax to their natural frequencies after a few oscillations and therefore we limit our measuring window to the first five minuts after the experiment.

We further characterize our system by measuring repeatedly the parameter ρ for different values of the maximum light intensity ϕ and pulse duration, as we show in panels (a) and (b) of Figure 5.7 respectively. For this purpose, we repeated several experiments under the same conditions and measured the firing dispersions σ as in the previous cases. We found that between $\phi = 0.5$ and $\phi = 1.0$ there is quite an espectrum of order levels that increase monotonically with ϕ. On the other hand, we are interested in knowing keeping the maximum light intensity at $\phi = 1.0$ we can increase the order in the experiment with pulses of just $D = 2$ seconds, although the variation from experiment to experiment was high and we never reached synchronization values higher than $\rho = 0.5$. For pulses of $D = 5$ seconds the situation was quite similar with slight increases in the order parameter. For $D = 10$ seconds, we obtain quite generally the synchronization levels found in Figure 5.6

5.3.3 Networks of coupled oscillators

Now, we validate our method with the second application of the setup: building a network of self-regulating chemical oscillators via light coupling. Here we present a first order approximation to the problem by considering a star network as the one shown in Figure 5.8(d). There we show the result of a control experiment where there is one master oscillator (green, top center) that sends light pulses to its peripheral connections (blue) every time it fires. These snapshots, recorded before (top row, panels (a-d)) and after (lower row, (e-h) the control experiment, show that the network of six oscillators that initially was asynchronous, now it is perfectly synchronized firing in unison at $t = 938$ and $t = 976$ seconds, thus showing a common

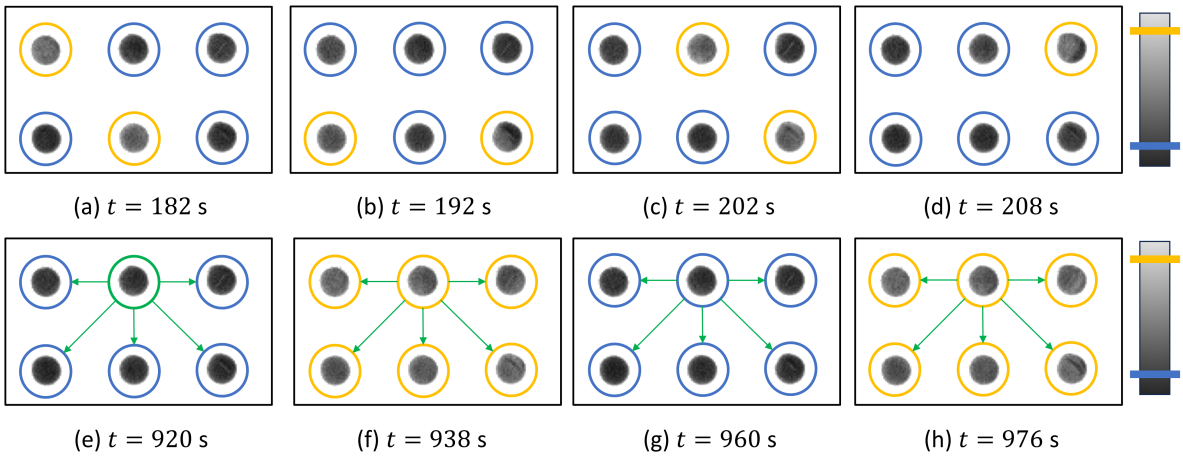


Figure 5.8: Consecutive snapshots of six BZ micro-reactors recorded before (top row,a-d) and after (lower row,e-h) a control experiment with coupled star networks. As in Figure 2.5, a blue circle means that the oscillator is resting while a yellow circle that the oscillator is firing. Panel (d) explicitly show the distribution of the start network topology, with the oscillator circled in green acting as the center node, sending light pulses to the ones next to it after firing. After this panel the previous color coding is recovered but the network structure is maintained. At $t = 938$ and $t = 976$, we can see all the oscillators firing together with a common period of $T = 38$ seconds. The time snapshots of these panels correspond to the experiment shown afterwards, in Figure 5.9

period of $T = 38$ seconds. A more complete description of this experiment is shown in Figure 5.9, following the same schematics as the previous subsection. From the results obtained there, we have selected for this experiment the optimal combination of control parameters that could grant synchronization, which were $\phi = 1.0$ and $D = 10$. Here we can grasp better how after the coupling, the peripheral oscillators have underwent a series of adaptations to the master's signals, so they eventually fire all together.

As we commented before, each experiment is indowed with a certain degree of noise related to the small heterogeneity in the natural periods of the oscillators. We saw in the Kuramoto model that those oscillators with closer natural frequencies are the ones to couple first, while those with larger frequencies will be absorbed by the main cluster depending on the coupling strength K. Similarly, we have observed in our coupled networks that to obtain a synchronized group the natural periods of the peripheral oscillators must not differ too much from that of the central one. We report this on Figure 5.10. For each control experiment, now we measure the final dispersion in the firings σ_f and the dispersion in the natural periods of the peripheral oscillators from the central one,

$$\sigma_T = \sqrt{\frac{1}{N}\sum_{j}^{n}(T_j - T_c)^2} \tag{5.2}$$

where n is the number of peripheral oscillators, T_j their natural period before the control experiment and T_c the natural period of the central oscillator before the experiment. Attending to these measures, we can grasp a monotonical increasing tendency between the two, finding that if the dispersion in the natural periods is larger than $\sigma_T > 3$ seconds, the peripheral oscillators are not able to adapt to the central one. For lower values of the dispersion, we see the significant degree of noise in the system, where experiments with the dispersions lower than $\sigma_T < 1$ seconds differ noticeably in their degree of synchronization.

USC DE SANTIAGO

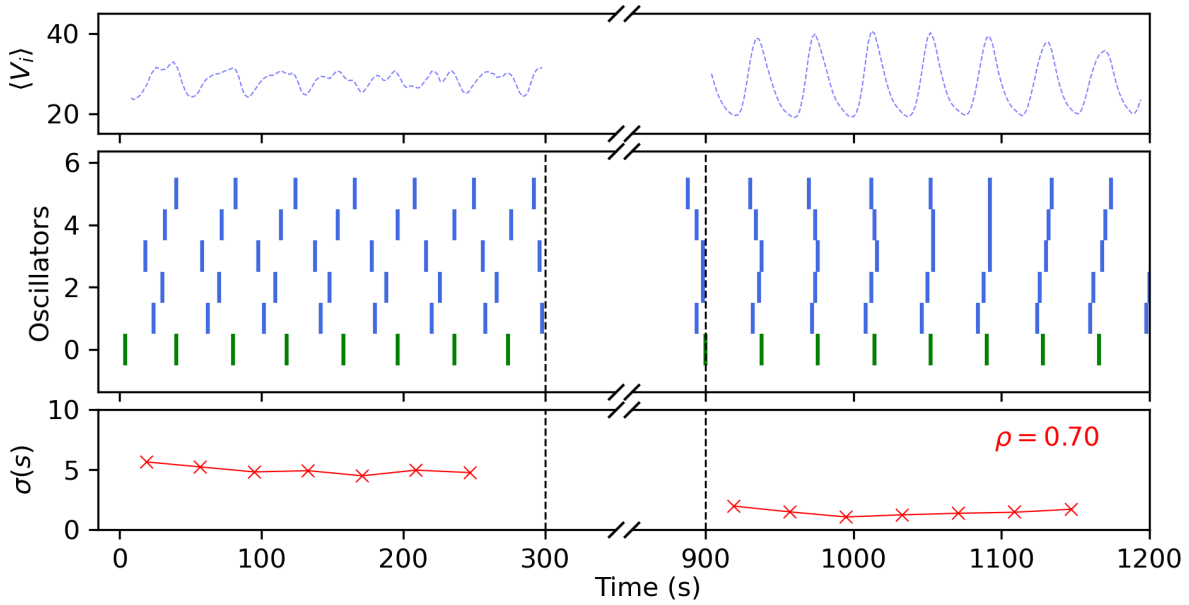


Figure 5.9: Collective oscillations before and after our control experiments with a star network coupling, following the disposition of Figure 5.8. Again, the area between the black dashed lines represent the control region where we applied the coupling. The green oscillator correspond to the central one, the master, while the blue ones are the peripheral oscillators that receive the pulses. The dashed blue line corresponds to the global averaged recorded signal of all the oscillators. For this experiment, $N = 6$, the background intensity is set to $\phi_0 = 0.4$ and the pulse coupling has a duration of $D = 10$ seconds and maximum light intensity of $\phi = 1.0$.

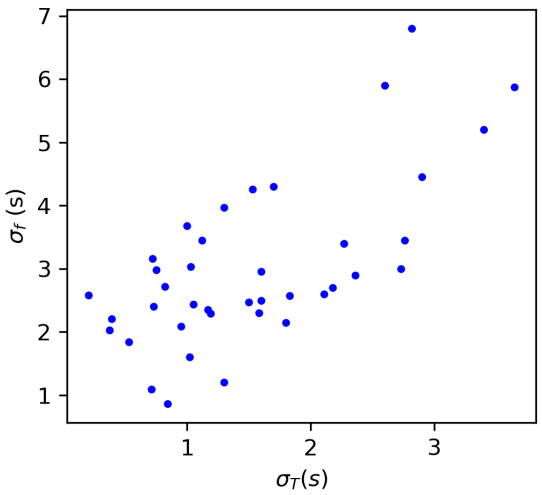


Figure 5.10: Dispersion in the firing of the oscillators after the control experiment σ_f against the dispersion in the natural periods between the peripheral oscillators and the central one, σ_T. Each point represents a different experiment under the same coupling conditions, $\phi_0 = 0.4$, $\phi = 1.0$ and $D = 10$.

USC UNIVERSIDADE DE SANTIAGO DE COMPOSTELA

5.4 Summary and conclussions

With this chapter we close our study of synchronization as an emergent property by tackling the problem from an experimental perspective, the one that was left. Here we described the recipes and methods to elaborate an ensemble of chemical oscillators using the reactants of the Belousov-Zhabotinsky reaction, with the particular feature that we used a photosensitive metal-ion catalyst to activate the reaction. Furthermore, the glass reactors with small wells carved with laser ablation were prepared explictly for this application.

We first approached the problem from the perspective of control, considering a periodic inhibitive signal that could force the oscillators to fire in unison. From the first round of experiments presented here, we determined a set of optimal parameters for the square signal (namely the light intensity ϕ and the pulse duration D) that best allowed to control the firing of the oscillators. We assessed this by measuring the standard deviations between the firings of the oscillators, finding that they were minimal for the maximum level of light intensity $\phi = 1$ and for a pulse duration of $D = 10$ seconds. For smaller values of both quantities, we saw that in each case some levels of control were exerted on the oscillators, although the overall levels of synchronization were not perfect. This was reflected by the presence of small clusters of synchronized activity whose population increased with increasing levels of the intensity ϕ, in a sort of partial synchronous state. This is reflected on Figure 5.7(b) and is most likely related to the dispersion of natural periods in contrast to the control signal, as we observed also for the networks in Figure 5.10. On the other hand, and probably also related to the mismatching of periods between the oscillators and the control signal, the presence of two clusters in opposing phase but similar periods T within this system was also observed in some experiments. However, this did not occur as a rule and therefore it was difficult to measure their appearance, or the necessary conditions to trigger them. Therefore, its investigation is left for future work.

We note here that there is also another mechanism to control the firing of the oscillators that is possible within this setup but that was not shown here. This is the mechanism of photoexcitation that was introduced in subsection 2.3.1 of the Methods chapter. This would consist in using negative values in the square pulse amplitude I, which should excite the oscillators to make them fire earlier. We also leave this mechanism for future work, as being able to use both mechanisms of photoinhibition together with photoexcitation would be an optimal scheme for the network couplings.

Moving on with the experiments with pulse-coupled networks, we proved the validity of our setup by showing the synchronization of directed star networks. Here, a central oscillator sent the square pulsed signals to its connections whenever it fired, finding that these networks were able to self-regulate and adapt if the dispersion of the natural periods of the peripheral oscillators was less than $\simeq 2$ seconds. With this promising result, the next step in our work aims on one hand to run experiments with more complex directed structures, such as trees of cascading connections or closed loops of $N \leq 3$ nodes. On the other hand, we are close to introduce feedback in the experiments in the form of bidirectional links, that could allow for considering other complex topologies as the ones reviewed in section 2.1 of the Methods chapter. This however requires first of refining one of our previous results: the ability of controlling the oscillators just with short pulses of light of 2 seconds or less. This would reduce the noise in the monitorization process that comes from illuminating the oscillators at maximum light intensity, which disrupts the real-time tracking of nearby oscillators. On the other hand,

USC DE COMPOSTELA

managing synchronization using the photoexcitation mechanism could also solve this problem, thus being another motive for its pursue.

USC
UNIVERSIDADE DE SANTIAGO DE COMPOSTELA

Part II

Collective behavior in diffusive processes: Opinion formation and epidemic spreading

USC
UNIVERSIDADE
DE SANTIAGO
DE COMPOSTELA

USC
UNIVERSIDADE
DE SANTIAGO
DE COMPOSTELA

Motivation and specific objectives

In this second part of the manuscript, we try to get closer to less abstract systems directly related to the human sphere, but that can be studied with methods similar to the ones already considered. We will tackle these more realistic scenarios with higher complexity in the network stucture, considering different topologies and different ways to refine the interaction structure by means of weighted adjacency matrices. In this sense, we approach two apparently new different problems, but that can also exhibit collective organized behaviors because of its organization in network structures. From them, we will unravel new insights on the dynamics of emergent phenomena while being able to apply some of the concepts already analyzed.

On the one hand, the concept of opinion polarization has been studied mathematically for some time now within the context of opinion formation[Hegselmann and Krause, 2002], although in the sociological context has been the focus of attention for plenty of decades [Poole and Rosenthal, 1983, McCarty et al., 2006, Baldassarri and Gelman, 2008, Fiorina and Abrams, 2008, Lee, 2015]. In this sense, a central question to many studies is whether the levels of mass polarization have been rising or not, and a huge debate exists on the topic. Regarding political matters and elections, the scientific literature seems to suggest that they do [DiMaggio et al., 1996, Abramowitz and Saunders, 2008, Prior, 2013, Lelkes, 2016], with increasing divisions among partisans of opposing parties that at the same time fuels and energizes political participation. Despite of this, there is not a clear responsible or explanation for it and some authors have tried to linked it to the internet and social media [Sunstein, 2018, de Wit and van der Linden a Cameron Brick, 2019]. The actual role of social networks in all of this is however very difficult to measure, and a study by [Boxell et al., 2017] between US adults showed that political polarization was highest among the age groups that use the Internet and social media the least, such as adults older than 65+. What is clear though, is that the boom of social media and its daily usage by millions of users leaves behind rich datasets where old and new metrics to identify polarized structures can be tested [Conover et al., 2011, Guerra et al., 2013, Morales et al., 2015]. In order to fully understand why this emergent property arises it is key to unveil which fundamental mechanisms related to the network structure are responsible for its appearance. This is what we will study in Chapter 6, the one that follows, with the main objective of connecting the emergence of polarization in social networks with the the Turing instability, a recursive tool of nature that induces differentiated patterns.

On the other side of things, motivated by the sanitary emergency of the COVID-19 pandemic that occured during the realization of this thesis, we looked for implementing the ideas implemented in the following Chapter related to perturbation growth and analysis of instabilities into epidemiological models. As we saw in the Methods, the growth rates derived in subsection 2.4 determine how a small perturbation may evolve, whether growing exponentially or decaying. In the case of epidemics, these perturbations can be naturally represented by

USC

new infection cases that, depending on where they are placed, they can result in a large-scale outbreak of the disease. As the COVID-19 was especially virulent and mutated continuously, it was observed to reappear consistently in the form of severe local outbreaks across the whole country, which at the large scale resulted in recurrent infection waves. As the approach we are considering can be applied too to a metapopulation network model describing a whole region, it could be especially useful for predicting the potentiality of each municipality to develop new outbreaks given their unique geographic and demographic features. This is what we will do in Chapter 7.

Simultaneously to the previous work, we were also interested in capturing the opinion state of a given social network. On the one hand, to test our preliminar findings of the polarization problem and on the other, to understand which was the state of opinion at the start of the COVID-19 pandemic. Do we obtain differentiated opinion distributions by running opinion models on top of real social networks? And, as the social network changes continuously in time, are different time snapshots of this network affected by the ongoing cultural and political events? In other words, is there a fingerprint left in the underlying pattern of interactions that we could unravel? With these objectives in our mind, we designed the methodology explained in chapter 8 to estimate opinion distributions from social media data at different moments in time. This work aimed also at contributing to raise awareness on the importance of following public health recommendations, showing how even small differences on the adherence to these policies could affect significantly on the appearance of new cases.

USC
UNIVERSIDADE DE SANTIAGO DE COMPOSTELA

Chapter 6

Polarized opinion structures in complex networks

So far, we have analyzed a particular type of collective behaviors that appears in the form of coherent oscillations. Here, we focus on another property caused purely by collective behavior in another kind of non-linear system: the emergence of two opposing clusters of opinion states. Although these clusters have not much to do in nature with those of phase or chemical oscillators, we will see similar phase transitions and we will use similar approaches to characterize the phase space of dynamical regimes.

Part of the text and figures for this chapter are reproduced from

* Carballosa A.[1,2], Crego A.[1] & Muñuzuri A.P.[1,2] *"Quantifying the potentiality for polarization in opinion networks"*, Chaos Solitons & Fractals Volume 173, 113697 (2023), `https://doi.org/10.1016/j.chaos.2023.113697`

[1] Group of Nonlinear Physics, Faculty of Physics, University of Santiago de Compostela
[2] Galician Centre for Mathematical Research (CITMAGa), University of Santiago de Compostela

6.1 Introduction

The attempts to understand polarization in opinion formation processes through mathematical modelling began with a seminal work by DeGroot [Degroot, 1974], where he showed how the averaged interaction between agents with different initial opinions tended to decrease the overall disagreement, eventually reaching a consensus. We know that this is however very idealistic, and to obtain disagreement states with this model it suffices to introduce an innate belief for each agent (a sort of stubbornness) and a set of weights in the averaging process to account for network influence [Friedkin and Johnsen, 1990]. Regarding the network structure, two important mechanisms that lead to or have been observed in polarized structures are homophily, the tendency of individuals to connect with others of similar thinking [McPherson et al., 2001, Axelrod, 1997, Bessi et al., 2016], and echo chambers [Vicario et al., 2016, Del Vicario et al., 2016, Cota et al., 2019, Cinelli et al., 2021], where the opinions of a segregated group are reinforced in time by a community or any kind of external media (television, radio or internet). Modelling both mechanisms simultaneously leads to an

even more robust model [Baumann et al., 2020], where meta-stable polarized states are reached from global consensus.

Here we take another direction, we aim to relate the study of opinion polarization with the ability of a certain network to exhibit the Turing instability. Note that we do not intend to use this as a direct explanation for the opinion polarization process, since as we have seen, it is a highly complex phenomena that involves several mechanisms. Rather, we propose it as a tool to identify already polarized network structures. For this purpose, we choose a suitable reaction-diffusion model where two ideas u and v evolve and compete, having several equilibrium states where one idea can completely erase the other. Another very interesting application of these models can be found in linguistic dynamics where two languages are competing for speakers. Initially considered for explaining the rapid historical decline of minority languanges [Abrams2003], more complex and recent models have shed light on the particular conditions needed for coexistence in situations of diglossia, predicting the evolution rates of the minoritory language [MussaJuane2019, Seoane2019]. In our case, the competition between ideas occur mainly at the individual level, as some kind of thought process, and afterwards through contact with other individuals there is an exchange of opinions. This is, there is diffusion of opinions across the links of the network. The equilibrium point of the system where both ideas can coexist will be the same for all the nodes and it will correspond to a neutral state corresponding to consensus, where each node is not radicalized to one idea or the other. As we saw in section 2.4 from the linear stability analysis, after introducing the network, the stability of this equilibrium point may change abruptly depending on the model parameters and the strength of diffusion. Furthermore, we saw that the conditions under which change occurs can be exactly determined by inspecting the sign of the dispersion relation $\lambda_\alpha(\Lambda_\alpha)$ (eq. 2.46). In this way, we can map the parameter space where the model undergoes the Turing instability and settles into a new differentiated stationary state where nodes radicalize into one of the opinions. Note that a key feature of this approach is that the state of opposing opinions did not existed a priori within the model, it emerges naturally because of the network. At the same time, this requires that we consider a more relaxed definition of polarization where nodes do not end up occupying opposing opinions known beforehand, like 0 and 1 or -1 and 1. This is specially true considering that since the linear stability analysis tells us mainly if the instability occurs or not (see section 2.4), it cannot distinguish if one of the opposing opinions is more populated than the other. Therefore, our approach does not give an exact measure of how polarized the state is but captures accurately the onset of the polarization. Since it is based in analytical calculation, once obtained the eigenvalues and eigenvectors from the Laplacian matrix, we only need to compute eq. 2.46 for each configuration of parameters which can be done in mere seconds. This makes the approach very efficient in exploratory stages of the model and as we shall see in the following, it is also able to capture significant differences between network topologies. Later on, in order to contrast our method, we will run extensive simulations in the same parameter space using the polarization metric proposed by [Morales et al., 2015], which quantifies exactly the degree of polarization based on the opinion dispersion and the population of each opinion cluster.

Our results show that the connectivity distribution and specially its dispersion are key in the differentiation process, in agreement with previous work in Turing patterns with other biological models [Mimar et al., 2019]. In this context, our descriptor shows that a network model with scale-free distribution presents a more continuous and extensive transition to the full-polarized state, where hub nodes become rapidly polarized and as we increase the diffusive coupling, the

rest of the nodes follow in an orderly fashion attending to their connectivity. Also, nodes with larger connectivities become polarized in a broader region of parameter space inducing thus some noise in the rest of the network. This could be interpreted as these highly connected nodes participating more in the conversation because they have something different to say, trying to spread their views to the whole network. On the other hand, for networks with finite, small dispersion in their connectivity distribution, the Turing instability region is less accessible in the parameter space but their Turing patterns reflect clearer polarized structures where almost all nodes differentiate into two extreme opinion clusters. This is, in this type of networks there is a direct and abrupt transition to the full-polarized state. From direct comparison with the polarization index proposed by [Morales et al., 2015], we found that our descriptor clearly outlines the region where consensus is broken in all the networks considered, thus measuring how different topological features of the networks affect the emergence of polarization.

6.2 Model

In the Methodology section we gave the general framework to compute the linear stability analysis of any model according to the functions $f(u,v)$, $g(u,v)$ and some given diffusion matrix $\mathscr{D}$. Let us now give a complete description of the model that we will be using and the derivation of its stability analysis. We consider a system of N interacting agents that debate between the opposing ideas u and v according to the following reaction-diffusion system

$$\begin{cases} \dfrac{du_i}{dt} &= f(u_i,v_i) + \varepsilon \displaystyle\sum_{j=1}^{N} L_{ij}\left[u_j(d + d_{uv}v_j)\right] \\ \dfrac{dv_i}{dt} &= g(u_i,v_i) + \varepsilon \displaystyle\sum_{j=1}^{N} L_{ij}\left[v_j(d + d_{vu}u_j)\right] \end{cases} \tag{6.1}$$

for $i = 1,...,N$. The reaction functions are given by

$$f(u_i,v_i) = u_i(a_1 - b_1u_i - cv_i) \qquad g(u_i,v_i) = v_i(a_2 - b_2v_i + cu_i) \tag{6.2}$$

where the dynamical parameters determine growth (a), decay (b) and competition (c) for each idea. Note that the sign of the competition term favors the increase of one of the ideas over the other, in this case v over u. On the other hand, we have two diffusive processes going on. If we recall from section 2, L_{ij} is the Laplacian matrix of the network that serves as a discrete operator that allows to model diffusion in networks. It is obtained from the network's adjacency matrix A_{ij} as $L_{ij} = A_{ij} - \delta_{ij}k_i$, where k_i is the connectivity of node i and δ_{ij} the Kronecker delta. Now, on one hand there is regular diffusion according to Fick's law, where each agent i receives inputs from its network as $\varepsilon\sum_{j=1}^{N} A_{ij}d(u_j - u_i)$. The parameter d modules this diffusion and tends to homogenize the system, increasing the opinion u where there is a lack of it. On the other hand, we consider cross-diffusion $\varepsilon\sum_{j=1}^{N} A_{ij}d_{uv}(u_jv_j - u_iv_i)$, a mechanism by which the concentration gradient of one variable induces an opposite gradient from the other. In our case, this means that opinions will diffuse further where there is low concentration of the opposite opinion favoring the communication flows between like-minded individuals. In this sense, we introduce the concept of homophily from the point of view of opinion dynamics instead from the network structure. Besides

UNIVERSITAT DE LES ILLES BALEARS

being a suitable mechanism for competing species, in many reaction-diffusion models it is necessary condition for the emergence of spatiotemporal structures [Vanag and Epstein, 2009, Wang et al., 2011, Xue, 2012, Ruiz Baier and Tian, 2013]. This is also true for our model and, what's more, as we shall see later, the cross diffusion from v to u (d_{vu}) will be one of the control parameters that drives the Turing instability.

In absence of diffusion, the equilibrium points of the system are given by the solutions,

$$f(u^*, v^*) = 0 = u^*(a_1 - b_1 u^* - c v^*) \rightarrow u^1 = 0,\ u^2 = \frac{c v^* - a_1}{b_1}$$
$$g(u^*, v^*) = 0 = v^*(a_2 - b_2 v^* + c u^*) \rightarrow v^3 = 0,\ v^2 = \frac{a_1 - b_1 u^2}{c}$$

where the superindex refers to the number of the solution. If we substitute the solutions in the other equation respectively, we recover the following fixed points

$$(u^1, v^1) = \left(0, \frac{a_2}{b_2}\right) \tag{6.3}$$
$$(u^2, v^2) = \left(\frac{b_2 a_1 - a_2 c}{b_1 b_2 + c^2}, \frac{b_1 a_2 + a_1 c}{b_1 b_2 + c^2}\right) \tag{6.4}$$
$$(u^3, v^3) = \left(\frac{a_1}{b_1}, 0\right) \tag{6.5}$$

Solutions 1 and 3 correspond to stationary states where one of the opinions go extinct. For $c < 0.3$, it can be proved that they are unstable solutions while the solution number 2 is the stable one. Thus, we obtain a stable manifold of solutions where there are positive finite values for both u and v that depend on the parameters. We will refer to this solution as the consensus state, as all the nodes in the network adopt this state agreeing on an intermediate point between u and v. From here one, we will denote this solution as (u^*, v^*) and discard the others.

When diffusion is turned on, the system will either return to this equlibrium point (if diffusion is not strong enough), or achieve a new stationary state where individuals in the network adopt new extreme positions by means of the Turing instability. Although this new values can't be predicted, they are not random but lie within the stable manifold given by solutions (u^*, v^*), with the differentiated nodes usually adopting the minimum and maximum possible value. In summary, we have an internal process whose natural tendency is to return to equilibrium while a tunable network influence tries to disrupt this state. Note that our model does not distinguish between intrinsic preferences so the emergence of polarization is purely a collective phenomenon where social connectivity is crucial. In this way, the Turing instability exemplifies the ability to break the system's homogeneity and differentiation in a natural way. Both the dynamical parameters and network topology strongly affect the model capability to undergo the instability and, thus, the region in the control parameter space where it is found.

6.2.1 Numerical details

Unless explicited otherwise, we will fix the model parameters at $a_1 = a_2 = 2.0$, $b_1 = 0.08$, $b_2 = 0.3$, $d = 0.001$ and $d_{uv} = 0.0$. The motivation behind the explicit choice for these parameter values resides mainly in exemplifying our approach, although we will also report in the following the effect of some of them in our results. On the other hand, we use as control

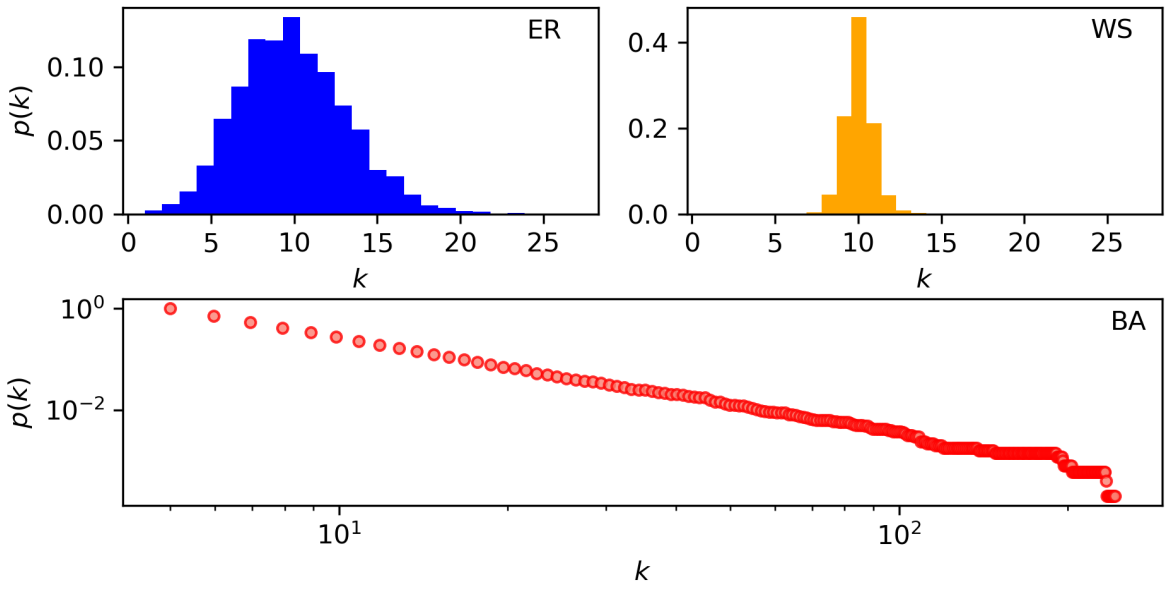


Figure 6.1: Connectivity distributions of the three network models used, the Erdos Renyi (ER), the Watts-Strogatz (WS) and the Barabasi-Albert (BA). Network sized was fixed at $N = 5000$, and the average connectivity of the three graphs is $\langle k \rangle = 10$. In panel (c), we show the cumulative probability distribution in logarithmic scale.

parameters the competition rate c, the cross-diffusion d_{vu} and the network influence ε as they are the main ones that trigger the Turing instability. For the integration of equations 6.1, we use a explicit Euler scheme with time step of $\delta t = 0.001$.

For the network structures, we will consider mainly the Erdos-Renyi (ER), the Watts-Strogatz (WS) and the Barabasi-Albert (BA) network models. For generating the graphs, we used the `Python` library `networkx`. In Figure 6.1 we show the connectivity distributions of these network models for $N = 5000$, corresponding to the ones used to obtain the main results (reported in Figure 6.3). We will also consider at some point star graphs, built from an adjacency matrix with 1s only in the first row or the first column, in function of the desired link direction. For the directed BA graphs, we built the graphs using the previous functionalities and made them directed by turning to 0 the upper/lower triangle of the adjacency matrix.

6.3 Polarization measures

6.3.1 Growth rates

As we saw in Methods (section 2.4), to estimate how a perturbation $(\delta u, \delta v)$ will grow in the system we can approximate eqs 6.1 with a linearization at first order around the fixed point as

$$\begin{cases} \dfrac{d\delta u_i}{dt} &= f_u \delta u_i + f_v \delta v_i + \varepsilon \displaystyle\sum_{j=1}^{N} L_{ij} \left[\mathscr{D}_{11} \delta u_j + \mathscr{D}_{12} \delta v_j \right] \\ \dfrac{d\delta v_i}{dt} &= g_u \delta u_i + g_v \delta v_i + \varepsilon \displaystyle\sum_{j=1}^{N} L_{ij} \left[\mathscr{D}_{21} \delta u_j + \mathscr{D}_{22} \delta v_j \right] \end{cases} \tag{6.6}$$

USC UNIVERSIDADE DE SANTIAGO DE COMPOSTELA

where the subindexes $f_u = \delta f/\delta u|_{u^*,v^*}$ denote the partial derivatives evaluated at the fixed point and the coefficients $\mathscr{D}_{ij}$ are the elements of the diffusion matrix $\mathscr{D}$, given by $\mathscr{D}_{11} = d + d_{uv}v^*$, $\mathscr{D}_{12} = d_{uv}u^*$, $\mathscr{D}_{21} = d_{vu}v^*$,$\mathscr{D}_{22} = d + d_{vu}u^*$.

We then proposed as solutions to the perturbations an expansion in terms of the Laplacian eigenvectors $\Phi^{(\alpha)} = \phi_1^\alpha, \phi_2^\alpha, ..., \phi_N^\alpha$,

$$\delta u_i(t) = \sum_\alpha^N B_\alpha e^{\lambda_\alpha t}\phi_i^{(\alpha)} \qquad\qquad \delta v_i(t) = \sum_\alpha^N C_\alpha e^{\lambda_\alpha t}\phi_i^{(\alpha)} \tag{6.7}$$

where each eigenvector $\Phi^{(\alpha)}$ has associated an eigenvalue Λ_α that can be determined from

$$\sum_j^N L_{ij}\phi_j^{(\alpha)} = \Lambda^\alpha \phi_i^{(\alpha)}, \text{ with } \alpha = 1, ..., N \tag{6.8}$$

Substituting solutions 6.7 into eqs.6.6 and repeating the calculus shown in the Methods (from eq. 2.32 to 2.35), we end up with a set of N independent linear equations for each normal mode α,

$$\lambda_\alpha = J^* + \Lambda_\alpha \mathscr{D} = \begin{pmatrix} f_u^* + D_{11}\Lambda_\alpha & f_v^* + D_{12}\Lambda_\alpha \\ g_u^* + D_{21}\Lambda_\alpha & g_v^* + D_{22}\Lambda_\alpha \end{pmatrix} \tag{6.9}$$

where we can obtain the the dispersion relation $\lambda_\alpha(\Lambda_\alpha)$ by solving the determinant. We saw in eq. 2.46 that the solutions to this system are given by,

$$\begin{aligned} \lambda_\alpha(\Lambda_\alpha) = \frac{1}{2}\Bigg(\tau(J^*) + \tau(\mathscr{D})\Lambda_\alpha \pm \Bigg[(\tau(J^*) + \tau(\mathscr{D}))^2 - \\ -4(\det(J^*) + \left(\sum_{ij} J_{ij}^* \text{adj}(\mathscr{D})_{ij}\right)\Lambda_\alpha + \det(\mathscr{D})\Lambda_\alpha^2 \Bigg]^{\frac{1}{2}} \Bigg) \end{aligned} \tag{6.10}$$

where now the matrix $\mathscr{D}$ includes all the elements so the term $\sum_{ij} J_{ij}^* \text{adj}(\mathscr{D})_{ij}$ is now given by

$$\sum_{ij} J_{ij}^* \text{adj}(\mathscr{D})_{ij} = f_u D_{22} - f_v D_{21} - g_u D_{12} + g_v D_{11}$$

These solutions are termed the growth rates of the perturbations, which tell us that the αth mode is unstable if $\text{Re}(\lambda_\alpha) > 0$. In other words, whenever $\text{Re}(\lambda_\alpha) > 0$ the Turing instability appears and the nodes separate from the consensus state. Our methodology will consist in solving 6.10 for a range of parameters c and d_{vu}, obtaining the phase space of the system where we can map where the instability occurs. We use these two parameters as we have seen they are the main ones that drive the instability. On one hand, increasing c increases the competition between the opinions, and in the other, d_{vu} increases the segregation between them. We have seen that these two mechanisms are the ones that most favor differentiation in our system, while on the contrary increasing d, d_{uv} tend to stabilize the system. This is caused because as we commented earlier, cross diffusion is necessary for the Turing instability to appear, and increasing any of the two other quantities counter-effects the cross-diffusion established by d_{vu}.

USC UNIVERSIDADE DE SANTIAGO DE COMPOSTELA

6.3.2 Polarization degree

We have also considered the polarization index proposed by [Morales et al., 2015] to contrast our results and analyze the polarized structures given by our model. Given the definition that a polarized state is that in which the opinions are equally distributed in opposing positions, we need to measure both the population of individuals in each position and the ideological distance between them. If the network undergoes the Turing instability, the new ideological positions will appear above and below the fixed point of the system u^* Thus, we define N^- as the relative population of individuals with opinions below the fixed point $(u_i < u^*)$ and N^+ the relative population of individuals above it $(u_i > u^*)$. The normalized difference in population sizes will then be given by

$$\Delta N = \frac{|N^+ - N^-|}{N} \tag{6.11}$$

Likewise, to measure the distance between the opinion clusters we start by considering the difference between the average value of each opinion cluster, divided by the difference of the maximum values in the opinion distribution,

$$\eta = \frac{\langle u^+ \rangle - \langle u^- \rangle}{u_{max} - u_{min}} \tag{6.12}$$

Again, the maximum and minimum values for u are given by the stable manifold of solutions $u^*(a,b,c)$. Finally, with these two measurements we can measure polarization as a function of the population differences and the distance between them, writing the polarization index as [Morales et al., 2015]:

$$\mu = (1 - \Delta N)\eta \tag{6.13}$$

with $0 \leq \mu \leq 1$. When the resulting opinion distribution is clearly bimodal, equally populated and with each opinion center located at each extremal value, the polarization index will be equal to 1. In this case we can talk about full-polarization, while in any other case we shall talk about partial polarization. On the other hand, μ will be zero or near zero when opinions do not differentiate at all or, even if they had acquired new extremal values, one of the clusters is more heavily populated than the other.

6.4 Results

We start this section by describing the qualitative behavior of the model, showing in Figure 6.2 two glimpses of the Turing instability depending on the network influence ε. For this purpose, we have integrated equations 6.1 for a system of $N = 1000$ nodes initialized around the fixed point (u^*, v^*) with a small random perturbation. For the moment, we have chosen two different network topologies, one constructed with the Erdos-Renyi (ER) random network model and another with the Barabasi-Albert (BA) network model (recap section 1.3 for details). For low values of the network influence (see upper part of panel (a)), we see that the ER network does not undergo the instability and that every node returns to the fixed point, i.e., the consensus state. On the other hand, in the BA network, we observe that a few nodes with the highest connectivities (the hubs) have adopted new differentiated positions that induce a small noise in the rest of the network, which remains around the consensus value. We refer to this as the onset of polarization, as some nodes have began to differentiate and as soon as we

USC

increase ε, more will follow. Note that for visualization purposes, the nodes of both networks are arranged in decreasing order of their connectivity. If we increase now the network influence sufficiently, to ε=0.5, both networks exhibit two clear differentiated states distributed across the whole network. In this case, we consider that we have achieved almost full polarization on every node (see lower part of panel (a)), that now have jumped to either the state at $u_i \simeq u_{max} = 25$ or $u_i \simeq u_{min} = 0$. We can understand why the networks underwent or not the instability in each case attending to their respective growth rate distributions (see panel (b)). The opinion differentiation starts at a certain critical eigenvalue Λ_{α_c}, from which the growth rates become positive. Panel (b) clearly shows that in the case of the ER with low network influence this critical eigenvalue is close but it is not reached. As we shall see later on, increasing the average connectivity of the ER leads also to an increase in the eigenvalues, so therefore it would be also possible for this topology to surpass the critical threshold. In the case of the BA network, the scale-free property and the spread distribution of connectivities allows the existence of larger Laplacian eigenvalues that overcome the critical threshold even for small values of the network influence. We have chosen this example with average connectivity fixed in both networks at $\langle k \rangle = 10$ to highlight this feature.

Attending now to the growth rates (GR) as a tracer of the Turing instability, we focus on the control parameters that drive best the instability: the competition rate c, the cross diffusion coefficient d_{vu} and the network influence ε. We sweep the competition c within the region that keep stable the manifold of solutions given by (u^*, v^*) (eq. 6.4), which is $c \in [0, 0.3)$; and for the cross-diffusion we choose a range sufficiently large enough so the results can be comparable (in this case, also $d_{vu} in [0, 0.3]$. For the network influence we choose the same cases as in Figure 6.2, one with low influence $\varepsilon = 0.1$ and another with high influence $\varepsilon = 0.5$. We compute the GR within this parameter space and for each parameter configuration we save the maximum growth rate between all modes α, this is, λ_α^{max}. We consider now systems of $N = 5000$ nodes in order to avoid finite-size effects, and besides the BA and ER models, we also introduce the Watts-Strogatz (WS) network model because of its even lower connectivity dispersion and its capability to tune the average path length of the graph from the probability of random shortcuts in the network. Since the average path length ℓ is the average distance between all pairs of nodes, the larger it is, the longer will take the diffusion process. Considering the total number of performed computations within the parameter space, we define the **Turing area** of the network as the fraction of these computations where the Turing instability appeared. Panels (a to c) of Figure 6.3 clearly shows the differences between the networks' capability to destabilize the system. The black drawn line demarks the contour where $\lambda_\alpha^{max} = 0$, so it bounds the region where the instability starts to appear, and therefore the onset of node polarization. We check that the larger dispersion in the connectivity of the scale-free topology given by the BA model plays a crucial role in the appearance of the Turing instability [Mimar et al., 2019], finding that for small values of the network influence (ε=0.1) it is considerably larger than for the ER and WS. This is directly related to the eigenvalues and eigenvectors of the Laplacian matrix and their dependence on the network connectivity. The connectivity distribution of the scale-free topology allows for a wider spectrum of eigenvalues, which makes it easier to reach the critical mode α_c and therefore the positive solutions of the GR. Besides, the eigenvectors associated to nodes with higher degrees have their normalization weights concentrated on a small subset of their components (they are "localized"), and this property is what makes these nodes to differentiate faster [Mimar et al., 2019]. On the other hand, the connectivity of the ER and the WS follow a Gaussian distribution with small dispersion, with their spectrum of eigenvalues

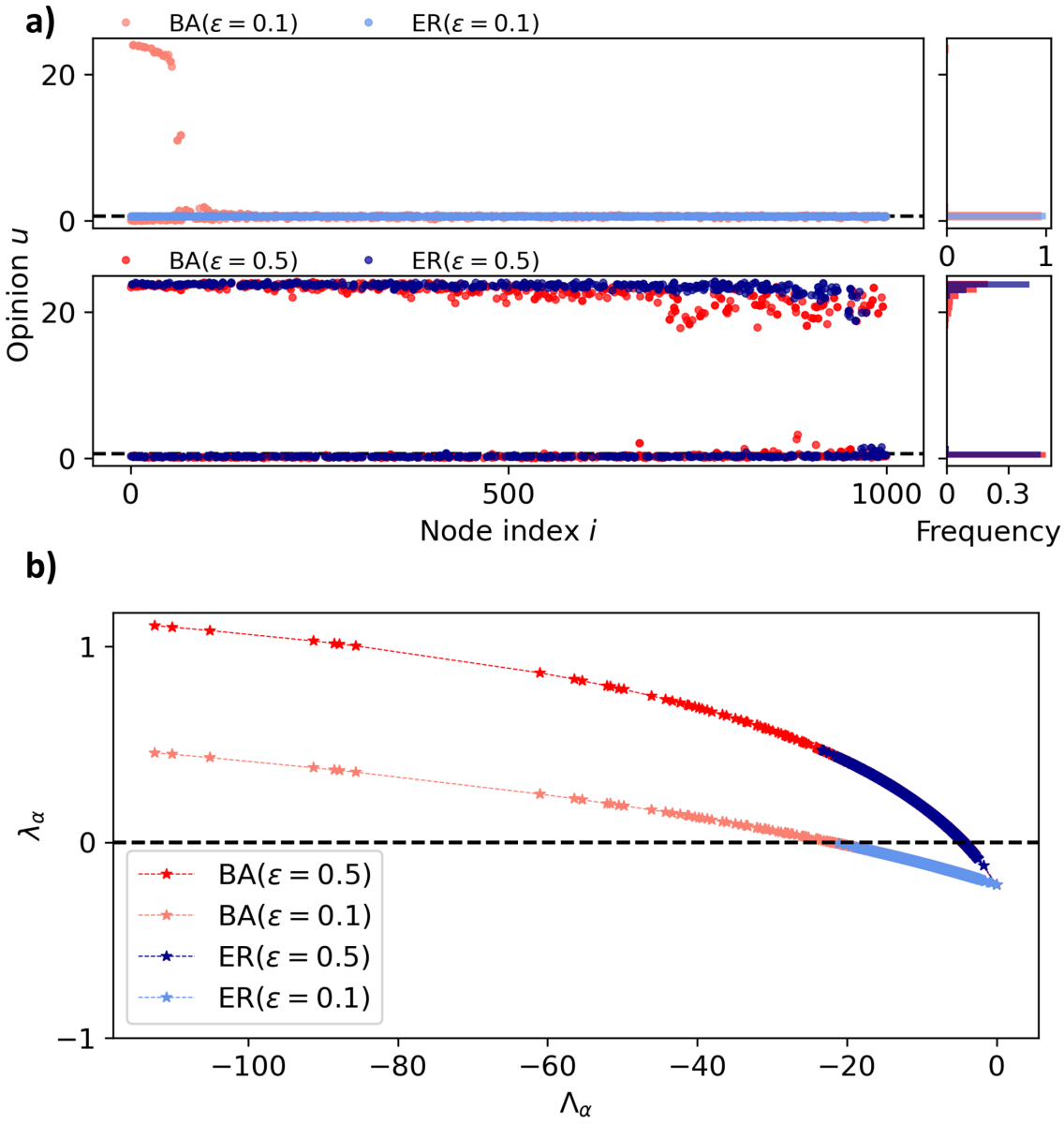


Figure 6.2: Turing instability for two different network topologies, the Erdos-Renyi (ER) in blue, and the Barabasi-Albert (BA) in red, both with size $N = 1000$. In panel (a), two different values of the network influence are considered, $\varepsilon = 0.1$ and $\varepsilon = 0.5$. Right sub-panels represent the histograms of each distribution. Panel (b) shows the growth rate distribution associated to each configuration of the sub-panels in (a). For these simulations, $c = 0.27$, $d_{uv} = 0.0$ and $d_{vu} = 0.17$. Both networks have a mean degree of $\langle k \rangle = 10$, with the nodes being shown in a decreasing order of their connectivity value. The black dashed line in panel (a) represents the fixed stable point of the system for the given parameters, namely $u^* = 0.62$, while in panel (b) is a visual aid at $\lambda_\alpha = 0$ to see when the growth rates become positive.

USC UNIVERSIDADE DE SANTIAGO DE COMPOSTELA

being more compact and their eigenvectors less localized, having their normalization weights distributed uniformly. Thus, the critical mode here is only reached when the dynamical parameters of the model are high enough, or the network influence is significantly increased (panels g-i).

Regarding the polarization index μ computed as in eq. 6.13, panels (d-f) and (j-l) show that the region of positive GR indeed outlines the onset of polarization. The comparison with the black contour given by the positive GR signals however that for node polarization to be noticeable, it does not only suffice that $\lambda_{max} > 0$, but it needs also to reach a certain value. Contrasting with the reddish region of the GR where $\lambda_{max} \geq 1$ approximates better the region where partial polarization appears. Going further, for $\varepsilon = 0.1$ and for the BA we saw already in Figure 6.2 that only nodes with large connectivities adopted new opinions. Therefore, the overall opinion distribution in this case remains practically unimodal (see the lateral panel of Figure 6.2) and thus the polarization index is considerably small, around $\mu = 0.25$. It is interesting to see, however, that in the ER network the colored region with non-zero polarization index is smaller than the BA but higher in value, reaching almost $\mu = 0.5$. This feature is highlighted in the bottom panels with $\varepsilon = 0.5$, where μ can reach the unity in the WS network but not in the BA. Again, this is related to the connectivity distribution and its dispersion, being in some way the opposite case of what we had earlier. Now, the less connected nodes of the BA are the last ones to adopt one of the extreme opinions (see this in the evolution of the right points of Figure 6.2(a)), contributing to the noise of the opinion distribution and decreasing the distance between the opinion clusters. For the ER and WS networks however, if the network influence is sufficiently large enough, almost all nodes will adopt one of the extreme opinions. This leaves as a result a clear bimodal distribution, which in turn results in a higher polarization index. In the case of the WS, since the dispersion in connectivity is even smaller (see Supplementary Information Figure S1), the dispersion in the opinion clusters is also smaller and thus the distance between them is maximal. This is what allows the WS to reach the full-polarization state with $\mu = 1.0$. Regarding the differences in the values of the μ-index of panels k and l, we have noticed that they are mainly due to differences in the cluster populations, with the cross-diffusion parameter d_{vu} acting as a driving force that makes one of the opinion clusters bigger than the other.

It is interesting also for our study characterize the effect of the other model parameters on the size of the Turing area measured with the GR. This is shown in Figures 6.4 and 6.5. First, in panel (a) we examine its growth as a function of the network influence ε, where we see a critical value ε_c at which the instability happens and that is different for each network. In the BA, the instability appears almost immediately, with the Turing area also growing faster than in the other networks and saturating earlier around the value of 0.65, the one previously shown in Figure 6.3(g). Between the ER and the WS, we see how the latter takes a bit longer to appear and that is also grows slower with ε. For these two we have also checked in panel (b) how their Turing area grows with the network average connectivity (with fixed $\varepsilon = 0.1$), seeing that the region with positive GR in the WS model is only slightly smaller than in the ER. As we mentioned earlier, these two parameters interplay with each other in the sense that ε modifies the threshold for the positive growth rates λ_c^{α}, but on the other hand, for the ER and the WS an increase in the average connectivity conveys an increase in their eigenvalues and therefore in the maximum growth rate that they can achieve. Thus, increasing any of these two parameters makes it easier for them to reach the onset of polarization and thus enlarge their Turing area. Besides, the difference among them can be closely related to the average path

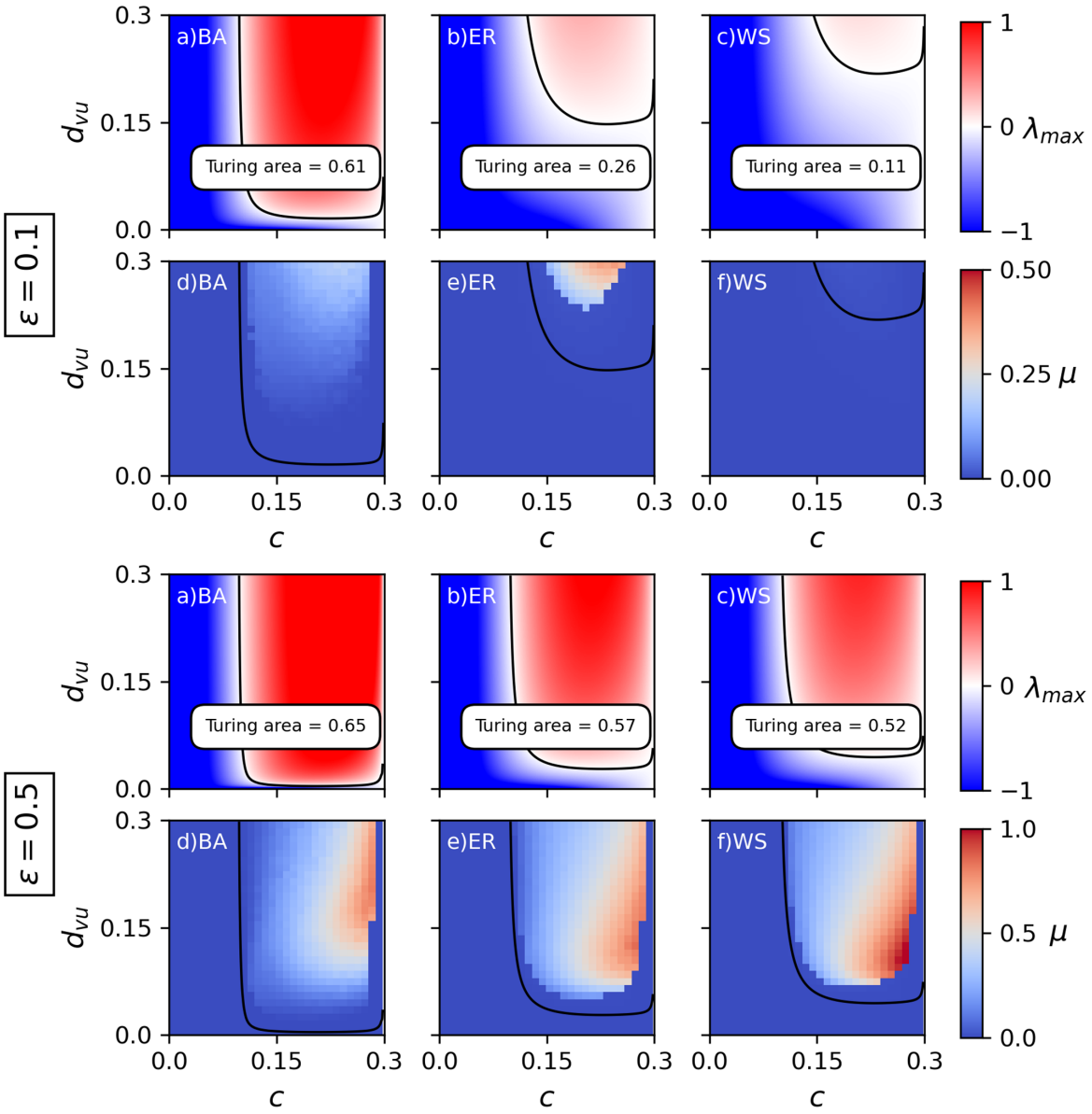


Figure 6.3: Maximum value of the growth rates λ_{max} ((a-c) and (g-i)) and polarization index μ ((d-f) and j-l) in the parameter space for $\varepsilon = 0.1$ and $\varepsilon = 0.5$, for three different network topologies. BA accounts for Barabasi-Albert, ER for Erdos-Renyi and WS for Watts-Strogatz. Here, network size was fixed to N=5000 for all panels to avoid finite-size effects (see panel 6.4(a)). The black drawn line drawn denotes the area where $\lambda_{max} = 0$, therefore signaling the beginning of the instability. Note that in panels (d-f) the colormap was adjusted between $\mu = 0$ and $\mu = 0.5$ to zoom in the values. Panel (f) do not show any significant trace of polarization attending to μ, since the instability only induces a small noise in the system.

USC
UNIVERSIDADE DE SANTIAGO DE COMPOSTELA

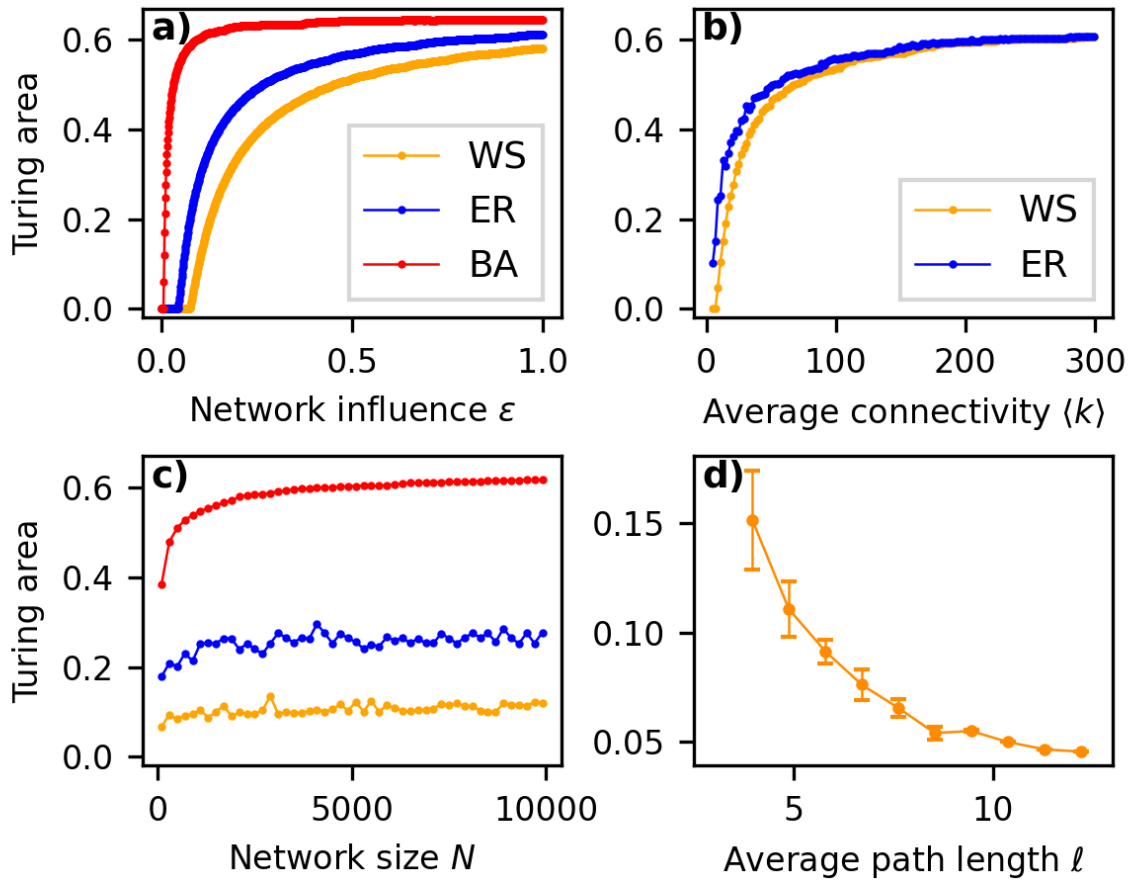


Figure 6.4: Size of the Turing area in function of the network influence ε (a), average network connectivity $\langle k \rangle$ (b), network size N(c) and average path length ℓ (only for the WS network) (d). For panels a, b and d, network size was fixed at N=5000, while for panels b, c and d network influence was fixed at $\varepsilon = 0.1$. Error bars in panel (d) account for multiple realizations of the network with very similar ℓ.

USC UNIVERSIDADE DE SANTIAGO DE COMPOSTELA

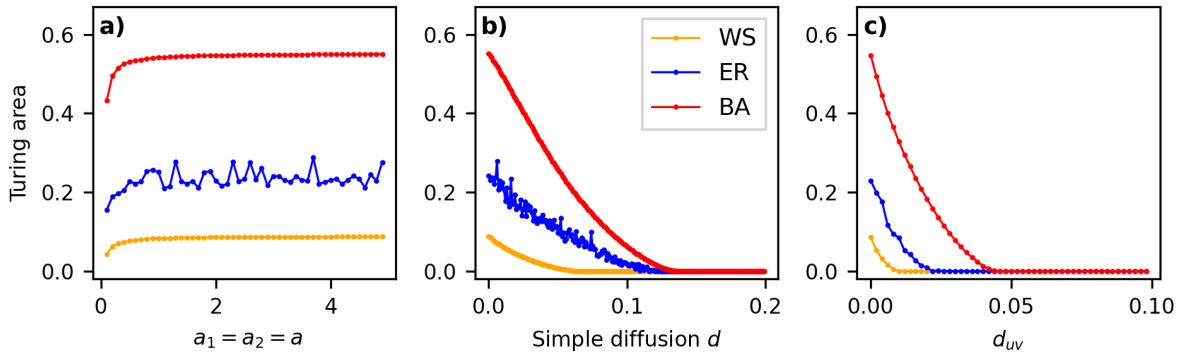


Figure 6.5: Size of the Turing area against the opinion growth a, simple diffusion d and cross diffusion d_{uv}, for the three different networks considered. For the three panels, network size was fixed at $N = 5000$ and network influence at $\varepsilon = 0.1$.

length ℓ suggesting that the time scale of the information flow, that is minimized in the BA model due to the presence of hubs, could be also one of the key features in the emergence of polarized non-homogeneous structures. Using the WS model as a reference, we can increase the average path length of the network by minimizing the number of existing shortcuts. In panel 6.4(d), we compare the size of the Turing region against the average path length for a WS network and show that, in fact, there exists an inverse proportionality between the two of them. This effect has been previously observed in diffusing epidemics [Moore and Newman, 2000] and it is related to the fact that decreasing the number of shortcuts halts the percolation of the system, which in our case, relates directly with the effective diffusion coefficient and so to the emergence of the Turing patterns.

In Figure 6.5, we report the effect of other model parameters that however do not have much effect in the Turing area, such as the local opinion growth a, simple diffusion d or cross diffusion from u to v, d_{uv}. We see respectively that from a certain value, well below the one used in our main results ($a = 2.0$), increasing the local opinion growth has no effect in the size of the Turing area. On the other hand, increasing simple diffusion d and cross diffusion d_{uv} tends to stabilize the system and remove heterogeneities, thus inhibiting the Turing instability for all three networks equally.

Finally, we pay some attention to link directionality, inspecting further the connection between a critical connectivity and polarizing effects. It is usual that users online communicate unilaterally, following someone who do not follow back or answering a post which do not receive another answer in return. We have seen so far that the degree heterogeneity above a certain critical value is a necessary condition for the polarization to occur, and we will see in the following that our model is very susceptible to the directionality of such interactions. Attending to eqs. 6.1, node i modifies its opinion in function of those nodes that i is looking up to, given by the rows of the adjacency matrix A_{ij} which represent the out-connectivity of i. Therefore, for each node, the opinion diffusion depends only on its outwards connectivity. In turn, the sum of connections that are following the opinion of node i are given by the columns of A_{ij}, and account for the in-connectivity of the node. Since they do not affect the equations, they have no relevance in its opinion value. In the case of social networks, this could represent a mechanism by which the opinion of a given user would be purely affected by how much activity they engage into, rather than by the attention they receive. Using directed star networks, we can highlight the latter to find that the central node is always potentially polarized (exhibits a differentiated state

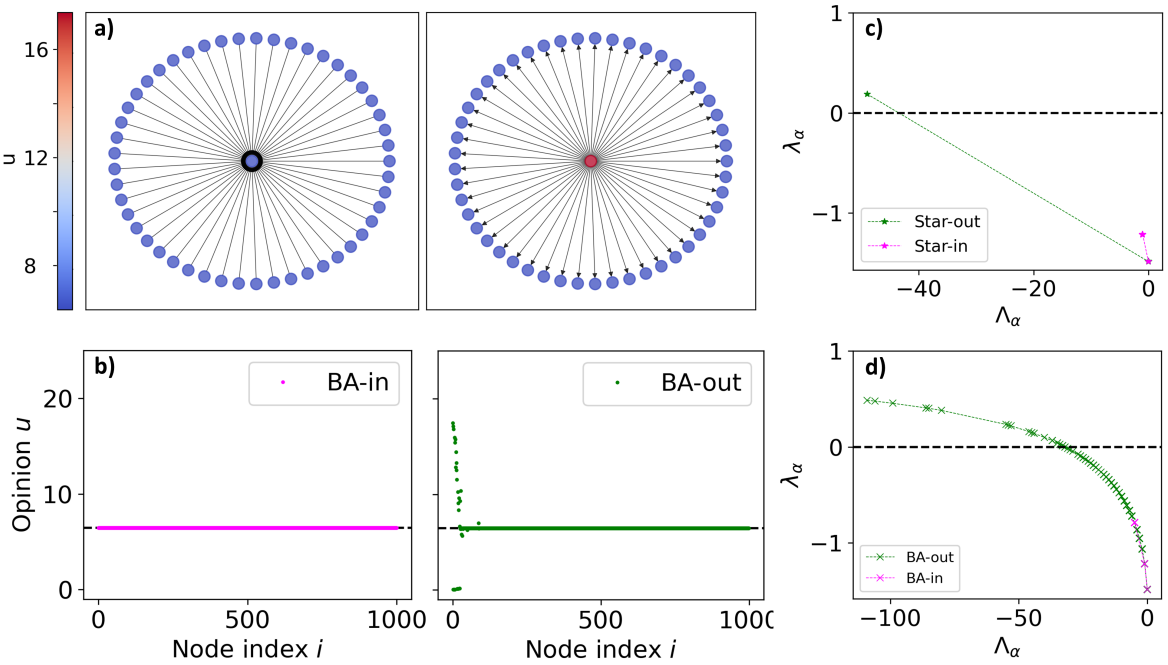


Figure 6.6: Effects of the link direction in the model. In star graphs (a) with $k = 50$, inward direction results in a return to the consensus while outward direction in a polarization of the central node, whenever k_{central} is higher than a critical value. This can be extrapolated to BA directed networks (c), where hubs with outward connectivity larger than a critical one become polarized while the rest of the nodes do not. Panels (b) and (d) show the growth rate distribution for each case. In all panels, $\varepsilon = 0.1$, while network size is $N = 50$ for the star networks and $N = 1000$ for the BA networks.

of opinion) whenever the out-connectivity is higher than the critical threshold (which is found near the critical value of the Laplacian eigenvalue, $k_c \simeq \Lambda_c$). On the other hand, if the central node only possesses inward connectivity, the polarization does not occur (see 6.6 panels (a) and (c)). The result is that the outward star network always has a positive growth rate if $k > k_c$ (green points) while the inward star graph does not (pink points). This outcome extrapolates to directed scale-free networks, as panels (c) and (d) show. As in Figure 6.2, the nodes in panel (c) are ordered in function of their connectivity, in descending order. Here, hub nodes with high out-connectivity are found polarized while nodes with small-to-none out-degree are found exactly at the fixed point without the slight dispersion previously observed at in Figure 6.2(a). In the opposite case, with a scale-free graph with fixed low out-connectivity and a power law distributed in-connectivity, the consensus remains and the network does not polarize. As a final note, notice that although in our model it is predefined that the outward direction is the preferential one, it could be arranged otherwise so the preferential direction would be the inward's and the outcome would be conceptually the same.

6.5 Conclusions

In this chapter, we have jumped into another complex system, one much more intricate and much more scary: a society of humans with something to say. We have introduced the problem of opinion formation from the pure perspective of nonlinear dynamics and demonstrated how polarization is an emergent property caused by the collective behavior of the system. Despite

the significant differences in nature between the systems, we can still see certain similarities to the synchronization chapters, as we could treat each polarized state as an opinion cluster and we have also seen two different paths to the full polarized state. In the case of an scale-free type of network, we have seen that it suffices that the network influence is finite $\varepsilon > 0$ in order to undergo the Turing instability. From here on, with increasing ε we obtain a partial polarization state where slowly more and more nodes become polarized attending to their connectivity values (in decreasing order). This results also in a certain difficulty to reach the full polarized state, as nodes with extremely low connectivity that hardly interact do not change their opinion, only inducing some noise in the system. On the other hand, for network topologies with finite, small variance $\langle k^2 \rangle$ in the connectivity distribution (such as the Erdos-Renyi or the Watts-Strogatz model), there appears a more defined critical value for the network influence ε_c. We have found also a smaller region of parameter space where the instability occurs for these networks, but, interestingly, the opinion states in this region are highly polarized, with polarization indexes (given by 6.1) higher than in the BA. This is also related to the connectivity, as now due to the small variance, once the network is able to induce a polarized state, the instability affects almost all nodes equally. This forces everyone to adopt one of the new states, reducing the noise in the system and increasing also the distance between the opinion clusters.

As we have seen in the Methods section, this is closely connected with the spectral properties of the Laplacian matrix. In the dispersion relation of the growth rates $\lambda_\alpha(\Lambda_\alpha)$, we have seen that there is a critical value for the Laplacian eigenvalues Λ_c at which the GR become positive. The higher the variance in the connectivity distribution, the broader is the spectrum of Laplacian eigenvalues and the more localized are the eigenvectors. This makes easier to reach the critical value and also to differentiate faster. This is also highlighted by specifying the link direction, where we show that opinion polarization strictly occurs in the direction where the exchange of opinions occurs and when the outward connectivity of a given node is high enough to overcome a critical threshold. With the help of star-shape and scale-free networks, we showed that the nodes with higher interactions pointing outwards become rapidly polarized while the rest remain at their original equilibrium state. In this sense, there are intrinsic features of the nodes that drives them to become polarized, although from this state they don't seem to be able to polarize their low-activity neighbors. In other words, here the Turing instability helps to detect which nodes have polarized in the circumstances given by the network parameters, which will be those that seem to have overcome the critical threshold set for the connectivity. We could find a suitable physical interpretation of this outcome in what is commented by [Baumann et al., 2020] based on empirical observations in social networks, that highly active users, more engaged in online discussions, are the ones that tend to present more extreme opinions. On the other hand, Λ_c depends strongly on ε, and so, the more we increase ε the more easy is for networks with small variance to overcome this threshold and induce full polarization.

To sum up, in this work we have defined the size of the parameter space where the Turing instability takes place as a measurement of a network's potentiality to sustain polarization states. In other words, our method shows the exact conditions at which a particular network topology is no longer fitted to support a consensus state and, thus, should evolve into a non-homogeneous configuration that we associate with polarization. As our descriptor is based on an stability calculus that do not recover the final state of the ndoes, it has some limitations to discern how much polarized the given state is. For this purpose, it is required to run the simulations and use another metric as the one presented by [Morales et al., 2015], and that we use to contrast

USC UNIVERSIDADE DE SANTIAGO

our metric. Future work involves then a more refined version of the descriptor that could capture more information on the final state, with application in more realistic models where the parameters are fine-tuned using empirical information from real social networks.

USC
UNIVERSIDADE DE SANTIAGO DE COMPOSTELA

Chapter 7

Evaluating risk descriptors in metapopulation epidemiologic models

We have seen in chapter 6 the potentiality of the growth rates $\lambda_\alpha(\Lambda_\alpha)$ to predict differentiation dynamics according to the network topology. Intrigued by this close connection between the spectral properties of the network and the dynamics that are nested in it, in this chapter we wonder if the growth rates can help us also to understand the collective behavior observed during epidemic spreading, i.e., the propagation of epidemic waves. Considering a spatially distributed network where the nodes represent cities and the links the amount of human mobility between them, here the instability appears directly when a small number of infected individuals are introduced in the pool of healthy ones. In this way, this small perturbation grows and evolve into a full epidemic outbreak. Using the previous knowledge obtained from the physical meaning of the growth rates, here we take them a step farther and aim to use them as a predictive tool epidemic spreading.

Part of the text and figures for this chapter are reproduced from the following publications

* Carballosa, A.[1,2], Balsa-Barreiro, J.[3,4], Garea, A.[1], García-Selfa, D.[1,5], Miramontes, A.[3] & Muñuzuri A.P[1,2], *"Risk evaluation at municipality level of a COVID-19 outbreak incorporating relevant geographic data: the study case of Galicia"*. Scientific Reports 11, 21248 (2021). `https://doi.org/10.1038/s41598-021-00342-2`.

* Carballosa, A.[1,2], Balsa-Barreiro, J.[3,4], Boullosa, P.[1], Garea, A.[1], Mira, J.[6,7], Miramontes, A.[3], & Muñuzuri, A.P.[1,2], *"Assessing the risk of pandemic outbreaks across municipalities with mathematical descriptors based on age and mobility restrictions"*, Chaos, Solitons & Fractals, Volume 160, 112156 (2022), `https://doi.org/10.1016/j.chaos.2022.112156`.

[1] Group of Nonlinear Physics, Faculty of Physics, University of Santiago de Compostela
[2] Galician Centre for Mathematical Research (CITMAGa), University of Santiago de Compostela
[3] Group of Territorial Analysis, Institute IDEGA, University of Santiago de Compostela
[4] MIT Media Lab, Massachusetts Institute of Technology, 75 Amherst St, Cambridge, MA, 02139 USA
[5] Galician Supercomputer Center (CESGA), University of Santiago de Compostela
[6] Applied Physics Department, Faculty of Physics, University of Santiago de Compostela
[7] Institute of Materials (IMATUS), University of Santiago de Compostela

USC UNIVERSIDADE DE SANTIAGO DE COMPOSTELA

7.1 Introduction

What we present here was an initial attempt to understand the rapid spatiotemporal spread of the COVID-19 in Galicia and Spain, that swept the whole country in just a matter of weeks. We wanted, at the same time, to develop a suitable and efficient computational tool that could demonstrate that each locality has a set of unique demographic and geographic features that affect how the disease spreads. In this sense, metapopulation network models represent one of the best modelling choices for this problem as they can be easily scaled to cover the population of a whole country [Watts et al., 2005, Colizza et al., 2007, Colizza and Vespignani, 2008, Balcan et al., 2010]. Thus, it is not rare to find them between the usual choices that were used to study the large-scale spreading patterns of the COVID-19 in different countries [Gatto et al., 2020, Bertuzzo et al., 2020, Calvetti et al., 2020, Arenas et al., 2020], as they allow for a detailed description of the greographical context and human mobility patterns, a key feature to understand epidemics [González et al., 2008, Ni and Weng, 2009, Balcan et al., 2010, Meloni et al., 2011, Dalziel et al., 2013]). Besides, unveiling which communities have a potentiality for becoming hotspots of the epidemic is crucial for policy making either regarding any kind of mobility restrictions or previsions in terms of medical preparations. This will be the main motivation for this chapter.

Based on this, a metapopulation model considers the different territorial subdivisions of a region as nodes, and the links connecting these nodes shape the structure of a network that act as the different means of transportation between the localities. This is, each link holds a weight that accounts for the flux of travelers and commuting between the nodes. Using this approach, one is able to differentiate between the most populated areas that act as hubs for human and economic activity, their surrounding localities that usually serve as dormitory towns and the rural areas, less populated and quiet. In other words, this set of nodes and links directly represent the spatial distribution of population. Within each node, it is nested an epidemiological model that should accurately describe the evolution of the infective dynamics. In our case, we will consider a deterministic reaction-diffusion model based on differential equations as the ones introduced in chapter 2. Different new variants of the SIR model were developed for the specific case of detailing the virulent spread of the COVID-19, and can be found applied for the cases of the city of Wuhan [Lin et al., 2020, Ndaïrou et al., 2020], China [Ivorra et al., 2020], Italy [Giordano et al., 2020] or Portugal [Silva et al., 2020], among others.

In our analysis, we will consider two important steps of increasing levels of complexity. First, we implement the model developed in [Silva et al., 2020] to the Galician network. It consists in a variation of the SIR model, with the inclusion of one compartment for Exposed yet asymptomatic individuals A and another compartment for Protected P individuals, introducing in the system the presence of non-pharmaceutical interventions such as isolations or social distancing. In the next step, we will consider an age-structure SEIR model more similar to the one in [Zhao et al., 2020] that divides the population into for age groups that mix and interact with each other, and we will implement it for the Spanish complete network of around 3000 municipalities.

Rather than providing an optimal fit to the incidence data on active cases, our goals were closer to those of [Calvetti et al., 2020], with the aim pointed towards the large-scale picture of finding which nodes were more likely to suffer an outbreak of the pandemic just by its situation on the network and socioeconomic reality. The particularities regarding the availability of data at different times of the pandemic and the quick pace with which new findings were being

USC DE COMPOSTELA

reported led us to considering significant variations from the model used in the Galician case to the Spanish one. These particularities will be explained in detail in each section. However, the important idea here is what is kept in common between the two case studies. In this work, we will use the main ideas derived from the applicability of the perturbation growth rates to trace Turing structures, in the study of epidemic spreading. We will derive the growth rates (GR) for each municipality, obtaining an estimator that defines the velocity and size of the epidemic outbreak. In this way, we relate the value of the GR with the risk that each node possess of developing a new outbreak. In this sense, this chapter is structured as follows. Section 7.2 describes the study case of Galicia. Within this section, we describe in detail the model used, how the mobility matrix is built and the derivation and calculation of the GR for this case. Beside them, a risk descriptor based on numerical simulations of the model is presented in order to assess the validity of the GR as a predictive tool. Afterwards, section 7.3 describes the study case of Spain. The age-structure model and a new mobility matrix based on commuting data is introduced, and again, the growth rates are computed for this model. The novelty of this section consists mainly in, after having proved the validity of the GR, assessing different confinement strategies regarding restrictions in the mobility and social mixing. Finally, section 7.4 concludes the chapter with a summary and the main results derived from the work.

7.2 Risk prediction for the Galician municipalities

7.2.1 Galician spatial network

Considering N_i and N_j to be the populations of any two localities i, j and t_{ij} the real travel-time distance in car between them, we define the weighted adjacency matrix of our spatial network as

$$M_{ij} = \frac{N_i N_j}{t_{ij}^2} = w_{ij} \tag{7.1}$$

With this undirected symmetric adjacency matrix, we are able to build a heterogeneous network where each node has a unique set of weights and connectivity pattern. In this way, we are modifying slightly the dynamics taking place at each node so it can account better for its unique properties. These weights attempt to model the flux of commuters from one node to another. In the absence of actual commuting census data, we considered more likely the exchange of travelers between heavily populated cities (the capital cities of the territories) and surrounding areas. We have considered the time distance instead of the geometrical distance because of the Galician orography as well as the road infrastructures, that eventually might result in significantly larger travel times between neighboring locations than the expected from their relative physical distance [Balsa-Barreiro et al., 2019]. In the case of the Atlantic coast, segmented because of abundant estuaries, travel-times from one city to the other in opposed locations of the estuary takes longer by car than it would take on a boat (the straightforward direction). Of course, we have considered the time distance by car since it is a more likely option for travelling than the boat one. These time distances were estimated using the Open Street Map API (`https://www.openstreetmap.org`), and all geographical and demographical information about each node is extracted from either the Galician or the Spanish Institutes of Statistics (`https://www.ige.eu`, `https://www.ine.es/`).

Regarding demographic and geographic data, Galicia is located in the northwest coast of Spain. It counts with 2.7 million inhabitants distributed in almost 30,000 square Kilometers,

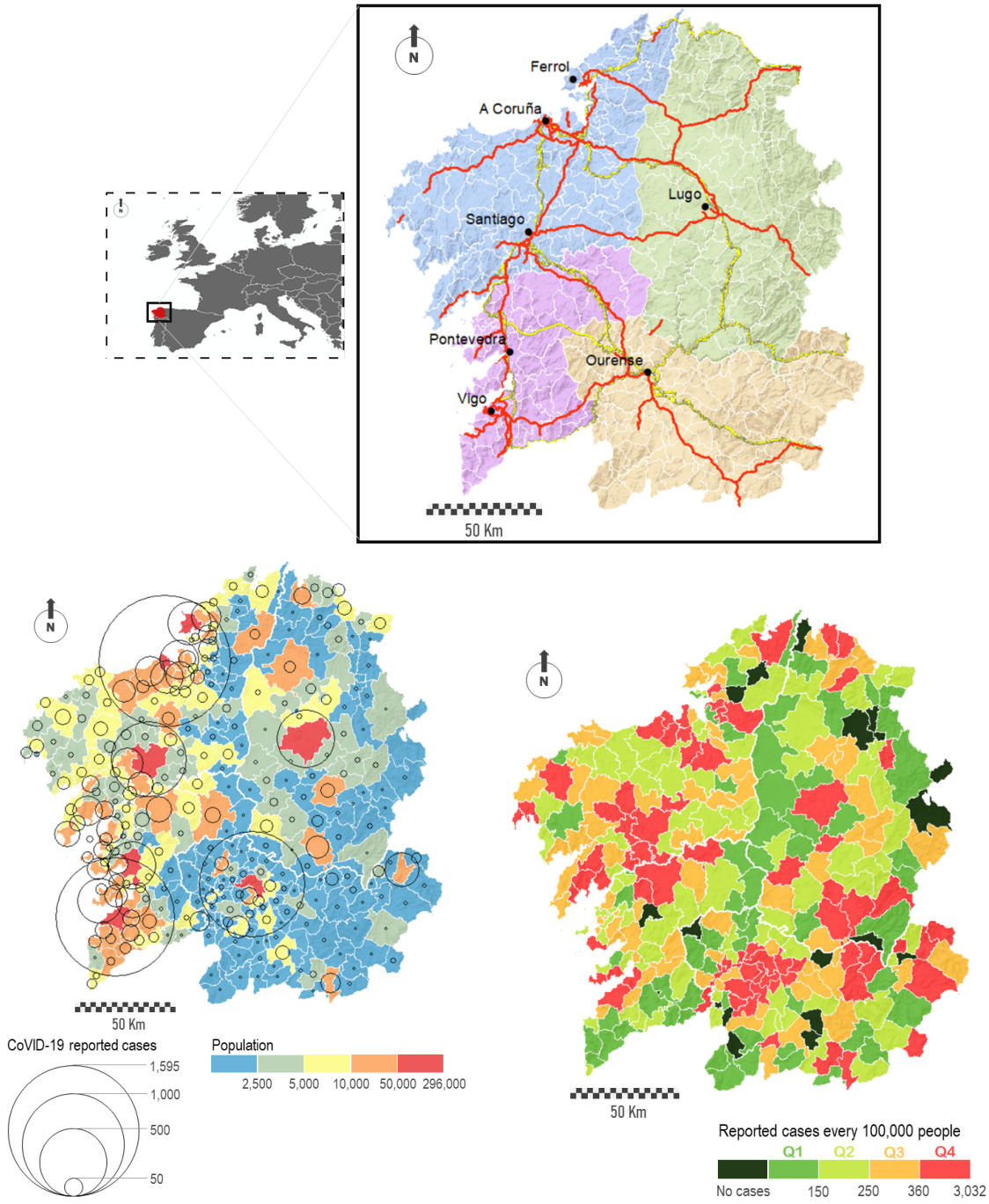


Figure 7.1: In the upper panel (a), location of Galicia within Europe and spatial subdivision of the territory into its elementary administrative units. In colored background is highlighted the distribution in provinces (second-level administration) and municipalities (third-level administration).The nodes of our spatial network will correspond to each one of this 313 municipalities. In the lower panels, we show the geographical spread of COVID-19 in Galicia at a municipal level: reported cases versus population (b), and Incidence rate (c). Here the colors are given by the colormaps. The maps are generated using ArcGIS Desktop software version 10.8 (from ESRI, `https://www.esri.com/en-us/arcgis/products/arcgis-desktop/overview`)

USC UNIVERSIDADE DE SANTIAGO DE COMPOSTELA

showing a population density of 91.3 people per square Kilometer. In administrative terms, it is divided into four provinces (second-level territorial and administration units) and 313 municipalities (third-level territorial and administration units), which will correspond to the nodes of our spatial network. The spatial pattern of population distribution is quite heterogeneous, with most of the population concentrating along the western coast, close to the so-called *Atlantic Urban Axis*, the area surrounding the AP-9 motorway that links northern Galicia with Portugal. In Figure 7.1(a) we show the spatial redistribution of the territory in provinces and municipalities, with the seven major cities highlighted in black and the highways in red; while in panel (b) we show the population distribution across the region (see colormap). There we can see that five of these seven are located along the commented western vertical axis. Vigo and A Coruña are the two most important cities with approximately 300,000 inhabitants each, while the others have populations between $60,000$ and $100,000$. The rest of localities hold populations of $< 30,000$, with the ones surrounding the metropolitan area of the capitals experiencing important increases in the last decades. In this way, the urban patterns shows a hierarchy dominated by the western sector, which presents in the surroundings of the Atlantic Urban Axis positive demographic dynamics both from a quantitative (higher fertility rates, positive migratory balances) and qualitative perspective (less aged population and more dynamic demographic structures). Just the opposite occurs in the eastern sector where the two main urban references are the two province's capitals, which concentrate a large part of the socioeconomic activity of their provinces. The rest of the territory, which is more rural in nature, is articulated based on a group of head towns that dominate large spaces, whose influence goes beyond their administrative units. In relation to this, another important socio-economic factor in Galicia is its close relation with the sea. In fact, along its more than 1,700 kilometers of coastline, it has 128 ports. Of which 122 are the responsibility of the regional government and 6 are managed by the Spanish government. The sea related activities in these ports is multiple and involves aspects ranging from purely fishing activities (deep-sea fishing activities, inshore, shellfish, commercial activities with loading and unloading of all kinds of merchandise), passengers (regular transport and cruises), recreational and tourist nautical activities. This generates a series of social and economic features that will have indirect consequences in the pandemic context as will be detailed below.

The territorial impact of the first wave of COVID-19 in Galicia (from around the beginning of March until June 2020) involved a total of 10,853 reported cases, with a clear spatial pattern that is displayed in choroplet maps in panels (b) and (c) of Figure 7.1. This data was provided by the Galician Health Service (SERGAS), the competent authority in health management in the region. On one hand, the geographical spread of the virus was clearly more significant in the western sector of the Atlantic Urban Axis, especially in the areas surrounding the major cities. Panel (b) relates the number of reported cases with the total population in each municipality, with reported cases being represented by proportional circles whereas the total population is distributed in five defined intervals, ranging from purely rural to urban municipalities (see colormap below). A priori, it is observed a strong spatial correlation between the total population and the number of reported cases in each municipality. Panel (c) on the other hand, represents the incidence rate of the disease, i.e., the number of cases every 100,000 people. Here, the previous affirmation is not only highlighted but we can observe also how the peri-urban areas surrounding the major cities acquire more prominence. This can be explained on one hand as many of these areas act as satellite towns where many of the people that work in the capital city live. On the other, in these locations there is also concentrated most of the

industrial activities.

7.2.2 Epidemiological network model

To describe the infection and transmission process of the COVID-19 pandemic, many different models have been considered and yet there is no clear consensus on how many compartments should the model contain. Increasing or reducing the number of compartments is often determined by the final goal of the research at hand. In our case, we model the epidemic spread across the subpopulations with the SAIRP deterministic model, a variation of the classic SEIR model that while maintaining certain simplicity was successfully applied in the case study of Portugal [Silva et al., 2020]. This model is composed of five differential equations that categorizes the human populations into five exclusive compartments, each governed by a set of transition rules. Basically, susceptible individuals S can become infected by interaction with either asymptotical A or symptomatic infected I individuals. This process occurs with a transmission rate β, for interactions with individuals of both categories. The asymptomatic ones become symptomatic infected with a rate ν, while symptomatic become removed or recovered with rate μ. The distinctive feature of this model compared to a typical SEIR is the category of protected individuals P. A fraction p of susceptible individuals becomes protected with a transition rate ϕ, but at each time step a fraction m of the protected individuals becomes susceptible again with a transition rate w. We believe that this factor offers a suitable approach for modelling the increasing measures of non-pharmaceutical interventions used to control the propagation of the virus observed in the current times, such as social distancing, protective facial masks or mobility restrictions.

This set of dynamics is now extrapolated and nested into each node of the spatial network. Thus, the population of each municipality is subdivided in all five compartments, with all individuals belonging initially to the susceptible compartment. Then, an initial seed of infected individuals is introduced randomly in the network and the disease propagates from there both locally and globally through the nodes of the network via the connections. The network interaction term only contributes positively to the transmission of the disease and represents both the interaction between susceptible residents with commuting infected individuals and vice versa. The larger the weight of the edge, the larger the amount of these interactions and the stronger the influence that highly infected nodes exert on their connections. Another parameter d was included in order to modulate the impact of these weights on the spreading dynamics.

The nonlinear differential equations that govern this model for any node i are then,

$$\begin{cases} \dot{S}_i &= -\beta_i(1-p_i)\left(\frac{A_i}{N_i}+\frac{I_i}{N_i}\right)S_i - \phi\, p_i S_i + wmP_i - d\beta S_i \sum_{j=1}^{n} M_{ij}\left(\frac{A_j+I_j}{N_j}\right) \\ \dot{A}_i &= \beta_i(1-p_i)\left(\frac{A_i}{N_i}+\frac{I_i}{N_i}\right)S_i - \nu A_i + d\beta S_i \sum_{j=1}^{n} M_{ij}\left(\frac{A_j+I_j}{N_j}\right) \\ \dot{I}_i &= \nu A_i - \mu I_i \\ \dot{R}_i &= \mu I_i \\ \dot{P}_i &= \phi\, p_i S_i - wmP_i \end{cases} \tag{7.2}$$

So far, the difference between nodes comes mainly from the connectivity term M_{ij} which is the one that contains the information on the population. Note that in equations 7.2 each infected

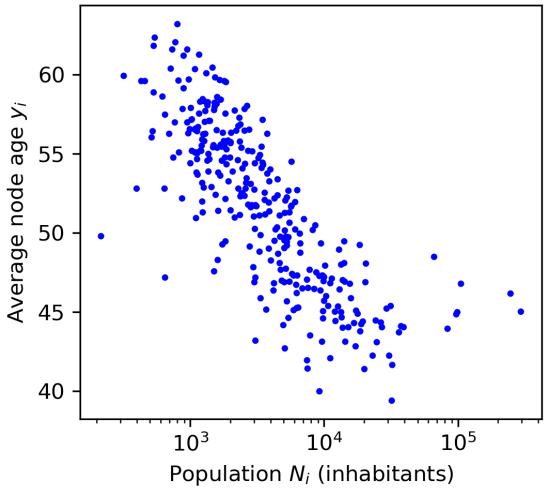


Figure 7.2: Average age y_i of each municipality in correspondence to node population. Data extracted from (`https://www.ige.eu`).

compartment is normalized over its own node population. This means that if each node were to evolve independently, the epidemic spread would be identical in each one. From contrasting with the data, this baseline mobility model was not sufficient to capture the infectivity patterns described previously in Figure 7.1 and so it must be refined. The reason behind this was already mentioned: there are many small villages that hold similar population levels but completely different from the demographic point of view. Especially, we have seen strong differences between those villages in the countryside and those located at the shore. As we commented earlier, localities at the shore have not only increased levels of economic activity caused by harbors and tourism but also because of the less aged, more active population. Idealistically, one would obtain each β_i from a fitting process to the data of each municipality. However, as we shall detail later in the Results section, for the case of the Galician network this was not possible as there was not sufficient available data at the time. Instead, we did a nonlinear fitting to the data at regional level in order to obtain an average infectivity rate β. In order to also account for the other demographical factors, we decided to incorporate additional layers of information that introduce slight modulations on the β and p parameters making them node-dependent. Notice however from equations 7.2 that for the network term coupling the municipalities, we leave the average infectivity rate β, since using specific transmission rates among municipalities was not feasible.

Layers of additional information

On one hand, we aim to relate the socioeconomic activity of a given node i with the average age of its population y_i. Attending to Figure 7.2 extracted from demographic data, we can see that there is a clear decreasing linear relation between the node population and its average age, and from what we already saw in the maps of Figure 7.1 the lesser populated nodes are found on the eastern rural areas of the region. We assume then that nodes with less aged population have higher rates of social mixing and physical interactions considering that in these nodes there would be more presence of schools and work-related activity. We incorporate this information

in the model by making the fraction of protected individuals p a function dependent of the mean age y_i as

$$p_i(y_i) = \begin{cases} \frac{1}{65} y_i, & y_i < 65 \\ 1, & y_i \geq 65 \end{cases} \tag{7.3}$$

Motivated by the dependence seen for $y_i(N_i)$, we considered as a first approximation also a linear dependence that increases with the average age of the location, saturating at the official age of retirement (65 years old), where it takes the value of 1. We are thus taking the assumptions that on one side elder individuals are more aware of the virus and take higher protective measures, and on the other that the more aged populations would also correspond to smaller, less active villages where people live in separated houses distributed across the village.

On the other hand, motivated by the previous observation regarding higher socio-economic activity in coastal cities, we considered for these nodes an increase in the infectivity rate β as

$$\beta_i = \beta + \beta_{port,i} \tag{7.4}$$

The list of municipalities that hold a harbor can be obtained from the government register of local portshttps://portosdegalicia.gal/gl/, from which we gathered a total of 41 localities that hold a significant harbor. Here we considered again the average age of each location, y_i, (extracted from demographic data) as an indicator of the level of economic activity in that coastal node. Here, we take again the assumption that locations with a higher average age will be inhabited by retired senior citizens, while younger populations will be more involved in busier activities that could imply a higher risk of infection. All this is incorporated in the term,

$$\beta_{port,i}(y_i) = \begin{cases} \beta, & y_i < 18 \\ \beta - \beta \frac{y_i - 18}{47}, & 18 > \quad y_i > 65 \\ 0, & y_i > 65 \end{cases} \tag{7.5}$$

In the rest of localities, we leave $\beta_i = \beta$, the one obtained from the parameter fitting.

Finally, we also accounted for an extra flux of travelers that may enter the region by plane. In Galicia there are three airports located in the cities of A Coruña, Vigo and Santiago de Compostela. The net flux of passengers could be only obtained monthly as a total number of travelers from the national air-traffic statistics (http://www.aena.es/csee/Satellite?pagename=Estadisticas/Home). For simplicity, we considered this flux to be divided equally within each day of the month and the incoming flux would the half of this total. The idea was to assume that in each daily flux of passengers there was at least a percentage of infected passengers according to the national incidence rate at that day. However, because at those times the flights were heavily restricted and infectivity rates were not very high, the net contribution of airplane travelers to the simulated incidence was almost negligible in comparison to the other sources.

The different layers of information considered helped to add the needed heterogeneity in the infection curves. This can be observed in Figure 7.3 where the local time evolution of the infected compartment is represented for a particular coastal node with the increasing layers of complexity from top to bottom. Left panels display the spatial distribution of the epidemic incidence. When the age or economic activity is incorporated (central panel), the effect becomes

USC DE COMPOSTELA

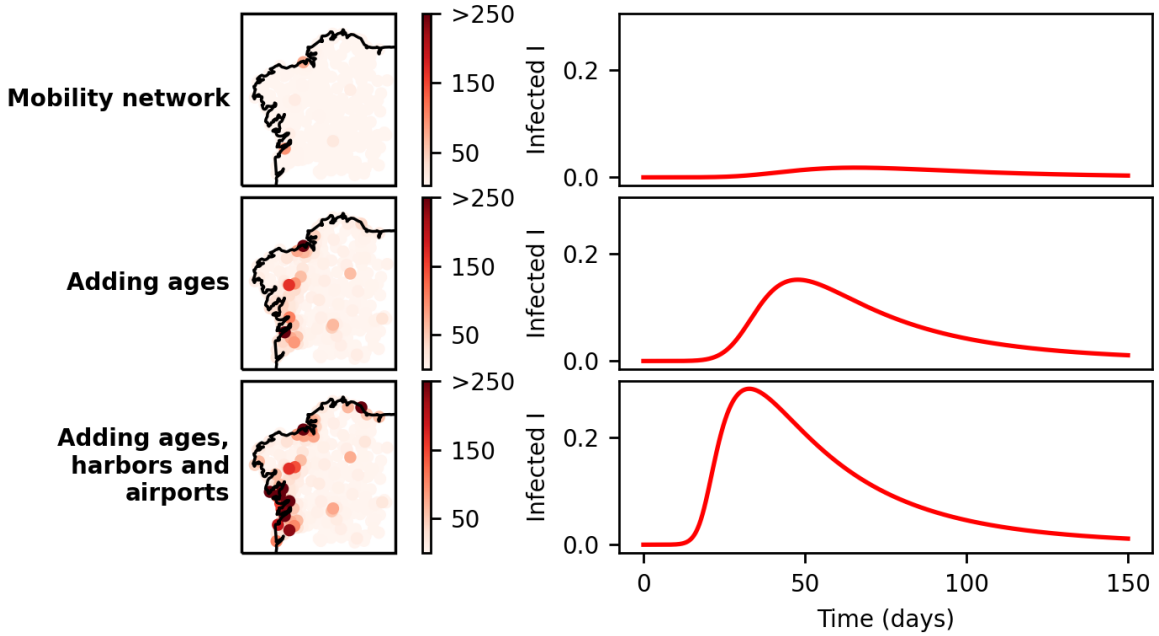


Figure 7.3: Different levels of complexity on the network model. The left panels show the normalized values of the infection peak for each one of the nodes, distributed spatially. The right panels show the time evolution of the infected individuals for one specific node, Burela, situated on the northeastern coast. To start the simulation, an initial infected seed was placed into each node.

more pronounced. Once the port activity is also incorporated, the description of the epidemic in the coastal areas becomes more complete. Observing the panel on the bottom left, it can be grasped the emergence of two main hubs of infection, both on the extremes of the western coast and mainly influenced by the two most populated cities in the region, Vigo (south) and A Coruña (north). Since these cities conform the main hubs of economic and industrial activity it could be expected that their urban and suburban areas would suffer the worst outcome of the pandemic, and this is mainly what the network model captures. Eastern nodes that are also highly affected by the pandemic (shown in brighter red on the map) belong to the capital cities of those provinces, and to high-activity harbor nodes on the north-eastern coast.

Simulation procedure for the risk determination

We devised the following scheme to obtain a statistical representation of those nodes that present the higher risk of developing an outbreak:

1. With all the individuals placed on the susceptible compartment, initiate the simulation with a seed of n_I infected individuals distributed randomly (with uniform probability) among all the nodes. This takes into consideration different scenarios from where the pandemic could have started, thus propagating quickly if all the initial seeds are in the urban hubs or slower if the first contact occured in a village.

2. Integrate equations 7.2 forward in time with a 4th order Runge-Kutta algorithm (see Appendix B for details), until the dynamics of the infection have totally died out. As a measure of the impact of the disease on each node, record the cumulative sum of its symptomatic infected individuals at the end of the simulation.

USC UNIVERSIDADE DE SANTIAGO DE COMPOSTELA

3. For each simulation run, sort the nodes as a function of this cumulative sum or total number of symptomatic infected individuals (from higher to lower) and keep for example, the first fifty nodes of each simulation (this is, the nodes with the larger number of symptomatic infected individuals)

4. Repeat steps 1-3 several times with different randomly-chosen initial seeds saving the ranking of most infected nodes until enough statistical significance is obtained.

5. From the complete list of rankings, count how many times each node appears among the whole list and sort them again in terms of this counting. Those nodes with a higher value count will be those assigned with the highest risk.

More precisely, we will use this count as a measure of the risk factor by normalizing them to the number of carried simulations. If the risk factor equals 1, it means that the node appeared among the top infected nodes in all simulations, while a risk factor of 0 means that the node was never among them.

7.2.3 Growth rates of the epidemic outbreaks

Here we will also introduce the idea of the *growth rates* obtained from linear stability analysis as possible descriptors of the node's potential of developing an outbreak. First of all, we can perform a simplification to the set of equations 7.2 considering that the total population of any node N_i is constant over time, this is, $S_i(t)+A_i(t)+I_i(t)+R_i(t)+P_i(t)=N_i$ at any time t. Thus, the number of recovered individuals can be computed at any time $t>0$ as

$$R(t)=R(0)+\mu\int_0^t I(u)du \tag{7.6}$$

In this way, the simplified SAIP model is described by

$$\begin{cases}\dot{S}_i=f(S_i,A_i,I_i,P_i)-d\beta S_i\sum_{j=1}^{n}M_{ij}\left(\frac{A_j+I_j}{N_j}\right)\\ \dot{A}_i=g(S_i,A_i,I_i)+d\beta S_i\sum_{j=1}^{n}M_{ij}\left(\frac{A_j+I_j}{N_j}\right)\\ \dot{I}_i=h(A_i,I_i)\\ \dot{P}_i=z(S_i,P_i)\end{cases} \tag{7.7}$$

where f, g, h and z denote the nonlinear functions of equations 7.2. We consider now a possible steady state of the system $(\overline{S}_i,\overline{A}_i,\overline{I}_i,\overline{P}_i)$, and introduce in each node a perturbation to this state,

$$(S_i,A_i,I_i,P_i)=(\overline{S}_i,\overline{A}_i,\overline{I}_i,\overline{P}_i)+(\delta S_i,\delta A_i,\delta I_i,\delta P_i)$$

where $(\overline{S}_i,\overline{A}_i,\overline{I}_i,\overline{P}_i)=(N_i,0,0,0)$, the state with all individuals in the susceptible compartment.

As we have done before, we obtain the time evolution of these perturbations linearizing the

USC UNIVERSIDADE DE SANTIAGO DE COMPOSTELA

system around the fixed point,

$$\begin{cases} \frac{d}{dt}\left(\delta\dot{S}_i\right) = \left(f_S - d\beta\sum_{j=1}^{n} M_{ij}\left(\frac{\overline{A}_j+\overline{I}_j}{N_j}\right)\right)\delta S_i + f_A\delta A_i + f_I\delta I_i + f_P\delta P_i - d\beta\overline{S}_i\sum_{j=1}^{n} M_{ij}\left(\frac{\delta A_j+\delta I_j}{N_j}\right) \\ \frac{d}{dt}\left(\delta\dot{A}_i\right) = \left(g_S + d\beta\sum_{j=1}^{n} M_{ij}\left(\frac{\overline{A}_j+\overline{I}_j}{N_j}\right)\right)\delta S_i + g_A\delta A_i + g_I\delta I_i + d\beta\overline{S}_i\sum_{j=1}^{n} M_{ij}\left(\frac{\delta A_j+\delta I_j}{N_j}\right) \\ \frac{d}{dt}\left(\delta\dot{I}_i\right) = h_A\delta A_i + h_I\delta I_i \\ \frac{d}{dt}\left(\delta\dot{P}_i\right) = z_S\delta S_i + z_P\delta P_i \end{cases} \tag{7.8}$$

where the subindex represents the partial derivative of the functions over the variables. Now, in this case, instead of using the Laplacian matrix, we consider directly that the perturbations can be decomposed along the spectra of the adjacency matrix M_{ij} without any loss of generality. This, we assume that the perturbation $\delta\mathbf{X_i}$ can be expanded over the set of eigenvectors $\Phi^{(\alpha)} = \phi_1^{(\alpha)},...,\phi_N^{(\alpha)}$ of $\sum_j^N M_{ij}\phi_j^{(\alpha)} = \Lambda_\alpha\phi_i$ as with the Laplacian matrix,

$$\delta\mathbf{X_i} = \sum_j^N c_\alpha e^{\lambda_\alpha t}\phi_i^{(\alpha)} \tag{7.9}$$

Substituting this in equations 7.8, we eventually reach the following eigenvalue problem

$$\lambda_\alpha\begin{pmatrix}1\\B_\alpha\\C_\alpha\\D_\alpha\end{pmatrix} = \begin{pmatrix} f_S - d\beta\sum_{j=1}^{n} M_{ij}\left(\frac{\overline{A}_j+\overline{I}_j}{N_j}\right) & f_A - d\beta\overline{S}_i\Lambda_\alpha & f_I - d\beta\overline{S}_i\Lambda_\alpha & f_P \\ g_S + d\beta\sum_{j=1}^{n} M_{ij}\left(\frac{\overline{A}_j+\overline{I}_j}{N_j}\right) & g_A + d\beta\overline{S}_i\Lambda_\alpha & g_I + d\beta\overline{S}_i\Lambda_\alpha & 0 \\ 0 & h_A & h_I & 0 \\ z_S & 0 & 0 & z_P \end{pmatrix}\begin{pmatrix}1\\B_\alpha\\C_\alpha\\D_\alpha\end{pmatrix} \tag{7.10}$$

In this case, solving analytically the previous system gets quite complicated as the resulting equation is of 4th order. Thus, we opt for solving the previous system numerically with the help of the linear algebra library of the `Python` package `numpy`, obtaining for each mode α a set of four different solutions λ_α. As we saw with the Turing instability, if any of these solutions satisfy that $\mathrm{Re}(\lambda_\alpha) > 0$, then the perturbation grows. Here we consider that the perturbation is a small number of new infected individuals and that, if it grows, it means that the perturbation has triggered an outbreak. Furthermore, the value of these *growth rates* will tell us how quickly it will evolve. Recording the maximum positive value of $\mathrm{Re}(\lambda_\alpha)$ for each node, we will use it as a reference hof how likely that node is to become reinfected.

7.2.4 Parameter estimation and model validation

In order to make the model the more realistic as possible, for the estimation of the parameters we used data at regional level from the start of the epidemic, around March 1st, until the end of the so-called *first wave*, around June 30 2020. This data was obtained from the Health Institute Carlos III (ISCIII)[1], which was the official national source for the temporal evolution

[1] `https://cnecovid.isciii.es/covid19/#documentacion-y-datos`

USC UNIVERSIDADE DE SANTIAGO DE COMPOSTELA

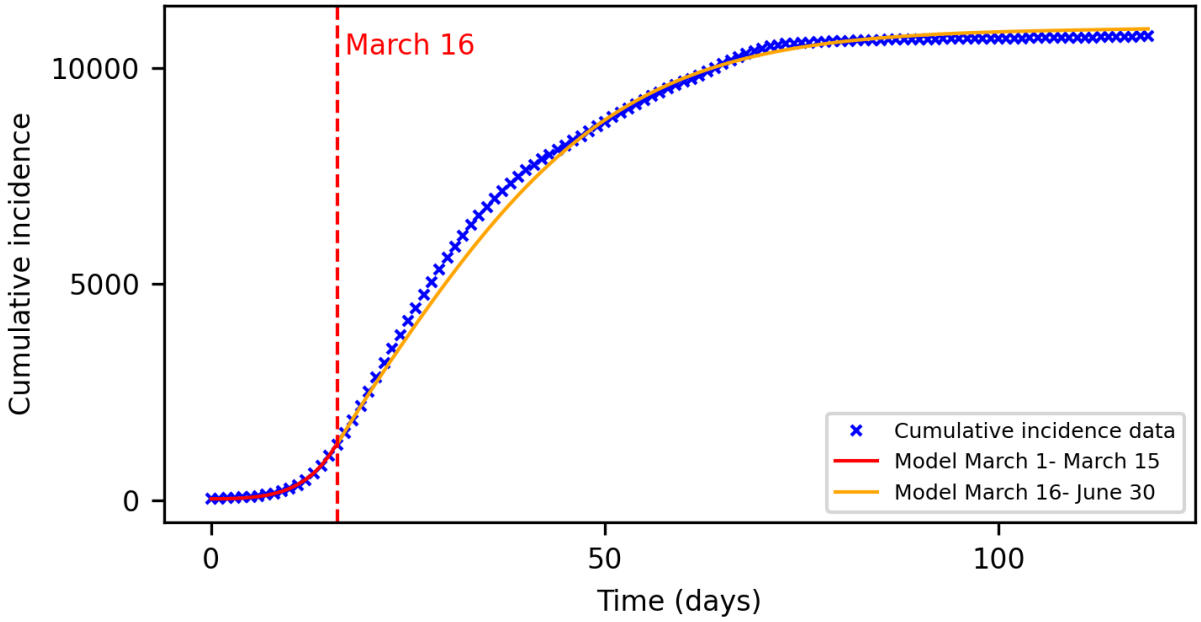


Figure 7.4: Estimated cumulative number of infected individuals with the SAIPR network model compared to the real cumulative incidence of the COVID-19's first wave, at the whole regional level. The fitting process of the model was separated on the two time-regions delimited by the vertical dashed red line, one before the start of the lockdown and one afterwards. The initial condition for the simulation was extracted from the first measured value of the dataset, with this number distributed proportionally among the four capital cities of the provinces plus the capital of the region (Santiago).

of COVID-19 in each region. When this work was first carried out, temporal municipality data was either not available or it lead to too large errors in the parameters to be accurate. Therefore, we opted for fitting the equations 7.2 to the cumulative number of infections at the regional level by means of a non-linear least squares minimization protocol. This is, we fitted the data to the sum of $\sum_{i=1}^{N}(I_i(t)+R_i(t))$ over the whole set of municipalities with the help of the `Python` function `curve_fit`. This fitting process involved integrating the system with all the layers of information and finding recursively the optimal parameters that minimized the deviation with the data. From this process we obtained the optimal values for the infective transmission rate β, the network coupling d and the fraction of people that leave protective measures m. Furthermore, from looking at the data (see Figure 7.4), we could see a clear turning point on which the daily incidence of the virus started to decelerate and to slowly decrease in time because of the strong lockdown measures imposed by the national government at earlier stages of the epidemic spread. With this in mind, we have considered two different time regions with its own set of model parameters, separated by the time when the lockdown started. The time duration of the second region goes until the isolation measures were strongly relaxed around the summer of 2020, three months later. The final result of this process is shown in Figure 7.4, alongside the obtained model parameters in Table 7.1. The initial number of infected individuals considered in the fitting was obtained directly from the first value in the dataset, which was $nI = 30$. Here, we distributed this initial cases proportionally along the regional capital cities for simplicity but the evolution of the epidemic spread has a significant dependence on the location of this seeds. This dependence is captured by the network model as we show in Figure 7.5, where the solid red line reproduces the average time evolution of the cumulative incidence over 1000 realizations of the system with the fitted parameters. This average recovers almost

Parameters	1st period (1 - 16 March)	2nd period (16 March - 30 June)	Reference
β	1.0692	0.3735	Estimated
m	0.2882	0.01	Estimated
d	1e-6	1e-6	Estimated
p	Age dependent (see subsection 7.2.2)		
ϕ	1/15 days$^-$1		Time until lockdown
w	1/75 days$^-$1		Time until lifting the lockdown
μ	1/30 days$^-$1		[Silva et al., 2020]
ν	0.15		[Silva et al., 2020]

Table 7.1: Summary of the parameter values used in our analysis. The first three, β, m and d were obtained from fitting to the cumulative incidence data at each time period.

exactly the fitted estimation of Figure 7.4, although we can see that the red shadow region representing the standard deviation of the sample is quite large. This sensitivity to the initial conditions will be also captured by our numerical risk descriptor, as we also consider a large number of system realizations to estimate the risk of each node (return to subsection 7.2.2 for the details).

7.2.5 Results

Following the procedures described in subsections 7.2.2 and 7.2.3, we estimated the chance that each municipality has of developing new outbreaks with the risk factors (RF) based on numerical simulations and the growth rates (GR) based on linear stability analysis. For both cases, we considered the complete model with all layers of information and the model parameters of Table 7.1. Looking at the maps displayed in Figure 7.6, panels (a) and (c) correspond to the RF and the GR respectively, along with the total cumulative incidence data of the COVID-19's first wave in panel (b). Note that for both the GR and the incidence data, we normalized each data series with its own maximum for the sake of comparison and that, for each case, the more intense the color the higher the value it represents. Doing the comparison between these maps we can see that both our descriptors capture really well the spatial patterns of the virus spread, especially taking into account that the infectivity rate β was estimated from the regional fit. The capital cities of each province which represent highly populated hubs of socioeconomic activity possess the higher risks of infection, increasing at the same time the risk values of surrounding less-populated areas. From this spatial distribution it can be highlighted again the contrast between the western "Atlantic Axis" near the coast that shows a significant stronger impact of the virus (and thus risk prediction), with the eastern municipalities where there was less reported cases and our descriptors also predict lower values of outbreak risk. In fact, those municipalities that are totally in blank refer to values of zero or almost zero for each case. Furthermore, our model is also able to differentiate between regions with specific local dynamics, such as the small region in the far north western coast named *"Costa da Morte"* where we can see decreased levels of infection. This could be related to a clear regression in demographic dynamic, despite being surrounded by the most dynamic axis in the region [BALSA-BARREIRO, 2013].

On the other hand, it may offer a clearest picture to analyze the previous distribution of

USC
DE SANTIAGO
DE COMPOSTELA

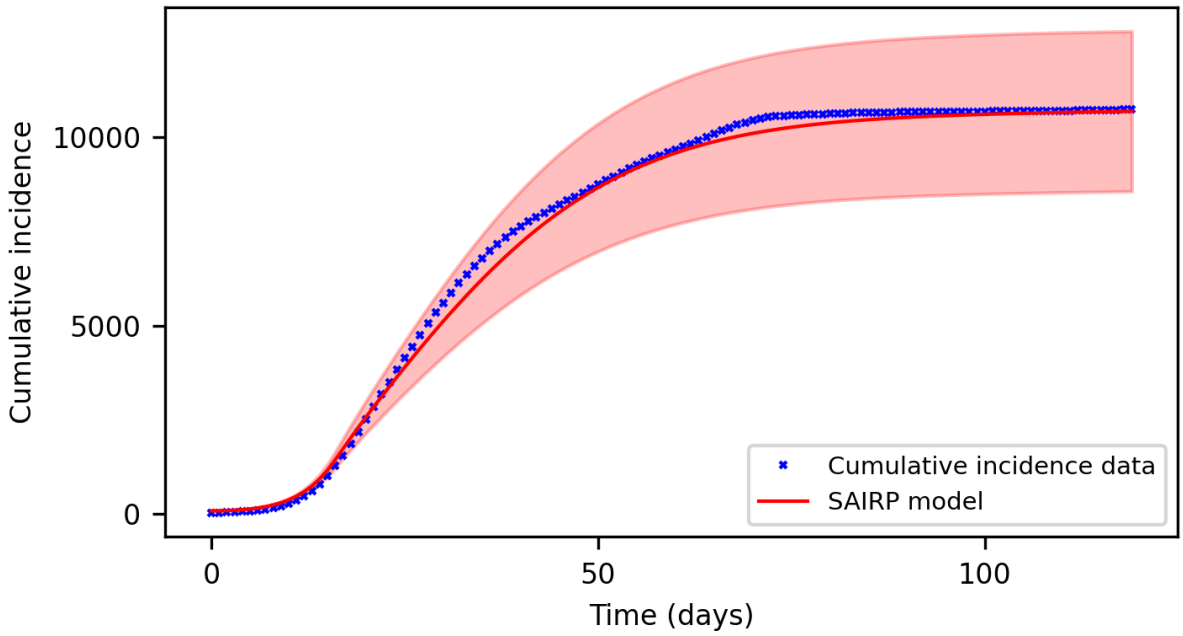


Figure 7.5: Time evolution of the cumulative infected individuals obtained with our fitted SAIRP network model over a 1000 realization of the initial state The red line represents the average over the sample, while the red shadow its the standard deviation.

estimators against the node's population (see Figure 7.7). In this case, we are showing also the total cumulative incidence of the pandemic's second wave (with estimated dates from August 1st to November 30th) in order to better assess the validity of our descriptors. This second wave involved, for the data considered, a total of 43569 reported cases, four times those of the first wave. Now, attending to the RF (the ones based on simulations, colored in red), for the most populated nodes, with $\sim 10^5$ inhabitants, they predict a value of 1 or near 1. This value means that independently on the initial conditions, these locations were always found between the top ones with most infected cases and that therefore, in case of new infections they are very likely to develop large outbreaks of the virus. It is interesting to see from the cumulative incidence data (see blue and orange marks in panel (a)) the behavior of these largest cities that in both cases reported (logically) the most number of cases. We can see, specially from the second wave, the clear exponential relationship with the population N_i, typical of epidemic processes. However, there are a couple of interesting peculiarities that highlight the unique socioeconomic features of each city. For example, notice that in both cases, the most infected node was the second to last, corresponding to A Coruña, while the previous four cities that possess very similar population ($\sim 1 \cdot 10^5$) are almost aligned vertically, also in both cases. Furthermore, the effect of the stronger isolation measures that were imposed during the first wave can be appreaciated from direct comparison of the two data series, especially in the two main populated cities where we could have expected a higher number of reported cases. In any case, we see that our RF captures well this abrupt difference between the main cities and the medium populated ones. For this latter region we actually see something very interest in our indicator. Here, our risk factor shows a plateau of municipalities with a significant value around ~ 0.3 that starts around $\sim 3 \cdot 10^3$ inhabitants and keeps going until $3 \cdot 10^4$, one whole order of population magnitude. This plateau makes sense considering that this descriptor was obtained from the top infective rankings where we took into account, for each simulation, the first 30

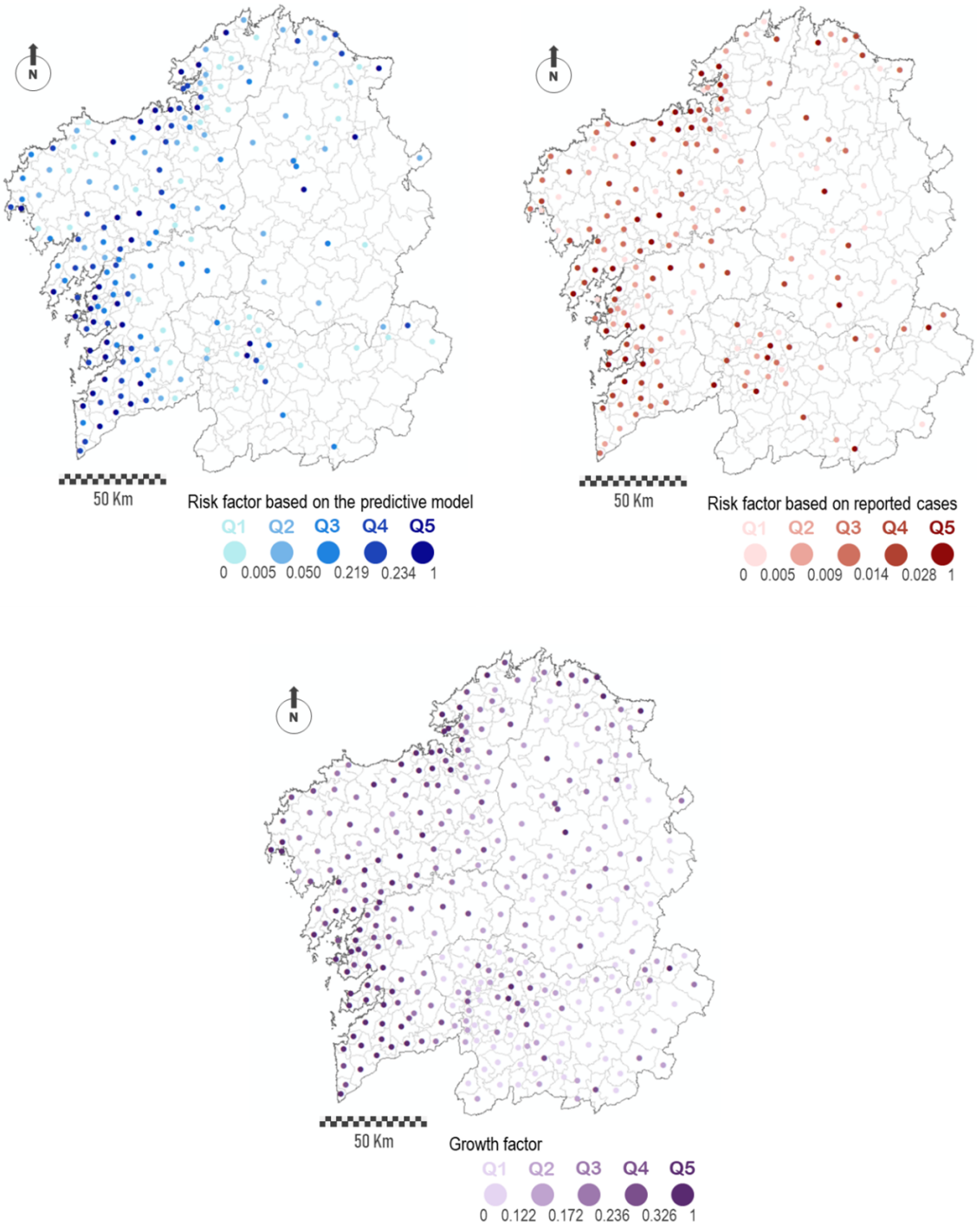


Figure 7.6: Spatial distribution of the risk factor (a), normalized cumulative incidence data (b), and growth rates (c) for each municipality. A value of 1 on the risk factor means that the node was found always among the top infected ones on each simulation. Following the same reasoning, a value of 0 means that that node was never found among the top ones. The ranking of the infective nodes was set with a total size of 30, and the cumulative incidence data was normalized over the highest value of reported cases. Maps are generated using ArcGIS Desktop software version 10.8 (from ESRI, `https://www.esri.com/en-us/arcgis/products/arcgis-desktop/overview`)

USC UNIVERSIDADE DE SANTIAGO DE COMPOSTELA

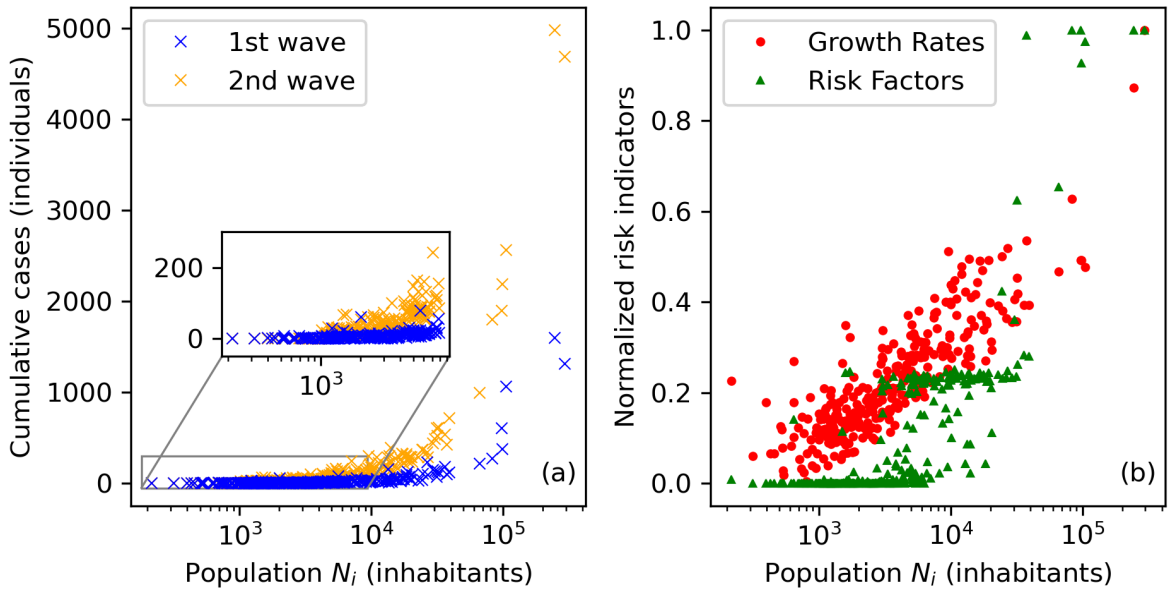


Figure 7.7: Comparative of the reported cumulative data from the first and second waves (a,blue and orange crosses) against the normalized risk indicators (b), i.e., the risk factors based on simulation (green triangles) and the growth rates based on stability analysis (red dots). Each point represents a different municipality, in increasing order of the population N_i (set in logarithmic scale).

more infected municipalities. In this sense, this value of ~ 0.3 tells that these municipalities ranked in the top 30 at least in one third of the simulations. We consider this descriptor to represent the risk of suffering a new outbreak because this information tells us that if the initial conditions would have been different, these municipalities would have at least a 30% chance of having suffered more from the virus. Finally, for a majority of nodes, mostly rural and low populated (less than 10^4 inhabitants), the risk of an outbreak was null or practically null and this can be easily contrasted with the reported cases (see the inset of panel (a)).

On the other side, the growth rates (obtained from the stability analysis and colored in green) seem to increase monotonically with the population, giving a more continuous description than the risk factors. In order to assess quantitatively the validity of our predictions, we have considerd the Spearman's rank [Zwillinger, 2014] to assess the correlation between the indicators and the data. This coefficient gives us a measure of how strong is the monotonic relationship between any two variables, making it ideal to compare the visible trends of our estimators. The correlation between the RF and the data of the first wave returns a positive value of 0.7195 suggesting that although not perfect, the model is able to capture at great extent the risk for each node. On the other hand, the correlation between the GR and the data is slightly better with a value of 0.7421, probably because of the continuous distribution of values. More surprisingly, these coefficients increase a few points when contrasting our risk estimators with the second wave, with correlation values of 0.7746 for the RF and 0.8091 for the GR. This confirms the robustness of the predictive capabilities of the model in an scenario where there was a significant larger number of incidence rates. This is especially true considering that we did not redo the fittings for this second wave. However, for further prediction of the consecutive waves this new fitting process could be desirable in order to increase accuracy. Furthermore, the Spearman correlation between GR and RF returned a value of 0.9567, implying a good agreement between the two quantities. Taking into account that the risk factors were evaluated

through intensive simulation in a high-performance super computer while the growth rates were calculated once from the analytical derivation in a laptop computer, we believe that this validates the GR as a very suitable approach with strong predictive qualities and very low computational cost.

7.3 Risk prediction for the Spanish network

Motivated by the findings of the previous work, and with the possibility of obtaining now temporal data and census mobility at the municipality level, we extrapolated our study to the whole Spanish network. For this case, previous assumptions as the weights of the mobility matrix M_{ij}, the local infectivities β_{ij} and the extra layers of information could be substituted directly by the data, making our approach quantitatively more realistic. With this in mind, we focus on the idea of the growth rates as descriptors of the municipality outbreak risk, as running the previous simulations for the whole Spanish network became problematic in terms of computational efficiency. Furthermore, as the growth rates include all the information on population, mobility and dynamical parameters, they constitute an excellent framework to test the effects of the previous quantities on our risk descriptors. In this sense, the focus of this second part of the chapter will be to implement restriction measures based on one side, on mobility lockdowns by territory, and on the other side on social mixing within each municipality.

7.3.1 Spanish spatial network

As we did with the Galician territory, we begin by examining the geographic and demographic aspects of the Spanish country. Administratively, Spain is fragmented into seventeen regions (so-called Autonomous Communities) and two autonomous cities with similar governmental status. All of them correspond to the first level of territorial administration, just after the central government. The second administrative level corresponds to provinces (50 in total), while the third one corresponds to municipalities (8,131). In the case of COVID-19 management, we must note that Spain is an administratively decentralized country with most of the relevant competences in health management transferred to the regions. While during the first wave (since COVID-19 emergence to around June 30th, 2020) the national government took charge of imposing the lockdown measures, the regional authorities mostly managed the successive waves considering the general guidelines suggested from the national government [Villalón et al., 2021].

According to the most recent census year (2021), Spain has 47.35 million inhabitants (`https://www.ine.es`). Uniquely four regions (Andalucia, Catalonia, Madrid and Valencia) concentrate around 58.8% of the population in the 29.7% of the total national area. The population density is about 92 people per km2, although spatially distributed in a very unbalanced way. Most of the population is concentrated in the coast, especially in the southern and eastern sectors, and some inland urban spots such as the metropolitan area of Madrid, besides a reduced number of cities with more than 250,000 inhabitants such as Zaragoza, Córdoba and Valladolid. In recent decades, the process of urbanization and concentration of the population has been very marked across multiple scales [Balsa-Barreiro et al., 2021], with more than 80% of urban population and 51% of people living in high-density agglomerations [Martínez et al., 2016]. At municipality level, 61.5% of them have fewer than 1,000 inhabitants

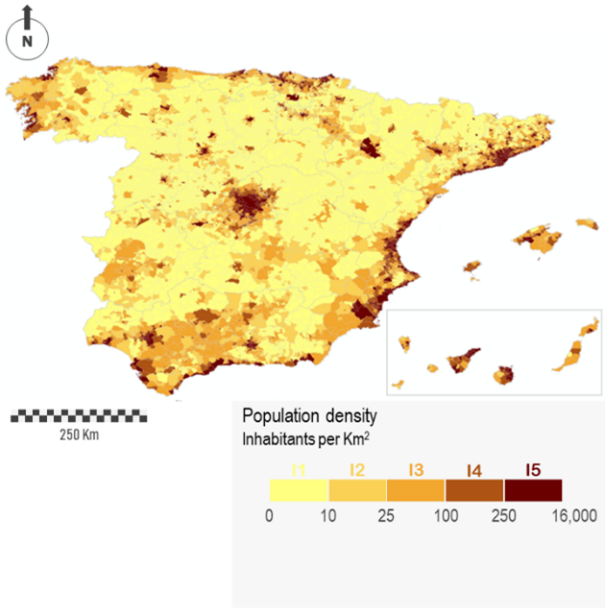


Figure 7.8: Population density of the Spanish region by municipalities.

and only 9.2% have more than 10,000 inhabitants. During the COVID-19 pandemic, the Spanish Statistical Office (in short, INE) periodically collected mobility data nation-wide (`https://www.ine.es/en/covid/covid_movilidad_en.htm?L=1`). A huge dataset with individual locations over time for more than 80% of cellphones was registered. People inflows and outflows were aggregated and presented across mobility areas. Thus, the whole country is spatially fragmented into 3,200 mobility areas, whose delimitation partially coincides with the municipal division. These mobility areas contain between 5,000 and 50,000 inhabitants. In depopulated regions, these mobility areas will be the sum of tiny, populated municipalities (less than 5,000 inhabitants), whereas in urban areas they correspond with urban districts.

In summary, we will run the mathematical model in the 3,121 most populated municipalities, which concentrate around 99% of the Spanish population. In this sense, the demographic data will be considered by municipalities, whereas the flows of people collected from the INE's mobility areas are estimated grouping or separating those mobility areas that do not territorially match the municipality area.

7.3.2 Age-structure epidemic model

Regarding the epidemic model, we opted here for an age-structured model that could be fitted to the data of each municipality. This means that the previous box compartments are now also subdivided according to age: less than 20 years old (AG1), 20-39 (AG2), 40-69 (AG3), and 70 years and older (AG4). All this together lead us to simplify the previous model considered for Galicia removing the protected compartment. Therefore, we go back to the SEIR model, susceptible (S), exposed (E), infected (I) and removed (R). Inside each one of the

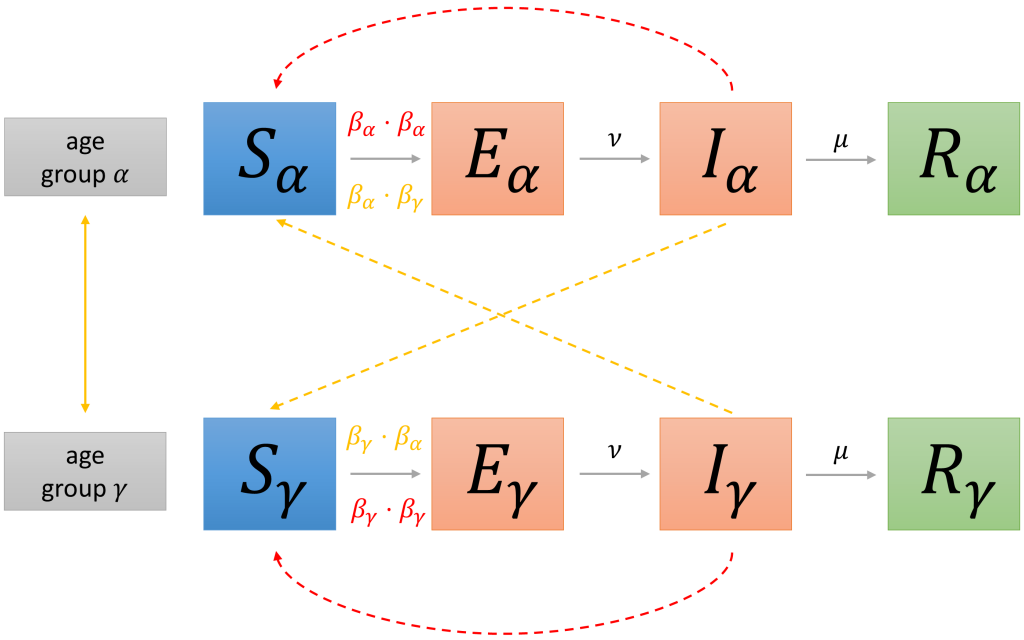


Figure 7.9: Compartments of the epidemic model for any two age groups α and γ. The solid grey arrows indicate the transition probabilities between compartments, the red dashed arrows indicate the interactions between infected and susceptible individuals of the same age group and the yellow dashed arrows the interactions among individuals of different age groups.

16 compartments, the main assumption is that the population is distributed homogeneously, but social mixing is allowed through different interaction rates between each possible combination of age groups, as in [Zhao et al., 2020]. On the other hand, the infection transmission here works as follows: susceptible individuals of any age in compartment l can become exposed at a rate β^{lr} via interaction with infected individuals of any age from compartment r. Exposed ones become infectious with rate ν and the infected ones are either removed or recovered with rate μ, as in the SAIRP model. This process is summarized in the flowchart shown in Figure 2.

Considering now that the previous dynamics are nested in each population i, the epidemic transitions for a given age group l at any municipality i are described by the equations

$$\begin{cases} \dot{S}_i^l = -\sum_{r=1}^{4} \frac{1}{2}\left(\frac{1}{N_i^l}+\frac{1}{N_i^r}\right)\beta_i^l \beta_i^r S_i^l I_i^r \\ \dot{E}_i^l = \sum_{r=1}^{4} \frac{1}{2}\left(\frac{1}{N_i^l}+\frac{1}{N_i^r}\right)\beta_i^l \beta_i^r S_i^l I_i^r - \nu E_i^l \\ \dot{I}_i^l = \nu E_i^l - \mu I_i^l \\ \dot{R}_i^l = \mu I_i^l \end{cases} \tag{7.11}$$

where the sum in r is performed over the four age compartments and $l = r$ is allowed. At this stage, the spatial distribution of the population is not yet included. As we now have good-enough data for the temporal evolution of each municipality, we fit this set of differential equations to the data of the pandemic's second wave. From each fit, we estimate the four

parameters β_i^l, one for each age group. Note that although the data is available for each age, similarly as it happened in the Galician case, fitting the curves to this high-resolution data was unsuccessful due to irregularities in the datasets. Therefore, the estimation was done at municipality level. Besides, the pairwise infective transmission rates β^{lr} were factorized into two separate terms $\beta^{lr} = \beta^l \cdot \beta^r$ to gain simplicity during the fitting process. This way, instead of pursuing a complex estimation of sixteen parameters at a time (the 4x4 elements of the β^{lr} matrix), we only need to fit four parameters simultaneously (note also that this fitting process had to be carried out for 3,121 nodes). The factorization of the infective transmission rates will also result useful for the computation of the growth rates. As a final note,the cumulative incidence data was again collected from the Health Institute Carlos III (ISCIII)[2] for the period covering the second wave that ranges from August 1st, 2020 to November 30th, 2020.

7.3.3 Metapopulation network and mobility map

Once the epidemic incidence across municipalities is estimated, we introduce a mobility-based coupling between each pair of communities, consisting mainly on people commuting among the different regions for whatever reason. This flux of mobile individuals between any two locations i and j is represented in the model by the quantity p_{ij}, then normalized by the local population in each community i, N_i. In order to consider different mobilities among the age groups, we define the matrix q_{ij}^l, whose elements follow,

$$q_{ij}^l = \begin{cases} 0 & i = j \\ r_l \dfrac{p_{ij}}{N_i^l} & i \neq j \end{cases} \tag{7.12}$$

where l refers to a specific age group and r_l is a control parameter that allows us to tune the relative mobilities among different age groups such that the age group l holds a percentage r_l of the total mobility. From this, we define the weighted connections of our new group-dependent adjacency matrix M_{ij}^l, which is directly built from the mobility fluxes q_{ij}^l,

$$M_{ij}^l = \begin{cases} \dfrac{1}{2}\left(1 + \displaystyle\sum_k^n (q_{ki}^l - q_{ik}^l)\right) & i = j \\ q_{ij}^l & i \neq j \end{cases} \tag{7.13}$$

In other words, in the same municipality ($i = j$), M_{ij}^l shows the proportion of people present at node i, taking into account those people of age l that leave node i, $\sum_k^n q_{ik}^l$, and at the same time those of age l that enter i from node k,$\sum_k^n q_{ki}^l$. The reason behind the factor $1/2$ is explained later. On the other hand, when $i \neq j$, M_{ij}^l directly represents the normalized flux of individuals

[2] https://www.isciii.es/QueHacemos/Servicios/VigilanciaSaludPublicaRENAVE/EnfermedadesTransmisibles/MoMo/Paginas/Informes-MoMo-2020.aspx

USC UNIVERSIDADE DE SANTIAGO DE COMPOSTELA

of age l from node i to node j. Thus, we can introduce the complete model,

$$\begin{cases} \dot{S}_i^l = -\sum_{j=1}^{n}\sum_{r=1}^{4}\left(\frac{M_{ji}}{N_i^l}+\frac{M_{ij}}{N_i^r}\right)\beta_i^l\beta_i^r S_i^l I_i^r \\ \dot{E}_i = \sum_{j=1}^{n}\sum_{r=1}^{4}\left(\frac{M_{ji}}{N_i^l}+\frac{M_{ij}}{N_i^r}\right)\beta_i^l\beta_i^r S_i^l I_i^r - \nu E_i^l \\ \dot{I}_i = \nu E_i - \mu I_i \\ \dot{R}_i = \mu I_i \end{cases} \tag{7.14}$$

The main idea behind the complete model is that susceptible individuals from node i and age group l can become exposed when they come into contact with any infected individuals of every age groups of node j, when they either travel to it (represented by the mobility term M_{ij}^l/N_j^l) or when the infected individuals from j are the ones traveling to i, M_{ji}^l/N_i^l. Population normalization is carried out by considering the population where the infective interactions take place. Although this normalization should consider the local variations due to daily mobility, we will assume for simplicity that these are negligible regarding the total population in each municipality

$$N_i^l + \sum_{j}^{n}(p_{ji}^l - p_{ij}^l) \sim N_i^l \tag{7.15}$$

Thus, we avoid intricate terms related to the derivation of the denominators (as will become evident in the next section). Notice that when we only check interactions within the same municipality ($i = j$), the mobility term is repeated and thus the $1/2$ factor in eq. 7.13. Also notice that, if we do not consider mobility between regions, $q_{ij} = 0$ for all i and j, then $M_{ij} = 1/2$ only when $i = j$ (otherwise its 0), recovering the single model used for fitting β^{rl} in eqs.7.11

With this model, notice that we can easily evaluate different possible scenarios by tuning either the force of infection of a given age group (β_i^l), the proportion of mobility corresponding to each group (r_l), or the mobility between different communities (q_{ij}). This means isolating a specific age group from the rest or to cut down the mobility across the country either by limiting interactions within the municipalities or selected groups of municipalities.

7.3.4 Growth rates in the Spanish network

In order to derive the computation of the growth rates for this case, we simplify the index notation and the summatory by combining all 4 ($n \times n$) adjacency matrices M^l into one, with dimension $(4n) \times (4n)$. This means that, in the complex network, each municipality is now split into 4 nodes, each representing a different age group. In other words, we had a network with four interconnected layers (one layer for each age group) and now we have condensed them into one where each pair of nodes has only a single link. With this transformation, equations

USC UNIVERSIDADE DE SANTIAGO DE COMPOSTELA

(4) become,

$$\begin{cases} \dot{S}_i = -\sum_{j=1}^{4} \beta_j I_j \beta_i S_i \left(\frac{M_{ji}}{N_i^l} + \frac{M_{ij}}{N_i^r} \right) \\ \dot{E}_i = \sum_{j=1}^{4} \beta_j I_j \beta_i S_i \left(\frac{M_{ji}}{N_i^l} + \frac{M_{ij}}{N_i^r} \right) - \nu E_i \\ \dot{I}_i = \nu E_i - \mu I_i \\ \dot{R}_i = \mu I_i \end{cases} \tag{7.16}$$

which are easier to work with from the point of view of our scheme. Again, we consider a perturbation in the form

$$(S_i, E_i, I_i, R_i) = (\overline{S}_i, \overline{E}_i, \overline{I}_i, \overline{R}_i) + (\delta S_i, \delta A_i, \delta I_i, \delta P_i)$$

where $(\overline{S}_i, \overline{E}_i, \overline{I}_i, \overline{R}_i) = (N_i, 0, 0, 0)$. As we have done so far, we expand the perturbations over the eigenvectors $\Phi^{(\alpha)}$ of the new adjacency matrix M_{ij}, with $\sum_j^n M_{ij}\phi_j^{(\alpha)} = \Lambda_\alpha \phi_i^{(\alpha)}$. The calculations of the growth rates for this model are included in Appendix B to avoid saturating further the chapter. There we perform the complete derivation of the growth rates with all the steps of the process. As we see there, in this case we can derive analytically the dispersion relation by solving the linear system for each mode α, obtaining two non-zero solutions for the growth rates given by

$$\lambda_\alpha = \frac{-(\mu+\nu) \pm \sqrt{(\mu+\nu)^2 - 4\nu(\mu - \beta_i N_i \Lambda_\alpha)}}{2} \tag{7.17}$$

Note that as with the Galician case, we will be interested only in the maximum values of the positive branch solutions, as they will be the ones to drive the perturbation. In fact, from eq. 7.17 we can derive exactly the critical condition that makes $\lambda_\alpha > 0$, which is given by

$$\beta_i > \frac{\mu}{\Lambda_\alpha^{max} N_i} \tag{7.18}$$

In other words, this defines the critical threshold at which an outbreak appears, revealing that the larger the population the easier the outbreak. Remarkably, note that the condition that we derived from our stability analysis is similar to the one for the SIR model, where the basic reproductive number is given by $R_0 = \beta N/\mu$ [Anderson, 1991]. Thus it is stablished a natural connection between the largest positive eigenvalue of our network Λ_α^{max} and the basic reproductive number as,

$$R_0 > \frac{1}{\Lambda_\alpha^{max}} \tag{7.19}$$

a relation that was observed before by [Chakrabarti et al., 2008] for the Kephart-White model [Kephart and White, 1991] in the context of computer viruses. In the general context, the basic reproductive number indicates the average number of secondary cases of infection produced by one primary case in a totally susceptible population. Thus, an infective agent spreads the disease if $R_0 \geq 1$, stablishing the condition for the epidemic threshold. As we shall see later, this condition will be fulfilled for almost all municipalities in the network, as our largest eigenvalue is in the order of $\Lambda_\alpha^{max} \sim 10^{-1}$.

USC DE COMPOSTELA

7.3.5 Results

Fitting the model and validation

We begin by estimating the age-group (AG from here on) infectivities β_i^l for each of the Spanish 3,121 municipalities by fitting equations 7.11 to the incidence data of the COVID-19's second wave. As we commented, at this step we do each fit separately, without taking into account the mobility network. In order to measure the goodness of each fit, we use the Pearson's correlation coefficient [Zwillinger, 2014] (with values ranging from 0 to 1 in function of the goodness of the fit), to compare the data from each AG with the simulated ones from the model. Their distribution, shown in Figure 7.10(b) for each AG, shows that for most municipalities the obtained β_i parameter is in good agreement with the data, finding correlation values around 0.8 or higher for most cases. In others, the fitting was unfeasible which was usually linked to municipalities with really low incidence or with data not smooth enough for the fitting to converge, achieving underestimated values for the $beta_i$ parameters. The latter was especially true for AG4, concerning people older than 70 years, where the data showed major differences from our simulated infection curves. From here on and for simplification, we shall refer to the group of people with ages between 0 and 19 as AG1 (age group 1), to people with ages 20-39 as AG2, people from 40-69 as AG3, and people with more than 70 years as AG4. On the other hand, on panel 7.10(a) we show the distribution of the estimated β_i over the populations N_i of each municipality. There we can see the huge dispersion on the infectivity rates across all levels of populations, having a large cloud of points between 0 and 0.5, specially at lower levels. This can be understood from the point of view of the previous section, where we showed that the unique geographic and demographic features significantly affect the evolution of the epidemic. Furthermore, the black dashed line drawn within each subplot represents the critical β_i^c from eq. 7.19 that is needed to obtain a positive growth rates, and therefore an epidemic outbreak. We see that this line is indeed crossed for almost every node, with the exceptions being in general those nodes that we were not able to fit (leaving $\beta_i = 0$). For the rest of the SEIR model parameters, we consider μ and ν from the geographical case study of COVID-19 in Italy [Bertuzzo et al., 2020], leaving $\mu = 0.0714$ and $\nu = 0.217$.

r_l (AG1-AG2-AG3-AG4)	0-19 (AG1)	20-39 (AG2)	40-69 (AG3)	70+(AG4)
0.1-0.4-0.4-0.1	0.7272	0.7916	0.7817	0.5345
0.01-0.49-0.49-0.01	0.7222	0.7933	0.7835	0.5342
0.2-0.3-0.3-0-2	0.7270	0.7905	0.7669	0.5363
0.25-0.25-0.25-0.25	0.7283	0.7894	0.7569	0.5370

Table 7.2: Spearman's correlation rank between the calculated GR (for each combination of the relative mobilities r_l) and the cumulative incidence data of each age group (AG). The relative mobility r_l represents the percentage of mobility that each AG holds to move freely between municipalities.

Once the local infectivity transmission rates β_i were estimated, we computed the distribution of growth rates (GR from here on) for each AG. The next control parameters to estimate are the relative mobilities of each AG (see eq. 7.12), this is, the fraction of commuting individuals that correspond to each AG. For this purpose, we adjust the relative mobilities r_l by comparing the GR obtained for each combination with the maximum values of cumulative incidence data and analyzing which outcome returns a higher Spearman's correlation. Again, we opt for this coefficient as the GR do not share a linear relation with the cumulative cases

USC DE SANTIAGO

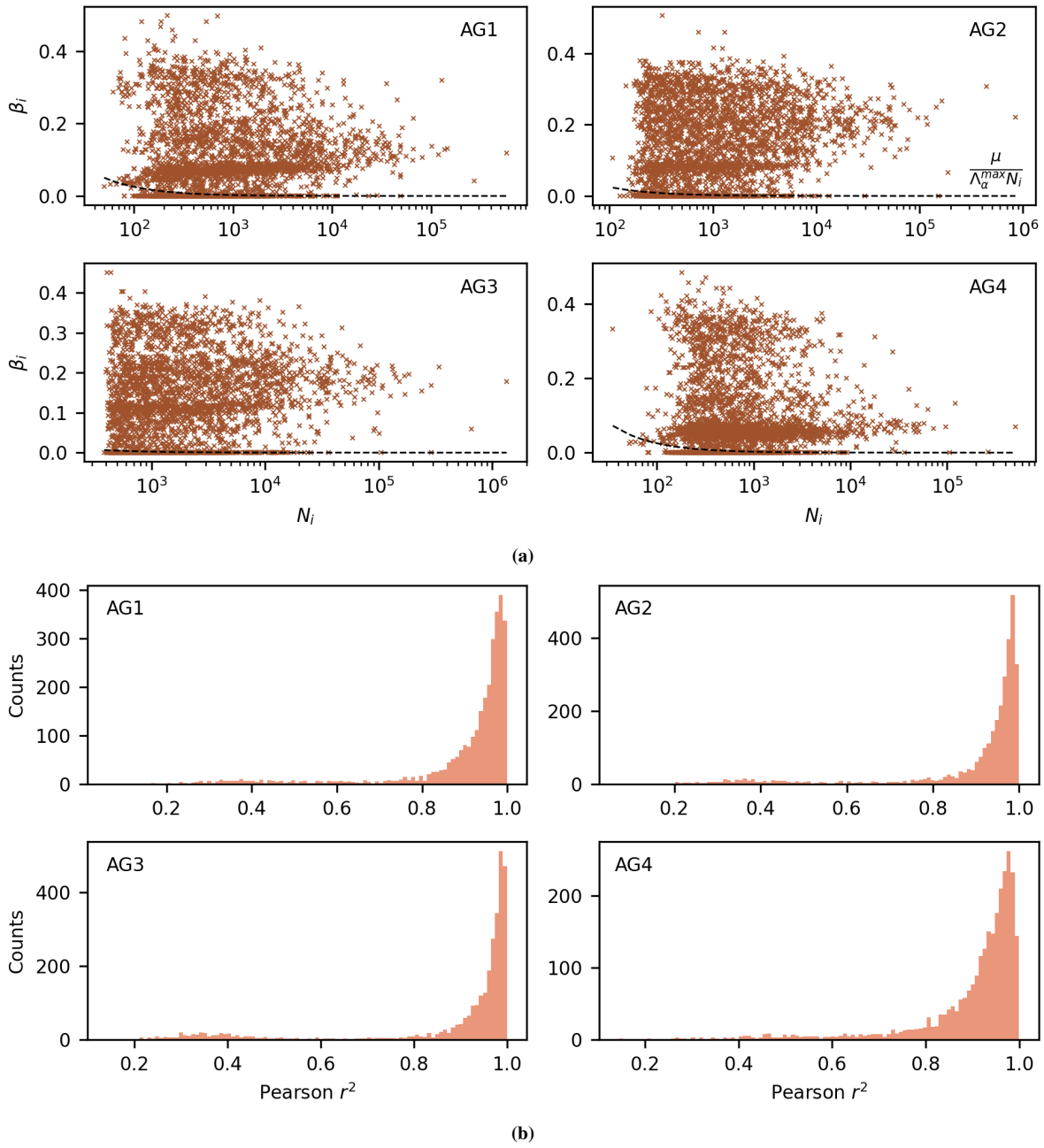


Figure 7.10: (a) Distribution of the fitted infectivities β_i over the populations N_i. The black-dashed line corresponds to the critical values defined by eq. 7.19 that state which nodes of the mobility network will have a positive value for the growth factos. (b) Distribution of the Pearson's correlation coefficients obtained for each age group, summing up to 3,121 fits, one for each municipality.

USC
UNIVERSIDADE DE SANTIAGO DE COMPOSTELA

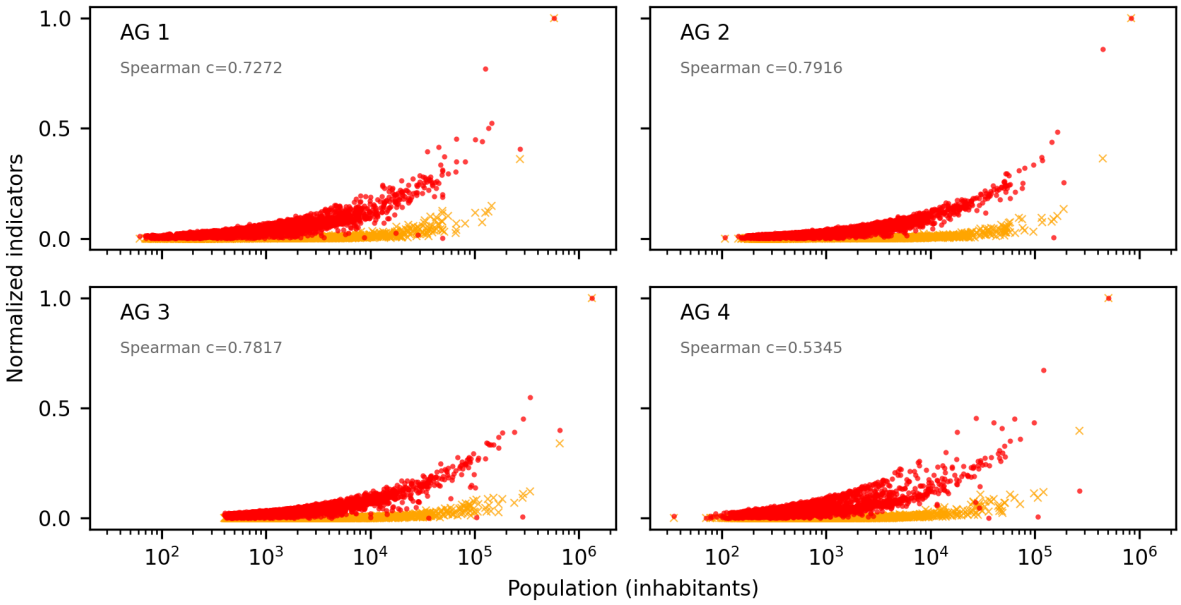


Figure 7.11: Sample distribution of growth rates (red) and maximum cumulative incidence data (black) against the node's population for the case with relative mobility of $r_l = (0.1, 0.4, 0.4, 0.1)$. Each variable was normalized to the maximum value its own series so the comparison could be feasible. Only a random sample of the 10% of the points are shown for visualization purposes

and thus the Pearson correlation loses applicability. Following the same trend as with the infectivities (Figure 7.10(b)), we obtained higher correlation values for AG2 and AG3 while medium ones for age AG4, as shown on Table 7.2 for different combinations of r_l. The latter can be understood as a result of the bad fittings for the infectivities. For this age group, there is a higher scattering in the GR values around the populations of 10^4 than in the incidence data, which induced the lower values in the correlation. Regarding the free parameters r_l, there were actually no significant differences between the tested combinations, at least attending to the correlation coefficient studied (see Table 7.2. In the following, we arbitrarily choose the combination $r_l = (0.1, 0.4, 0.4, 0.1)$ as the main one for our computations and further analysis, setting out a clear difference between the adult population (groups 2 and 3) which contains the main bulk of working population that is involved in periodic mobility patterns, from the retired elderly people and the younger individuals who are still attending school but may leave town on the weekends for whatever purpose. The GR distribution for this configuration is shown in Figure 7.11 where they are compared against the data of cumulative cases. Based on this comparison, the correlation values of Table 7.2 can be better understood.

From all this, we can conclude then that the growth rates constitute again an appropriate parameter to describe the pandemic risk at the municipality level and we shall use them as a framework to analyze different confinement strategies.

Spatial distribution of the GR

Regarding the spatial distribution of the growth rates across Spain (see Figure 7.12), they seem to be highly correlated to the spatial pattern of population distribution (see again Figure 7.8 for contrast). The metropolitan area of Madrid, the Mediterranean coastline (especially in the eastern sector) and certain areas located on the north coast concentrate the largest urban

regions. These urban regions with higher economic dynamism contain then the highest values of the growth rates. The inland provincial capital cities also emerge as isolated foci presenting significantly higher growth rates (scattered red points). Notice that the GR is able to trace this spatial patterns, presenting the highest values in the active population groups (AG2+AG3). From panel 7.12(d) we can observe that for AG4 the GR are consistently smaller across the country, mainly as a result of the smaller values in the infectivity β_i^4 as we saw earlier.

Now, as we are obtaining one distribution of growth rates for each age group it will be of interest (specially for the next section) to define a set of suitable statistics that can summarize all the information at hand. We opted for defining an "upper bound" of the distribution as an average of the ten highest growth rates and for considering the median value of each distribution. This gives us an idea of which are the highest values of the distribution (highest risk factors therefore) while reducing the bias of the most populated cities, which show exponential growing values. Thus, the upper bound anticipates how fast the outbreaks emerge in the most critical locations, whereas the median value shows the behavior in the majority of them. In Figure 7.13, we show these measures averaged over the four AG, for each one of the autonomous communities of Spain, that correspond to the first administrative subdivision. Here we can see that in general the maximum values of the GR (panel (a)) grow proportionally with the population, being therefore Andalucía (far south), la Comunidad de Madrid (center) and Cataluña (north east) the ones with highest GR. This could be also grasped from the previous maps. Now, regarding the medians of the distribution (panel (b)), we find that for the majority of municipalities in each autonomous community, the impact predicted by the GR is almost the same, although at medium levels of population (between 1 and $2{\cdot}10^6$ inhabitants) there are some communities that have equal or even higher median values than the most populated ones. The specific cases of Murcia and Canarias could be interpreted as statistical outliers, as it can be grasped from looking at the maps of Figure 7.12, that these communities have a smaller number of municipalities from which many have GR values over than 3 (thus painted in red) increasing therefore the median value.

Epidemic control with confinement measures

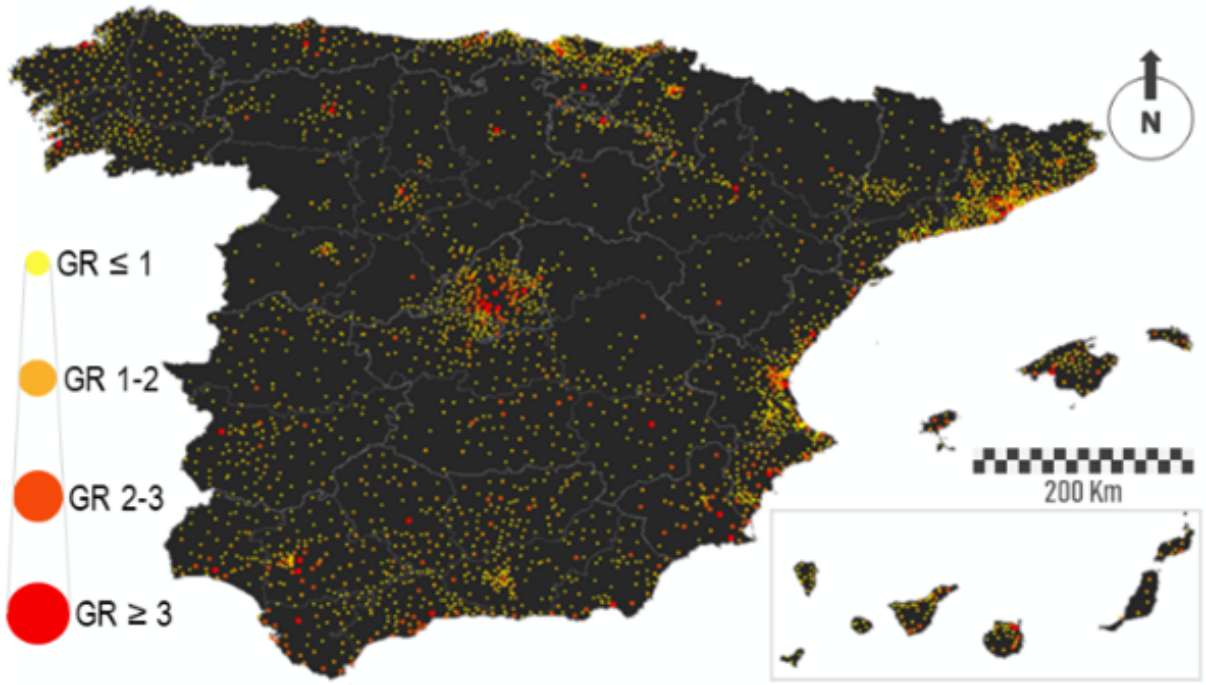
The implemented model allows two different approaches to halt a possible epidemic outbreak. The first one consists in severing the mobility across different scales nationwide modifying the mobility fluxes of matrix M_{ij} (and so the set of eigenvalues Λ_α of the network's Laplacian matrix that are used in the computing of the growth rates). The second one consists of removing or isolating a given age group (or a combination of two age groups) by turning their infectivity β_i^l to almost zero. The latter translates to these groups being unable to become carriers of the disease, so it could be interpreted either as a totally effective protection or simply a home isolation of the given group. Notice that this is different to equating the parameter r_l to zero since the latter means mobility among different municipalities and the former would also affect the infections at a local scale. Regarding the mobility scales, we remind that Spain is hierarchically subdivided into three different administrative levels (regional autonomous communities, provinces and municipalities). We will analyze then the effect of breaking down the mobility across these three different scales.

Attending to these considerations, we summarized in Figure 7.14 the effect on the GR of all the confinement strategies considered. Panel (a) of Figure 7.14 shows the averaged 10 maximums and the medians of the GR averaged over the four age groups in each one of

USC DE COMPOSTELA

the confinement strategies, considering the standard deviation from the mean as a dispersion' estimator. Panel 7.14(b) on the other side, breaks down all this information by age group, highlighting the impact of the different configurations in each one of the groups. Regarding the mobility restrictions, we observe that cutting the mobility down by provinces has a very small

(a) Age Group 1 (AG1)



(b) Age Group 2 (AG2)

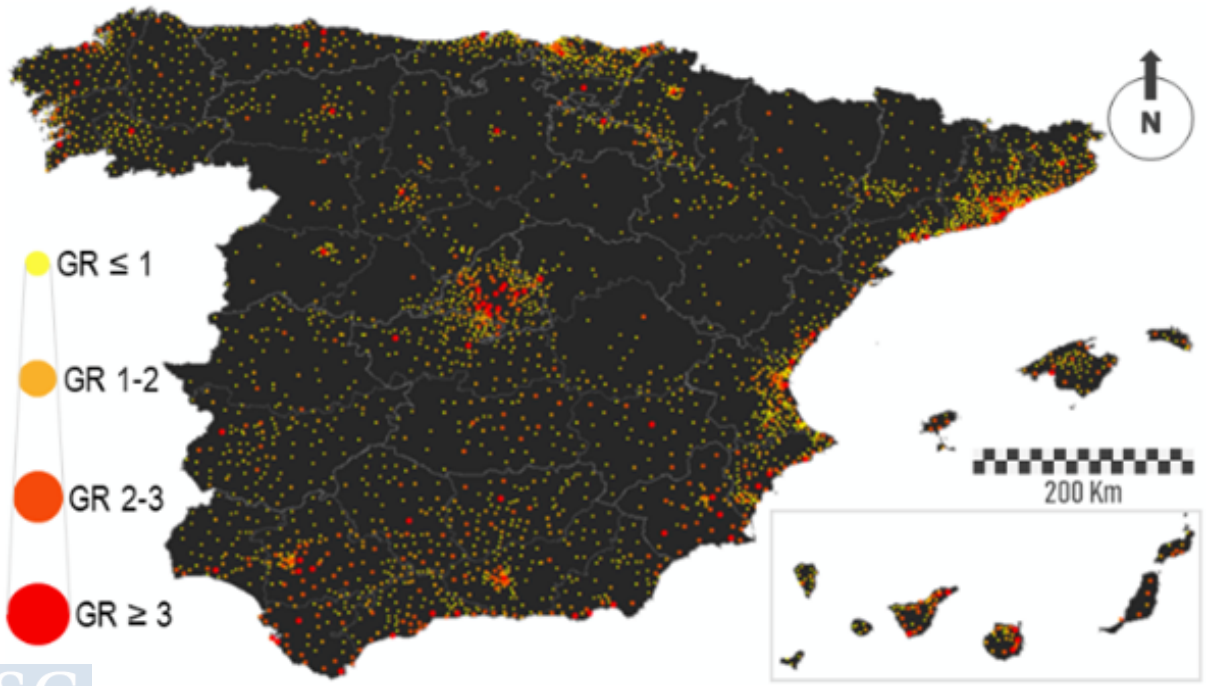
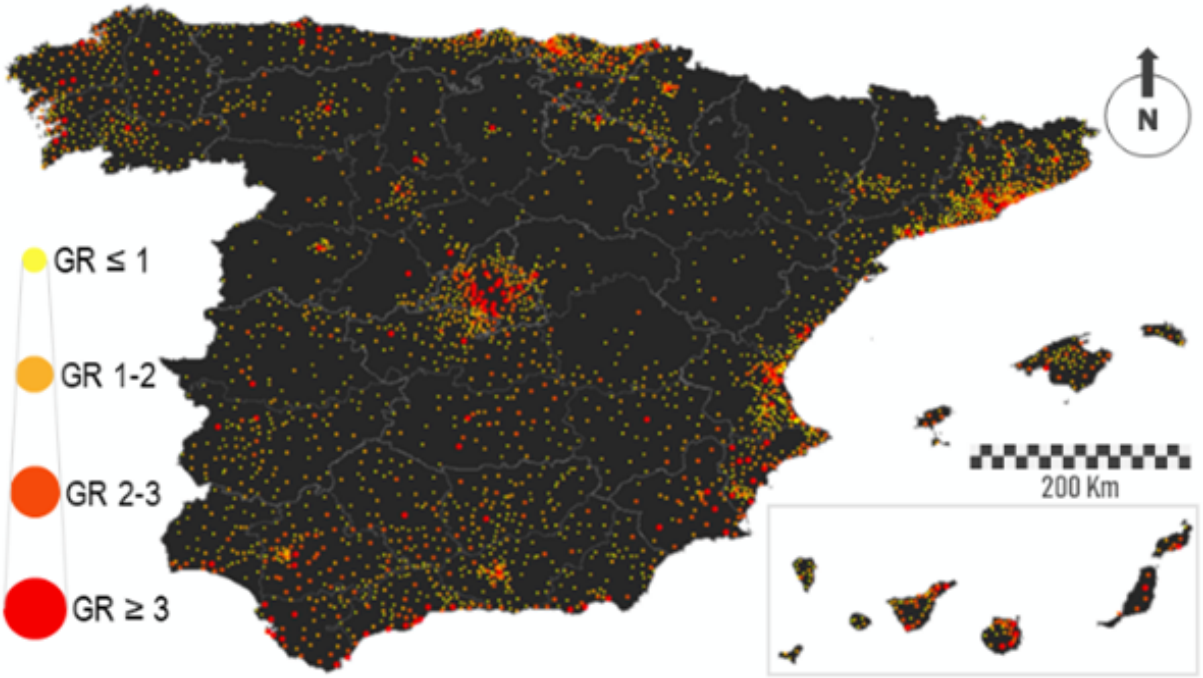


Figure 7.12: Spatial distribution of the growth rates by age group. Relative mobility between municipalities by age groups is fixed to (0.1, 0.4, 0.4, 0.1).

(c) Age Group 3 (AG3)



(d) Age Group 4 (AG4)

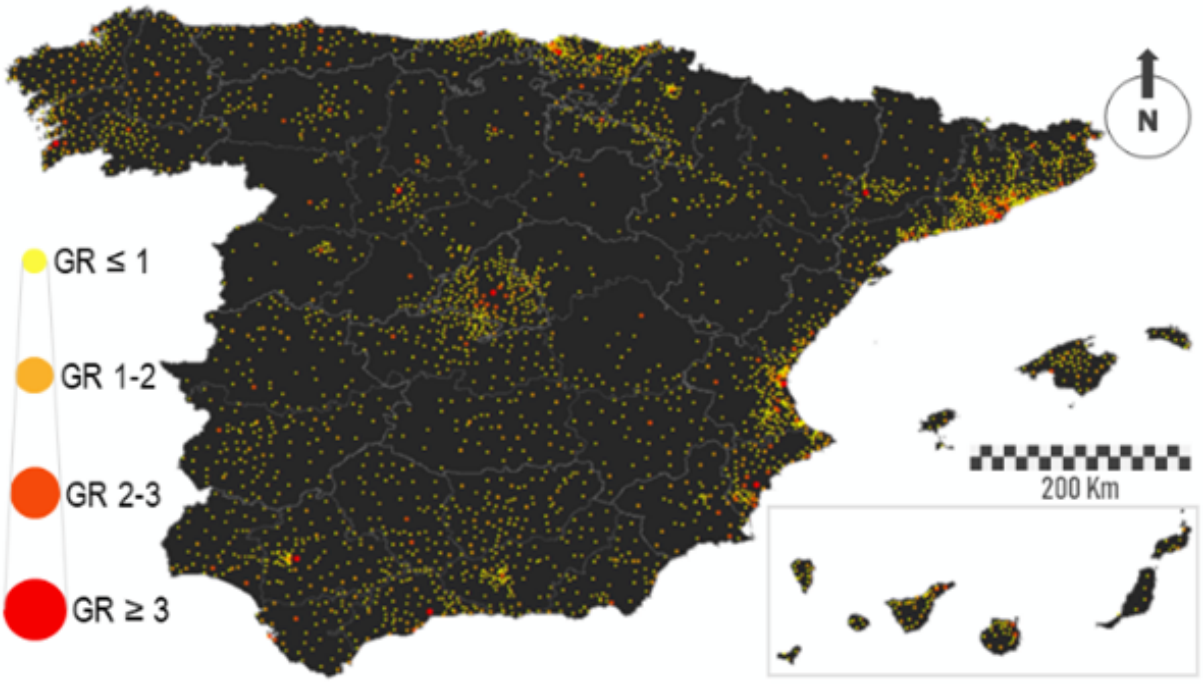


Figure 7.12: Spatial distribution of the growth rates by age group. Relative mobility between municipalities by age groups is fixed to (0.1, 0.4, 0.4, 0.1).

USC UNIVERSIDADE DE SANTIAGO DE COMPOSTELA

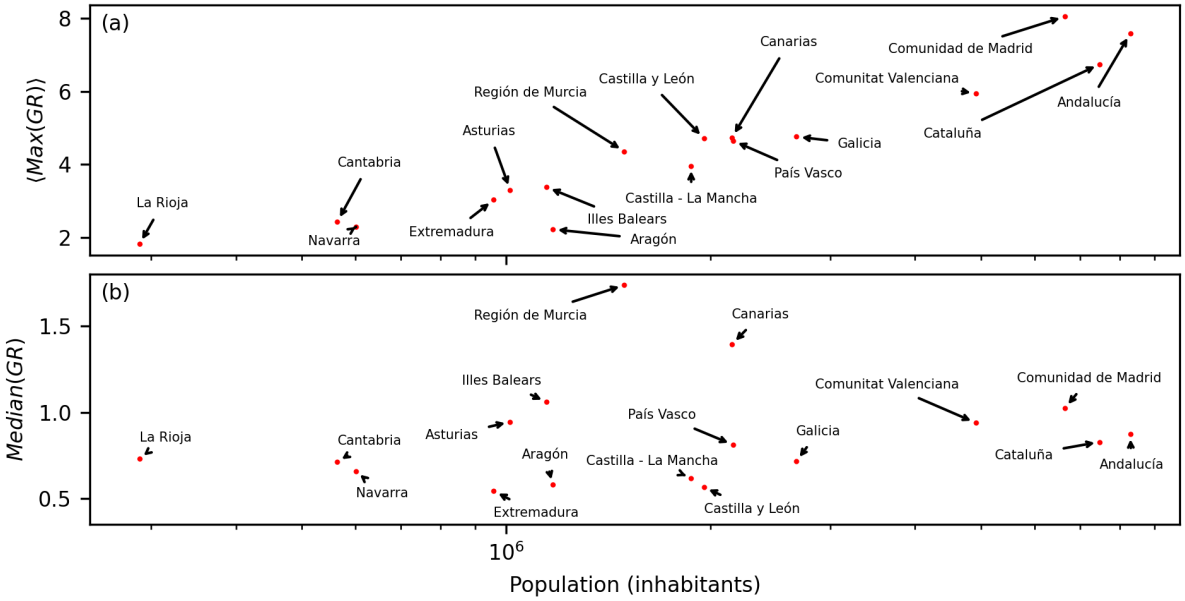


Figure 7.13: Averaged ten maximum values (a) and medians (b) of the GR distributions for each autonomous community. Each point show the average over the four age groups to simplify the visualization.

effect on the GR, while the control measure at local scales seems to be the most efficient, decreasing the overall risk in more than half in almost every scenario. The restriction by autonomous communities (AC) returns an almost exact outcome as the one by provinces, thus it appears overlapped in panel 7.14(a). We believe that this is related to the mobility data rather than a model prediction, since during the second wave there were still some restrictions to travel even among different provinces and thus the existing variations were not strong enough to induce a different outcome with our model.

Focusing now only on the protection by age groups, it is especially significant the impact that comes from isolating a combination of AG1 with any of the other groups. In absence of any kind of mobility restrictions (red line), while isolating separately AG1 or AG2 carries an important reduction of the GR, notice that the combinations of AG1 manage to decrease the overall GR distributions below the situation of local mobility restrictions with no age isolation measures (first point of the blue line). This is highlighted on panel 7.14(a) by the dashed black line, where we can also see that isolating AG2 and AG3 at the same time returns a similar outcome. In particular, from looking at both panels, the combination of AG1 and AG4 seems to be the one that best reduces the GR in the remaining age groups, very closedly follow by the combination AG2+AG3. While isolating a substantial portion of the population logically halts the virus spreading, it is interesting that the rest of the combinations with AG4 cannot achieve such improvements on the other age groups. Furthermore, looking more closely at the color maps of panel 7.14(b) it is noticeable that isolating separately AG3 or AG4 (or even the combination of AG3+AG4) leaves the values of AG1 and AG2 almost as in the case with none isolations at all. We believe that this could be mainly related to the fact that AG4 has in general lower transmission rates than any of the other three groups (see Figure 7.10), but it could be also slightly biased by the underestimation of some of these rates from the fitting issues commented above.

USC UNIVERSIDADE DE SANTIAGO DE COMPOSTELA

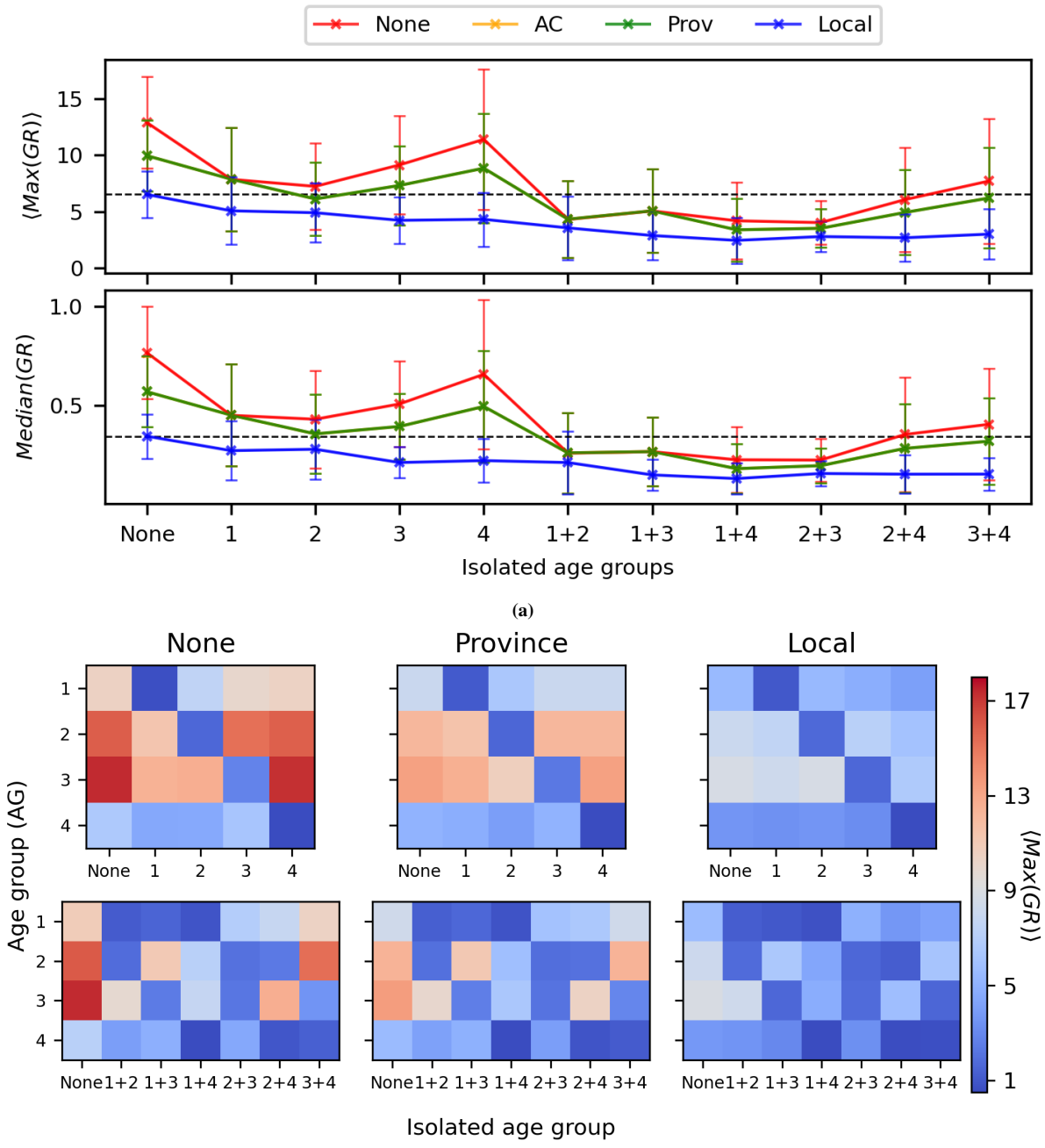


Figure 7.14: (a) Average of the 10 maximum values (a, upper panel) and the median values (a, lower panel) of the growth rates (GR) distributions for different scenarios of isolation and mobility restriction for different age groups. The points represent averaging over the four age groups and the error bars the standard deviation for each case. The black dashed line is drawn to guide the eye when comparing the two control measures at hand, this is, local mobility restrictions with no isolation to no-mobility restrictions with age groups isolation. It must be remarked that the mobility restriction by autonomous communities' results in a very similar outcome as the mobility restriction by provinces, so they appear overlapped. (b) Break down of the upper panel over all the age groups and in a color-coded map. The numbers on the x axis refer to isolation of a single or a combination of age groups, while restrictions to the mobility are shown in different colors (a) and consecutive columns (b). Relative mobility between municipalities is fixed to $r_l = (0.1, 0.4, 0.4, 0.1)$.

7.4 Summary and conclusions

In this chapter, we have modelled the geographic spread of the COVID-19 across the Galician and the Spanish whole territories during the first and second waves of the pandemic. For each case, we have detailed different schemes that allowed us to estimate the impact of the viral disease in each one of the municipalities that conform the territory. In the Galician study case, have analyzed mainly the first wave of the pandemic, where estimating exactly the infectivity of each single locality was unfeasible due to lack of data. Therefore, we used demographic data based on the average age and the presence of harbors to give each node a set of particular features. Furthermore, we considered the population of each locality and the travel distance by car between them to stablish the weights of a mobility matrix. In the Spanish study case, we focused on the data from the second wave and managed to fit an infectivity parameter β_i for each single locality, recovering the particular features of each node directly from the fit. Regarding the mobility matrix, for this case there was available national mobility data based on commuting individuals during the pandemic that we used for building the matrix. In both cases, we reproduced to a great extent the spatial patterns of the epidemic spread, with our final results being in good agreement with the data.

As the main conclusion, we have presented here a mathematical descriptor based on the differentiated infective dynamics and the spectra of the mobility matrix with the aim of predicting the infective risk map across municipalities. The aim of this approach lies in developing and efficient tool in which several scenarios can be simulated while keeping the computational cost minimized. In the study case of Galicia, we introduced the growth rates (GR) in contrast to extensive simulations of the network metapopulation model, showing the validity of this approach for the study of epidemic spreading. Afterwards, we extrapolated this approach to an age-structured model at national scale, and used it to examine different confinement scenarios. One of the main results from this analysis shows that isolating individuals younger than 19 (AG1) shows a particular impact on the GR, especially when the isolation restrictions are combined with any of the other groups. In fact, the combination of the latter with the eldest people (AG4) seems to be the one to reduce the most the risk factors in the other remaining groups; closely followed by a combined isolation of AG2 and AG3, that is, between 20 and 69 years old. However, the latter would imply a total freezing of the population's active sector that would be one of the less desirable outcomes. On the other hand, our mobility analysis shows that, given the mobility traffic allowed during the second wave, only restrictions adopted by municipalities would have significantly reduced the risk of new pandemic outbreaks. Furthermore, by combining all the control measures by mobility and age, one of the key implications of our model is that the already discussed combination of AG1 with any other achieves a further reduction in the risk factors than imposing local mobility restrictions across the whole country. This could suggest that efficiently protecting AG1 and AG4 simultaneously while allowing AG2 and AG3 to pursue their normal activity would achieve one of the optimal scenarios with the ongoing pandemic. Although our model does not incorporate a time variable and therefore is not able to predict for how long these restrictions should hold, it points the direction towards new insighst and opens the door to new ways to explore.

USC UNIVERSIDADE DE SANTIAGO DE COMPOSTELA

USC
UNIVERSIDADE
DE SANTIAGO
DE COMPOSTELA

Chapter 8

Coupling opinions with epidemic models

The previous chapters dealt with opinion models and epidemic models separately, carefully studying the effect of the network topology in the dynamics of each one through means of the adjacency matrix's spectra. In this chapter, we move forward and consider the effect of opinion on the propagation of an epidemic in order to estimate the impact of adhering to public health recommendations such as social distancing measures.

Part of the text and figures for this chapter are reproduced from the following publications

* Carballosa, A.[1,2], Mussa-Juane, M.[1,3] & Muñuzuri, A.P.[1,2] *"Incorporating social opinion in the evolution of an epidemic spread"*. Scientific Reports 11, 1772 (2021). `https://doi.org/10.1038/s41598-021-81149-z`.

* Carballosa, A.[1,2], Mussa-Juane, M.[1,3] & Muñuzuri, A.P.[1,2] *"Social Opinion Influence on Epidemic Scenarios"*. In: Agarwal, P., Nieto, J.J., Ruzhansky, M., Torres, D.F.M. (eds) Analysis of Infectious Disease Problems (Covid-19) and Their Global Impact (2021). Springer, Singapore. `https://doi.org/10.1007/978-981-16-2450-6_21`, Chapter 22, p. 465-482.

* Silva, C.J., Cruz, C., Torres, D.F.M., Muñuzuri, A. P., Carballosa, A. et al. *"Optimal control of the COVID-19 pandemic: controlled sanitary deconfinement in Portugal"*. Scientific Reports 11, 3451 (2021), eISSN 2045-2322. `https://doi.org/10.1038/s41598-021-83075-6`

[1] Group of Nonlinear Physics, Faculty of Physics, University of Santiago de Compostela
[2] Galician Centre for Mathematical Research (CITMAGa), University of Santiago de Compostela
[3] Galician Supercomputer Center (CESGA), University of Santiago de Compostela

8.1 Introduction

How does the opinion of the society affect the spreading of a viral disease? During the recent COVID-19 pandemic, non-pharmaceutical interventions (NPI) such as social distancing, closures, higher levels of hygiene or wearing a face mask proved to be key in preventing the propagation of the disease [Perra, 2021, Prem et al., 2020, Cowling et al., 2020] but despite of this, many surveys (see f.e.[Kasting et al., 2020, Lüdecke and von dem Knesebeck, 2020, Muto et al., 2020, Xu et al., 2020b, Gray et al., 2020]) identified that although there was a

general disposition to adopt these measures, a significant number of population was still not adhering to them for many different reasons. As a consequence, it could be expected that when these measures were not enforced by the government, each individual would be left to their own opinions on whether to apply them or not. In this way, a real polarized spectrum of opinion emerges, and we attempt here to highlight its repercussion by incorporating it into an epidemic spreading process occurring on a network. The idea is the following: nodes are endowed with an opinion value that will alter the infectivity patterns, the more likely the given node is to adopt the NPI, the less probably is that the node will become infected. Similar ideas where there is an interplay between polarized opinions and epidemic spreading have been implemented before in relation to being pro or anti vaccination [Alvarez-Zuzek et al., 2017, Pires et al., 2018].

As an overview of the chapter, we first explain our approach to gather data from social media at different moments in time and reconstruct it in the form of a complex network. Then, we generate an opinion distribution for each network using an opinion model whose dynamics reflect the potentiality of each nodes to change its baseline opinion and adhere to a new one. In this case, the desired new opinion would be to follow the public health recomendation adhering to social distancing and other NPI. Then, we will incorporate these opinions into an stochastic SIR network model, studying which control parameters and opinion states are better or worse to halt the epidemic spread. As the methodology of this chapter contains several layers of information and middle steps, we present a summary diagram in Figure 8.1.

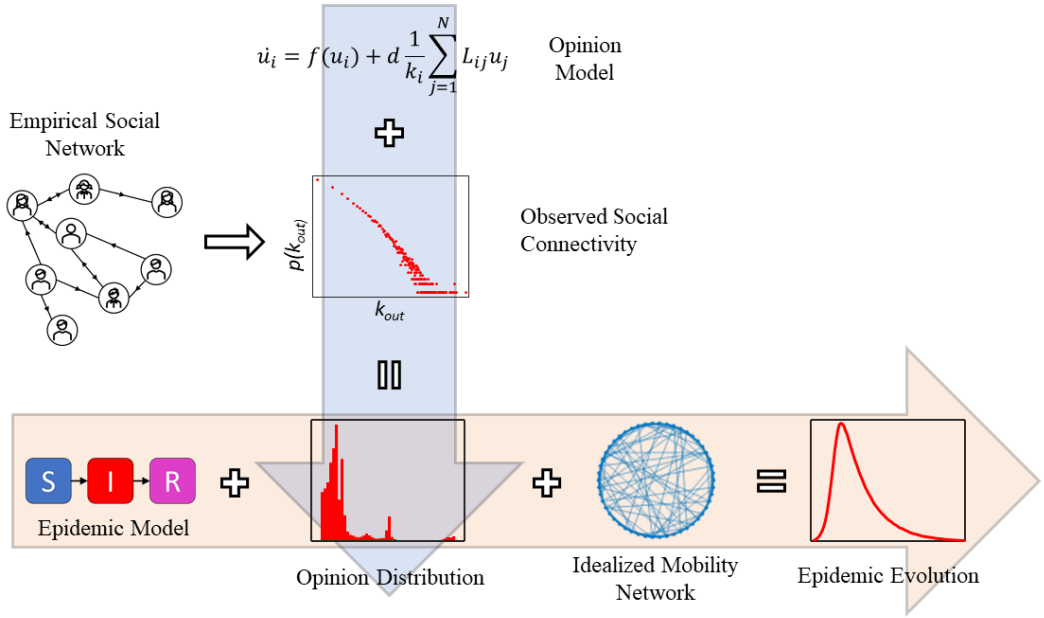


Figure 8.1: Summary of the methodology of our approach to simulate an opinion biased epidemic model.

8.2 Analysis and reconstruction of the social networks

Our first step is then to reconstruct complex networks from social media data. Because of the free availability and easy aquisition, we chose to download data from the website Twitter, a microblogging social media where users post ideas and opinions in form of short messages or

”tweets”. Besides freely interacting with other user’s messages, either diffusing the content in form of ”retweet” or posting a reply, one can follow other users in order to see their updates. This establishes two kind of networks, one mainly social that evolves slowly in time composed of followers and followees, and another one based on diffusion of information composed of cascades of retweets and replies. Because of its nature, Twitter changes constantly in time [Cataldi et al., 2010, Abel et al., 2011, Pereira et al., 2016], specially with socio-political events that rapidly give raise to several topic-centered conversations in which users engage heavily (usually sharing a same keyword or ”hashtag”). Using these key words and the Twitter API, we can make a query to download a list of tweets containing the given keyword with a time limitation of the last seven days, obtaining information on whether the tweet is an original post, a reply or a retweet. Then, from the users that posted those tweets, one can download their sets of followers and friends in order to start building a more robust network. We collected this data of the social network over a set of two weeks in two different time periods, one in October 2019, in the midst of the elections (therefore a convulsive political situation of the Spanish life); and another period in April 2020 right after the start of the COVID-19 lockdown, another convulsive moment where the Spanish Twitter website was a hotspot of activity. We used hashtags of different contents, ones directly related to COVID-19 (like ”#QuedateEnCasa” (#StayAtHome), ”#CuarentenaExtendida” (#ExtendedQuarantine)) and the political events (”#PlenoDelCongreso” (#CongressSession),”#EleccionesGenerales” (#GeneralElections)), but also more general ones from entertainment such as TV shows (”#Superviviente2020”, ”#HouseParty”). In this way, we intended to build a representative sample of the whole network reaching for the most diverse possible content. These subnetworks were then overlapped through bridge users that had participated in both hashtags, or that were found to connect through the network of follower/followees, in order to build the complete network for each date. To ensure that our networks were statistically significant for each time period, we computed the scale-free exponents of the network as more and more hashtags were overlapped until the exponent converged to a certain number. It’s important to note that all the personal information and the tweets’ content are removed in the process of building the global network. Our aim lies in the network topology, focusing on the study of the social interaction patterns rather than in their specific content. Nevertheless, it would be interesting to see if another approach focusing on the sentiment analysis of the posts’ content could be used for similar purposes, but that is not within the scope of the present work. These approaches require of carefully selecting the targeted key topics and that the posts’ content has sufficient information so a given sentiment (good or bad) can be assigned. With the sampling and time limited restrictions imposed by the API plus our aim to build the most representative snapshot possible of the whole network, we couldn’t afford to handpick the hashtags. Thus, for a more empirical analysis in which behavioral patterns of several users are studied, we refer the reader to [Xiong and Liu, 2014].

The networks obtained from this process and at these two moments in time are represented in panels (a) and (b) of Figure 8.2, with their outward and inward connectivity distributions shown in panels (c-f). The direction of the links go in the sense of who-sees-who, so the out-connectivity represents the number of people that each node i follows or has interacted with, while the in-connectivity the number of people that is following or has reached node i. We can see from these panels that they can be fitted to power-laws, although a rigorous analysis requires us to break down the distributions into two sections that show different slopes (distinguishing low connectivity from medium-large connectivity). This procedure

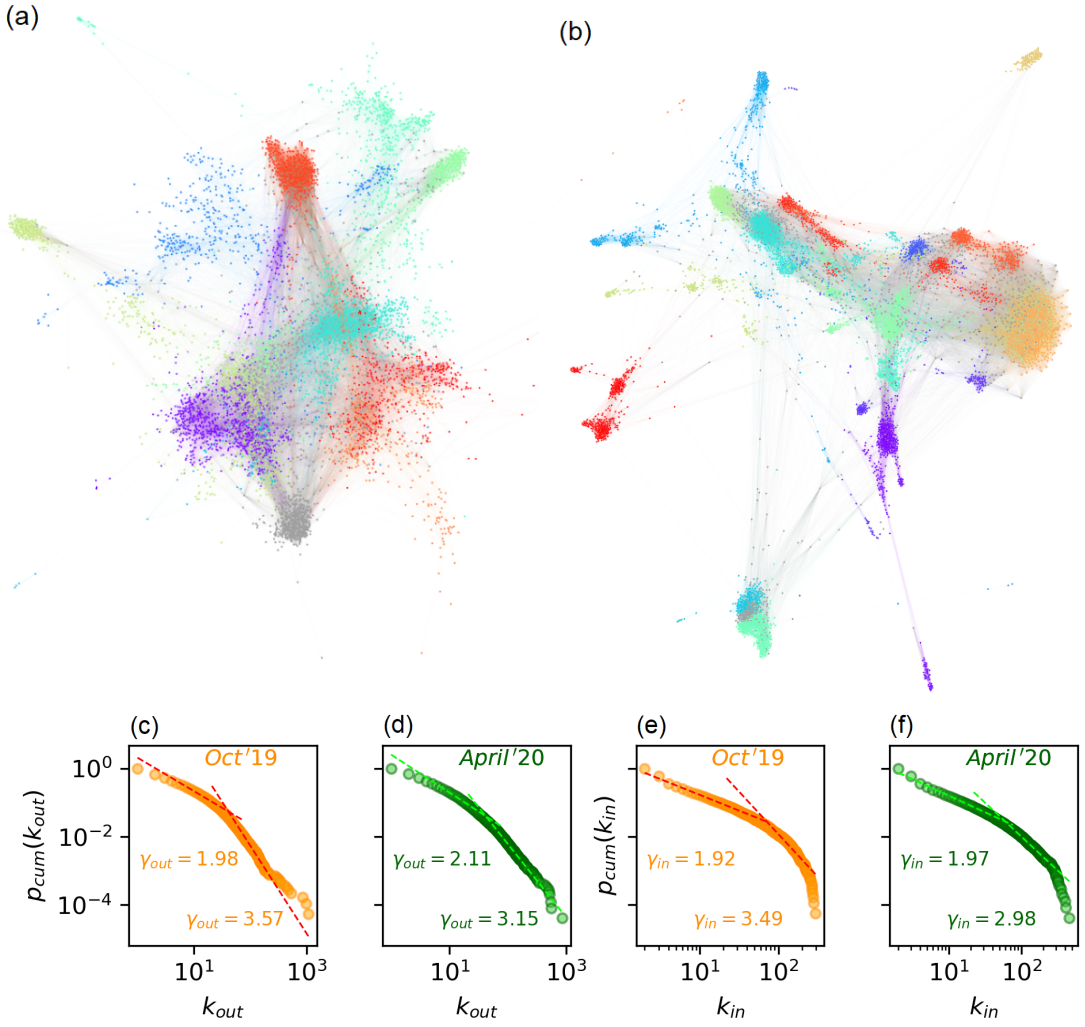


Figure 8.2: (a) October 2019 Twitter network with $N = 17665$ accounts and (b) April 2020 Twitter network with $N = 24337$ accounts. Each color represents the nodes corresponding with each keyword subnetwork. Accounts in grey are the junction accounts. (c,d) Out-connectivity distribution and in-connectivity distributions (e,f) for each network fitted to power-laws, with October'19 in orange and April'20 in green.

USC UNIVERSIDADE DE SANTIAGO DE COMPOSTELA

of breaking down the connectivity distribution is not rare when one has to deal with real data[Barabási and Pósfai, 2016a], and even some points at the beginning and end of the distribution have also been excluded of the fits as they were clear outliers of the power-law trend. For the two moments in time considered, we see that the exponents for low connectivity are higher in April'20 but then, for medium-large connectivities, the slope increases more drastically in October'19. This sudden variations in the slope indicates us that the hubs were smaller than expected, if the whole distribution followed the power-law dictated by the majority of nodes. One hypothesis about this could be that the Twitter network is not scale-free as both fitted exponent are not between 2 and 3, but this could be easily proven wrong by previous studies on the network where it clearly shows an scale-free distribution [Weng et al., 2012, Xiong and Liu, 2014, Paramés-Estévez et al., 2023]. Then, other hypothesis for this is that it could be due to an artifact of the data sampling. Since the Twitter API restricts the amount of downloads per time and user, one possible hypothesis is that the software used did not collect all the interactions that the hubs possessed in the real network which resulted in lower values for the hub's connectivities. In fact, one important limitation that could be the responsible for this is that with a free-license (the one used for this results) it only allows to gather 5000 of connections per user. Considering that Twitters is a massive social network where most influential nodes have over 1 million followers, this could especially explain the abrupt change in the γ_{in} exponents at the tail of the distributions (as this is the connectivity that measures the number of followers). Despite of this, the differences in the exponents of both networks are sufficient to foreshadow that once we incorporate a dynamic model in each network, the outcome will also be different.

Regarding the more technical aspects of the data acquisition, in order to access the Twitter API, there are two main different routes (that we know of). The one used here for building the previous networks uses third-party softwares (in our case, the free-version of the software NodeXL [1]) that already automates the data aquisition and only needs the key-words of each subnetwork as its input. This software was therefore subject to the free-license of the Twitter API, with all the limitations that it carries. The other route entails the development of your own software in order to access the main functionalities of the API (this is possible for exmample with the `Python` language through the open source library `tweepy` [2]). This route allows for farther control in your data queries, as you can access all of the functions and filters. It also requires however of deeply understanding the API documentation and dealing with the raw data acquisition. Both methods however allow to recover the cascading network of retweets as well as the complete social network of follower/followees, although with quite strong accessing limitations for the latter. The networks presented in Figure 8.2 were built with a mix of this data.

With an academic license[3], however, the time limitation of the 7-day searches can be overcome as they allow the access to almost all historical data for research purposes. Using this tool, we were able to study the time evolution of the γ scale-free exponents of the Spanish retweet network, alongside other important network metrics such as the average shortest path ℓ and the network diameter (the largest between all the shortest paths of the network). Using the same methodology described above, we overlapped the top 5 most important hashtags for each day over a time stamp ranging from the 01/06/2019 to the 01/02/2021 . The result

[1] `https://nodexl.com/`
[2] `https://www.tweepy.org/`
[3] `https://developer.twitter.com/en/use-cases/do-research/academic-research`

USC UNIVERSIDADE DE SANTIAGO DE COMPOSTELA

of this analysis and the complete details of the methodology are documented in detail in [Paramés-Estévez et al., 2023], from which we will give here some quick remarks looking at the time evolution of the network metrics (see Figure 8.3, taken from the reference). An important consideration here is that the vertical yellow line marks the 15th of March, 2020, the starting date of the Spanish lockdown. The horizontal red lines on the other hand, show the time average of the metric before and after this landmark.

At a first glance, the measure of the in-exponents γ_{in} (panel (a)) returned values between 2 and 2.5, revealing scale-free distributions with longer tail and therefore larger differences between the hubs and low-connectivity users. Their evolution in time seems to be somehow regular, with very small oscillations in the metric and almost no difference at all between the two time averages. This could be suggesting that there is always a similar proportion between the amount of attention that some nodes receive and the number of nodes who don't, independently of the times. On the other hand, the out-exponent γ_{out} is closer to 3 and shows more clearly the presence of increasing and decreasing local trends. As the out-connectivity represents the activity of each user in the form of replies or retweets, it is expected that the size of the hubs is smaller and therefore makes sense that exponent would be bigger than γ_{in}. On the other hand, the spikes shown in the time series reveal bursts of activity, indicating differences in how users engage with each other depending on the trending topics. This can be understood from the empirical analysis we carried of the hashtag's contents, as there were relatively calm weeks where the most cited topics where related to TV shows or to sport and cultural events. In these hashtags, there is usually an official account that promotes the key words and only users related to that community interact with it. There are other weeks however, where some particular event triggers the emergence of hashtags where there are moral, political or controversial topics involved. This type of hashtags persist longer in the network and not only appeal to more users of the whole network but reach broader audiences as they are also highlighted by the website. This increase of γ_{out} could then be caused by the sudden increase in the frequency of lower activity nodes that decided to participate midly with a retweet (for example) in the conversation. Interestingly, from the four metrics considered it is in the γ_{out} exponent where we observe a higher difference after the sudden appearence of COVID-19, an observation that is consistent with the analysis of the two networks of Figure 8.2 (at least for the fitting of lower connectivity nodes). Following the previous logic, this increase would imply that after the start of the lockdown, there was higher engage with the topics. This could be very reasonable as during those times, people were not only forced to stay at home but it could be assumed that overall levels of concern were increased.

On the other hand, the average shortest path returned values usually smaller than 5, showing that Twitter is yet another network where the six-degrees of separation rule is fulfilled [Samoylenko et al., 2023]. On the other hand, its time evolution seems to be quite regular in time, with sudden spikes to lower values of ℓ that could be related to very viral trends. The comparison between the two time averages show that the information flow of the network seems to stay the same independently of the time. Since the γ_{in} exponent revealed that the size of popular users (i.e., the super spreaders of information) barely changed in time, it would make sense then that the average shortest path would not change much either. The diameter of the network, on the other side, seems to show strong fluctuations in time, although as we are dealing with heavily directed networks it is difficult to estimate correctly this quantity.

USC UNIVERSIDADE DE SANTIAGO DE COMPOSTELA

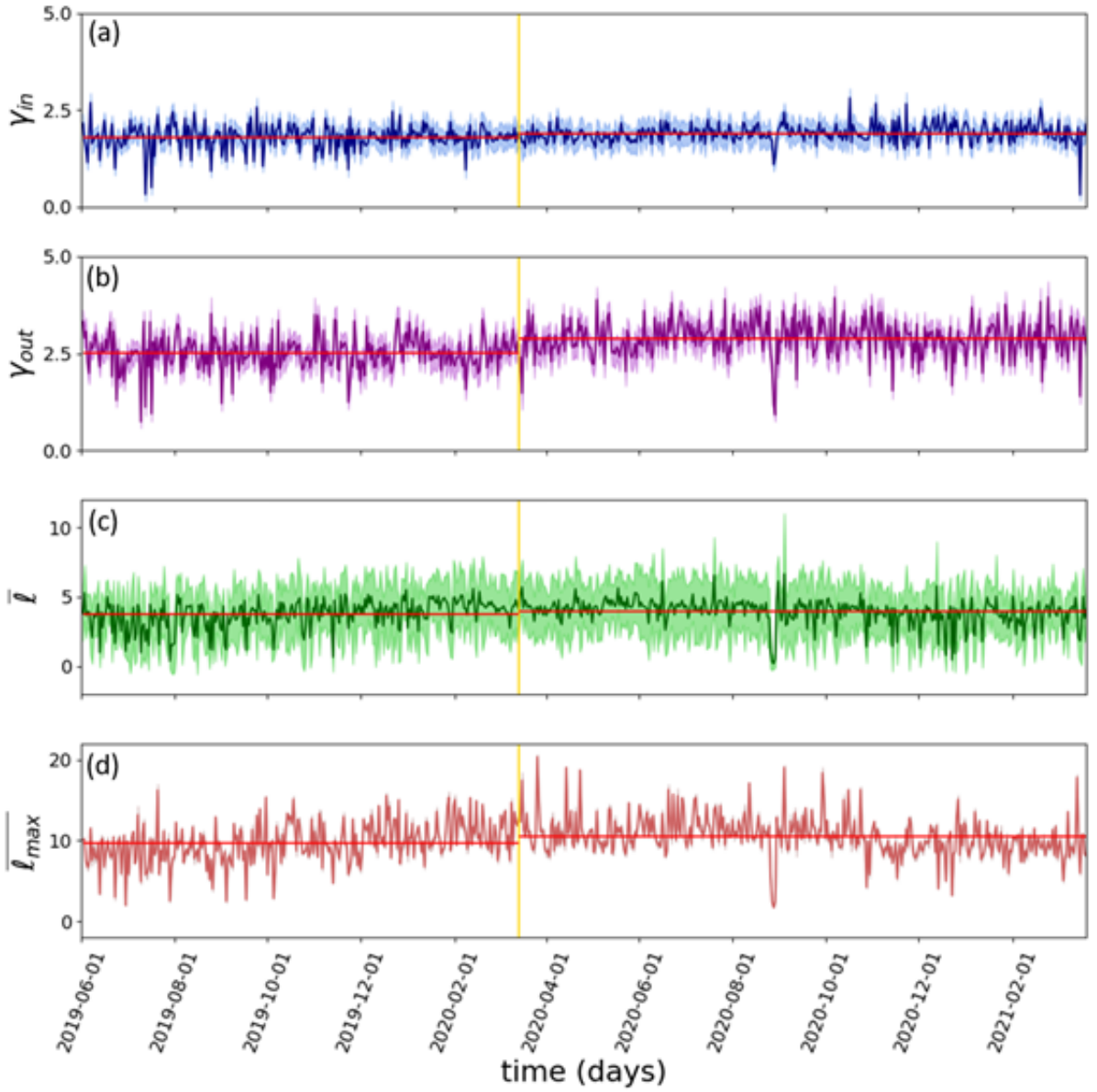


Figure 8.3: Time evolution of the scale-free exponents γ_in (a), γ_out (b), average shortest path ℓ (c) and network diameter ℓ_{max} (d) for the Spanish retweet network between 01/06/2019 and 01/02/2021. The yellow vertical line indicates the starting date of the COVID-19 lockdown by the Spanish government, March 15, 2020, while the red horizontal lines the average values of each parameter before and after this date. Figure taken from [Paramés-Estévez et al., 2023].

8.2.1 Opinion model

We consider the following opinion model based on the logistic equation that has been of use in other social contexts [Lloyd, 1995][Tarasova and Tarasov, 2017]:

$$\begin{cases} \dfrac{du}{dt} = f(u,v) = Au\left(1-\dfrac{u}{B}\right) + guv \\ \dfrac{dv}{dt} = g(u,v) = Cv\left(1-\dfrac{v}{D}\right) - guv \end{cases} \tag{8.1}$$

USC UNIVERSIDADE DE SANTIAGO DE COMPOSTELA

where u and v account for two different opposing opinions, A and C control the evolution rate of the variables, B and D the stationary values and g is the coupling constant. As $u+v=1$ must remain constant, we can reduce the system to the following equation:

$$\frac{du}{dt} = f(u) = u\left[A\left(1-\frac{u}{B}\right)+g(1-u)\right] \tag{8.2}$$

In this simple reduced system, we only have two fixed points, the unstable $u^0=0$ and the stable, absorbing state $u^* = \frac{A+g}{A/B+g}$. We assume that this equation models the internal dynamic law given by $f(u)$, which will be equal for every individual. In absence of external inputs, we have a state of consensus where everyone has their opinion fixed at u^* and that won't change by themselves, either for this lack of new external feedback or for mere stubbornness. We endow these dynamics in each node of the social network, with the possibility now of acquiring a new opinion as a consequence of the network interaction (in the same way as in Chapter 6). In this sense, the new dynamic equation for each node i becomes:

$$\frac{du_i}{dt} = f(u_i) + \frac{d}{k_i}\sum_{j=1}^{N} L_{ij}u_j \tag{8.3}$$

where k_i is the connectivity of node i, d is a diffusive constant and L_{ij} is the Laplacian matrix computed from the network's adjacency matrix $L_{ij} = A_{ij} - \delta_{ij}k_i$ (review subsection 2.4 for details).

To obtain the opinion distribution for each social network, we proceed as follows. We consider that all nodes have an initial opinion around u^* with a 10% of random noise as a small perturbation. By carefully selecting the parameters A, B and g we tune u^* to be close to zero, one of the opposing opinions. Then, we choose a subset r of accounts that we consider that have a certain level of centrality in the network and placed them far outside the fixed point, changing their initial opinion value to $u_i = 1$ also with a 10% of noise. From this initial configuration, we let the whole system evolve following equation 8.3. Note that the opinion value that can acquire each node, u_i, is real and any value between 0 and 1 is accessible. This is consistent with the situation we are trying to describe, where most of the people may not have a clear opinion on how to face a pandemic and, thus, their opinion will be neither completely 0 neither 1. On the other hand, a value of 0.5 may indicate different behaviors depending on the occasion or simply decide to reduce their interactions but not completely. In this sense, we assume that the fixed opinion u^* is an sceptic one, going against the public health measures, while the opinion that high influence nodes are trying to spread is to stay at home. What will happen is that the internal rule of every node will try to return its opinion to the absorbing state u^* at a rate given by the dynamical parameters, while, because of this initial strong perturbation promoted by the ratio r of popular accounts (the network contribution), the overall node's opinion will be shifted in function of their connectivity. We note that this is not the same mechanism seen in Chapter 6, as this model is not complex enough to undergo the Turing instability. In fact, the growth rates for equation 8.3 can be easily computed to see that they are all negative, independently of the model parameters and Laplacian eigenvalues.[4] Thus, the differentiation of opinions here are due to the balance imposed between the internal process of trying to return to their initial fixed position and the network pull of adhering to a new one. This results in a differentiated opinion distribution of values $P(u)$ ranging from 0 to 1 that we interpret as a probability distribution of

[4] As $f_u(u^*) < 0$ for any parameter value and $\frac{d}{k_i}\Lambda_\alpha \leq 0$ for all the eigenvalues of the Laplacian matrix.

nodes eager to change their opinion and adhere to new politics. Although the dynamics of the model would lead to u^* at an infinite time, we adjusted the model parameters so the shape of the distribution was almost stationary in time. Besides, the quantitative values of the opinions will be re-scaled later for their coupling in the epidemic model, so it is this connectivity dependent shape what we are mainly interested about.

Following this methodology, we obtain for each social network the opinion distributions shown in Figure 8.4 for three different values of r, the initial ratio of accounts switched to $u_i = 1$. The rest of parameters are fixed so $u^* = 0.02$, a value very close to zero. In overall, we see for both cases that most counts are found at lower values of u showing that the tendency to stay around the fixed point is stronger than the network effect. This is especially true for $r = 0.2$, while increasing levels of differentiation are found as we increase r. For the network of April '20 (green histograms) however, there is a noticeable difference as we can grasp the appeareance of a small peak of indecisive individuals near $u = 0.5$, a peak that increases its population for increasing values of r. As we shall see in the next subsection, these small set of counts will mark a difference once we incorporate these distributions into the epidemic model. Note however that for this coupling with the epidemic model, we will consider only the case of $r = 0.3$, as it already shows significant differences between both networks in order to exemplify our approach and the differences in respect to other two cases is not that large.

In order to explore a wider spectra of opinion distributions we consider to be more suitable generating them with synthetic bimodal distributions. This allows us to consider other different scenarios, more or less polarized, in order to give a farther sense of completeness. For this, we considered two half-Gaussians centered at zero and one, with different values of their standard deviations σ to account for how spread the distributions are around the maxima. In this way, σ will denote how defined is the opinion next to the extreme values of 0 and 1, representing thus different degrees of polarization according to the metric studied in Chapter 6 (see eq. 6.13)). We can also control the population of each half-Gaussian, in such a way that if there is a higher number of counts in the Gaussian centered at 0, the distribution represents a state where the majority of population are contrarians to the given opinion; while if the majority is found near 1, it follows that the population tends to agree with the given opinion. In this way, we define the population around each mode as N_0, N_1 so we can stablish the ratio:

$$\nu = \frac{N_1}{N_0} \tag{8.4}$$

Attending to this ratio, we have generated plenty of different distributions that, for low dispersion σ, can be characterized as contrarian, polarized or agreeing if ν tends to zero, one or higher than 2, respectively. On the other side, considering σ also as a control parameter, we can tune the shape of the bimodal distributions making the narrower or wider. In the next sections, we intend to study also the effect of these two parameters on the epidemic spread.

USC
UNIVERSIDADE DE SANTIAGO DE COMPOSTELA

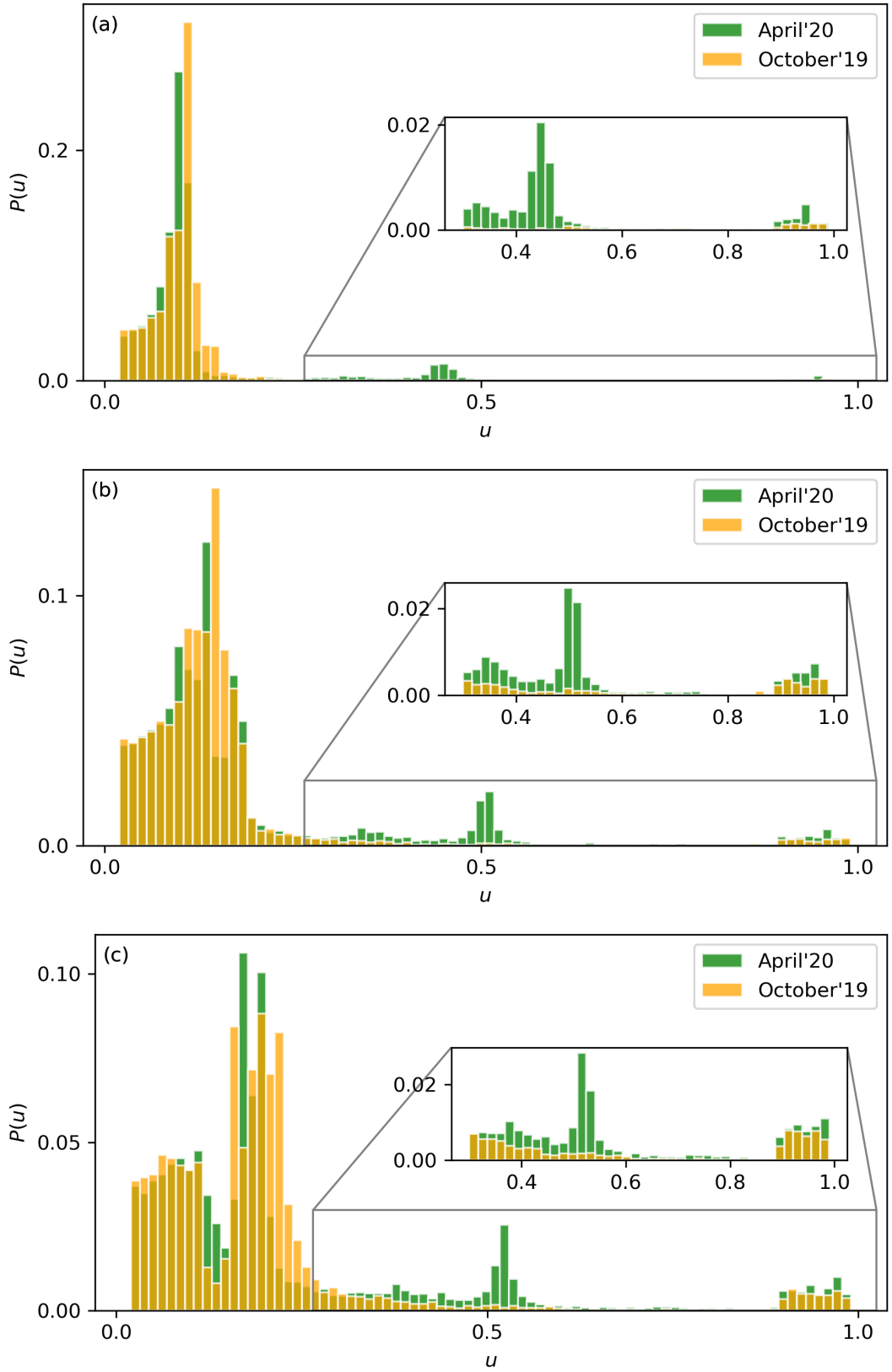


Figure 8.4: Normalized opinion distribution for the October'19 (orange) and April '20 (green) Twitter networks, for three values of the parameter r, i.e., the initial % of accounts in the state $u_i = 1$. The rest of model parameters were fixed at $A = 0.0001, B = 0.01$ and $g = 0.0001$, to obtain $u^* = 0.02$ and $d = 20000$ to equilibrate the interplay between internal dynamics and network effects.

8.3 Opinion biased SIR model

For the epidemic process in this chapter, we reduce the scale and focus just on one of the subpopulations of the metapopulation network. However, what we use here, is another network approach to break the homogeneity of the SIR compartments, where we consider that each node is a single individual that can be in one of the three compartments. In this way, the links between nodes represent face-to-face interactions and aim to model the daily life of individuals in a certain town. This implies also a big change in the computation of the dynamics, as we face now an stochastic simulation of agent-based models instead of integrating numerically the differential equations of the system. In order to account for the propagation of the disease, at each time step and for each link, the infected nodes can transmit the disease to the susceptible ones with a probability of β. Simultaneously, each infected individual has the probability μ of recovering from the disease.

Adhering to the COVID-19 situation, we consider that the mobility should be heavily reduced. Therefore, instead of using the previous social networks obtained from Twitter, we considered another topology to model our face-to-face interaction epidemic network. We chose here the Watts-Strogatz model (see subsection 2.1 of the Methods chapter) for its ability to produce a clustered graph, where interactions occur mainly between nearest neighbors while still leaving some room for long distance connections or random encounters given by the shortcuts. As commented in previous sections, networks built according to the Watts-Strogatz model require only of two parameters, the average number of connections to nearest neighbors $\langle k \rangle$ and the probability of p_r of the random shortcuts. In this way, we relate this type of network structure to the spatial distribution of individuals during the strong lockdown measures imposed in the pandemic, as we can see a direct connection between a small p_r that restricts random interactions with individuals outside our immediate neighborhood, thus resembling strict mobility restrictions. This feature makes the Watts-Strogatz model suitable for our study as it allows us to impose additional mobility restrictions in a straightforward manner. Besides, clustering effects in small-world networks with epidemic models have been thoroughly studied and proven to be significant [Moore and Newman, 2000, Keeling, 1999, Newman, 2003, Zanette, 2001].

The next step is to incorporate the opinion distributions into the epidemic spread model. There are different forms in which one could implement this idea of opinion-based interaction networks. One procedure, consists in coupling both processes dynamically, considering that they evolve together in time and introducing a time-evolving interplay between opinions and infective rates [Ni et al., 2011, Alvarez-Zuzek et al., 2017, Pires et al., 2018]. Another general procedure is based on adaptive network schemes, where links are broken when infected nodes appear [Gross et al., 2006, Zhan et al., 2018]. In the first one, both dynamics happen at the same time in a fixed static network, while in the latter, nodes rearrange their connections attending to some rules related to the dynamics in what is called an adaptive network scheme [Sayama et al., 2013]. Here we consider an approach that takes on ideas from both sides taking into account the possibility given by weighted networks. First, we consider the opinion distribution $P(u)$ obtained from the opinion model on whether the nodes of our network will follow or not the public health directives and then endow each node with an opinion according to this distribution. Then, the links of the nodes are weighted according to their own opinion value modifying how the epidemic process will spread along the network. In this way, if β is the infection rate and u_i is the opinion of node i of following the social distancing, then this

USC DE COMPOSTELA

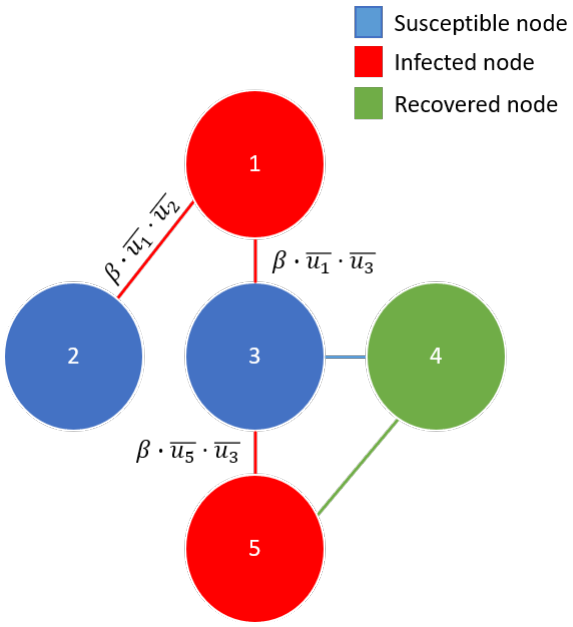


Figure 8.5: Representative diagram of the infection process. Infected nodes spread the disease to neighbor susceptible nodes with probability $\beta'_{ij} = \beta \cdot \overline{u}_i \cdot \overline{u}_j$.

node will have a modified infective rate of $\beta_i \cdot (1 - u_i)$. Thus, a node with $u_i = 1$ will be in any case isolated from the network in terms of infectivity. For clarification purposes, from here on instead of using directly the opinion u_i, we prefer to use the inversed value, $\overline{u_i} = 1 - u_i$, which will represent the disagreement with adhering to public health policies. We do this transformation because when node i interacts with node j, we must also take into account the opinion of the latter. Thus, the effective probability of infection between any infected node i and a susceptible node j is actually given by the weight $\beta'_{ij} = \beta \cdot \overline{u}_i \cdot \overline{u}j$. In the worst-case scenario, $\overline{u}_i = \overline{u_j} = 1$ and we recover $\beta'_{ij} = \beta$, while if one of the nodes has no disagreement, $\overline{u}_i = 0$, the infection probability is zero. At each time step of the simulation, the infection probabilities are evaluated based on the β'_{ij} weights of the connections, and the process is repeated until the number of infected individuals reaches zero or the stopping criterion is met. In Figure 8.5, we provide a network diagram to exemplify this process, where blue, red, and green nodes represent susceptible, infected, and recovered individuals, respectively. Red connections indicate possible infections with a probability of β'_{ij}. For estimating the parameter values β and μ, we have chosen $\beta = 0.05$ and $\mu = 0.06$ as it was a suitable set of parameters where the dynamics were either not too slow nor too fast.

Note that this approach could be extended to more complicated epidemic models discussed in the literature [Pastor-Satorras et al., 2015]. In fact, we have described this methodology for the study case of the Spanish social network, but we have also applied this same methodology in [Silva et al., 2021], where we have also extracted data from the Twitter Portuguese network and applied it into the SAIRP model considered in the previous chapter (see 7.2 for the equations). As we saw there, the Asymptomatic A, and Protected P compartments, made it more suitable to model the dynamics of the COVID-19. In that case, the coupling of the SAIRP model with the opinion distributions makes it more interesting as we can relate the opinions u_i of adhering to public health policies with the model probability of being moved to the protected compartment, p_i, and $\overline{u_i}$ with the probability of leaving it, w_i. We will present the results of this application at

the end of the following section, as they complement the main results of this chapter.

8.4 Epidemic Results

The Spanish Twitter network

We have simulated the advance of the epidemic spread in networks of size $N = 10000$, with average connectivity $\langle k \rangle = 50$ and a shortcut probability of $p_r = 0.25$. In absence of the opinion weights, this leaves a net global infection rate of $\beta \langle k \rangle = 2.5$ (as $\beta = 0.05$) and $\simeq 12$ random shortcuts per node. This selection of network parameters aims to simulate a first order approximation to the daily routines of each individual, with the opinion cutting down the possibility of infection of each node according to its value between 0 and 1. This allow us to induce strong degrees of heterogeneity, as a node with $k_i = 50$ but $u_i = 1.0$ would be equivalent to another with $k_i = 0$ in what concerns the infection process. On the other hand, the heavy restrictions imposed on the non-pharmaceutical-interventions (NPI) and the mobility during the COVID-19 in Spain, led to us to assume a further restriction in our model. We decided to re-scale the probability density of disagreement opinions $P(\overline{u})$ (obtained directly from the inverse of $P(u)$ in Figure 8.4)(b), to values between 0 and a maximum cutoff that we left as a free parameter. This allows us to model different intensities of lockdown/NPI imposition too, as each value of the cutoff is equivalent to a reduction of the overall connectivity by that value. In Figure 8.6 we explore the case of this cutoff being fixed at $\overline{u} = 0.3$, leading to the probability densities shown in panel (a). We also remind here that for the coupling with the epidemic model we have only considered here the opinion distributions obtained with $r = 0.3$.

Following the previous reasoning, since the opinion distribution represents the effective probability of interaction between individuals, the cutoff means that the government policy is enforced reducing up to 70% the usual number of interactions of each individual. Within the other 30% of free interactions, the population will adhere further or not to the restrictions according to their own opinion on the subject. In panel (b) we show the epidemic curves obtained for each networks' opinion distribution, color coded in orange (October '19) and green (April '20), against a simulated scenario (blue) where all individuals have the same opinion fixed at the cutoff. We use the latter to quantitatively measure in panels (c,d) how much the epidemic curve has been flattened thanks to each opinion distribution, obtaining in % the ratio of reduction and time delay of the infection peaks. We see that the small differences captured by the opinion distributions are highlighted within the epidemic model, where the further agreement with adhering to public health measures results in a quantitative impact reducing and delaying the epidemic dynamics. In contrast with the theoretical case where individuals are only doing what they are enforced to, in the case of April'20, the simulated infection peak was reduced almost to a half, and delayed in near a 60% of its time units. Between both opinion cases, we see a further 12% reduction of the infection peak in the April network, and almost a 20% of delay in the timing at which it takes place. The vertical blue bar shown in these last panels account for another theoretical case where we imposed the cutoff at $\overline{u} = 0.1$. In this case the disease is not able to percolate through the network as the interactions have been highly reduced and the epidemic threshold is not reached.

We said initially that the value of this cutoff can be interpreted as the degree of confinement or NPI enforcement and that therefore, we can use it to model from stronger to milder measures. In Figure 8.7 we examine different values for the cutoff and analyze the peak statistics of the

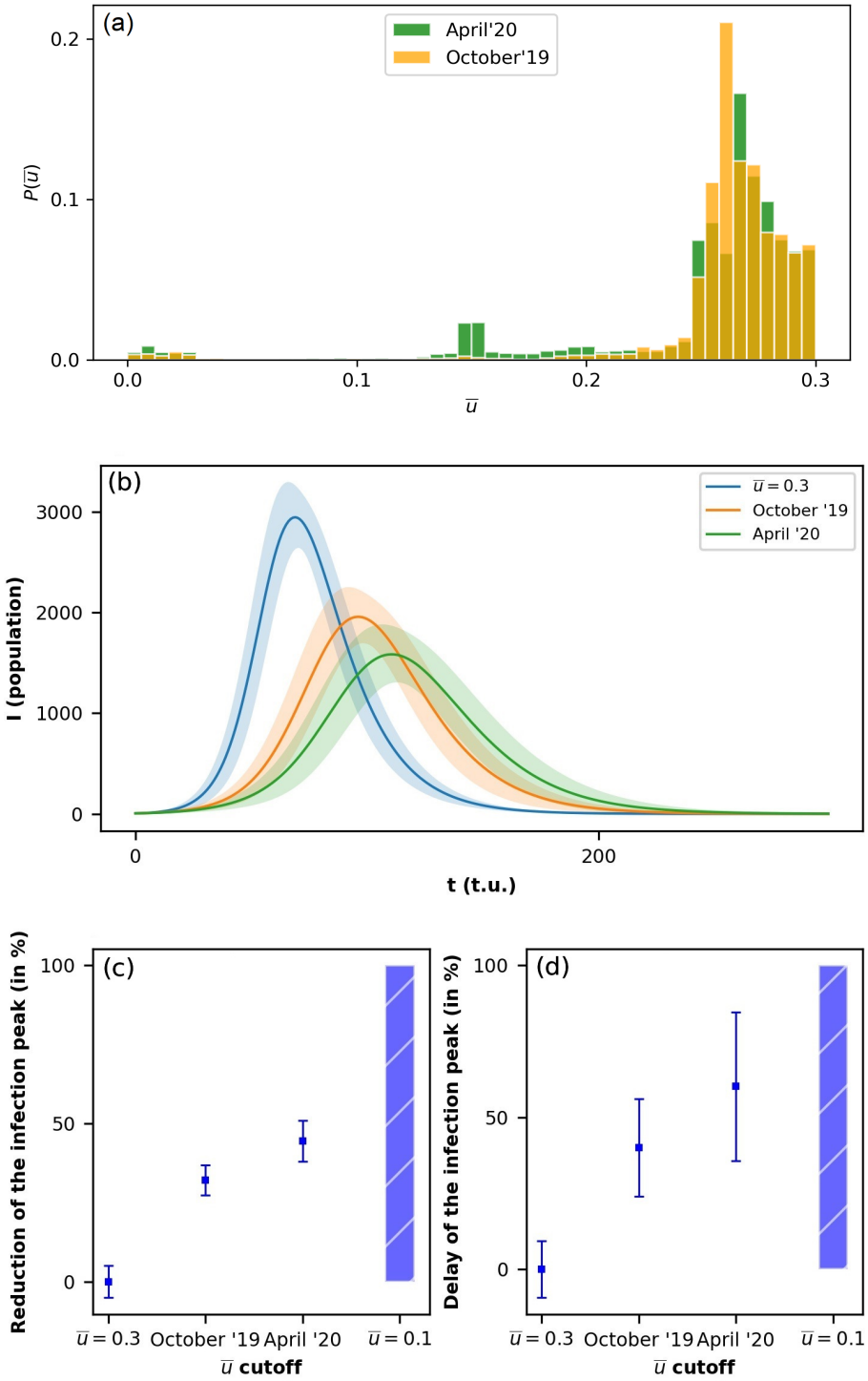


Figure 8.6: (a) Re-scaled probability density of the variable $\overline{u} = 1 - u$ representing the disagreement, obtained from Figure 8.4 (b) ($r = 0.3$). (b) Time evolution of the infected individuals for the three opinion distributions considered. Reduction (c) and time delay (d)in % of the infection peaks in comparison to the uniform case where all nodes have their opinion at the cutoff value, $\overline{u} = 0.3$. The vertical bar in the last case, $\overline{u} = 0.1$, represents that the outbreak of the epidemic did not occur. Error bars represent the standard deviations from a sample of several simulations run with the same parameters but different random configurations of the network's adjacency matrix. For this Figure, $N = 10000, \beta = 0.05, \mu = 0.06, p_r = 0.25$.

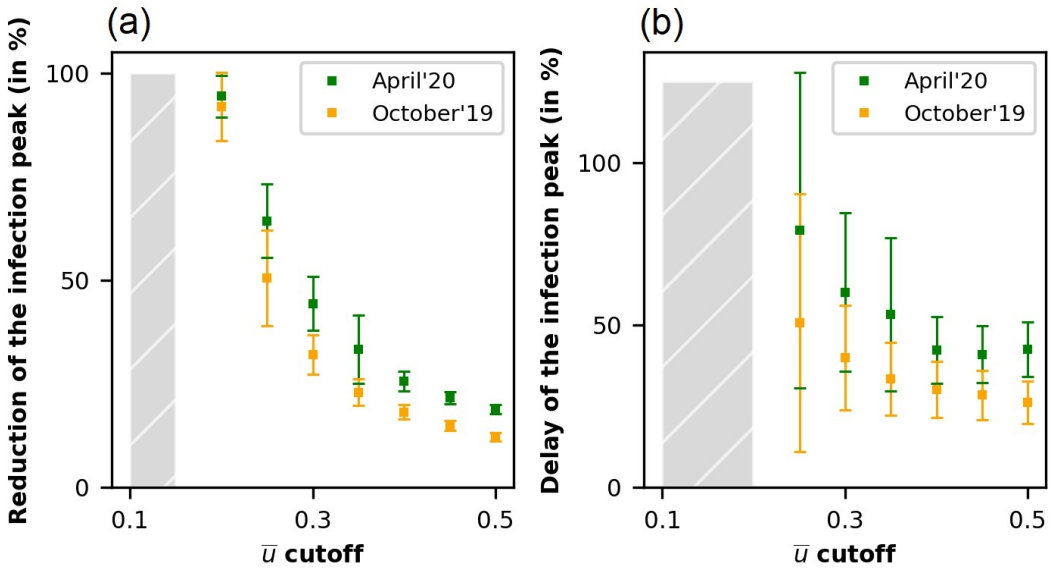


Figure 8.7: Reduction (a) and time delay (b) of the infection peak for different values of the cutoff in $\overline{u}$, for both the opinion models. For each cuttoff, the values of each model are scaled over the value of the theoretical scenario where all nodes have the opinion at the cutoff. The dashed filled bar represents the abscence of a clear infection peak. Error bars represent the standard deviation over a ensemble of several simulations. Simulation parameters are set to $N = 10000, \beta = 0.05, \mu = 0.06, p_r = 0.25$.

epidemic curves as before. For each value, note that we scaled the results obtained for the October and April opinion networks in respect to the virtual case as we did for the cutoff in 0.3. There, we see that the percentage of reduction and delay decrease exponentially with the increase of the cutoff in a similar proportion for both opinion networks. This important decrease as we shift the cutoff could be reasonable taking into account that the majority of nodes for both opinion networks had lower values for the opinions (as was shown in 8.4). Therefore, the infection process is dominated by these nodes that are less protected and allow the disease to percolate exponentially. In this case, the difference with the virtual scenario is probably related to those nodes at the extremes of the opinion distribution that are almost isolated thanks to $\overline{u}_i \simeq 0$. On the other hand, for cutoff values below 0.3, the error between different random realizations of the epidemic network (but same dynamical parameters) becomes quite large as we approached the critical point of the epidemic threshold. This is specially true for the cutoff in $\overline{u} = 0.2$, where the infection curve was almost flat and therefore we could obtain a measure for its average value but it was difficult to assess where the peak was. All in all, we see that in all scenarios, the social network of April'20 represents a more optimal situation in both terms of peak reduction and time delay thanks to that small subset of counts that decided to adhere further to the public health policies.

Bimodal distributions and the case of polarization

We now proceed to assess our opinion-biased epidemic model with the bimodal distributions of opinion generated according to different values of the population ratio ν and the opinion dispersion σ. Following the previous reasoning, we investigate here the effect of these parameters in the statistics of the infection peak, scaling now the obtained results over the baseline scenario where all opinions are zero. We start with coupling the epidemic model to the

bimodal distributions shown in Figure 8.8(a), where we explored two cases with low dispersion ($\sigma = 0.05$ and $\sigma = 0.2$) for three different ratios ν, one with more density of contrarians $\nu = 0.5$, another with more density of agreers ($\nu = 2$), and the middle ground where the distribution was perfectly polarized ($\nu = 1$). We also consider a third case with $\sigma = 1.0$ where the distribution shows to be almost uniform by the overlapping of the two Gaussians, with very slight deviations in function of ν.

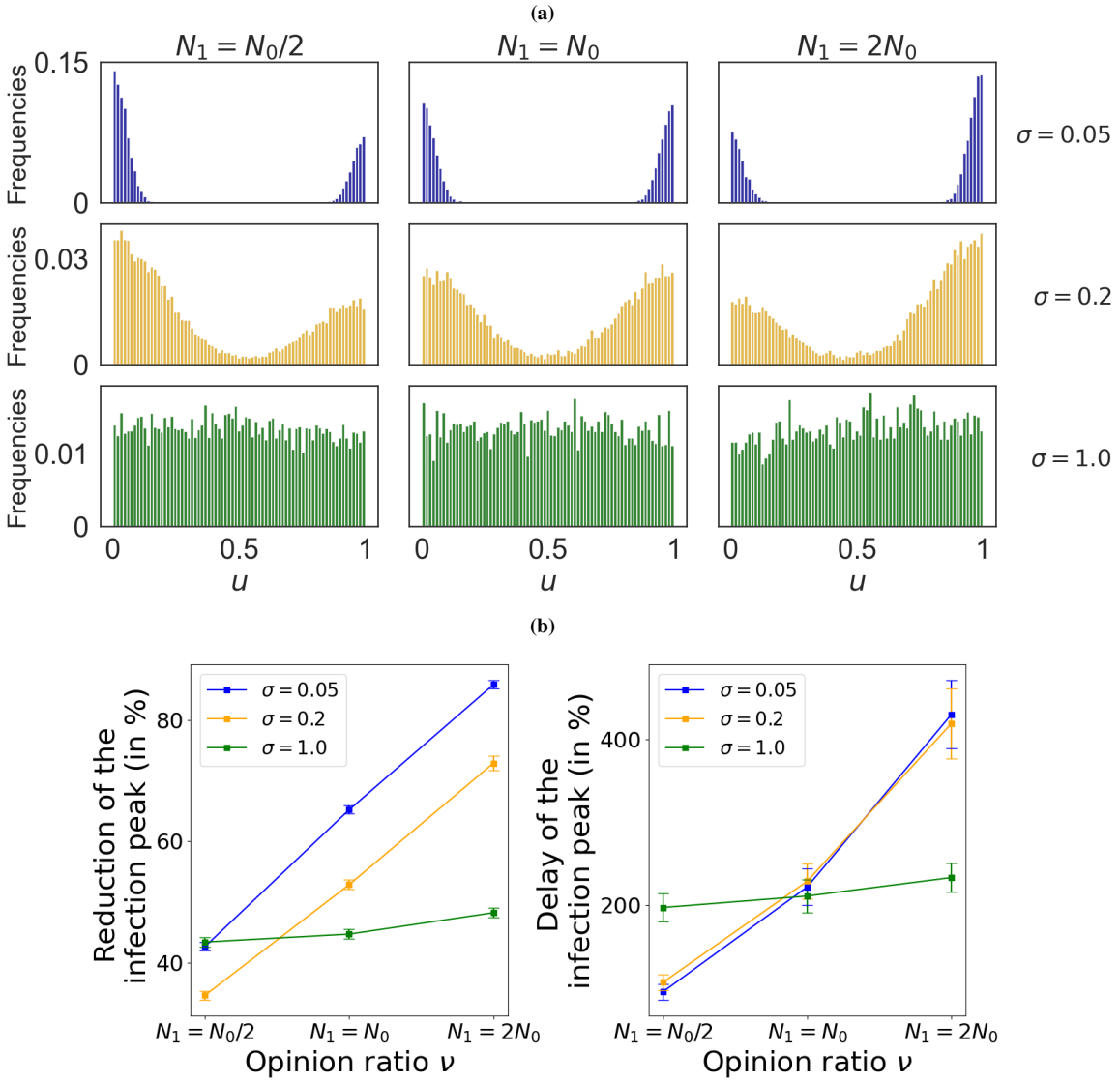


Figure 8.8: (a) Normalized bimodal opinion distributions, generated with different sets of populations $N_{0,1}$ and dispersion sizes σ. (b) Peak statistics from the opinion distributions shown in panel (a), scaled over the baseline epidemic model without opinions.

Figure 8.8(b) shows the peak statistics for each scenario, with $\sigma = 0.05$ shown in blue, $\sigma = 0.2$ in yellow and the homogeneous case $\sigma = 1.0$ in green. Attending to the reduction of the infection peak, low dispersions in the distributions appear to be the best configuration, with a net reduction of $\simeq 40\%$ for $\nu = 0.5$ and scaling up to an 85% reduction in the most optimistic scenario, $\nu = 2$, where there is a majority of nodes adhering to the public health recommendations. Increasing σ slightly to 0.2 results in a worse outcome, as now the peak

of infection appears to be also slightly larger and the previously obtained values shift down the previous values between 5 and 10 points for each ν. For $\sigma = 1.0$ we see something very interesting in both peak statistics, where the net reduction of the infection peak coincides with that of $\sigma = 0.05$ at $\nu = 0.5$, but showing a larger net reduction than the one obtained for $\sigma = 0.2$. For higher values of ν where there is at least a 50% of people who committed strongly with the public health recommendations, it would make sense that increasing here the dispersion would result in a worst outcome, but the case of $\nu = 0.5$ deserves further inspection (as we will do shortly after). On the other hand, attending to the delay in the infection peak, we see that in this case the outcome for both lower sigmas is curiously the same independently of the population distribution. For $\sigma = 1.0$, we see again a surprising higher delay of around the 200% in the case of $\nu = 0.5$ where the lower sigmas resulted in a delay only of the $\simeq 100\%$. This former value is the same for the three configurations in the symmetric scenario $\nu = 1$ while for $\nu = 2$ we can obtain a delay of almost 4 times with the lower σ values.

Motivated by these findings, we fix now the population ratio at $\nu = 0.5$ and sweep now the values of σ in Figure 8.9. From inspecting the reduction peak over the dispersion values σ (see panel (b)), we can see that there is indeed a minima around $\sigma = 0.25$ where the reduction in the infection peak is at its lowest. Furthermore, we can also see here that increasing σ leads to a monotonic increase in the delay of the timing of the peak (see panel (c)). Both these effects can be better grasped by looking in panel (a) at the infected curves for each value of σ, where the peak of infection indeed increases for low values of σ while taking place at later times. We find here an interesting interplay between opinion dispersion and the network infectivity pattern. With $\sigma \simeq 0$, counts located at the pole of 1 are isolated and thus cannot be infected by any means, while counts near 0 are all susceptible to the disease with no kind of protection at all. In other words, for $\sigma \simeq 0$ the pool of susceptible individuals is only N_0, while as σ increases, counts that before had a value very close to 1, start to become vulnerable increasing the pool of susceptible individuals. Meanwhile the opposite process occurs with those in the vicinity of 0, creating a balance between counts that are increasingly more protected and others that are increasingly more vulnerable. For lower values of σ, this translates in the epidemic wave being able to reach more individuals but at a slower rate, as the disease now spreads slower between the slightly more protected individuals. This is highlighted by the epidemic curves in panel (a). A turning point seems to be found around $\sigma = 0.25$, from which the net reduction of network interactions caused by the wider spread of opinions involves an increasing reduction in the infection peak. From this point, the bimodals start to overlap and the nodes that were completely vulnerable have now decreased in favor of acquiring higher levels of protection, increasing the accumulation of accounts at the center of the distribution. As in overall there are higher levels of protection, there is also a net reduction of overall face-to-face interactions which directly translates in smaller global values of the effective transmission rate β',

Finally, in Figure 8.10 we explore the peak statistics against the control parameter ν, from where we can appreciate two clear asymptotic behaviors. For $\nu \to 0$ almost all opinions tend to strongly disagree with following social distancing, and so the dynamics of the baseline SIR model are recovered. Conversely, for $\nu > 2$ the epidemic outbreak either quickly dies out or fails to occur (with the dashed blue and orange bars in panel indicating the absence of a clear infection peak). For larger values of the dispersion parameter σ, namely $\sigma = 0.2$ and $\sigma = 0.5$, although the same tendency is observed, larger values of ν are required for the epidemic outbreak to die out. Note how for $\nu = 3$ and $\nu = 4$ there is still a peak of infection with dispersion $\sigma = 0.2$, although it is heavily delayed (7 to 10 times the original peak predicted by

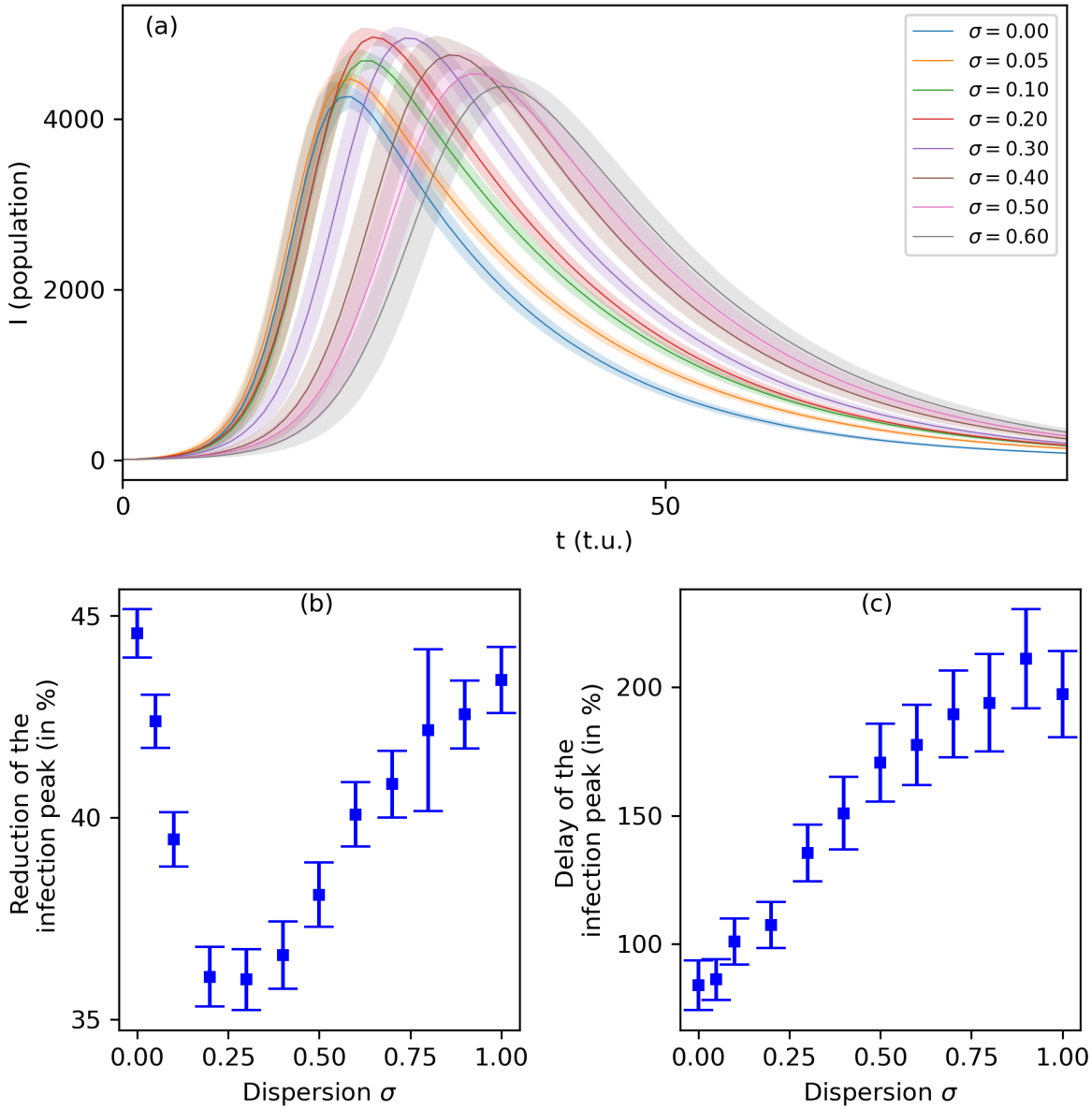


Figure 8.9: Time evolution of the infected individuals (a) and peak statistics (b,c) of the bimodal opinion distributions with $\nu = 0.5$ for different values of σ.

USC
UNIVERSIDADE DE SANTIAGO DE COMPOSTELA

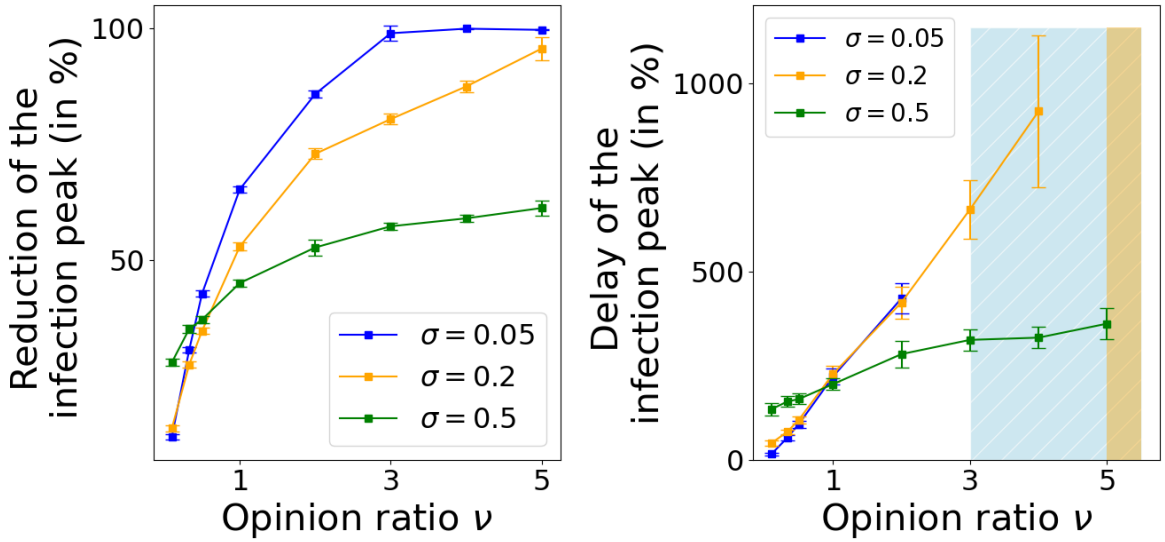


Figure 8.10: Peak statistics of the opinion distribution with $\sigma = 0.05, 0.2 and 0.5$ against ν. $N = 10000, p_r = 0.25$

the SIR model). For a higher value of the dispersion parameter, $\sigma = 0.5$, the slope of the trend is significantly reduced with increasing ν, until this slope becomes practically zero as we saw on figure 8.8 with the dispersion parameter $\sigma = 1.0$. For values of $\sigma > 0.5$ the distribution begins to become more and more uniform, homogenizing the number of counts of the opinion spectrum. This effect is the responsible for the higher values on the statistics obtained for $\sigma = 0.5$ when ν is smaller than 0.5.

The Portuguese Twitter network with the SAIRP model

In this subsection, we demonstrate that the methodology presented in this chapter can be adapted to capture the opinion of other social networks and applied to more complex SIR-like models. For this purpose, we tracked the list of popular hashtags in the Portuguese Twitter network during the periods of time of April 2020 and July 2020. To our surprise, the behavior of this social network in respect to the Spanish one was found to be completely different, with much lower levels of overall activity and with relatively tranquil hashtags, usually related just to TV shows, concerts or international news. Furthermore, in this study we had to deal with the strong restrictions of the Twitter API as we needed to go back to data older than 7 days and the academic license was not available by that time. For that purpose, we found and used the python open source library GetOldTweets3[5] that managed to download older tweets without the need of accessing the API. It had other limitations though, so we could only obtain the retweet network, the volume of available data was considerably smaller and the download times were also larger. Despite all of this, we managed to reconstruct a social network for each month, with sizes $N = 5154$ and $N = 4394$ for April and July respectively. The connectivity distributions for both networks, shown in Figure 8.11, also recover scaling exponents in the region of the scale-free networks, with $\gamma_{out} = 2.99$ for April and $\gamma_{out} = 2.14$ for July.

Applying the same opinion model as in the Spanish case (eq. 8.3), we recover the opinion distributions reported in Figure 8.12. The strong differences between these distributions and

[5] https://pypi.org/project/GetOldTweets3/

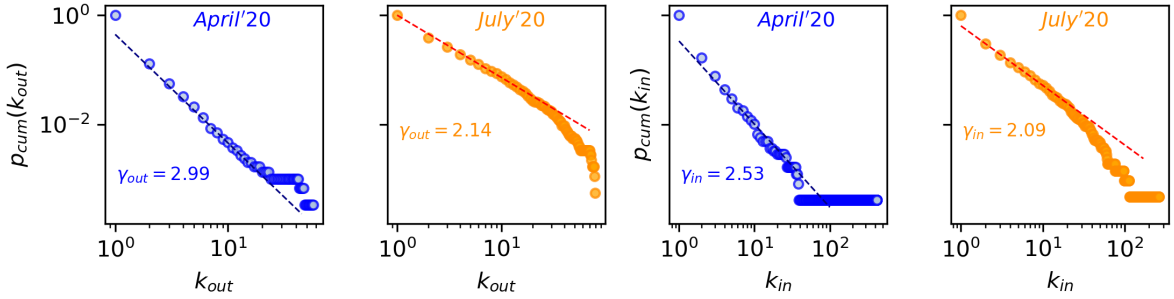


Figure 8.11: Connectivity distributions of the social networks obtained for the Portuguese Twitter network. Dots in blue, represent the network obtained in April 2020, while orange dots correspond to the situation in July 2020. In both cases, the network topology corresponds to a scale free networks with exponents $\gamma_{out} = 2.99$, $\gamma_{in} = 2.53$ in April and $\gamma_{out} = 2.14$, $\gamma_{in} = 2.09$ in July 2020.

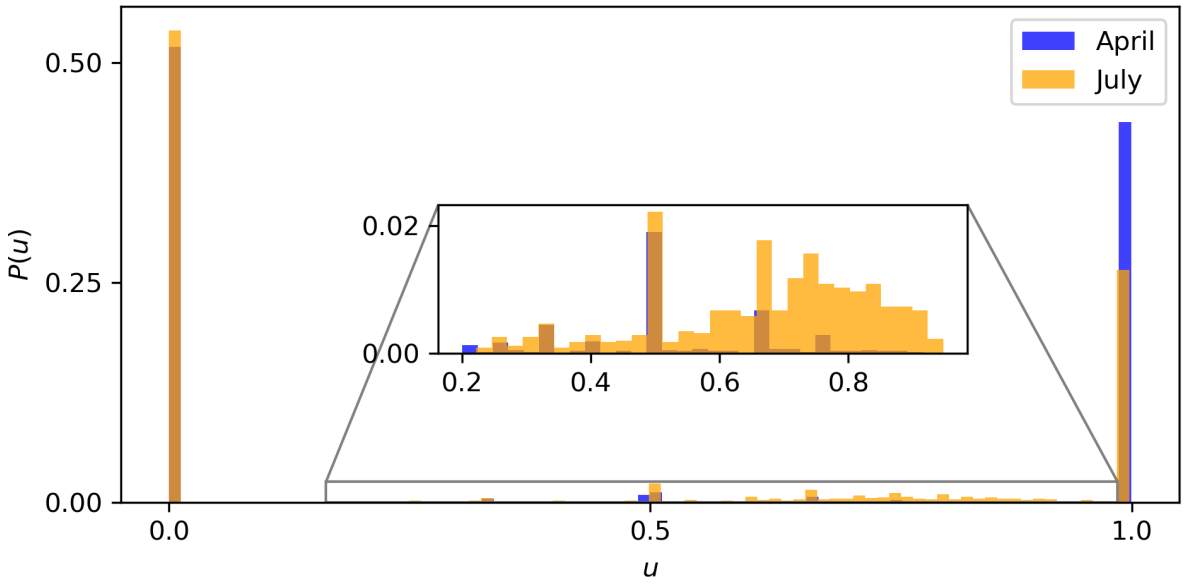


Figure 8.12: Normalized opinion distributions for the April '20 (green) and July '20 for the Portuguese Twitter networks.

those of the Spanish case can be attributed mainly to the differences in the connectivity. Notice that the Spanish networks were between 4 to 5 times bigger, with a more continuum spectrum of connectivities. In this case, these retweet networks showed to be also considerably more sparse in links. In fact, most of the counts found at zero possessed only inward links and zero outward links, which left them unaffected by the network contribution. The opposite case occurs with the hubs, which are left almost at the initial perturbed position in 1 as the distribution became stationary quite fast. In this sense, the opinions shown in the inset of the graph would correspond to those nodes with intermediate values of the connectivities.

Regarding the epidemic model, we considered the SAIRP model presented in equations 7.2 but adapted to the mobility network used in the previous subsection with the Watts-Strogatz model. This is, we still consider face-to-face between single nodes of the network, but now the susceptible nodes before becoming infected I, they become first Asymptomatic A. Susceptible nodes may also become protected P at each time step with a probability p_i given by the

Parameter/Initial condition	Value
β	0.2
ϕ	1/6.486 day^{-1}
w	1/24.32 day^{-1}
ν	1 day $^{-1}$
q	0.15
delta	1/16.216 day^{-1}
$N = S_0 + A_0 + I_0 + R_0 + P_0$	25000
S_0	(N-2-2/0.15)/N
I_0	2/N
A_0	(2/0.15)/N
R_0	0
P_0	0

Table 8.1: Estimated parameter values and initial conditions for the simulation of the COVID-19 incindence in Portugal from March 2, 2020 to May 17, 2020, 2020 for the SAIRP model.

opinions u_i. On the other hand, they may leave the protected compartment with probabilities w_i given by the inverse opinions $\overline{u}_i$. The rest of model parameters and initial conditions are presented in Table 8.1, which were adapted from those presented in [Silva et al., 2020] with their fitting process to the incidence data of Portugal (see panel (a) of Figure 8.13). In this way, we translated their boxed-compartment deterministic approach into our mobility network approach, and substituted their estimated parameters for the transitions between the susceptible and protected compartments with the results of our opinion coupling. The final aim of our contribution consisted in reproducing the fitted infection curve up to May 17, while considering the opinions obtained for the April Twitter network. This is what we show in panel (b) of Figure 8.13. The red crosses mark the experimental observations until May 17 and the blue line is the fit to the SAIRP model with the opinion distribution. As the errors due to the random estimation of the probabilities were not negligible, this model simulation was repeated 12000 times in order to gain statistical significance. In this way, the evolution of the number of infected individuals shown in the Figure is consistent and does not depend on a limited number of realizations. We see that the prediction of our epidemic model coupled with the opinions was able to recover to a very large extent the temporal evolution of real infected cases. From the original fitted parameters, we only needed to adjust β slightly in order to match data and simulations, plus some temporal rescaling of the other parametres was needed to adjust the dynamics of our stochastic discrete model to those of the deterministic, continuous ones.

After these findings, we incorporated the opinion distribution of July 2020 and repeated the simulations. In this case, shown in Figure 8.13, as a direct conclusion of the change in the opinions we see that the case of July results in a much worse scenario as the curve of infected individuals continued to grow further, ending with a higher level of infections. These differences can be understood going back to Figure 8.12. There we can distinguish that the main difference comes from those nodes highly protected by $u \simeq 1$, which are more frequent with the April distribution.

USC UNIVERSIDADE DE SANTIAGO DE COMPOSTELA

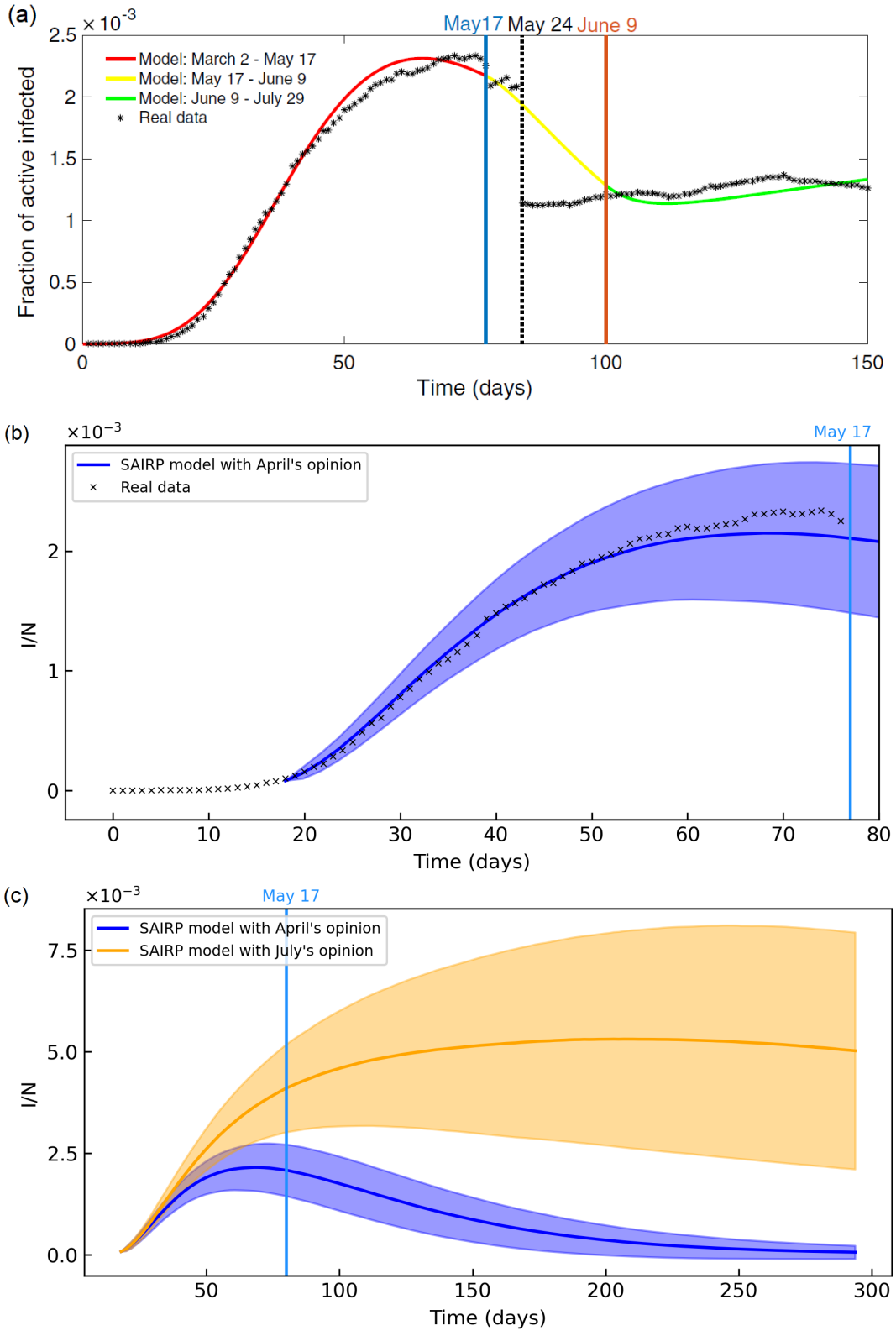


Figure 8.13: (a) Fraction of confirmed active cases per day in Portugal (black), with the red line being the nonlinear fit of the deterministic SAIRP model from March 2 to May 17, 2020, the yellow line the fit from May 17 to June 9, 2020, and the green line the one from June 9 to July 29, 2020. (b) Time evolution of the SAIRP network model coupled with the April 2020 opinion distribution (blue line) for the time period between March 2 to May 17, 2020; in contrast to the fraction of confirmed active cases (red crosses here, black stars in panel (a)). The bluish shadow marks the uncertainty of the model caused by the random estimation of the probabilities and the effect of initial random conditions. (c) Comparison of the SAIRP model coupled with the April 2020 opinion distribution (blue line), with the SAIRP model coupled with the July 2020 opinion distribution (orange line). For both panels (b) and (c), mobility networks of size $N = 25000$ with a Watts-Strogatz network topology of mean connectivity $\langle k \rangle = 5$ and rewiring probability $p_r = 0.01$

8.5 Conclusions

Throughout this chapter, we introduced a systematic approach to incorporate the state of opinion within a society into the dynamics of an epidemic. By leveraging data from social media platforms, we parameterize the social situation of a society at different time points and uncover significant variation in opinions and behavioral responses. Then, we introduced a weighted network approach for coupling the opinion dynamics into epidemic models. By capturing the population's willingness to adhere to preventive measures, we effectively modified individuals' susceptibility to infection, providing valuable insights for public health interventions.

The observed differences between the social situations found between October 2019 and April 2020, demonstrate the crucial role of public behavior in shaping the course of an epidemic and therefore, the importance of its consideration in the modelling process. The higher acceptance and adherence to public health recommendations in the opinion distribution obtained from the April 2020 network, contributed to a more favorable outcome in terms of infection peak reduction and delayed occurrence. This findings emphasize therefore the need to consider societal opinion as a crucial factor in epidemic modeling and decision-making. By accurately capturing the evolving opinions and behavioral habits of the population, we can enhance the accuracy and effectiveness of epidemic predictions and control strategies. Furthermore, the incorporation of opinion dynamics opens up new avenues for research, such as exploring the role of influential nodes in shaping collective behavior and designing targeted interventions to promote positive opinion adoption.

Another key conclusion of this work is the importance of raising awareness about the significance of non-pharmaceutical interventions. We carefully parametrized how the higher the awareness in the population (represented by larger values of the opinion ratio ν), the lower was the infection peak, with also significant delays in the timing of the peak (see Figure 8.10). The dispersion in the opinions was also found to be of great importance and can either help to control the epidemic or to exacerbate it depending on the majority trend ν. Figure 8.9 illustrates both behaviors at the same time. In a situation where scepticism predominates ($\nu = 0.5$), we see that it is best to keep the highest number possible of individuals protected ($\sigma \to 0$), as increasing slightly the dispersion in both sides of the opinion leads to higher peaks of infection. We have also seen in this case that larger values of σ help to increase the overall levels of protection, which although does not reduce the peak of infection, at least helps to delay it. For situations where there is at least a 50% of the population adhering to the social distancing, increasing the dispersion leads always to worse outcomes.

USC UNIVERSIDADE DE SANTIAGO DE COMPOSTELA

USC
UNIVERSIDADE
DE SANTIAGO
DE COMPOSTELA

Chapter 9

Summary and Conclusion

Throughout this thesis, we have investigated the dynamics of multiple populations of different individuals, with each population doing its own thing. We have seen phase oscillators that moved around in circles looking at each other. We have seen chemical particles that swam and bathed in a reacting solution changing their colors periodically. We have seen more or less stubborn individuals taking the sides of a debate, and we have seen cities suffering the invasion of epidemic waves. Different systems yes, but connected by the same mathematical principles, complex structures and nonlinear mathematical equations. In each case, the behaviors of the elementary units were strongly influenced by the topology of the networks connecting them. From this connections always emerged something, either phase synchronization, polarization of ideas or epidemic waves. We could also say that each chapter of this thesis forms a node of its own, with some of them being tied closer than others but yet forming a network whose emergent property are the conclusions of this dissertation. One of this conclusions is a general one of the field: that to fully comprehend the dynamics of the complex system, you need then to understand thoroughly the way in which its parts communicate. In each chapter, and as we summarized below, we have considered ways of increasing the complexity of the interactions between this individuals, and in each case modifying the interaction structure resulted in new emergent amazing properties or strong modifications of the pre-existing ones, either by including higher order network structures or by introducing opinion biased weights. All this lead either to new and remarkable dynamic regimes or to significant changes in the emerging phenomena at hand.

We started from the most level of abstraction in Chapter 3, with one of the simpler dynamical models that can show collective behavior. We started here with the case of regular networks, where all the phase oscillators were connected in an all-to-all fashion, the most ordered level of network structure. The increasing in complexity that we considered here came from the introduction of higher order structures in the geometry of interactions, or in simpler words, considering group interactions of three oscillators simultaneously. Here we saw how this increase in complexity resulted in the emergence of two types of multi-stable clustering states, with one of them being able to synchronize even when the coupling forces were fully repulsive. At the same time, we observed how the phase transitions of the system were abruptly changed (literally), with enigmatic discontinuities arising where they were least expected.

In our following step, we reduced the abstraction by considering more realistic oscillators based on the Belousov-Zhabotinsky chemical reaction, where now not only the phase but the amplitude and the period of oscillation could change with the control parameters. For Chapter

USC DE COMPOSTELA

4, the network passed from being global to purely local (although yet quite regular). Here, the increase in the complexity translated in richer behaviors from those observed in the mean-field scenario. Now, intermittent but synchronized regimes could emerge, showing complicated and irregular oscillating patterns caused by low-mixing rates in the system. Spatial clusters of synchronized activity were also found in the case of zero mixing. On the other hand, in Chapter 5, we introduced the experimental counterpart of the BZ reaction, presenting an experimental setup where we could control the dynamics of the chemical oscillators. Furthermore, this setup allowed us to stablish connections between them, building an experimental network of self-regulating oscillators. This seminal work has opened the doors to future investigations including much complex interactions, allowing us to consider any arbitrary topology of connections. What's more, the use of this setup could be applied for considering group interactions too, a very recent subfield of study of complex systems where there is still an important lack of experimental ground. In this way, we closed our study of synchronization as an emergent phenomena having almost closed the loop. We started from the simplest case of simulated phase oscillators on the Kuramoto model, studying how group interactions could modify some well-known dynamics; and ended up with an experimental setup where this theory could be tested eventually.

In the second part of this thesis, we focused on a set of dynamics more applied to human and social sphere where the nodes represented people and the links their different ways of communication. In Chapter 6, we saw how opinion polarization is an emergent property that is purely caused by the collective behavior. Inspired by the Turing instability as a plausible mechanism for opinion differentiation, we connected the spectra of a given interaction matrix with the potentiality for sustaining polarized states in opinion models. In this way, we showed how the different network topologies affect this process, where large values of the second order moment of the connectivity distribution $\langle k^2 \rangle$ were key to induce the differentiation of node's opinions. In this sense, and as occurs both in synchronization and epidemics when scale-free networks are considered, the divergence of the $\langle k^2 \rangle$ could also explain here why the polarization levels have been increasing, as the polarization threshold for opinions has also vanished. Further developing the application of the growth rates to opinion models will help us clarify this hypothesis in future investigation.

We have seen also that the linear stability analysis carried in the study of polarization has also very promising features to predict emerging epidemic waves. With metapopulation spatial networks, we have modelled the large-scale network structure of the regions of Galicia and Spain, and have estimated the degree of instability for each municipality, or in other words, the level of risk of an emergent outbreak. For this estimation to be the most realistic as possible, we have considered both the unique geographical and demographical properties of each town, with a mobility adjacency matrix connecting every pair of towns based on the commuting of individuals between the locations. Using certain control parameters, we modified on one hand the levels of mobility of this matrix and on the other the social mixing between individuals in order to assess different confinement strategies. Besides reproducing to well agreement the complex geographical evolution of the COVID-19, the descriptor presented here allowed us to tackle such a computationally demanding task and simplify it to an analytical calculations. This allowed us to afford hours of simulation time and computing resources, offering a very efficient benchmark where we could test plenty of confinement strategies within the limits of a personal computer. With this benchmark, one of our main findings suggested that an isolation by age groups, reducing completely the social mixing of half of the groups, could be more optimal

than a mobility restriction by municipalities, where all travels between different localities would have been prohibited.

Finally, we considered an approach that merges both previous dynamics, and studies the interplay between polarized opinion distributions and epidemic waves. First we analized the Spanish social network of Twitter, showing how its structure and emergent properties fluctuate and evolve in time, as an accurate mirror of the state of society. In this way, we estimated the opinion state at two moments in time near the start of the COVID-19 pandemic, relating the opinion values with the willingness to adhere to non-pharmaceutical interventions. Coupling these opinions with epidemic models proved that even the slightest differences in the opinion distributions could affect the evolution of the pandemic waves. Furthermore, considering polarized bimodal distributions, we have found that, curiously, the more polarized is the distribution (in the sense of lower dispersion values), the more can be halted the epidemic spread. Of course, the best results regarding halting the epidemic were found for situations where the agreers dominated the distrbution, but we have seen in general that increasing the dispersion in both sides of the opinions leads to higher peaks of infection. As the dispersion is increased and the opinion starts to be more distributed, the effect of the contrarians is way more harmful for the overall population than what is achieved from the protection managed by the agreers. This occurs because as the disease spreads quickly between most of the contrarians, it will eventually reach those nodes that are not perfectly protected. This could reveal thus the importance of committing fully to the public health measures, as adhering to them only at some times (with opinions of $u \simeq 0.5$) does help to delay the timing of the peak but not to reduce the final ammount of infected cases.

In summary, we have tackled several problems from the perspective of complex networks, gaining from each one, new and transversal insights of how emergent dynamics origin.

USC
UNIVERSIDADE DE SANTIAGO DE COMPOSTELA

USC
UNIVERSIDADE
DE SANTIAGO
DE COMPOSTELA

Appendices

USC
UNIVERSIDADE
DE SANTIAGO
DE COMPOSTELA

USC
UNIVERSIDADE
DE SANTIAGO
DE COMPOSTELA

Appendix A

A.1 Growth rates of the age-structure SEIR model

Here we show the complete derivation of the linear stability analysis and growth rate calculus for the age-structure SEIR model (eq. 7.16):

$$\begin{cases} \dot{S}_i = -\sum_{j=1}^{4} \beta_j I_j \beta_i S_i \left(\frac{M_{ji}}{N_i^l} + \frac{M_{ij}}{N_i^r} \right) \\ \dot{E}_i = \sum_{j=1}^{4} \beta_j I_j \beta_i S_i \left(\frac{M_{ji}}{N_i^l} + \frac{M_{ij}}{N_i^r} \right) - \nu E_i \\ \dot{I}_i = \nu E_i - \mu I_i \\ \dot{R}_i = \mu I_i \end{cases} \tag{A.1}$$

We consider a perturbation in the form

$$(S_i, E_i, I_i, R_i) = (\overline{S}_i, \overline{E}_i, \overline{I}_i, \overline{R}_i) + (\delta S_i, \delta A_i, \delta I_i, \delta P_i)$$

where $(\overline{S}_i, \overline{E}_i, \overline{I}_i, \overline{R}_i) = (N_i, 0, 0, 0)$. Applying the linearization at first order around the fixed point, we obtain that these perturbation evolves according to,

$$\begin{cases} \dot{\delta S}_i = -\sum_{j=1}^{4} \left(\frac{M_{ji}}{N_i^l} - \frac{M_{ij}}{N_i^r} \right) \beta_j \bar{I}_j \beta_i \delta S_i + \sum_{j=1}^{4} \left(\frac{M_{ji}}{N_i^l} + \frac{M_{ij}}{N_i^r} \right) \beta_j \delta I_j \beta_i \overline{S}_i \\ \dot{\delta E}_i = \sum_{j=1}^{4} \left(\frac{M_{ji}}{N_i^l} + \frac{M_{ij}}{N_i^r} \right) \beta_j \bar{I}_j \beta_i \delta S_i + \sum_{j=1}^{4} \left(\frac{M_{ji}}{N_i^l} + \frac{M_{ij}}{N_i^r} \right) \beta_j \delta I_j \beta_i \overline{S}_i - \nu \delta E_i \\ \dot{\delta I}_i = \nu \delta E_i - \mu \delta I_i \\ \dot{\delta R}_i = \mu \delta I_i \end{cases} \tag{A.2}$$

As demonstrated in the methods, these perturbations might grow over the set of eigenvectors of the adjacency matrix that describes the structures of the interactions. For this purpose, it is convenient to redefine our adjacency matrix of our problem as,

$$A_{ij} = \left(\frac{M_{ij}}{N_i} + \frac{M_{ij}}{N_j} \right) \beta_j \tag{A.3}$$

USC UNIVERSIDADE DE SANTIAGO DE COMPOSTELA

Its eigenvalues Λ_α and eigenvectors $\Phi^(\alpha) = \{\phi_1^{(\alpha)}, ..., \phi_N^{(\alpha)}\}$ for each mode α are given by

$$\sum_{\alpha=1}^{n} A_{ij}\phi_j^{(\alpha)} = \Lambda_\alpha \phi_i, \qquad \alpha = 1, ..., n \tag{A.4}$$

Over this set of adjacency eigenvectors, any perturbation δX_i expandas as,

$$\delta X_i = \sum_{\alpha=1}^{n} c_\alpha e^{\lambda_\alpha t}\phi_i^{(\alpha)} \tag{A.5}$$

where c_α are the coefficients associated to each variable and mode. Introducing the previous solution in eqs.A.6, we obtain,

$$\begin{cases} \sum_{\alpha=1}^{n} \lambda_\alpha \cancel{e^{\lambda_\alpha t}}\phi_i^{(\alpha)} &= -\beta_i \sum_{j=1}^{4} A_{ij}\bar{I}_j \sum_{\alpha=1}^{n} \cancel{e^{\lambda_\alpha t}}\phi_i^{(\alpha)} - \beta_i \sum_{j=1}^{4} A_{ij}\bar{S}_i \sum_{\alpha=1}^{n} C_\alpha \phi_i^{(\alpha)} \cancel{e^{\lambda_\alpha t}} \\ \sum_{\alpha=1}^{n} B_\alpha \lambda_\alpha \phi_i^{(\alpha)} &= \beta_i \sum_{j=1}^{4} A_{ij}\bar{I}_j \sum_{\alpha=1}^{n} \phi_i^{(\alpha)} + \beta_i \sum_{j=1}^{4} A_{ij}\bar{S}_i \sum_{\alpha=1}^{n} C_\alpha \phi_i^{(\alpha)} - \nu \sum_{\alpha=1}^{n} B_\alpha \phi_i^{(\alpha)} \\ \sum_{\alpha=1}^{n} C_\alpha \lambda_\alpha \phi_i^{(\alpha)} &= \nu \sum_{\alpha=1}^{n} B_\alpha \phi_i^{(\alpha)} - \mu \sum_{\alpha=1}^{n} C_\alpha \phi_i^{(\alpha)} \\ \sum_{\alpha=1}^{n} D_\alpha \lambda_\alpha \phi_i^{(\alpha)} &= \mu \sum_{\alpha=1}^{n} C_\alpha \phi_i^{(\alpha)} \end{cases} \tag{A.6}$$

where we can cancel the exponential terms $e^{\lambda_\alpha t}$ as we showed in the first equation. Exchanging the order of the sums, we can simplify the equations using the eigenvalue eq. A.4,

$$\begin{cases} \sum_{\alpha=1}^{n} \lambda_\alpha \phi_i^{(\alpha)} &= -\beta_i \sum_{j}^{n} \sum_{\alpha=1}^{n} \bar{I}_j \Lambda_\alpha \phi_i^{(\alpha)} - \beta_i \bar{S}_i \sum_{\alpha=1}^{n} C_\alpha \Lambda_\alpha \phi_i^{(\alpha)} \\ \sum_{\alpha=1}^{n} B_\alpha \lambda_\alpha \phi_i^{(\alpha)} &= \beta_i \sum_{j}^{n} \sum_{\alpha=1}^{n} \bar{I}_j \Lambda_\alpha \phi_i^{(\alpha)} + \beta_i \bar{S}_i \sum_{\alpha=1}^{n} C_\alpha \Lambda_\alpha \phi_i^{(\alpha)} \\ \sum_{\alpha=1}^{n} C_\alpha \lambda_\alpha \phi_i^{(\alpha)} &= \nu \sum_{\alpha=1}^{n} B_\alpha \phi_i^{(\alpha)} - \mu \sum_{\alpha=1}^{n} C_\alpha \phi_i^{(\alpha)} \\ \sum_{\alpha=1}^{n} D_\alpha \lambda_\alpha \phi_i^{(\alpha)} &= \mu \sum_{\alpha=1}^{n} C_\alpha \phi_i^{(\alpha)} \end{cases} \tag{A.7}$$

In this way, for each node i and mode α, we have a set of n independent equations that conform the following eigenvalue problem,

$$\lambda_\alpha \begin{pmatrix} 1 \\ B_\alpha \\ C_\alpha \\ D_\alpha \end{pmatrix} = \begin{pmatrix} -\beta_i \sum_j^n \bar{I}_j \Lambda_\alpha & 0 & -\beta_i \bar{S}_i \Lambda_\alpha & 0 \\ \beta_i \sum_j^n \bar{I}_j \Lambda_\alpha & -\nu & \beta_i \bar{S}_i \Lambda_\alpha & 0 \\ 0 & \nu & -\mu & 0 \\ 0 & 0 & \mu & 0 \end{pmatrix} \begin{pmatrix} 1 \\ B_\alpha \\ C_\alpha \\ D_\alpha \end{pmatrix} \tag{A.8}$$

In our case, we considered that the stationary state consists of every individual of the population being in the susceptible compartment, therefore $\overline{S_i} = N_i$ and $\overline{I_j} = 0$ elsewhere. In

order to compute λ_α and obtain the dispersion relation, we need to solve the determinant,

$$\begin{vmatrix} -\lambda_\alpha & 0 & -\beta_i N_i \Lambda_\alpha & 0 \\ 0 & -\nu-\lambda_\alpha & \beta_i N_i \Lambda_\alpha & 0 \\ 0 & \nu & -\mu-\lambda_\alpha & 0 \\ 0 & 0 & \mu & -\lambda_\alpha \end{vmatrix} = 0 \tag{A.9}$$

Operating, starting from the left,

$$-\lambda_\alpha \left[(-\nu-\lambda_\alpha)(mu-\lambda_\alpha)(-\lambda_\alpha)+\beta_i N_i \Lambda_\alpha(\nu\lambda_\alpha)\right] = 0 \tag{A.10}$$

From here we can already see that one solution goes to zero, while the another one follows from substracting the common factor λ_α to the parenthesis. This leaves only the second order equation,

$$(\nu+\lambda_\alpha)(\mu+\lambda_\alpha)-\beta_i N_i \nu \Lambda_\alpha = \lambda_\alpha^2+(\mu+\nu)\lambda_\alpha+\mu\nu-\beta_i N_i \nu \Lambda_\alpha = 0 \tag{A.11}$$

whose solutions are obtained as,

$$\lambda_\alpha = \frac{-(\mu+\nu) \pm \sqrt{(\mu+\nu)^2-4(\mu\nu-\beta_i N_i \nu \Lambda_\alpha}}{2} \tag{A.12}$$

This is the equation shown in (7.17) in the main text of the chapter.

USC UNIVERSIDADE DE SANTIAGO DE COMPOSTELA

USC
UNIVERSIDADE
DE SANTIAGO
DE COMPOSTELA

Appendix B

B.1 Numerical integration of ODEs

Along the different chapters of this thesis, we are presented with different non-linear differential equations that we can solve doing the integration numerically. For that purpose, we generated our own software based mainly in `Python` that automated the input for any nonlinear function and any number of variables.

Given a set of N first order ordinary differential equations:

$$\frac{dx_k}{dt} \equiv \dot{x}_k(t) = f_k(t, x_1(t), ..., x_N(t)), \text{ with } k = 1, ..., N \text{ and } t \in [t_0, T] \tag{B.1}$$

we want to solve the initial value problem, this is, obtaining the trajectory of a given initial condition $x_k(t_0) = x_{k,0}$ across the dynamics of the system. For this purpose, we assume that $x_{k,0} \in \mathbb{R}$, $t_0, T \in \mathbb{R}$ and that functions f_k are continuous. We aim to discretize the interval $[t_0, T]$ in N equal parts $h = \frac{T-t_0}{N}$, obtaining at each time step $t_i = t_0 + ih$ the solution values of each variable k.

The easiest approach to solve this problem is with the **explicit Euler method**. For the moment, to simplify notation, let us focus on just one variable and subtitute the variable sub-index k by the time sub-index i. Using the definition of the derivative of a function and assuming that h is sufficiently small,

$$\dot{x}(t) = \lim_{h \to 0} \frac{x(t+h) - x(t)}{h} \simeq \frac{x(t+h) - x(t)}{h} \tag{B.2}$$

In this way, we can approximate the derivative at time t_i, $\dot{x}(t_i) = f(t_i, x(t_i))$, as

$$\frac{x(t_{i+1}) - x(t_i)}{h} \simeq f(t_i, x(t_i)) \tag{B.3}$$

or, in numerical notation:

$$\frac{x_{i+1} - x_i}{h} = f(t_i, x_i) \tag{B.4}$$

where now x_i is an approximation of the exact solution $x(t)$ at time t_i. In this way, starting from the initial condition x_0, we can approximate the integration of equations B.1 recursively, obtaining the solution at the next step in time as

$$x(t_{i+1}) = x_i + hf(t_i, x_i) \tag{B.5}$$

USC UNIVERSIDADE DE SANTIAGO DE COMPOSTELA

However, simplicity only gets you so far. The local truncation error of a method is the difference between the numerical solution of the method and the exact solution of the equations at each time step. It gives a measure of the method's precision, and in the case of the Euler method it grows with $\mathcal{O}(h^2)$. So, it is suitable when the dynamics do not change too much between time steps or when you are in a exploratory phase with your new model and you don't need to integrate over long periods of time. If your model is highly nonlinear and you require a lot of precision, then something more sophisticated is needed.

The explicit Runge-Kutta family of methods are derived from the following expansion:

$$x_{i+1} = x_i + h \sum_{n=1}^{r} c_n k_n(t, x_i, h) \tag{B.6}$$

with

$$k_n(t, x_i, h) = f\left(t + hb_n, x_i + h \sum_{j=1}^{r} a_{nj} k_j(t, x_i, h)\right),\ n = 1, 2, ..., r \tag{B.7}$$

where constants c_n, b_n and a_{nj} are tabled in the *Butcher tableau* and are chosen accordingly to the order of precision desired. Each choice determines a different method, being the most common the 4th order Runge-Kutta (RK4) because of its balance between precision order, with a local truncation error of $\mathcal{O}(h^5)$ and computational cost. It has the following functions k_n,

$$\begin{aligned}
k_1 &= f(t_i, x_i) \\
k_2 &= f(t_i + h/2, x_i + h\frac{k_1}{2}) \\
k_3 &= f(t_i + h/2, x_i + h\frac{k_2}{2}) \\
k_4 &= f(t_i + h/2, x_i + hk_3)
\end{aligned}$$

with each function being an estimated slope of the function f at different increments given by the product of the method's coefficients and the time step h (see Figure B.1)

Thus, following eq. B.6, the integration scheme for this case is obtained as:

$$x_{i+1} = x_i + \frac{h}{6}(k_1 + 2k_2 + 2k_3 + k_4) \tag{B.8}$$

This is the numerical method that we have mainly chosen to produce the findings presented in this thesis.

USC UNIVERSIDADE DE SANTIAGO DE COMPOSTELA

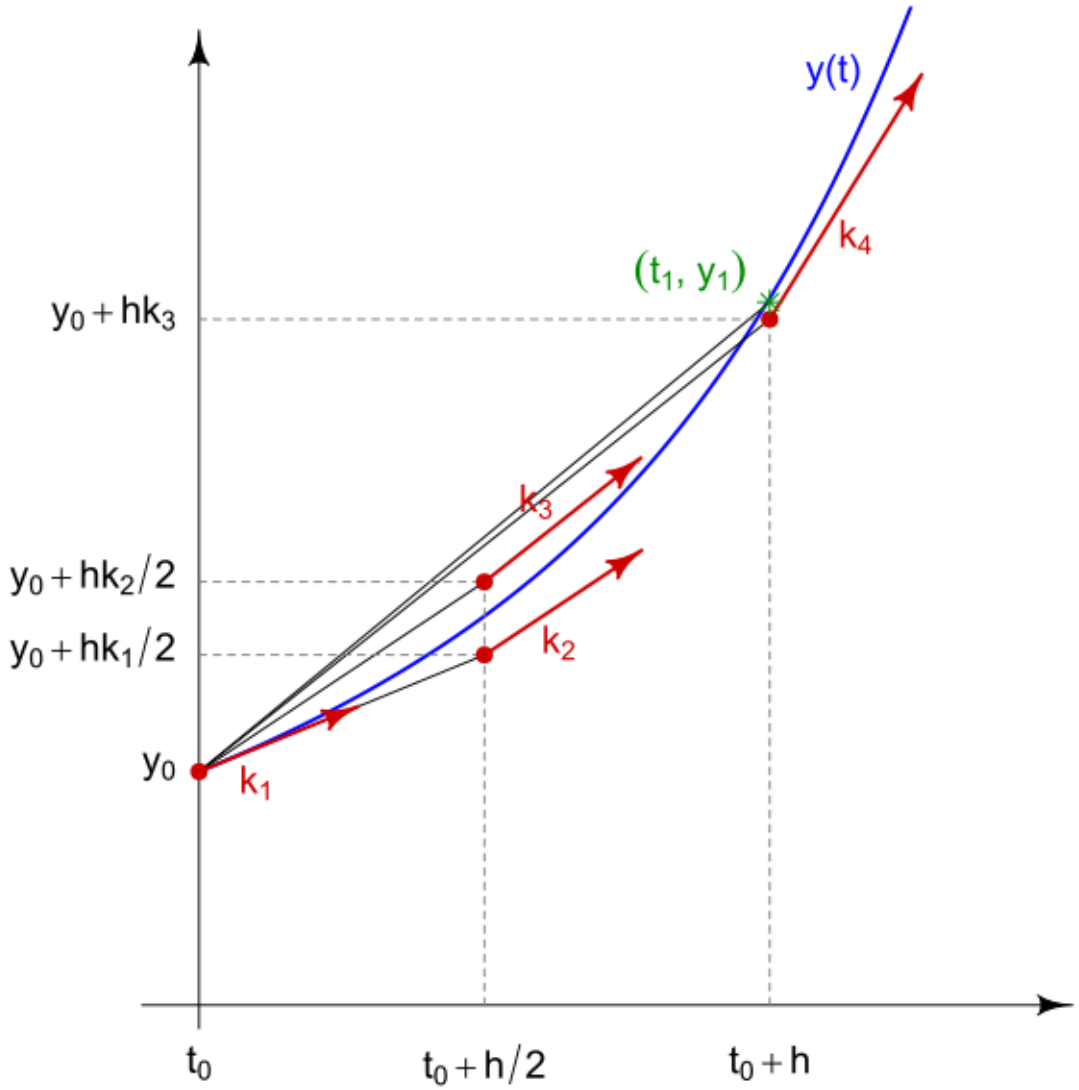


Figure B.1: Estimation of the different slopes by the functions k_n of the RK4 method. [`https://en.wikipedia.org/wiki/RungeKutta_methods`]

USC UNIVERSIDADE DE SANTIAGO DE COMPOSTELA

USC
UNIVERSIDADE
DE SANTIAGO
DE COMPOSTELA

List of Publications

From the work carried out in this thesis stems the following list of publications. Below it is stated the work carried out by the author in each contribution and the details and impact metrics of each journal.

1. Carballosa, A., Mussa-Juane, M. & Muñuzuri, A.P. *"Incorporating social opinion in the evolution of an epidemic spread"*. Scientific Reports 11, 1772 (2021), eISSN 2045-2322, https://doi.org/10.1038/s41598-021-81149-z.

2. Carballosa, A., Mussa-Juane, M. & Muñuzuri, A.P. *"Social Opinion Influence on Epidemic Scenarios"*. In: Agarwal, P., Nieto, J.J., Ruzhansky, M., Torres, D.F.M. (eds) Analysis of Infectious Disease Problems (Covid-19) and Their Global Impact (2021). Springer, Singapore. Chapter 22, p. 465-482, online ISBN 978-981-16-2450-6. https://doi.org/10.1007/978-981-16-2450-6_21

3. Silva, C.J., Cruz, C., Torres, D.F.M., Muñuzuri, A. P., Carballosa, A. et al. *"Optimal control of the COVID-19 pandemic: controlled sanitary deconfinement in Portugal"*. Scientific Reports 11, 3451 (2021), eISSN 2045-2322. https://doi.org/10.1038/s41598-021-83075-6

4. Carballosa, A., Balsa-Barreiro, J., Garea, A.,García-Selfa, D., Miramontes, A., & Muñuzuri, A.P., *"Risk evaluation at municipality level of a COVID-19 outbreak incorporating relevant geographic data: the study case of Galicia"*. Scientific Reports 11, 21248 (2021), eISSN 2045-2322. https://doi.org/10.1038/s41598-021-00342-2

5. Carballosa, A., Balsa-Barreiro, J., Boullosa, P., Garea, A., Mira, J., Miramontes, A., & Muñuzuri, A.P., *"Assessing the risk of pandemic outbreaks across municipalities with mathematical descriptors based on age and mobility restrictions"*, Chaos, Solitons & Fractals, Volume 160, 112156 (2022), eISSN 1873-2887. https://doi.org/10.1016/j.chaos.2022.112156.

6. Carballosa A. & Muñuzuri, A.P, *"Intermittency regimes of poorly-mixed chemical oscillators"*, Chaos, Solitons & Fractals, Volume 157, 111920 (2022), eISSN 1873-2887.https://doi.org/10.1016/j.chaos.2022.111920.

7. Flores-Arias M.T., Gómez-Varela A.I., Muñuzuri A.P., Carballosa A., Bao-Varela C. *"Micro-reactors fabricated by Subaquatic indirect Laser-Induced Plasma-Assisted Ablation on soda-lime glass substrates"*, European Physical Journal Web of Conferences 266, 13012 (2022), eISSN: 2100-014X. https://doi.org/10.1051/epjconf/202226613012

USC UNIVERSIDADE DE SANTIAGO DE COMPOSTELA

8. Paramés-Estévez S., Carballosa A., García-Selfa D. & Muñuzuri A.P. *"Artificial Intelligence Techniques Used to Extract Relevant Information from Complex Social Networks"*, Entropy 25 (3), 507 (2023), eISSN 1099-4300. https://doi.org/10.3390/e25030507

9. Carballosa A., Crego A. & Muñuzuri A.P. *"Quantifying the potentiality for polarization in opinion networks"*, Chaos Solitons & Fractals Volume 173, 113697 (2023), eISSN 1873-2887. https://doi.org/10.1016/j.chaos.2023.113697

10. Carballosa A., Muñuzuri A.P., Boccaletti S., Torcini A. & Olmi S. *"Cluster states and the π-transition in the Kuramoto model with higher order interactions"* arXiv (2023), https://doi.org/10.48550/arXiv.2308.05406 (in press)

Authorship

As main author or main co-author of publications 1,2,4,5,6, 9 and 10, my contributions in these works involved all aspects of the papers, that range from the discussions of the original idea till the elaboration of the manuscripts, including also most of the numerical modelling, simulations and preparation of the Figures. In publication number 3, I mainly contributed with a full subsection of the results, with own numerical simulations, data analysis and participation in the writing of the text. In 7, I participated in the text revision, study design and the preparation of the supporting figures. In 8, I participated in the development of the software used for data recollection and was involved significantly in the revision, discussion and writing of the manuscript.

Journal details and quality indexes

- *Scientific Reports* is a multidisciplinary (Q1) open access journal from the Nature publishing group with a 2-year impact factor (IF) of 4.996 (2021), a cite-score of 7.1 (2022) and an h-index of 282.

- *Chaos, Solitons & Fractals* is an applied mathematics (Q1) and physics and astronomy (Q1) journal from the Elsevier Ltd. publishing group that supports open access, with a 2-year impact factor (IF) of 7.8 (2022), a cite-score of 11.8 and an h-index of 160

- *Entropy* is a multidisciplinary (Q2) and applied mathematics (Q1) open access journal from the MDPI publishing group with an impact factor (IF) of 2.7 (2022), a cite-score of 4.7 and an h-index of 91.

Patents

From the work carried out in Chapter 8 also stemmed the software patent "EIRCAPIT", registered under number 03/2022/779. We developed this software in order to access to the Twitter API and design the queries needed for automate the download and processing of data.

USC UNIVERSIDADE DE SANTIAGO DE COMPOSTELA

Copyright permissions

Journal publications

All the journal publications reproduced in this thesis are published either within open-access journals or with the open-access option as stated below.

1. For articles [1],[3] and [4] published in *Scientific Reports* (ISSN 2045-2322), it is explicitly stated by the Copyright Clearing Center (CCC) that *"this is an open access article distributed under the terms of the Creative Commons CC BY license which permits unrestricted use, distribution, and reproduction in any medium, provided the original work is properly cited. You are not required to obtain permission to reuse this article."*

2. Articles [5], [6], and [9] are published in *Chaos, Solitons & Fractals* (ISSN 1873-2887) with an open access option, also under the terms of a Creative Commons CC-BY license. Besides, it is stated by the CCC that *´´as the author of this Elsevier article, you retain the right to include it in a thesis or dissertation, provided it is not published commercially. Permission is not required, but please ensure that you reference the journal as the original source.".*

3. Article [8] is published in *Entropy* (ISSN 1099-4300) also in open access under a Creative Commons CC BY license. The same applies for article [7] in *EPJ Web of Conferences* (ISSN 2100-014X).

4. Only for book chapter [2] *"Social Opinion Influence on Epidemic Scenarios"* was required an explicit authorization from *Springer Nature* in the form of license, which is attached in what-follows.

Figures not of own making

- Panels (a) and (b) of Figure 1.1 contain images from the free copyright website `https://pixabay.com/` that are subject to a Creative Commons Zero (CC0) license. In the Terms of Service, they state that "the CC0 Content can be used for all personal and commercial purposes without attributing the author/ content owner of the CC0 Content or Pixabay". Here we declare that the use given to these photos do not represent one of the cases declared in the exceptions to these terms.

- Panel (c) of Figure 1.1 contains an imaged acquired from the Wikipedia article `https://en.wikipedia.org/wiki/Lichen_growth_forms#/media/File:Variospora_flavescens_232782.jpg` under a Creative Commons 3 license that

USC UNIVERSIDADE DE SANTIAGO DE COMPOSTELA

allows for reproducing with proper attribution. Original image by user zaca at Mushroom Observer, a source for mycological images. This image is Image Number 232782 at Mushroom Observer, a source for mycological images., with license CC BY-SA 3.0.

- Figure B.1 contains an image acquired from the Wikipedia article `https://en.wikipedia.org/wiki/Runge%E2%80%93Kutta_methods#/media/File:Runge-Kutta_slopes.svg` with license Creative Commons CC-BY 4 that allows for reproducing with proper attribution. Original image by HilberTraum, with license CC BY-SA 4.0.
- Figure 1.6(a) contains an image acquired from the Wikipedia article `https://en.wikipedia.org/wiki/Leopard#/media/File:African_leopard_male_(cropped).jpg` with license Creative Commons CC-BY 4 that allows for reproducing with proper attribution. Original image by Sumeet Moghe, with license CC BY-SA 4.0.
- Figure 1.6(b,c) contain images of not own making but lent by Dr. Alberto P. Muñuzuri, director of this thesis.
- We declare that all the rest of the figures shown in this thesis were either of own making or reproduced from the publications stated above.

USC UNIVERSIDADE DE SANTIAGO DE COMPOSTELA

SPRINGER NATURE LICENSE
TERMS AND CONDITIONS

Jul 24, 2023

This Agreement between University of Santiago de Compostela -- Alejandro Carballosa Calleja ("You") and Springer Nature ("Springer Nature") consists of your license details and the terms and conditions provided by Springer Nature and Copyright Clearance Center.

License Number	5595271145465
License date	Jul 24, 2023
Licensed Content Publisher	Springer Nature
Licensed Content Publication	Springer eBook
Licensed Content Title	Social Opinion Influence on Epidemic Scenarios
Licensed Content Author	Alejandro Carballosa, Mariamo Mussa-Juane, Alberto P. Muñuzuri
Licensed Content Date	Jan 1, 2021
Type of Use	Thesis/Dissertation
Requestor type	academic/university or research institute
Format	print and electronic
Portion	full article/chapter
Will you be translating?	no

USC UNIVERSIDADE DE SANTIAGO DE COMPOSTELA

Circulation/distribution	1 - 29
Author of this Springer Nature content	yes
Title	Collective phenomena and coherent structures in complex networks (provisional)
Institution name	University of Santiago de Compostela
Expected presentation date	Dec 2023
Order reference number	12131415
Requestor Location	University of Santiago de Compostela Rúa do Escultor Asorey 12, Segundo Santiago de Compostela, A Coruña 15704 Spain Attn: University of Santiago de Compostela
Billing Type	Invoice
Billing Address	University of Santiago de Compostela Rúa do Escultor Asorey 12, Segundo Santiago de Compostela, Spain 15704 Attn: University of Santiago de Compostela
Total	0.00 EUR

Terms and Conditions

Springer Nature Customer Service Centre GmbH Terms and Conditions

The following terms and conditions ("Terms and Conditions") together with the terms specified in your [RightsLink] constitute the License ("License") between you as Licensee and Springer Nature Customer Service Centre GmbH as Licensor. By clicking

'accept' and completing the transaction for your use of the material ("Licensed Material"), you confirm your acceptance of and obligation to be bound by these Terms and Conditions.

1. Grant and Scope of License

1. 1. The Licensor grants you a personal, non-exclusive, non-transferable, non-sublicensable, revocable, world-wide License to reproduce, distribute, communicate to the public, make available, broadcast, electronically transmit or create derivative works using the Licensed Material for the purpose(s) specified in your RightsLink Licence Details only. Licenses are granted for the specific use requested in the order and for no other use, subject to these Terms and Conditions. You acknowledge and agree that the rights granted to you under this License do not include the right to modify, edit, translate, include in collective works, or create derivative works of the Licensed Material in whole or in part unless expressly stated in your RightsLink Licence Details. You may use the Licensed Material only as permitted under this Agreement and will not reproduce, distribute, display, perform, or otherwise use or exploit any Licensed Material in any way, in whole or in part, except as expressly permitted by this License.

1. 2. You may only use the Licensed Content in the manner and to the extent permitted by these Terms and Conditions, by your RightsLink Licence Details and by any applicable laws.

1. 3. A separate license may be required for any additional use of the Licensed Material, e.g. where a license has been purchased for print use only, separate permission must be obtained for electronic re-use. Similarly, a License is only valid in the language selected and does not apply for editions in other languages unless additional translation rights have been granted separately in the License.

1. 4. Any content within the Licensed Material that is owned by third parties is expressly excluded from the License.

1. 5. Rights for additional reuses such as custom editions, computer/mobile applications, film or TV reuses and/or any other derivative rights requests require additional permission and may be subject to an additional fee. Please apply to journalpermissions@springernature.com or bookpermissions@springernature.com for these rights.

2. Reservation of Rights

Licensor reserves all rights not expressly granted to you under this License. You acknowledge and agree that nothing in this License limits or restricts Licensor's rights in or use of the Licensed Material in any way. Neither this License, nor any act, omission, or statement by Licensor or you, conveys any ownership right to you in any Licensed Material, or to any element or portion thereof. As between Licensor and you, Licensor owns and retains all right, title, and interest in and to the Licensed Material subject to the license granted in Section 1.1. Your permission to use the Licensed Material is expressly conditioned on you not impairing Licensor's or the applicable copyright owner's rights in the Licensed Material in any way.

3. Restrictions on use

3. 1. Minor editing privileges are allowed for adaptations for stylistic purposes or formatting purposes provided such alterations do not alter the original meaning or intention of the Licensed Material and the new figure(s) are still accurate and representative of the Licensed Material. Any other changes including but not limited to, cropping, adapting, and/or omitting material that affect the meaning, intention or moral rights of the author(s) are strictly prohibited.

3. 2. You must not use any Licensed Material as part of any design or trademark.

3. 3. Licensed Material may be used in Open Access Publications (OAP), but any such reuse must include a clear acknowledgment of this permission visible at the same time as the figures/tables/illustration or abstract and which must indicate that the Licensed Material is not part of the governing OA license but has been reproduced with permission. This may be indicated according to any standard referencing system but must include at a minimum 'Book/Journal title, Author, Journal Name (if applicable), Volume (if applicable), Publisher, Year, reproduced with permission from SNCSC'.

4. STM Permission Guidelines

4. 1. An alternative scope of license may apply to signatories of the STM Permissions Guidelines ("STM PG") as amended from time to time and made available at https://www.stm-assoc.org/intellectual-property/permissions/permissions-guidelines/.

4. 2. For content reuse requests that qualify for permission under the STM PG, and which may be updated from time to time, the STM PG supersede the terms and conditions contained in this License.

4. 3. If a License has been granted under the STM PG, but the STM PG no longer apply at the time of publication, further permission must be sought from the Rightsholder. Contact journalpermissions@springernature.com or bookpermissions@springernature.com for these rights.

5. Duration of License

5. 1. Unless otherwise indicated on your License, a License is valid from the date of purchase ("License Date") until the end of the relevant period in the below table:

Reuse in a medical communications project	Reuse up to distribution or time period indicated in License
Reuse in a dissertation/thesis	Lifetime of thesis
Reuse in a journal/magazine	Lifetime of journal/magazine
Reuse in a book/textbook	Lifetime of edition
Reuse on a website	1 year unless otherwise specified in the License
Reuse in a presentation/slide kit/poster	Lifetime of presentation/slide kit/poster. Note: publication whether electronic or in print of presentation/slide kit/poster may require further

	permission.
Reuse in conference proceedings	Lifetime of conference proceedings
Reuse in an annual report	Lifetime of annual report
Reuse in training/CME materials	Reuse up to distribution or time period indicated in License
Reuse in newsmedia	Lifetime of newsmedia
Reuse in coursepack/classroom materials	Reuse up to distribution and/or time period indicated in license

6. Acknowledgement

6. 1. The Licensor's permission must be acknowledged next to the Licensed Material in print. In electronic form, this acknowledgement must be visible at the same time as the figures/tables/illustrations or abstract and must be hyperlinked to the journal/book's homepage.

6. 2. Acknowledgement may be provided according to any standard referencing system and at a minimum should include "Author, Article/Book Title, Journal name/Book imprint, volume, page number, year, Springer Nature".

7. Reuse in a dissertation or thesis

7. 1. Where 'reuse in a dissertation/thesis' has been selected, the following terms apply: Print rights of the Version of Record are provided for; electronic rights for use only on institutional repository as defined by the Sherpa guideline (www.sherpa.ac.uk/romeo/) and only up to what is required by the awarding institution.

7. 2. For theses published under an ISBN or ISSN, separate permission is required. Please contact journalpermissions@springernature.com or bookpermissions@springernature.com for these rights.

7. 3. Authors must properly cite the published manuscript in their thesis according to current citation standards and include the following acknowledgement: '*Reproduced with permission from Springer Nature*'.

8. License Fee

You must pay the fee set forth in the License Agreement (the "License Fees"). All amounts payable by you under this License are exclusive of any sales, use, withholding, value added or similar taxes, government fees or levies or other assessments. Collection and/or remittance of such taxes to the relevant tax authority shall be the responsibility of the party who has the legal obligation to do so.

9. Warranty

9. 1. The Licensor warrants that it has, to the best of its knowledge, the rights to license reuse of the Licensed Material. **You are solely responsible for ensuring that**

the material you wish to license is original to the Licensor and does not carry the copyright of another entity or third party (as credited in the published version). If the credit line on any part of the Licensed Material indicates that it was reprinted or adapted with permission from another source, then you should seek additional permission from that source to reuse the material.

9. 2. EXCEPT FOR THE EXPRESS WARRANTY STATED HEREIN AND TO THE EXTENT PERMITTED BY APPLICABLE LAW, LICENSOR PROVIDES THE LICENSED MATERIAL "AS IS" AND MAKES NO OTHER REPRESENTATION OR WARRANTY. LICENSOR EXPRESSLY DISCLAIMS ANY LIABILITY FOR ANY CLAIM ARISING FROM OR OUT OF THE CONTENT, INCLUDING BUT NOT LIMITED TO ANY ERRORS, INACCURACIES, OMISSIONS, OR DEFECTS CONTAINED THEREIN, AND ANY IMPLIED OR EXPRESS WARRANTY AS TO MERCHANTABILITY OR FITNESS FOR A PARTICULAR PURPOSE. IN NO EVENT SHALL LICENSOR BE LIABLE TO YOU OR ANY OTHER PARTY OR ANY OTHER PERSON OR FOR ANY SPECIAL, CONSEQUENTIAL, INCIDENTAL, INDIRECT, PUNITIVE, OR EXEMPLARY DAMAGES, HOWEVER CAUSED, ARISING OUT OF OR IN CONNECTION WITH THE DOWNLOADING, VIEWING OR USE OF THE LICENSED MATERIAL REGARDLESS OF THE FORM OF ACTION, WHETHER FOR BREACH OF CONTRACT, BREACH OF WARRANTY, TORT, NEGLIGENCE, INFRINGEMENT OR OTHERWISE (INCLUDING, WITHOUT LIMITATION, DAMAGES BASED ON LOSS OF PROFITS, DATA, FILES, USE, BUSINESS OPPORTUNITY OR CLAIMS OF THIRD PARTIES), AND WHETHER OR NOT THE PARTY HAS BEEN ADVISED OF THE POSSIBILITY OF SUCH DAMAGES. THIS LIMITATION APPLIES NOTWITHSTANDING ANY FAILURE OF ESSENTIAL PURPOSE OF ANY LIMITED REMEDY PROVIDED HEREIN.

10. Termination and Cancellation

10. 1. The License and all rights granted hereunder will continue until the end of the applicable period shown in Clause 5.1 above. Thereafter, this license will be terminated and all rights granted hereunder will cease.

10. 2. Licensor reserves the right to terminate the License in the event that payment is not received in full or if you breach the terms of this License.

11. General

11. 1. The License and the rights and obligations of the parties hereto shall be construed, interpreted and determined in accordance with the laws of the Federal Republic of Germany without reference to the stipulations of the CISG (United Nations Convention on Contracts for the International Sale of Goods) or to Germany´s choice-of-law principle.

11. 2. The parties acknowledge and agree that any controversies and disputes arising out of this License shall be decided exclusively by the courts of or having jurisdiction for Heidelberg, Germany, as far as legally permissible.

11. 3. This License is solely for Licensor's and Licensee's benefit. It is not for the benefit of any other person or entity.

Questions? For questions on Copyright Clearance Center accounts or website issues please contact springernaturesupport@copyright.com or +1-855-239-3415 (toll free in the US) or +1-978-646-2777. For questions on Springer Nature licensing please visit https://www.springernature.com/gp/partners/rights-permissions-third-party-distribution

Other Conditions:

Version 1.4 - Dec 2022

Questions? customercare@copyright.com.

USC UNIVERSIDADE DE SANTIAGO DE COMPOSTELA

USC
UNIVERSIDADE
DE SANTIAGO
DE COMPOSTELA

List of Figures

1.1 Examples of self-organization and spontaneous order in the form of spatiotemporal patterns in natural complex systems. (a) Beehive collective beehavior to produce and store honey in hexagonal formation, (b)Flock of migrating birds arranged in V-shape, (c) Licken growth under complex patterns and (d) auto-waves in the Belousov-Zhabotinsky reaction. Images (a) and (b) were taken from the copyright free repository `https://pixabay.com/`, image (c) from `https://commons.wikimedia.org/wiki/File:Variospora_flavescens_232782.jpg`, while image (d) is of own making. 2

1.2 Phase space of different dynamical states in function of two variables X and Y of the system and different system parameters. Different colors represent trajectories originating at different initial conditions, with arrows in (a) and (b) denoting the direction of the flow towards the stable attractor. Note that the dynamics of (a,b) and (c) are obtained through different toy models in order to highlight these behaviors. 6

1.3 Relevant considerations of possible network interactions. 8

1.4 Different network topologies based on their interaction pattern. From left to right, fully random network, "small-world" network (top row), regular/grid network and scale-free network (bottom row). See Methods for their description. 10

1.5 Collective synchrony in a set of phase oscillators for increasing values of the coupling strength K. Each blue point represents a different oscillator, whose phases are distributed in (a) between 0 and 2π. 11

1.6 Examples of spatial Turing patterns: Black dots in a leopard skin (a), simulated dots (b) and stripes (c) with the CARD model. In (d), autowaves in the BZ reaction. Image (a) is originally by Sumeet Moghe from `https://en.wikipedia.org/wiki/Leopard#/media/File:African_leopard_male_(cropped).jpg`; (b) and (c) are lended by Dr. Alberto P. Muñuzuri, while image (d) is of own making. 13

1.7 (a) Schematic of a metapopulation model, where each circle corresponds to a different population. In each town are nested the dynamics of the SIR model (b), where β represents the infectivity rate and μ the recovery rate. An example of the time evolution of its dynamics is shown in panel (c). 15

2.1 Network connectivity distributions for the Erdos-Renyi (ER), Watts-Strogatz(WS) and Scale-free (SF). We do not show the regular network as it would show a unique bar of probability 1 at a given value k, as all nodes have the same connectivity. 20

USC UNIVERSIDADE DE SANTIAGO DE COMPOSTELA

2.2 Geometric interpretation of the order parameter (eq. 2.7) and the global phase Φ for increasing levels of the coupling K. 21
2.3 Numerical simulations of the Kuramoto order parameter R versus the coupling strength K for a network of $N = 5 \cdot 10^4$ oscillators. The transition to the full-synchronization regime is of second-order type, characterized by a critical coupling K_c at which the order parameter starts to grow continuosly but exponentially. The black dashed line represents the critical value predicted by eq. 2.15 in the thermodinamic limit, which agrees quite well with our numerical results. 23
2.4 Schematic diagram of the key processes involved in the BZ reation. The bromous acid $HBrO_2$ is produced autocatalitically in step I, oxidizing the Ruthenium catalyst in the process. Then, the catalyst is reduced in step II because of the action of the bromo-malonic acid. Finally, the reaction between Br^- and $HBrO_2$ inhibits the autocatalytic oxidation of step I. This cycle repeats again when the concentration of Br^- decreases enough, and so the autocatalytic oxidation starts again. 27
2.5 Simulated dynamics of the Belousov-Zhabotinsky reaction with the oregonator model. IN (a), oscillations in the concentration of the catalyst z (a), and in (b), the limit-cycle in the phase space of (x,z). 29
2.6 (a) Effects of the light intensity (red dashed line) in the dynamics of the Belousov-Zhabotinsky reaction simulated with a variation of the oregonator model. The increasing oscillation period with the light intensity is shown in panel (b). 30
2.7 Three dispersion relation curves $\lambda_\alpha(\Lambda_\alpha)$ obtained from eq. 2.46 for different values of the model parameters. Those modes with $\mathrm{Re}(\lambda_\alpha > 0)$ will trigger an instability changing the system to another dynamical state. 35

3.1 Order parameters (b) against the inter-cluster angle α (a). R_1 is the global Kuramoto order parameter, R_D is the Daido-Kuramoto order parameter and R_B is our clustering order parameter defined in eq. 3.3 43
3.2 Potential $V(\phi)$ 3.12(in black) and frequencies $\Omega(\phi)$ 3.13 (red) versus the phase ϕ for positive $\lambda_2 = 15$ (a-b) and negative $\lambda_2 = -100$ (c-d). Panels (a,b) refers to $\lambda_1 = 3$,$\lambda_1 = -3$ respectively, while panels (c,d) to $\lambda_1 = 10$ and $\lambda_1 = -10$. The red solid curves identify the stable branches associated to phases locked oscillators, while the dashed lines the unstable ones. The dashed green (blue) vertical lines denote the angles $\pm\alpha$ ($\pm\beta$) demarking the stable/unstable regions. For all panels, $R_1 = 0.5$ and $\Omega = 0$. 46

USC
UNIVERSIDADE DE SANTIAGO DE COMPOSTELA

3.3 Numerical simulations from eq.3.8 of the order parameter R_1 as a function of the coupling parameters λ_1 and λ_2, for different frequency distributions. Namely, (a,b) unimodal Gaussian distribution centered at $\omega_0 = 0$ with a dispersion of $\Delta = 0.25$; (c,d,e,f) bimodal distributions centered at $\omega_0 = 1$ and $\omega_0 = 3$ respectively, both with $\Delta = 0.25$. Within the figures, the abbreviations distinguish the possible states of the system, namely the asynchronous state (AS), the fully-synchronous state (FS), the standing waves (SWs) and the bi-cluster states (BCs) and (UCs), depending on their phase distribution. Panels (a,c,e) correspond to simulations according to protocol (I) while panels (b,d,f) to simulations with protocol (II). For each point, the initial conditions are reset. The total number of oscillators is set to $N = 5000$. 49

3.4 Microscopical details of the dynamical states: asynchronous (AS) with (λ_1,λ_2)=(-10,-10), standing wave (SW) with (λ_1,λ_2)=(3,-5), clustering state (CS) (λ_1,λ_2)=(10,-1000) and travelling wave (TW) also with (λ_1,λ_2)=(10,-1000). Row-wise, instantaneous phase (a-d) and time-averaged velocity (e-h) against the natural frequencies of the oscillators, and time evolution of the order parameters (i-l), for each dynamical state. CS is obtained from simulation protocol (II) while TW is obtained from simulation protocol (I). For all cases, $N = 10000$, $\omega_0 = 1.0$ and $\Delta = 0.25$. 50

3.5 Phase transitions for the unimodal Gaussian distribution of natural frequencies and positive $\lambda_2 = 15$. (a) R_1 versus λ_1 : the blue and maroon circles refer to simulations performed by following protocols (I A) and (II A), respectively. The value reported for R_1 represents the average in time over a simulation time T_s. The diamonds of different colours denote the self consistent evaluation of the order parameter R_1, for different σ values, obtained by employing eq. (3.20). In the inset it is shown σ versus λ_1 as estimated by following protocol (I A). In panels (b-e) are reported snapshots of the natural frequencies ω_i versus their phases θ_i for different values of λ_1 obtained by following protocol (I A). Analogous snapshots are shown in (f) for simulations done by following protocol (II A). When necessary, the snapshots are arbitrarly shifted along the x-axis to improve readability. The displayed results refer to $\Delta = 0.25$ for $g_U(\omega)$, $\Delta\lambda_1 = 0.2$, $T_t = 10$, $T_s = 200$, integration step $dt = 0.001$ for the adiabatic simulations, and a network size $N = 10000$. 52

3.6 Phase transitions for the unimodal Gaussian distribution of natural frequencies and negative $\lambda_2 = -100$. (a) R_1 versus λ_1 : the blue and maroon circles refer to simulations performed by following protocols (I A) and (II A), respectively. The cyan (magenta) line refers to the self consistent evaluation of the order parameter R_1 by employing eq. (3.22) estimated in the whole range of frequencies (restriced to positive frequencies). In panels (b) and (c) are reported snapshots of the natural frequencies ω_i versus their phases θ_i for different values of λ_1 for simulations obtained by following protocols (I A) and (II A), respectively. In the inset of panel (c) we report the instantaneous values of $R_1(t)$ (black curve) and $R_B(t)$ (red curve) versus time for $\lambda_1 = 3$ obtained by following protocol (II A). The displayed results refer to $\Delta = 0.25$ for $g_U(\omega)$, $\Delta\lambda_1 = 0.2$ for the adiabatic simulations, and a network size $N = 10000$. 55

USC UNIVERSIDADE DE SANTIAGO DE COMPOSTELA

3.7 Phase transitions for the bimodal Gaussian distribution of natural frequencies with positive $\lambda_2 = 15$. (a) R_1 versus λ_1 : the blue and maroon circles refer to simulations performed by following protocols (I A) and (II A), respectively. The diamonds of different colours denote the self consistent evaluation of the order parameter R_1, for different σ values, obtained by employing eq. (3.20). In the inset it is shown σ versus λ_1 as estimated by following protocol (I A). In panels (b-e) are reported snapshots of the natural frequencies ω_i versus their phases θ_i for different values of λ_1 for simulations obtained by following protocol (I A). Analogous snapshots are shown in (f) for simulations done by following protocol (II A). The displayed results refer to $\omega_0 = 1$ and $\Delta = 0.25$ for $g_B(\omega)$, $\Delta\lambda_1 = 0.2$ for the adiabatic simulations, and a network size $N = 10000$. 57

3.8 Phase transitions for the bimodal Gaussian distribution of natural frequencies and negative $\lambda_2 = -100$. (a) R_1 versus λ_1 : the blue and maroon circles refer to simulations performed by following protocols (I A) and (II A), respectively. The cyan (magenta) line refers to the self consistent evaluation of the order parameter R_1 by employing eq. (3.22) estimated in the whole range of frequencies (restriced to positive frequencies). In panels (b) and (c) are reported snapshots of the natural frequencies ω_i versus their phases θ_i for different values of λ_1 for simulations obtained by following protocols (I A) and (II A), respectively. In the inset of panel (c) we report the instantaneous values of $R_1(t)$ (black curve) and $R_B(t)$ (red curve) versus time for $\lambda_1 = 8.8$ obtained by following protocol (II A). The displayed results refer to $\omega_0 = 1$ and $\Delta = 0.25$ for $g_B(\omega)$, $\Delta\lambda_1 = 0.2$ for the adiabatic simulations, and a network size $N = 10000$. 60

3.9 Numerical analysis of BC state. In (a), the order parameter R_B is a function of the coupling strengths λ_1 and λ_2, only for the simulation protocol (II A). The white arrows give the sense and direction to the de-synchronization transitions shown in panels (b) and (c), obtained by varying quasi-adiabatically the coupling parameters. For (b) $\lambda_2 = -30$, while for (c) $\lambda_1 = -20$. The pink and blue circles highlighted in panel (c) refer to (λ_1,λ_2)=(-20,-450) and (λ_1,λ_2)=(-20,-250) respectively. Using the same colorcode (pink and blue), these states are analyzed in panels (d,e) in terms of their instantaneous phases and averaged velocities. The snapshot presented in (d) is related to the instantaneous phases against their natural frequencies. In (e) the time-averaged velocity of each oscillator is reported against its natural frequency. For all panels, the bimodal parameters were fixed at $\omega_0 = 1$ and $\Delta = 0.25$. 61

3.10 Time averaged velocity of the ensemble $W = \frac{1}{N}\sum_j^N \langle \dot{\theta}_j \rangle$ versus the center of the symmetric bimodal peaks. The error bars denote an average over a significant number of system realizations to state the effects of different realizations of the natural frequencies. Panel (a) correspond to simulations started from synchronous initial conditions ($\eta = 1$), while the orange points correspond to simulations started from asynchronous ones ($\eta = 0$). For each point $(\lambda_1, \lambda_2) = (10, -1000), \Delta = 0.25, N = 5000$ and $n_{sim} = 100$. 62

USC
UNIVERSIDADE DE SANTIAGO DE COMPOSTELA

3.11 Clustering order parameter R_B for increasing values of the initial degree of phase-locking η, and different values of the higher order coupling λ_2. In (a), with $\lambda_1 = 10$, the labelled points correspond to panels (c) and (d) of Figure 3.4, and in the middle we can see all the intermediate steps from one state to the other. In (b), with $\lambda_1 = -10$, we see tje transition from the asynchronous state AS to the bimodal cluster state BCS at different critical points in function of the value of λ_2. For every point, $\omega_0 = 1.0, \Delta = 0.25, N = 5000$. 63

4.1 Phase diagram of the model with high mixing rate, $r > 0.01$, $N_s = 2000$ fluid particles and an interaction radius $R_0 = 0.01$. In the right panels, the blue line represents the average concentration u of the bead ensemble while the red line is the average concentration u_S of the solution particles 70
4.2 Random spatial distribution of the solution (red) and bead (blue) particles in a simulation box of size $L = 0.1$, $N_B = 1000$ and $N_S = 2000$. 71
4.3 Distribution of bead periods and phases for the parameter values considered. In this case, $K_{ex} = 0$ and $N_B = 1000$. 72
4.4 Numerical results obtained with our simulations for a low value of the interaction radius $R_0 = 0.01$ and two different mixing rates (a) r=0.1 and (b) r=0.001. In each subfigure, top panels account for bead particles while the bottom panels for solution particles. The simulations presented here were carried out with a total number of N_S=2000 fluid particles. The quantities shown represent the Kuramoto order parameter, the oscillating amplitudes and the synchronized periods of the particles. In the oscillation death region, the Kuramoto parameter is set to zero as it loses its physical meaning. 73
4.5 Phase diagrams of the model for increasing values of the mixing rate r. The (red,green,blue) color scheme follows the meaning of Figure 4.1, while the yellowed region represents the parameter space where irregular behavior and de-synchronization was found. The orange region represents a regime of oscillating beads coexisting with beads in oscillation death, the violet one denotes synchronized intermittence between oscillation death and super-synchronization and cyan colored points represent the synchronized intermittent state between synchronization and super-synchronization. 74

USC UNIVERSIDADE DE SANTIAGO DE COMPOSTELA

4.6 Characterization of the transition from synchronization to super-synchronization, corresponding to the ensemble behavior of the yellow region of Figure 4.5. Panel a) shows the de-synchronization with amplitude dispersion and panel b) the double peak oscillation of some particular beads in the close vicinity of super synchronization. Panels c) and d) represent the spatial visualization of the system at different times, showing the presence of multiple auto-waves in the system and the double peak oscillation. Panel e) shows the averaged Kuramoto parameter, period and amplitude of the particle ensembles, extracted from the corresponding cut in Figure 4.4. The number of bead particles is fixed at $N_B = 2100$, panel (a) corresponds to $K_{ex} = 0.2$ and panel (b) to $K_{ex} = 0.25$. In panel a), the solution de-synchronizes by breaking the synchronization waves in the system and the beads show strong dispersions in their amplitude. In panel b), right before super-synchronization is achieved, some particular beads show double peaked oscillations (black curves) in contrast to the overall behavior of the system (blue and red curves). . 76

4.7 Characterization of the synchronized intermittent state between synchronization and super synchronization, corresponding to the ensemble behavior of the cyan region of Figure 4.5. a) Averaged temporal series of the beads' (red line) and solution's (blue line) concentration, namely $\langle u_B \rangle$ and $\langle u_S \rangle$. b) Spatial representation of beads at different times of the particles' behavior using u_B as the coloring. c) Time evolution of the order parameter. d) Return map of the large oscillations of a continued simulation in time, with the time series for this simulation presented below in Figure 4.10(a). The black dashed lines are included to guide the eye for certain moments of the behavior in the different panels. The parameter configuration of these simulations is $N_B = 2100$,$K_{ex=0.2}$ and $r = 0.005$. 77

4.8 Characterization of the transition from synchronization to oscillation death in the static case ($r = 0$), corresponding to the ensemble behavior of the orange region of Figure 4.5(a). In (a), time series for the average ensemble concentrations and three separate particles. (b,c) Spatial representation of the beads' amplitudes, showing that the oscillating particles are localized in a spatial clusters that are likely linked to the initial distribution of particles. For (b), the number of bead particles is $N_B = 1700$ and the interaction exchange is $K_{ex} = 0.4$ while panel (c) shows other oranged points at lower densities. 78

4.9 Characterization of the synchronized intermittent state between super-synchronization and oscillation death, corresponding to the ensemble behavior of the violet region in Figure 2. a) Averaged temporal series of the beads' (red line) and solution's (blue line) concentration. b) Spatial representation of beads at different times of the particles' behavior using u_B as the coloring. c) Time evolution of the order parameter. d) Return map of the large oscillations of a continued simulation in time, with the time series for this simulation presented below in Figure 4.10(b). The black dashed lines are included to guide the eye for certain moments of the behavior in the different panels. The parameter configuration is $N_B = 1300$,$K_{ex} = 0.75$ and $r = 0.001$. . 79

USC UNIVERSIDADE DE SANTIAGO DE COMPOSTELA

4.10 Extended time series of the averaged bead concentrations $\langle u_B \rangle$ for the intermittent states presented in Figures 4.7 and 4.9. Panel (a) corresponds to the cyan state with a parameter configuration of $N_B = 2100$, $K_{ex} = 0.2$ and $r = 0.005$, while panel b) corresponds to $N_B = 1300$,$K_{ex} = 0.75$ and $r = 0.001$. 81
4.11 (a) Transition from the super synchronized state (with $K_{ex} = 0.5$) to the synchronized state ($K_{ex} = 0.1$) by decreasing K_{ex}, with the intermittent state appearing in between ($K_{ex} = 0.2$). We show the average ensemble concentrations $\langle u \rangle$ for beads (blue) and solution (red), with the associated instantaneous Kuramoto order parameter at each time step (b). The configuration for this simulation corresponds to that of the cyan state in 4.10(a), with $N_B = 2100$, $N_S = 2000$ and $r = 0.005$ 82

5.1 (a) Schematic representation of the experimental setup. (1) video projector, (2) collimating lens, (3) reflexive mirror at 45º, (4) light diffusor, (5) Petri disc with the microreactors and BZ solution, (6) CCD camera, (7). (b) glass microreactors fabricated via SLIPAA techniques. (c) snapshot of an ongoing experiment where each dark circle is a BZ oscillating microreactor. The yellow-rounded are showing oscillations.(d) Photograph of the experimental setup. 87
5.2 Consecutive snapshots of six BZ micro-reactors recorded in an experiment. The oscillations can be seen from the contrast between black and gray. As this contrast can be difficult to graps, we add as a visual aid a yellow circle that means the oscillator is firing, while a blue one means that is resting (see color bar in the side). At $t = 0$, only oscillator 3 is activated. At $t = 8$, oscillators 2 and 6 fire together, while at $t = 24$, it is the turn of oscillators 1 and 5. Finally at $t = 36$, oscillator 3 fires again and the cycle repeats. 88
5.3 Square signal of period P, size D and amplitude I used for the periodic control experiments. Note that this pulse actually results in a total light intensity experienced by the oscillators of $\phi = \phi_0 + I$. 90
5.4 Effects of the background light illumination ϕ_0 on the chemical oscillators. Panel (a) reports the recorded pixel value V_i of a single oscillator, showing the oscillations in the metal-ion catalyst, while panel (b) shows the average period and standard deviation of the whole ensemble of $N = 20$ oscillators. 91
5.5 Decay of the oscillation periods in time. A linear regresison to this data returns a slope of $m = -0.002s^{-1}$, revealing a decay of $1.2s$ every 10 minutes. 92
5.6 Collective oscillations before and after our control experiments with periodic square pulses, for (a,b,c) low pulse intensity $\phi = 0.5$, and (d,e,f) high pulse intensity $\phi = 1.0$. The skipped area in between the black dashed lines represent the control region where we applied the square signal. Panels (a) and (c) correspond to the average values of the pixel intensity of the whole ensemble $\langle V_i \rangle$, while panels (b) and (e) show the firings in time of each oscillator (in colors). Panels (c) and (f) correspond to the standard deviation σ between the firing times of the oscillators, measured in seconds. For both panels, $N = 21$, background intensity is set to $\phi_0 = 0.4$ and pulse duration is set to $D = 10$. . . . 93

USC UNIVERSIDADE DE SANTIAGO DE COMPOSTELA

5.7 (a) Overall levels of synchronization ρ of the control experiments in function of the pulse duration D in seconds, and (b) ρ in function of the pulse intensity ϕ. For panels (a), pulse intensity is fixed at $\phi = 1.0$ while in panel (b) pulse duration is fixed at $D = 10$. In both panels, error bars represent the standard deviation of our synchronization measures between different realizations of the experiment, with at least 5-10 experiments for each point and 20-25 oscillators in each experiment. 94
5.8 Consecutive snapshots of six BZ micro-reactors recorded before (top row,a-d) and after (lower row,e-h) a control experiment with coupled star networks. As in Figure 2.5, a blue circle means that the oscillator is resting while a yellow circle that the oscillator is firing. Panel (d) explicitly show the distribution of the start network topology, with the oscillator circled in green acting as the center node, sending light pulses to the ones next to it after firing. After this panel the previous color coding is recovered but the network structure is maintained. At $t = 938$ and $t = 976$, we can see all the oscillators firing together with a common period of $T = 38$ seconds. The time snapshots of these panels correspond to the experiment shown afterwards, in Figure 5.9 95
5.9 Collective oscillations before and after our control experiments with a star network coupling, following the disposition of Figure 5.8. Again, the area between the black dashed lines represent the control region where we applied the coupling. The green oscillator correspond to the central one, the master, while the blue ones are the peripheral oscillators that receive the pulses. The dashed blue line corresponds to the global averaged recorded signal of all the oscillators. For this experiment, $N = 6$, the background intensity is set to $\phi_0 = 0.4$ and the pulse coupling has a duration of $D = 10$ seconds and maximum light intensity of $\phi = 1.0$. 96
5.10 Dispersion in the firing of the oscillators after the control experiment σ_f against the dispersion in the natural periods between the peripheral oscillators and the central one, σ_T. Each point represents a different experiment under the same coupling conditions, $\phi_0 = 0.4$, $\phi = 1.0$ and $D = 10$. 96

6.1 Connectivity distributions of the three network models used, the Erdos Renyi (ER), the Watts-Strogatz (WS) and the Barabasi-Albert (BA). Network sized was fixed at $N = 5000$, and the average connectivity of the three graphs is $\langle k \rangle = 10$. In panel (c), we show the cumulative probability distribution in logarithmic scale. 107

USC UNIVERSIDADE DE SANTIAGO DE COMPOSTELA

6.2 Turing instability for two different network topologies, the Erdos-Renyi (ER) in blue, and the Barabasi-Albert (BA) in red, both with size $N = 1000$. In panel (a), two different values of the network influence are considered, $\varepsilon = 0.1$ and $\varepsilon = 0.5$. Right sub-panels represent the histograms of each distribution. Panel (b) shows the growth rate distribution associated to each configuration of the sub-panels in (a). For these simulations, $c = 0.27$, $d_{uv} = 0.0$ and $d_{vu} = 0.17$. Both networks have a mean degree of $\langle k \rangle = 10$, with the nodes being shown in a decreasing order of their connectivity value. The black dashed line in panel (a) represents the fixed stable point of the system for the given parameters, namely $u^* = 0.62$, while in panel (b) is a visual aid at $\lambda_\alpha = 0$ to see when the growth rates become positive. 111

6.3 Maximum value of the growth rates λ_{max} ((a-c) and (g-i)) and polarization index μ ((d-f) and j-l) in the parameter space for $\varepsilon = 0.1$ and $\varepsilon = 0.5$, for three different network topologies. BA accounts for Barabasi-Albert, ER for Erdos-Renyi and WS for Watts-Strogatz. Here, network size was fixed to N=5000 for all panels to avoid finite-size effects (see panel 6.4(a)). The black drawn line drawn denotes the area where $\lambda_{max} = 0$, therefore signaling the beginning of the instability. Note that in panels (d-f) the colormap was adjusted between $\mu = 0$ and $\mu = 0.5$ to zoom in the values. Panel (f) do not show any significant trace of polarization attending to μ, since the instability only induces a small noise in the system. 113

6.4 Size of the Turing area in function of the network influence ε (a), average network connectivity $\langle k \rangle$ (b), network size N(c) and average path length ℓ (only for the WS network) (d). For panels a, b and d, network size was fixed at N=5000, while for panels b, c and d network influence was fixed at $\varepsilon = 0.1$. Error bars in panel (d) account for multiple realizations of the network with very similar ℓ. 114

6.5 Size of the Turing area against the opinion growth a, simple diffusion d and cross diffusion d_{uv}, for the three different networks considered. For the three panels, network size was fixed at $N = 5000$ and network influence at $\varepsilon = 0.1$. . . 115

6.6 Effects of the link direction in the model. In star graphs (a) with $k = 50$, inward direction results in a return to the consensus while outward direction in a polarization of the central node, wheneve k_{central} is higher than a critical value. This can be extrapolated to BA directed networks (c), where hubs with outward connectivity larger than a critical one become polarized while the rest of the nodes do not. Panels (b) and (d) show the growth rate distribution for each case. In all panels, $\varepsilon = 0.1$, while network size is $N = 50$ for the star networks and $N = 1000$ for the BA networks. 116

USC UNIVERSIDADE DE SANTIAGO DE COMPOSTELA

7.1 In the upper panel (a), location of Galicia within Europe and spatial subdivision of the territory into its elementary administrative units. In colored background is highlighted the distribution in provinces (second-level administration) and municipalities (third-level administration).The nodes of our spatial network will correspond to each one of this 313 municipalities. In the lower panels, we show the geographical spread of COVID-19 in Galicia at a municipal level: reported cases versus population (b), and Incidence rate (c). Here the colors are given by the colormaps. The maps are generated using ArcGIS Desktop software version 10.8 (from ESRI, https://www.esri.com/en-us/arcgis/products/arcgis-desktop/overview) 122
7.2 Average age y_i of each municipality in correspondence to node population. Data extracted from (https://www.ige.eu). 125
7.3 Different levels of complexity on the network model. The left panels show the normalized values of the infection peak for each one of the nodes, distributed spatially. The right panels show the time evolution of the infected individuals for one specific node, Burela, situated on the northeastern coast. To start the simulation, an initial infected seed was placed into each node. 127
7.4 Estimated cumulative number of infected individuals with the SAIPR network model compared to the real cumulative incidence of the COVID-19's first wave, at the whole regional level. The fitting process of the model was separated on the two time-regions delimited by the vertical dashed red line, one before the start of the lockdown and one afterwards. The initial condition for the simulation was extracted from the first measured value of the dataset, with this number distributed proportionally among the four capital cities of the provinces plus the capital of the region (Santiago). 130
7.5 Time evolution of the cumulative infected individuals obtained with our fitted SAIRP network model over a 1000 realization of the initial state The red line represents the average over the sample, while the red shadow its the standard deviation. 132
7.6 Spatial distribution of the risk factor (a), normalized cumulative incidence data (b), and growth rates (c) for each municipality. A value of 1 on the risk factor means that the node was found always among the top infected ones on each simulation. Following the same reasoning, a value of 0 means that that node was never found among the top ones. The ranking of the infective nodes was set with a total size of 30, and the cumulative incidence data was normalized over the highest value of reported cases. Maps are generated using ArcGIS Desktop software version 10.8 (from ESRI, https://www.esri.com/en-us/arcgis/products/arcgis-desktop/overview) 133
7.7 Comparative of the reported cumulative data from the first and second waves (a,blue and orange crosses) against the normalized risk indicators (b), i.e., the risk factors based on simulation (green triangles) and the growth rates based on stability analysis (red dots). Each point represents a different municipality, in increasing order of the population N_i (set in logarithmic scale). 134
7.8 Population density of the Spanish region by municipalities. 136

USC UNIVERSIDADE DE SANTIAGO DE COMPOSTELA

7.9 Compartments of the epidemic model for any two age groups α and γ. The solid grey arrows indicate the transition probabilities between compartments, the red dashed arrows indicate the interactions between infected and susceptible individuals of the same age group and the yellow dashed arrows the interactions among individuals of different age groups. 137
7.10 (a) Distribution of the fitted infectivities β_i over the populations N_i. The black-dashed line corresponds to the critical values defined by eq. 7.19 that state which nodes of the mobility network will have a positive value for the growth factos. (b) Distribution of the Pearson's correlation coefficients obtained for each age group, summing up to 3,121 fits, one for each municipality. 142
7.11 Sample distribution of growth rates (red) and maximum cumulative incidence data (black) against the node's population for the case with relative mobility of $r_l = (0.1, 0.4, 0.4, 0.1)$. Each variable was normalized to the maximum value its own series so the comparison could be feasible. Only a random sample of the 10% of the points are shown for visualization purposes 143
7.12 Spatial distribution of the growth rates by age group. Relative mobility between municipalities by age groups is fixed to (0.1, 0.4, 0.4, 0.1). 145
7.12 Spatial distribution of the growth rates by age group. Relative mobility between municipalities by age groups is fixed to (0.1, 0.4, 0.4, 0.1). 146
7.13 Averaged ten maximum values (a) and medians (b) of the GR distributions for each autonomous community. Each point show the average over the four age groups to simplify the visualization. 147
7.14 (a) Average of the 10 maximum values (a, upper panel) and the median values (a, lower panel) of the growth rates (GR) distributions for different scenarios of isolation and mobility restriction for different age groups. The points represent averaging over the four age groups and the error bars the standard deviation for each case. The black dashed line is drawn to guide the eye when comparing the two control measures at hand, this is, local mobility restrictions with no isolation to no-mobility restrictions with age groups isolation. It must be remarked that the mobility restriction by autonomous communities' results in a very similar outcome as the mobility restriction by provinces, so they appear overlapped. (b) Break down of the upper panel over all the age groups and in a color-coded map. The numbers on the x axis refer to isolation of a single or a combination of age groups, while restrictions to the mobility are shown in different colors (a) and consecutive columns (b). Relative mobility between municipalities is fixed to $r_l = (0.1, 0.4, 0.4, 0.1)$. 148

8.1 Summary of the methodology of our approach to simulate an opinion biased epidemic model. 152
8.2 (a) October 2019 Twitter network with $N = 17665$ accounts and (b) April 2020 Twitter network with $N = 24337$ accounts. Each color represents the nodes corresponding with each keyword subnetwork. Accounts in grey are the junction accounts. (c,d) Out-connectivity distribution and in-connectivity distributions (e,f) for each network fitted to power-laws, with October'19 in orange and April'20 in green. 154

USC UNIVERSIDADE DE SANTIAGO DE COMPOSTELA

8.3 Time evolution of the scale-free exponents γ_in (a), γ_out (b), average shortest path ℓ (c) and network diameter ℓ_{max} (d) for the Spanish retweet network between 01/06/2019 and 01/02/2021. The yellow vertical line indicates the starting date of the COVID-19 lockdown by the Spanish government, March 15, 2020, while the red horizontal lines the average values of each parameter before and after this date. Figure taken from [Paramés-Estévez et al., 2023]. 157
8.4 Normalized opinion distribution for the October'19 (orange) and April '20 (green) Twitter networks, for three values of the parameter r, i.e., the initial % of accounts in the state $u_i = 1$. The rest of model parameters were fixed at $A = 0.0001, B = 0.01$ and $g = 0.0001$, to obtain $u^* = 0.02$ and $d = 20000$ to equilibrate the interplay between internal dynamics and network effects. 160
8.5 Representative diagram of the infection process. Infected nodes spread the disease to neighbor susceptible nodes with probability $\beta'_{ij} = \beta \cdot \overline{u}_i \cdot \overline{u}_j$. 162
8.6 (a) Re-scaled probability density of the variable $\overline{u} = 1 - u$ representing the disagreement, obtained from Figure 8.4 (b) ($r = 0.3$). (b) Time evolution of the infected individuals for the three opinion distributions considered. Reduction (c) and time delay (d)in % of the infection peaks in comparison to the uniform case where all nodes have their opinion at the cutoff value, $\overline{u} = 0.3$. The vertical bar in the last case, $\overline{u} = 0.1$, represents that the outbreak of the epidemic did not occur. Error bars represent the standard deviations from a sample of several simulations run with the same parameters but different random configurations of the network's adjacency matrix. For this Figure, $N = 10000, \beta = 0.05, \mu = 0.06, p_r = 0.25$. 164
8.7 Reduction (a) and time delay (b) of the infection peak for different values of the cutoff in $\overline{u}$, for both the opinion models. For each cuttoff, the values of each model are scaled over the value of the theoretical scenario where all nodes have the opinion at the cutoff. The dashed filled bar represents the abscence of a clear infection peak. Error bars represent the standard deviation over a ensemble of several simulations. Simulation parameters are set to $N = 10000, \beta = 0.05, \mu = 0.06, p_r = 0.25$. 165
8.8 (a) Normalized bimodal opinion distributions, generated with different sets of populations $N_{0,1}$ and dispersion sizes σ. (b) Peak statistics from the opinion distributions shown in panel (a), scaled over the baseline epidemic model without opinions. 166
8.9 Time evolution of the infected individuals (a) and peak statistics (b,c) of the bimodal opinion distributions with $\nu = 0.5$ for different values of σ. 168
8.10 Peak statistics of the opinion distribution with $\sigma = 0.05, 0.2 and 0.5$ against ν. $N = 10000, p_r = 0.25$ 169
8.11 Connectivity distributions of the social networks obtained for the Portuguese Twitter network. Dots in blue, represent the network obtained in April 2020, while orange dots correspond to the situation in July 2020. In both cases, the network topology corresponds to a scale free networks with exponents $\gamma_{out} = 2.99$, $\gamma_{in} = 2.53$ in April and $\gamma_{out} = 2.14$, $\gamma_{in} = 2.09$ in July 2020. 170
8.12 Normalized opinion distributions for the April '20 (green) and July '20 for the Portuguese Twitter networks. 170

USC UNIVERSIDADE DE SANTIAGO DE COMPOSTELA

8.13 (a) Fraction of confirmed active cases per day in Portugal (black), with the red line being the nonlinear fit of the deterministic SAIRP model from March 2 to May 17, 2020, the yellow line the fit from May 17 to June 9, 2020, and the green line the one from June 9 to July 29, 2020. (b) Time evolution of the SAIRP network model coupled with the April 2020 opinion distribution (blue line) for the time period between March 2 to May 17, 2020; in contrast to the fraction of confirmed active cases (red crosses here, black stars in panel (a)). The bluish shadow marks the uncertainty of the model caused by the random estimation of the probabilities and the effect of initial random conditions. (c) Comparison of the SAIRP model coupled with the April 2020 opinion distribution (blue line), with the SAIRP model coupled with the July 2020 opinion distribution (orange line). For both panels (b) and (c), mobility networks of size $N = 25000$ with a Watts-Strogatz network topology of mean connectivity $\langle k \rangle = 5$ and rewiring probability $p_r = 0.01$ 172

B.1 Estimation of the different slopes by the functions k_n of the RK4 method. [https://en.wikipedia.org/wiki/RungeKutta_methods] 187

USC UNIVERSIDADE DE SANTIAGO DE COMPOSTELA

USC
UNIVERSIDADE
DE SANTIAGO
DE COMPOSTELA

List of Tables

5.1 Recipe for the solution of 5 ml of silica gel loaded with Ruthenium catalyst . . 89
5.2 Recipe for the solution of 20 ml of catalyst free BZ 89

7.1 Summary of the parameter values used in our analysis. The first three, β, m and d were obtained from fitting to the cumulative incidence data at each time period. 131
7.2 Spearman's correlation rank between the calculated GR (for each combination of the relative mobilities r_l) and the cumulative incidence data of each age group (AG). The relative mobility r_l represents the percentage of mobility that each AG holds to move freely between municipalities. 141

8.1 Estimated parameter values and initial conditions for the simulation of the COVID-19 incindence in Portugal from March 2, 2020 to May 17, 2020, 2020 for the SAIRP model. 171

USC UNIVERSIDADE DE SANTIAGO DE COMPOSTELA

USC
UNIVERSIDADE
DE SANTIAGO
DE COMPOSTELA

Bibliography

[Abel et al., 2011] Abel, F., Gao, Q., Houben, G.-J., and Tao, K. (2011). Analyzing temporal dynamics in Twitter profiles for personalized recommendations in the social web. In *Proceedings of the 3rd International Web Science Conference*, WebSci '11, pages 1–8, New York, NY, USA. Association for Computing Machinery.

[Abramowitz and Saunders, 2008] Abramowitz, A. I. and Saunders, K. L. (2008). Is Polarization a Myth? *The Journal of Politics*, 70(2):542–555.

[Acebrón et al., 2005] Acebrón, J. A., Bonilla, L. L., Pérez Vicente, C. J., Ritort, F., and Spigler, R. (2005). The Kuramoto model: A simple paradigm for synchronization phenomena. *Reviews of Modern Physics*, 77(1):137–185.

[Albert and Barabási, 2002] Albert, R. and Barabási, A.-L. (2002). Statistical mechanics of complex networks. *Reviews of Modern Physics*, 74(1):47–97.

[Albert et al., 1999] Albert, R., Jeong, H., and Barabási, A.-L. (1999). Diameter of the World-Wide Web. *Nature*, 401(6749):130–131.

[Albert et al., 2000] Albert, R., Jeong, H., and Barabási, A.-L. (2000). Error and attack tolerance of complex networks. *Nature*, 406(6794):378–382.

[Aliev and Panfilov, 1996] Aliev, R. R. and Panfilov, A. V. (1996). A simple two-variable model of cardiac excitation. *Chaos, Solitons & Fractals*, 7(3):293–301.

[Alvarez-Zuzek et al., 2017] Alvarez-Zuzek, L. G., Rocca, C. E. L., Iglesias, J. R., and Braunstein, L. A. (2017). Epidemic spreading in multiplex networks influenced by opinion exchanges on vaccination. *PLOS ONE*, 12(11):e0186492.

[Anderson and May, 1991] Anderson, R. and May, R. M. (1991). *Infectious diseases of humans : dynamics and control*. Oxford University Press, Oxford New York.

[Anderson, 1991] Anderson, R. M. (1991). Discussion: The Kermack-McKendrick epidemic threshold theorem. *Bulletin of Mathematical Biology*, 53(1):3–32.

[Arenas et al., 2020] Arenas, A., Cota, W., Gómez-Gardeñes, J., Gómez, S., Granell, C., Matamalas, J. T., Soriano-Paños, D., and Steinegger, B. (2020). Modeling the Spatiotemporal Epidemic Spreading of COVID-19 and the Impact of Mobility and Social Distancing Interventions. *Physical Review X*, 10(4):041055.

[Arenas et al., 2008] Arenas, A., Díaz-Guilera, A., Kurths, J., Moreno, Y., and Zhou, C. (2008). Synchronization in complex networks. *Physics Reports*, 469(3):93–153.

USC DE COMPOSTELA

[Axelrod, 1997] Axelrod, R. (1997). The Dissemination of Culture: A Model with Local Convergence and Global Polarization. *Journal of Conflict Resolution*, 41(2):203–226.

[Balcan et al., 2010] Balcan, D., Gonçalves, B., Hu, H., Ramasco, J. J., Colizza, V., and Vespignani, A. (2010). Modeling the spatial spread of infectious diseases: the GLobal Epidemic and Mobility computational model. *Journal of computational science*, 1(3):132–145.

[Baldassarri and Gelman, 2008] Baldassarri, D. and Gelman, A. (2008). Partisans without Constraint: Political Polarization and Trends in American Public Opinion. *American Journal of Sociology*, 114(2):408–446.

[BALSA-BARREIRO, 2013] BALSA-BARREIRO, J. (2013). Insostenibilidad de modelos territoriales desde un punto de vista demográfico. el caso de costa da morte (galicia, españa). *Papeles de Población*.

[Balsa-Barreiro et al., 2019] Balsa-Barreiro, J., Ambuühl, L., Menéndez, M., and Pentland, A. (2019). Mapping Time-Varying Accessibility and Territorial Cohesion With Time-Distorted Maps. *IEEE Access*, 7:41702–41714.

[Balsa-Barreiro et al., 2021] Balsa-Barreiro, J., Morales, A. J., and Lois-González, R. C. (2021). Mapping Population Dynamics at Local Scales Using Spatial Networks. *Complexity*, 2021:e8632086.

[Barabasi, 2002] Barabasi, A.-l. (2002). *Linked: How Everything Is Connected to Everything Else and What It Means for Business, Science, and Everyday Life*. Perseus Books Group.

[Barabási and Albert, 1999] Barabási, A.-L. and Albert, R. (1999). Emergence of Scaling in Random Networks. *Science*, 286(5439):509–512.

[Barabási and Pósfai, 2016a] Barabási, A.-L. and Pósfai, M. (2016a). *Network Science*, chapter 4. The Scale Free property, pages 112–163. Cambridge University Press. Google-Books-ID: ZVHesgEACAAJ.

[Barabási and Pósfai, 2016b] Barabási, A.-L. and Pósfai, M. (2016b). *Network Science by Albert-László Barabási*. Cambridge University Press.

[Barrat et al., 2008] Barrat, A., Barthélemy, M., and Vespignani, A. (2008). *Epidemic spreading in population networks*, page 180–215. Cambridge University Press.

[Battiston et al., 2020] Battiston, F., Cencetti, G., Iacopini, I., Latora, V., Lucas, M., Patania, A., Young, J.-G., and Petri, G. (2020). Networks beyond pairwise interactions: Structure and dynamics. *Physics Reports*, 874:1–92.

[Baumann et al., 2020] Baumann, F., Lorenz-Spreen, P., Sokolov, I. M., and Starnini, M. (2020). Modeling Echo Chambers and Polarization Dynamics in Social Networks. *Physical Review Letters*, 124(4):048301.

[Bertuzzo et al., 2020] Bertuzzo, E., Mari, L., Pasetto, D., Miccoli, S., Casagrandi, R., Gatto, M., and Rinaldo, A. (2020). The geography of COVID-19 spread in italy and implications for the relaxation of confinement measures. *Nature Communications*, 11(1).

[Bessi et al., 2016] Bessi, A., Petroni, F., Vicario, M. D., Zollo, F., Anagnostopoulos, A., Scala, A., Caldarelli, G., and Quattrociocchi, W. (2016). Homophily and polarization in the age of misinformation. *The European Physical Journal Special Topics*, 225(10):2047–2059.

[Bi et al., 2016] Bi, H., Hu, X., Boccaletti, S., Wang, X., Zou, Y., Liu, Z., and Guan, S. (2016). Coexistence of Quantized, Time Dependent, Clusters in Globally Coupled Oscillators. *Physical Review Letters*, 117(20):204101.

[Bianconi et al., 2023] Bianconi, G., Arenas, A., Biamonte, J., Carr, L. D., Kahng, B., Kertesz, J., Kurths, J., Lü, L., Masoller, C., Motter, A. E., Perc, M., Radicchi, F., Ramaswamy, R., Rodrigues, F. A., Sales-Pardo, M., Miguel, M. S., Thurner, S., and Yasseri, T. (2023). Complex systems in the spotlight: next steps after the 2021 Nobel Prize in Physics. *Journal of Physics: Complexity*, 4(1):010201.

[Boccaletti et al., 2002] Boccaletti, S., Kurths, J., Osipov, G., Valladares, D. L., and Zhou, C. S. (2002). The synchronization of chaotic systems. *Physics Reports*, 366(1):1–101.

[Boccaletti et al., 2006] Boccaletti, S., Latora, V., Moreno, Y., Chavez, M., and Hwang, D. U. (2006). Complex networks: Structure and dynamics. *Physics Reports*, 424(4):175–308.

[Boxell et al., 2017] Boxell, L., Gentzkow, M., and Shapiro, J. M. (2017). Greater Internet use is not associated with faster growth in political polarization among US demographic groups. *Proceedings of the National Academy of Sciences*, 114(40):10612–10617.

[Broder et al., 2000] Broder, A., Kumar, R., Maghoul, F., Raghavan, P., Rajagopalan, S., Stata, R., Tomkins, A., and Wiener, J. (2000). Graph structure in the Web. *Computer Networks*, 33(1):309–320.

[Calvetti et al., 2020] Calvetti, D., Hoover, A. P., Rose, J., and Somersalo, E. (2020). Metapopulation network models for understanding, predicting, and managing the coronavirus disease COVID-19. *Frontiers in Physics*, 8.

[Carballosa et al., 2020] Carballosa, A., Mussa-Juane, M., and Muñuzuri, A. P. (2020). Incorporating social opinion in the evolution of an epidemic spread.

[Cataldi et al., 2010] Cataldi, M., Di Caro, L., and Schifanella, C. (2010). Emerging topic detection on Twitter based on temporal and social terms evaluation. In *Proceedings of the Tenth International Workshop on Multimedia Data Mining*, MDMKDD '10, pages 1–10, New York, NY, USA. Association for Computing Machinery.

[Chakrabarti et al., 2008] Chakrabarti, D., Wang, Y., Wang, C., Leskovec, J., and Faloutsos, C. (2008). Epidemic thresholds in real networks. *ACM Transactions on Information and System Security*, 10(4):1:1–1:26.

[Chua et al., 1993] Chua, L. O., Itoh, M., Kocarev, L., and Eckert, K. (1993). Chaos synchronization in chua's circuit. *Journal of Circuits, Systems and Computers*, 03(01):93–108.

[Cinelli et al., 2021] Cinelli, M., Morales, G. D. F., Galeazzi, A., Quattrociocchi, W., and Starnini, M. (2021). The echo chamber effect on social media. *Proceedings of the National Academy of Sciences*, 118(9).

USC UNIVERSIDADE DE SANTIAGO DE COMPOSTELA

[Cohen et al., 2000] Cohen, R., Erez, K., ben Avraham, D., and Havlin, S. (2000). Resilience of the Internet to Random Breakdowns. *Physical Review Letters*, 85(21):4626–4628.

[Colizza et al., 2007] Colizza, V., Pastor-Satorras, R., and Vespignani, A. (2007). Reaction–diffusion processes and metapopulation models in heterogeneous networks. *Nature Physics*, 3(4):276–282.

[Colizza and Vespignani, 2008] Colizza, V. and Vespignani, A. (2008). Epidemic modeling in metapopulation systems with heterogeneous coupling pattern: Theory and simulations. *Journal of Theoretical Biology*, 251(3):450–467.

[Conover et al., 2011] Conover, M., Ratkiewicz, J., Francisco, M., Goncalves, B., Menczer, F., and Flammini, A. (2011). Political Polarization on Twitter. *Proceedings of the International AAAI Conference on Web and Social Media*, 5(1):89–96.

[Cota et al., 2019] Cota, W., Ferreira, S. C., Pastor-Satorras, R., and Starnini, M. (2019). Quantifying echo chamber effects in information spreading over political communication networks. *EPJ Data Science*, 8(1):1–13.

[Cowling et al., 2020] Cowling, B. J., Ali, S. T., Ng, T. W. Y., Tsang, T. K., Li, J. C. M., Fong, M. W., Liao, Q., Kwan, M. Y., Lee, S. L., Chiu, S. S., Wu, J. T., Wu, P., and Leung, G. M. (2020). Impact assessment of non-pharmaceutical interventions against coronavirus disease 2019 and influenza in Hong Kong: an observational study. *The Lancet Public Health*, 5(5):e279–e288.

[Crawford, 1994] Crawford, J. D. (1994). Amplitude expansions for instabilities in populations of globally-coupled oscillators. *Journal of Statistical Physics*, 74(5):1047–1084.

[Cuomo and Oppenheim, 1993] Cuomo, K. M. and Oppenheim, A. V. (1993). Circuit implementation of synchronized chaos with applications to communications. *Physical Review Letters*, 71(1):65–68.

[Dai et al., 2021] Dai, X., Kovalenko, K., Molodyk, M., Wang, Z., Li, X., Musatov, D., Raigorodskii, A. M., Alfaro-Bittner, K., Cooper, G. D., Bianconi, G., and Boccaletti, S. (2021). D-dimensional oscillators in simplicial structures: Odd and even dimensions display different synchronization scenarios. *Chaos, Solitons & Fractals*, 146:110888.

[Daido, 1996] Daido, H. (1996). Multibranch Entrainment and Scaling in Large Populations of Coupled Oscillators. *Physical Review Letters*, 77(7):1406–1409.

[Dalziel et al., 2013] Dalziel, B. D., Pourbohloul, B., and Ellner, S. P. (2013). Human mobility patterns predict divergent epidemic dynamics among cities. *Proceedings of the Royal Society B: Biological Sciences*, 280(1766):20130763.

[de Wit and van der Linden a Cameron Brick, 2019] de Wit, L. and van der Linden a Cameron Brick, S. (2019). Are Social Media Driving Political Polarization?

[Degroot, 1974] Degroot, M. H. (1974). Reaching a Consensus. *Journal of the American Statistical Association*, 69(345):118–121.

USC
UNIVERSIDADE DE SANTIAGO DE COMPOSTELA

[Del Vicario et al., 2016] Del Vicario, M., Vivaldo, G., Bessi, A., Zollo, F., Scala, A., Caldarelli, G., and Quattrociocchi, W. (2016). Echo Chambers: Emotional Contagion and Group Polarization on Facebook. *Scientific Reports*, 6(1):37825.

[Dezső and Barabási, 2002] Dezső, Z. and Barabási, A.-L. (2002). Halting viruses in scale-free networks. *Physical Review E*, 65(5).

[DiMaggio et al., 1996] DiMaggio, P., Evans, J., and Bryson, B. (1996). Have American's Social Attitudes Become More Polarized? *American Journal of Sociology*, 102(3):690–755.

[Elger and Lehnertz, 1998] Elger, C. E. and Lehnertz, K. (1998). Seizure prediction by non-linear time series analysis of brain electrical activity. *European Journal of Neuroscience*, 10(2):786–789.

[Epstein et al., 1998] Epstein, I. R., Pojman, J. A., Epstein, I. R., and Pojman, J. A. (1998). *An Introduction to Nonlinear Chemical Dynamics: Oscillations, Waves, Patterns, and Chaos*. Topics in Physical Chemistry. Oxford University Press, Oxford, New York.

[Erdös and Renyi, 1959] Erdös, P. and Renyi, A. (1959). On random graphs I. *Publ. math. debrecen*, 6(290-297):18.

[Estrada, 2023] Estrada, E. (2023). What is a Complex System, After All? *Foundations of Science*.

[Faloutsos et al., 1999] Faloutsos, M., Faloutsos, P., and Faloutsos, C. (1999). On power-law relationships of the Internet topology. *ACM SIGCOMM Computer Communication Review*, 29(4):251–262.

[Field, 2000] Field, R. J. (2000). An Introduction to Nonlinear Chemical Dynamics: Oscillations, Waves, Patterns, and Chaos (Epstein, I. R.; Pojman, J. A.). *Journal of Chemical Education*, 77(4):450.

[Field and Burger, 1985] Field, R. J. and Burger, M. (1985). *Oscillations and traveling waves in chemical systems*. Wiley, New York. OCLC: 11029269.

[Field et al., 1972] Field, R. J., Koros, E., and Noyes, R. M. (1972). Oscillations in chemical systems. II. Thorough analysis of temporal oscillation in the bromate-cerium-malonic acid system. *Journal of the American Chemical Society*, 94(25):8649–8664.

[Field and Noyes, 1974] Field, R. J. and Noyes, R. M. (1974). Oscillations in chemical systems. IV. Limit cycle behavior in a model of a real chemical reaction. *The Journal of Chemical Physics*, 60(5):1877–1884.

[Filatrella et al., 2001] Filatrella, G., Straughn, B., and Barbara, P. (2001). Emission of radiation from square arrays of stacked Josephson junctions. *Journal of Applied Physics - J APPL PHYS*, 90.

[Fiorina and Abrams, 2008] Fiorina, M. P. and Abrams, S. J. (2008). Political polarization in the american public. *Annual Review of Political Science*, 11(1):563–588.

USC UNIVERSIDADE DE SANTIAGO DE COMPOSTELA

[Flores-Arias et al., 2022] Flores-Arias, M. T., Gómez-Varela, A. I., Munuzuri, A. P., Carballosa, A., and Bao-Varela, C. (2022). Micro-reactors fabricated by subaquatic indirect laser-induced plasma-assisted ablation on soda-lime glass substrates. *EPJ Web of Conferences*, 266:13012.

[Friedkin and Johnsen, 1990] Friedkin, N. and Johnsen, E. (1990). Social Influence and Opinions. *Journal of Mathematical Sociology - J MATH SOCIOL*, 15:193–206.

[Fries, 2005] Fries, P. (2005). A mechanism for cognitive dynamics: neuronal communication through neuronal coherence. *Trends in Cognitive Sciences*, 9(10):474–480.

[Garaboa-Paz et al., 2016] Garaboa-Paz, D., Muñuzuri, A. P., and Pérez-Muñuzuri, V. (2016). Nonperfect mixing affects synchronization on a large number of chemical oscillators immersed in a chemically active time-dependent chaotic flow. *Physical Review E*, 94(1):013103.

[García-Selfa et al., 2021] García-Selfa, D., Ghoshal, G., Bick, C., Pérez-Mercader, J., and Muñuzuri, A. P. (2021). Chemical oscillators synchronized via an active oscillating medium: Dynamics and phase approximation model. *Chaos, Solitons & Fractals*, 145:110809.

[García-Selfa et al., 2019] García-Selfa, D., Muñuzuri, A. P., Pérez-Mercader, J., and Simakov, D. S. A. (2019). Resonant Behavior in a Periodically Forced Nonisothermal Oregonator. *The Journal of Physical Chemistry A*, 123(38):8083–8088.

[Gatto et al., 2020] Gatto, M., Bertuzzo, E., Mari, L., Miccoli, S., Carraro, L., Casagrandi, R., and Rinaldo, A. (2020). Spread and dynamics of the COVID-19 epidemic in italy: Effects of emergency containment measures. *Proceedings of the National Academy of Sciences*, 117(19):10484–10491.

[Ghoshal et al., 2016] Ghoshal, G., Muñuzuri, A. P., and Pérez-Mercader, J. (2016). Emergence of a super-synchronized mobbing state in a large population of coupled chemical oscillators. *Scientific Reports*, 6(1):19186.

[Giordano et al., 2020] Giordano, G., Blanchini, F., Bruno, R., Colaneri, P., Filippo, A. D., Matteo, A. D., and Colaneri, M. (2020). Modelling the COVID-19 epidemic and implementation of population-wide interventions in italy. *Nature Medicine*, 26(6):855–860.

[Gladwell, 2006] Gladwell, M. (2006). *The Tipping Point: How Little Things Can Make a Big Difference*. Little, Brown. Google-Books-ID: yBDBEGBIUmgC.

[González et al., 2008] González, M. C., Hidalgo, C. A., and Barabási, A.-L. (2008). Understanding individual human mobility patterns. *Nature*, 453(7196):779–782.

[Gray et al., 2020] Gray, L., MacDonald, C., Tassell-Matamua, N., Stanley, J., Kvalsvig, A., Zhang, J., Murton, S., Wiles, S., Puloka, V., Becker, J., Johnston, D., Baker, M. G., Gray, L., MacDonald, C., Tassell-Matamua, N., Stanley, J., Kvalsvig, A., Zhang, J., Murton, S., Wiles, S., Puloka, V., Becker, J., Johnston, D., and Baker, M. G. (2020). Wearing one for the team: views and attitudes to face covering in New Zealand/Aotearoa during COVID-19 Alert Level 4 lockdown. *Journal of Primary Health Care*, 12(3):199–206.

USC DE COMPOSTELA

[Gray and Jalife, 1996] Gray, R. and Jalife, J. (1996). Spiral waves and the heart. *International Journal of Bifurcation and Chaos*, 6:415.

[Gross et al., 2006] Gross, T., D'Lima, C. J. D., and Blasius, B. (2006). Epidemic Dynamics on an Adaptive Network. *Physical Review Letters*, 96(20):208701.

[Guerra et al., 2013] Guerra, P., Meira Jr, W., Cardie, C., and Kleinberg, R. (2013). A measure of polarization on social media NetworksBased on community boundaries. *Proceedings of the 7th International Conference on Weblogs and Social Media, ICWSM 2013*, pages 215–224.

[Gutiérrez et al., 2020] Gutiérrez, R., Materassi, M., Focardi, S., and Boccaletti, S. (2020). Steering complex networks toward desired dynamics. *Scientific Reports*, 10(1):20744.

[Gutiérrez et al., 2012] Gutiérrez, R., Sendiña-Nadal, I., Zanin, M., Papo, D., and Boccaletti, S. (2012). Targeting the dynamics of complex networks. *Scientific Reports*, 2(1):396.

[Gáşpár et al., 1983] Gáşpár, V., Bazsa, G., and Beck, M. T. (1983). The Influence of Visible Light on the Beloasoy-Zhabotinskii Oscillating Reactions applying Different Catalysts. *Zeitschrift für Physikalische Chemie*, 264O(1):43–48.

[Gómez-Gardeñes et al., 2007] Gómez-Gardeñes, J., Moreno, Y., and Arenas, A. (2007). Paths to Synchronization on Complex Networks. *Physical Review Letters*, 98(3):034101.

[Hanazaki et al., 1995] Hanazaki, I., Mori, Y., Sekiguchi, T., and Rábai, G. (1995). Photo-response of chemical oscillators. *Physica D: Nonlinear Phenomena*, 84(1):228–237.

[Hansel et al., 1993] Hansel, D., Mato, G., and Meunier, C. (1993). Clustering and slow switching in globally coupled phase oscillators. *Physical Review E*, 48(5):3470–3477.

[Hartwell et al., 1999] Hartwell, L. H., Hopfield, J. J., Leibler, S., and Murray, A. W. (1999). From molecular to modular cell biology. *Nature*, 402(6761):C47–C52.

[Hegselmann and Krause, 2002] Hegselmann, R. and Krause, U. (2002). Opinion dynamics and bounded confidence: models, analysis and simulation. *Jasss-the Journal of Artificial Societies and Social Simulation*, 5(3):2. WOS:000176884300002.

[Hilgetag and Kaiser, 2004] Hilgetag, C. C. and Kaiser, M. (2004). Clustered organization of cortical connectivity. *Neuroinformatics*, 2(3):353–360.

[Hodgkin and Huxley, 1952] Hodgkin, A. L. and Huxley, A. F. (1952). A quantitative description of membrane current and its application to conduction and excitation in nerve. *The Journal of Physiology*, 117(4):500–544.

[Hoertel et al., 2020] Hoertel, N., Blachier, M., Blanco, C., Olfson, M., Massetti, M., Rico, M. S., Limosin, F., and Leleu, H. (2020). A stochastic agent-based model of the SARS-CoV-2 epidemic in france. *Nature Medicine*, 26(9):1417–1421.

[Holme and Saramäki, 2012] Holme, P. and Saramäki, J. (2012). Temporal networks. *Physics Reports*, 519(3):97–125.

USC UNIVERSIDADE DE SANTIAGO DE COMPOSTELA

[Ivorra et al., 2020] Ivorra, B., Ferrández, M., Vela-Pérez, M., and Ramos, A. (2020). Mathematical modeling of the spread of the coronavirus disease 2019 (COVID-19) taking into account the undetected infections. the case of china. *Communications in Nonlinear Science and Numerical Simulation*, 88:105303.

[Jankowski et al., 1995] Jankowski, S., Londei, A., Mazur, C., and Lozowski, A. (1995). Synchronization and association in a large network of coupled Chua's circuits†. *International Journal of Electronics*, 79(6):823–828.

[Jeong et al., 2000] Jeong, H., Tombor, B., Albert, R., Oltvai, Z. N., and Barabási, A. L. (2000). The large-scale organization of metabolic networks. *Nature*, 407(6804):651–654.

[Kasting et al., 2020] Kasting, M. L., Head, K. J., Hartsock, J. A., Sturm, L., and Zimet, G. D. (2020). Public perceptions of the effectiveness of recommended non-pharmaceutical intervention behaviors to mitigate the spread of SARS-CoV-2. *PLOS ONE*, 15(11):e0241662.

[Kauffman, 1996] Kauffman, S. A. (1996). *At Home in the Universe: The Search for Laws of Self-organization and Complexity*. Penguin. Google-Books-ID: qBbAQgAACAAJ.

[Keeling, 1999] Keeling, M. J. (1999). The effects of local spatial structure on epidemiological invasions. *Proceedings of the Royal Society of London. Series B: Biological Sciences*, 266(1421):859–867.

[Keeling and Eames, 2005] Keeling, M. J. and Eames, K. T. D. (2005). Networks and epidemic models. *Journal of the Royal Society, Interface*, 2(4):295–307.

[Kephart and White, 1991] Kephart, J. and White, S. (1991). Directed-graph epidemiological models of computer viruses. In *Proceedings. 1991 IEEE Computer Society Symposium on Research in Security and Privacy*, pages 343–359.

[Kermack et al., 1927] Kermack, W. O., McKendrick, A. G., and Walker, G. T. (1927). A contribution to the mathematical theory of epidemics. *Proceedings of the Royal Society of London. Series A, Containing Papers of a Mathematical and Physical Character*, 115(772):700–721.

[Kiss and Hudson, 2001] Kiss, I. Z. and Hudson, J. L. (2001). Phase synchronization and suppression of chaos through intermittency in forcing of an electrochemical oscillator. *Physical Review E*, 64(4):046215.

[Kiss et al., 2002] Kiss, I. Z., Zhai, Y., and Hudson, J. L. (2002). Emerging Coherence in a Population of Chemical Oscillators. *Science*, 296(5573):1676–1678.

[Kocarev et al., 1992] Kocarev, L., Halle, K. S., Eckert, K., Chua, L. O., and Parlitz, U. (1992). Experimental demonstration of secure communications via chaotic synchronization. *International Journal of Bifurcation and Chaos*, 02(03):709–713.

[Koch and Meinhardt, 1994] Koch, A. J. and Meinhardt, H. (1994). Biological pattern formation: from basic mechanisms to complex structures. *Reviews of Modern Physics*, 66(4):1481–1507.

[Kohn, 1999] Kohn, K. W. (1999). Molecular Interaction Map of the Mammalian Cell Cycle Control and DNA Repair Systems. *Molecular Biology of the Cell*, 10(8):2703–2734.

[Komarov and Pikovsky, 2014] Komarov, M. and Pikovsky, A. (2014). The kuramoto model of coupled oscillators with a bi-harmonic coupling function. *Physica D: Nonlinear Phenomena*, 289:18–31.

[Komarov and Pikovsky, 2015] Komarov, M. and Pikovsky, A. (2015). Finite-size-induced transitions to synchrony in oscillator ensembles with nonlinear global coupling. *Physical Review E*, 92(2):020901.

[Kovalenko et al., 2021] Kovalenko, K., Dai, X., Alfaro-Bittner, K., Raigorodskii, A., Perc, M., and Boccaletti, S. (2021). Contrarians Synchronize beyond the Limit of Pairwise Interactions. *Physical Review Letters*, 127(25):258301.

[Kudela et al., 2003] Kudela, P., Franaszczuk, P. J., and Bergey, G. K. (2003). Changing excitation and inhibition in simulated neural networks: effects on induced bursting behavior. *Biological Cybernetics*, 88(4):276–285.

[Kuramoto, 1984] Kuramoto, Y. (1984). *Chemical Oscillations, Waves, and Turbulence*. Springer Berlin Heidelberg.

[Kádár et al., 1997] Kádár, S., Amemiya, T., and Showalter, K. (1997). Reaction Mechanism for Light Sensitivity of the Ru(bpy)32+-Catalyzed BelousovZhabotinsky Reaction. *The Journal of Physical Chemistry A*, 101(44):8200.

[Ladyman et al., 2013] Ladyman, J., Lambert, J., and Wiesner, K. (2013). What is a complex system? *European Journal for Philosophy of Science*, 3(1):33–67.

[Lapicque, 1907] Lapicque, L. (1907). Recherches quantitatives sur l'excitation electrique des nerfs. *J Physiol Paris*, 9:620–635.

[Lee, 2015] Lee, F. E. (2015). How Party Polarization Affects Governance. *Annual Review of Political Science*, 18(1):261–282.

[Lehnertz and Elger, 1998] Lehnertz, K. and Elger, C. E. (1998). Can Epileptic Seizures be Predicted? Evidence from Nonlinear Time Series Analysis of Brain Electrical Activity. *Physical Review Letters*, 80(22):5019–5022.

[Lelkes, 2016] Lelkes, Y. (2016). Mass Polarization: Manifestations and Measurements. *Public Opinion Quarterly*, 80(S1):392–410.

[Lenton et al., 2008] Lenton, T. M., Held, H., Kriegler, E., Hall, J. W., Lucht, W., Rahmstorf, S., and Schellnhuber, H. J. (2008). Tipping elements in the Earth's climate system. *Proceedings of the National Academy of Sciences*, 105(6):1786–1793.

[Lenton et al., 2019] Lenton, T. M., Rockström, J., Gaffney, O., Rahmstorf, S., Richardson, K., Steffen, W., and Schellnhuber, H. J. (2019). Climate tipping points — too risky to bet against. *Nature*, 575(7784):592–595.

USC UNIVERSIDADE DE SANTIAGO DE COMPOSTELA

[Li and Erneux, 1993] Li, R.-d. and Erneux, T. (1993). Stability conditions for coupled lasers: series coupling versus parallel coupling. *Optics Communications*, 99(3):196–200.

[Lin et al., 2020] Lin, Q., Zhao, S., Gao, D., Lou, Y., Yang, S., Musa, S. S., Wang, M. H., Cai, Y., Wang, W., Yang, L., and He, D. (2020). A conceptual model for the coronavirus disease 2019 (COVID-19) outbreak in Wuhan, China with individual reaction and governmental action. *International Journal of Infectious Diseases*, 93:211–216.

[Lloyd, 1995] Lloyd, A. L. (1995). The coupled logistic map: a simple model for the effects of spatial heterogeneity on population dynamics. *Journal of Theoretical Biology*, 173(3):217–230.

[Lorenz, 1963] Lorenz, E. N. (1963). Deterministic nonperiodic flow. *Journal of atmospheric sciences*, 20(2):130–141.

[Lotka, 1925] Lotka, A. J. (1925). Elements of Physical Biology. *Williams Wilkins*.

[Lüdecke and von dem Knesebeck, 2020] Lüdecke, D. and von dem Knesebeck, O. (2020). Protective Behavior in Course of the COVID-19 Outbreak—Survey Results From Germany. *Frontiers in Public Health*, 8.

[MacKay, 2008] MacKay, R. S. (2008). Nonlinearity in complexity science. *Nonlinearity*, 21(12):T273.

[Makki et al., 2014] Makki, R., Muñuzuri, A. P., and Perez-Mercader, J. (2014). Periodic perturbation of chemical oscillators: entrainment and induced synchronization. *Chemistry (Weinheim an Der Bergstrasse, Germany)*, 20(44):14213–14217.

[Mantegna and Stanley, 2000] Mantegna, R. N. and Stanley, H. E. (2000). *An Introduction to Econophysics: Correlations and Complexity in Finance*. Cambridge University Press. Google-Books-ID: VLBXoAEACAAJ.

[Martens et al., 2009] Martens, E. A., Barreto, E., Strogatz, S. H., Ott, E., So, P., and Antonsen, T. M. (2009). Exact results for the Kuramoto model with a bimodal frequency distribution. *Physical Review E*, 79(2):026204.

[Martín et al., 2011] Martín, G., Marinescu, M.-C., Singh, D. E., and Carretero, J. (2011). Leveraging social networks for understanding the evolution of epidemics. *BMC Systems Biology*, 5(Suppl 3):S14.

[Martínez et al., 2016] Martínez, E. R., Gisbert, F. J. G., and Martí, I. C. (2016). *Delimitacion de areas rurales y urbanas a nivel local*. Fundacion BBVA, Bilbao.

[Masia et al., 2001] Masia, M., Marchettini, N., Zambrano, V., and Rustici, M. (2001). Effect of temperature in a closed unstirred Belousov–Zhabotinsky system. *Chemical Physics Letters*, 341:285–291.

[May, 1973] May, R. M. (1973). *Stability and Complexity in Model Ecosystems*. Princeton University Press.

usc UNIVERSIDADE DE SANTIAGO DE COMPOSTELA

[McCarty et al., 2006] McCarty, N., Poole, K. T., and Rosenthal, H. (2006). *Polarized America: The Dance of Ideology and Unequal Riches*. Walras-Pareto Lectures. MIT Press, Cambridge, MA, USA.

[McPherson et al., 2001] McPherson, M., Smith-Lovin, L., and Cook, J. M. (2001). Birds of a feather: Homophily in social networks. *Annual Review of Sociology*, 27(1):415–444.

[Meloni et al., 2011] Meloni, S., Perra, N., Arenas, A., Gómez, S., Moreno, Y., and Vespignani, A. (2011). Modeling human mobility responses to the large-scale spreading of infectious diseases. *Scientific Reports*, 1(1).

[Mersing et al., 2021] Mersing, D., Tyler, S. A., Ponboonjaroenchai, B., Tinsley, M. R., and Showalter, K. (2021). Novel modes of synchronization in star networks of coupled chemical oscillators. *Chaos: An Interdisciplinary Journal of Nonlinear Science*, 31(9):093127.

[Mimar et al., 2019] Mimar, S., Juane, M. M., Park, J., Muñuzuri, A. P., and Ghoshal, G. (2019). Turing patterns mediated by network topology in homogeneous active systems. *Physical Review E*, 99(6):062303.

[Mitchell and Mitchell, 2011] Mitchell, M. and Mitchell, M. (2011). *Complexity: A Guided Tour*. Oxford University Press, Oxford, New York.

[Moore and Newman, 2000] Moore, C. and Newman, M. E. (2000). Epidemics and percolation in small-world networks. *Physical Review. E, Statistical Physics, Plasmas, Fluids, and Related Interdisciplinary Topics*, 61(5 Pt B):5678–5682.

[Morales et al., 2015] Morales, A. J., Borondo, J., Losada, J. C., and Benito, R. M. (2015). Measuring political polarization: Twitter shows the two sides of Venezuela. *Chaos*, 25(3):033114. WOS:000352314600015.

[Murray, 2002] Murray, J. D., editor (2002). *Mathematical Biology I. An Introduction*. Springer New York.

[Murray, 2003] Murray, J. D., editor (2003). *Mathematical Biology II. Spatial models and biomedical applications*. Springer New York.

[Muto et al., 2020] Muto, K., Yamamoto, I., Nagasu, M., Tanaka, M., and Wada, K. (2020). Japanese citizens' behavioral changes and preparedness against COVID-19: An online survey during the early phase of the pandemic. *PLOS ONE*, 15(6):e0234292.

[Muñuzuri et al., 1996] Muñuzuri, A. P., Davydov, V. A., Gómez-Gesteira, M., Pérez-Muñuzuri, V., and Pérez-Villar, V. (1996). Frequency-modulated autowaves in excitable media. *Physical Review E*, 54(6):R5921–R5924.

[Muñuzuri and Markus, 1997] Muñuzuri, A. P. and Markus, M. (1997). Simple optical feedback loop: Excitation waves and their mirror image. *Physical Review E*, 55(1):R33–R35.

[Muñuzuri and Pérez-Mercader, 2017] Muñuzuri, A. P. and Pérez-Mercader, J. (2017). Noise-Induced and Control of Collective Behavior in a Population of Coupled Chemical Oscillators. *The Journal of Physical Chemistry A*, 121(9):1855–1860.

USC UNIVERSIDAD DE SANTIAGO DE COMPOSTELA

[Muñuzuri and Pérez-Mercader, 2022] Muñuzuri, A. P. and Pérez-Mercader, J. (2022). Unified representation of Life's basic properties by a 3-species Stochastic Cubic Autocatalytic Reaction-Diffusion system of equations. *Physics of Life Reviews*, 41:64–83.

[Muñuzuri et al., 1997] Muñuzuri, A. P., Pérez-Villar, V., and Markus, M. (1997). Splitting of Autowaves in an Active Medium. *Physical Review Letters*, 79(10):1941–1944.

[Nakao and Mikhailov, 2010] Nakao, H. and Mikhailov, A. S. (2010). Turing patterns in network-organized activator–inhibitor systems. *Nature Physics*, 6(7):544–550.

[Ndaïrou et al., 2020] Ndaïrou, F., Area, I., Nieto, J. J., and Torres, D. F. (2020). Mathematical modeling of COVID-19 transmission dynamics with a case study of wuhan. *Chaos, Solitons & Fractals*, 135:109846.

[Newman, 2003] Newman, M. E. J. (2003). Properties of highly clustered networks. *Physical Review E*, 68(2):026121.

[Newman, 2011] Newman, M. E. J. (2011). Resource Letter CS–1: Complex Systems. *American Journal of Physics*, 79(8):800–810.

[Ni and Weng, 2009] Ni, S. and Weng, W. (2009). Impact of travel patterns on epidemic dynamics in heterogeneous spatial metapopulation networks. *Physical Review. E, Statistical, Nonlinear, and Soft Matter Physics*, 79(1 Pt 2):016111.

[Ni et al., 2011] Ni, S., Weng, W., and Zhang, H. (2011). Modeling the effects of social impact on epidemic spreading in complex networks. *Physica A: Statistical Mechanics and its Applications*, 390(23):4528–4534.

[Nishikawa and Motter, 2015] Nishikawa, T. and Motter, A. E. (2015). Comparative analysis of existing models for power-grid synchronization. *New Journal of Physics*, 17(1):015012.

[Okuda, 1993] Okuda, K. (1993). Variety and generality of clustering in globally coupled oscillators. *Physica D: Nonlinear Phenomena*, 63(3):424–436.

[Olmi et al., 2014] Olmi, S., Navas, A., Boccaletti, S., and Torcini, A. (2014). Hysteretic transitions in the Kuramoto model with inertia. *Physical Review E*, 90(4):042905.

[Othmer and Scriven, 1971] Othmer, H. G. and Scriven, L. E. (1971). Instability and dynamic pattern in cellular networks. *Journal of Theoretical Biology*, 32(3):507–537.

[O'Keeffe et al., 2017] O'Keeffe, K. P., Hong, H., and Strogatz, S. H. (2017). Oscillators that sync and swarm. *Nature Communications*, 8(1):1504.

[Paramés-Estévez et al., 2023] Paramés-Estévez, S., Carballosa, A., Garcia-Selfa, D., and Munuzuri, A. P. (2023). Artificial Intelligence Techniques Used to Extract Relevant Information from Complex Social Networks. *Entropy*, 25(3):507.

[Pastor-Satorras et al., 2015] Pastor-Satorras, R., Castellano, C., Mieghem, P. V., and Vespignani, A. (2015). Epidemic processes in complex networks. *Reviews of Modern Physics*, 87(3):925–979.

USC DE COMPOSTELA

[Pazó and Montbrió, 2009] Pazó, D. and Montbrió, E. (2009). Existence of hysteresis in the Kuramoto model with bimodal frequency distributions. *Physical Review E*, 80(4):046215.

[Pecora and Carroll, 1990] Pecora, L. M. and Carroll, T. L. (1990). Synchronization in chaotic systems. *Physical Review Letters*, 64(8):821–824.

[Pecora and Carroll, 1991] Pecora, L. M. and Carroll, T. L. (1991). Driving systems with chaotic signals. *Physical Review A*, 44(4):2374–2383.

[Pecora and Carroll, 1998] Pecora, L. M. and Carroll, T. L. (1998). Master Stability Functions for Synchronized Coupled Systems. *Physical Review Letters*, 80(10):2109–2112.

[Pereira et al., 2016] Pereira, F. S., de Amo, S., and Gama, J. (2016). Evolving Centralities in Temporal Graphs: A Twitter Network Analysis. In *2016 17th IEEE International Conference on Mobile Data Management (MDM)*, volume 2, pages 43–48. ISSN: 2375-0324.

[Perez and Dragicevic, 2009] Perez, L. and Dragicevic, S. (2009). An agent-based approach for modeling dynamics of contagious disease spread. *International Journal of Health Geographics*, 8(1):50.

[Perra, 2021] Perra, N. (2021). Non-pharmaceutical interventions during the COVID-19 pandemic: A review. *Physics Reports*, 913:1–52.

[Pessoa, 2021] Pessoa, L. (2021). Complex Systems: The Science of Interacting Parts. Technical report. type: article.

[Pires et al., 2018] Pires, M. A., Oestereich, A. L., and Crokidakis, N. (2018). Sudden transitions in coupled opinion and epidemic dynamics with vaccination. *Journal of Statistical Mechanics: Theory and Experiment*, 2018(5):053407.

[Poole and Rosenthal, 1983] Poole, K. and Rosenthal, H. (1983). The Polarization of American Politics. *The Journal of Politics*, 46.

[Prem et al., 2020] Prem, K., Liu, Y., Russell, T. W., Kucharski, A. J., Eggo, R. M., Davies, N., Flasche, S., Clifford, S., Pearson, C. A. B., Munday, J. D., Abbott, S., Gibbs, H., Rosello, A., Quilty, B. J., Jombart, T., Sun, F., Diamond, C., Gimma, A., van Zandvoort, K., Funk, S., Jarvis, C. I., Edmunds, W. J., Bosse, N. I., Hellewell, J., Jit, M., and Klepac, P. (2020). The effect of control strategies to reduce social mixing on outcomes of the COVID-19 epidemic in Wuhan, China: a modelling study. *The Lancet Public Health*, 5(5):e261–e270.

[Prigogine and Balescu, 1956] Prigogine, I. and Balescu, R. (1956). Phénomènes cycliques dans la thermodynamique des processus irréversibles. *Bulletins de l'Académie Royale de Belgique*, 42(1):256–265.

[Prior, 2013] Prior, M. (2013). Media and political polarization. *Annual Review of Political Science*, 16(1):101–127.

[Reddy et al., 1994] Reddy, M. K. R., Nagy-Ungvarai, Z., and Mueller, S. C. (1994). Effect of Visible Light on Wave Propagation in the Ruthenium-Catalyzed Belousov-Zhabotinsky Reaction. *The Journal of Physical Chemistry*, 98(47):12255–12259.

USC UNIVERSIDADE DE SANTIAGO DE COMPOSTELA

[Ricker, 1954] Ricker, W. E. (1954). Stock and Recruitment. *Journal of the Fisheries Research Board of Canada*, 11(5):559–623.

[Rosen, 1977] Rosen, R. (1977). Complexity as a System Property†. *International Journal of General Systems*, 3(4):227–232.

[Rosenblum and Pikovsky, 2003] Rosenblum, M. and Pikovsky, A. (2003). Synchronization: From pendulum clocks to chaotic lasers and chemical oscillators. *Contemporary Physics*, 44(5):401–416.

[Roy and Thornburg, 1994] Roy, R. and Thornburg, K. S. (1994). Experimental synchronization of chaotic lasers. *Physical Review Letters*, 72(13):2009–2012.

[Ruiz Baier and Tian, 2013] Ruiz Baier, R. and Tian, C. (2013). Mathematical analysis and numerical simulation of pattern formation under cross-diffusion. *Nonlinear Analysis Real World Applications*, 14.

[Ruoff, 1995] Ruoff, P. (1995). Antagonistic balance in the oregonator: about the possibility of temperature-compensation in the Belousov-Zhabotinsky reaction. *Physica D: Nonlinear Phenomena*, 84(1):204–211.

[Rössler, 1976] Rössler, O. E. (1976). An equation for continuous chaos. *Physics Letters A*, 57(5):397–398.

[Samoylenko et al., 2023] Samoylenko, I., Aleja, D., Primo, E., Alfaro-Bittner, K., Vasilyeva, E., Kovalenko, K., Musatov, D., Raigorodskii, A., Criado, R., Romance, M., Papo, D., Perc, M., Barzel, B., and Boccaletti, S. (2023). Why Are There Six Degrees of Separation in a Social Network? *Physical Review X*, 13(2):021032.

[Sayama et al., 2013] Sayama, H., Pestov, I., Schmidt, J., Bush, B. J., Wong, C., Yamanoi, J., and Gross, T. (2013). Modeling complex systems with adaptive networks. *Computers & Mathematics with Applications*, 65(10):1645–1664.

[Sendiña-Nadal et al., 1998] Sendiña-Nadal, I., Muñuzuri, A. P., Vives, D., Pérez-Muñuzuri, V., Casademunt, J., Ramírez-Piscina, L., Sancho, J. M., and Sagués, F. (1998). Wave Propagation in a Medium with Disordered Excitability. *Physical Review Letters*, 80(24):5437–5440.

[Silva et al., 2020] Silva, C. J., Cruz, C., Torres, D. F. M., Munuzuri, A. P., Carballosa, A., Area, I., Nieto, J. J., Fonseca-Pinto, R., da Fonseca, R. P., dos Santos, E. S., Abreu, W., and Mira, J. (2020). Optimal control of the covid-19 pandemic: controlled sanitary deconfinement in portugal.

[Silva et al., 2021] Silva, C. J., Cruz, C., Torres, D. F. M., Muñuzuri, A. P., Carballosa, A., Area, I., Nieto, J. J., Fonseca-Pinto, R., Passadouro, R., Santos, E. S. d., Abreu, W., and Mira, J. (2021). Optimal control of the COVID-19 pandemic: controlled sanitary deconfinement in Portugal. *Scientific Reports*, 11(1):3451.

[Skardal and Arenas, 2019] Skardal, P. S. and Arenas, A. (2019). Abrupt Desynchronization and Extensive Multistability in Globally Coupled Oscillator Simplexes. *Physical Review Letters*, 122(24):248301.

[Skardal and Arenas, 2020] Skardal, P. S. and Arenas, A. (2020). Higher order interactions in complex networks of phase oscillators promote abrupt synchronization switching. *Communications Physics*, 3(1):1–6.

[Sorrentino et al., 2007] Sorrentino, F., di Bernardo, M., Garofalo, F., and Chen, G. (2007). Controllability of complex networks via pinning. *Physical Review E*, 75(4):046103.

[Sporns et al., 2005] Sporns, O., Tononi, G., and Kötter, R. (2005). The Human Connectome: A Structural Description of the Human Brain. *PLOS Computational Biology*, 1(4):e42.

[Strogatz, 2003] Strogatz, S. (2003). *Sync: The Emerging Science of Spontaneous Order*. New York.

[Strogatz, 2000] Strogatz, S. H. (2000). From Kuramoto to Crawford: exploring the onset of synchronization in populations of coupled oscillators. *Physica D: Nonlinear Phenomena*, 143(1):1–20.

[Strogatz, 2001] Strogatz, S. H. (2001). Exploring complex networks. *Nature*, 410(6825):268–276.

[Strogatz, 2015] Strogatz, S. H. (2015). *Nonlinear Dynamics and Chaos: With Applications to Physics, Biology, Chemistry, and Engineering, Second Edition*. CRC Press, Boulder, CO, 2nd edition edition.

[Sugawara et al., 1994] Sugawara, T., Tachikawa, M., Tsukamoto, T., and Shimizu, T. (1994). Observation of synchronization in laser chaos. *Physical Review Letters*, 72(22):3502–3505.

[Sunstein, 2018] Sunstein, C. R. (2018). *#Republic: Divided Democracy in the Age of Social Media*. Princeton University Press.

[Tanaka and Aoyagi, 2011] Tanaka, T. and Aoyagi, T. (2011). Multistable Attractors in a Network of Phase Oscillators with Three-Body Interactions. *Physical Review Letters*, 106(22):224101.

[Tarasova and Tarasov, 2017] Tarasova, V. V. and Tarasov, V. E. (2017). Logistic map with memory from economic model. *Chaos, Solitons & Fractals*, 95:84–91.

[Taylor et al., 2009] Taylor, A. F., Tinsley, M. R., Wang, F., Huang, Z., and Showalter, K. (2009). Dynamical quorum sensing and synchronization in large populations of chemical oscillators. *Science*, 323(5914):614–617.

[Tinsley et al., 2012] Tinsley, M. R., Nkomo, S., and Showalter, K. (2012). Chimera and phase-cluster states in populations of coupled chemical oscillators. *Nature Physics*, 8(9):662–665.

[Tinsley et al., 2009] Tinsley, M. R., Taylor, A. F., Huang, Z., and Showalter, K. (2009). Emergence of collective behavior in groups of excitable catalyst-loaded particles: spatiotemporal dynamical quorum sensing. *Physical Review Letters*, 102(15):158301.

[Tinsley et al., 2010] Tinsley, M. R., Taylor, A. F., Huang, Z., Wang, F., and Showalter, K. (2010). Dynamical quorum sensing and synchronization in collections of excitable and oscillatory catalytic particles. *Physica D: Nonlinear Phenomena*, 239(11):785–790.

USC UNIVERSIDADE DE SANTIAGO DE COMPOSTELA

[Totz et al., 2018] Totz, J. F., Rode, J., Tinsley, M. R., Showalter, K., and Engel, H. (2018). Spiral wave chimera states in large populations of coupled chemical oscillators. *Nature Physics*, 14(3):282–285.

[Turing, 1952] Turing, A. M. (1952). The chemical basis of morphogenesis. *Philosophical Transactions of the Royal Society of London. Series B, Biological Sciences*, 237(641):37–72.

[Tyson, 1979] Tyson, J. J. (1979). Oscillations, Bistability, and Echo Waves in Models of the Belousov-Zhabotinskii Reaction*. *Annals of the New York Academy of Sciences*, 316(1):279–295.

[Vanag and Epstein, 2009] Vanag, V. K. and Epstein, I. R. (2009). Cross-diffusion and pattern formation in reaction–diffusion systems. *Physical Chemistry Chemical Physics*, 11(6):897–912.

[VanWiggeren and Roy, 1998] VanWiggeren, G. D. and Roy, R. (1998). Communication with chaotic lasers. *Science*, 279(5354):1198–1200.

[Vasiliev et al., 1987] Vasiliev, V. A., Romanovskii, Y. M., Chernavskii, D. S., and Yakhno, V. G. (1987). *Autowave Processes in Kinetic Systems*. Springer Netherlands.

[Vicario et al., 2016] Vicario, M. D., Bessi, A., Zollo, F., Petroni, F., Scala, A., Caldarelli, G., Stanley, H. E., and Quattrociocchi, W. (2016). The spreading of misinformation online. *Proceedings of the National Academy of Sciences*, 113(3):554–559.

[Villalón et al., 2021] Villalón, J. C., González, R. C. L., Carballada, M., and Cantos, J. O. (2021). Le Covid-19 en Espagne. Les défis géopolitiques de la gouvernance d'un problème de santé. *Herodote*, 183(4):197–225.

[Volterra, 1928] Volterra, V. (1928). Variations and fluctuations of the number of individuals in animal species living together. *ICES Journal of Marine Science*, 3(1):3–51.

[Wang et al., 2011] Wang, W., Lin, Y., Zhang, L., Rao, F., and Tan, Y. (2011). Complex patterns in a predator–prey model with self and cross-diffusion. *Communications in Nonlinear Science and Numerical Simulation*, 16(4):2006–2015.

[Watanabe and Strogatz, 1993] Watanabe, S. and Strogatz, S. H. (1993). Integrability of a globally coupled oscillator array. *Physical Review Letters*, 70(16):2391–2394.

[Watts et al., 2005] Watts, D. J., Muhamad, R., Medina, D. C., and Dodds, P. S. (2005). Multiscale, resurgent epidemics in a hierarchical metapopulation model. *Proceedings of the National Academy of Sciences*, 102(32):11157–11162.

[Watts and Strogatz, 1998] Watts, D. J. and Strogatz, S. H. (1998). Collective dynamics of 'small-world' networks. *Nature*, 393(6684):440–442.

[Weng et al., 2012] Weng, L., Flammini, A., Vespignani, A., and Menczer, F. (2012). Competition among memes in a world with limited attention. *Scientific Reports*, 2(1):335.

[Winfree, 1967] Winfree, A. T. (1967). Biological rhythms and the behavior of populations of coupled oscillators. *Journal of Theoretical Biology*, 16(1):15–42.

USC DE COMPOSTELA

[Winfree, 1984] Winfree, A. T. (1984). The prehistory of the Belousov-Zhabotinsky oscillator. *Journal of Chemical Education*, 61(8):661.

[Winfree, 2001] Winfree, A. T. (2001). *The Geometry of Biological Time*. Springer Science & Business Media. Google-Books-ID: 5YktgBuoglAC.

[Winful and Rahman, 1990] Winful, H. G. and Rahman, L. (1990). Synchronized chaos and spatiotemporal chaos in arrays of coupled lasers. *Physical Review Letters*, 65(13):1575–1578.

[Xiong and Li, 2017] Xiong, F. and Li, Z.-Y. (2017). Effective methods of restraining diffusion in terms of epidemic dynamics. *Scientific Reports*, 7(1).

[Xiong and Liu, 2014] Xiong, F. and Liu, Y. (2014). Opinion formation on social media: An empirical approach. *Chaos: An Interdisciplinary Journal of Nonlinear Science*, 24(1):013130.

[Xu et al., 2020a] Xu, C., Wang, X., and Skardal, P. S. (2020a). Bifurcation analysis and structural stability of simplicial oscillator populations. *Physical Review Research*, 2(2):023281.

[Xu et al., 2020b] Xu, H., Gan, Y., Zheng, D., Wu, B., Zhu, X., Xu, C., Liu, C., Tao, Z., Hu, Y., Chen, M., Li, M., Lu, Z., and Chen, J. (2020b). Relationship Between COVID-19 Infection and Risk Perception, Knowledge, Attitude, and Four Nonpharmaceutical Interventions During the Late Period of the COVID-19 Epidemic in China: Online Cross-Sectional Survey of 8158 Adults. *Journal of Medical Internet Research*, 22(11):e21372.

[Xue, 2012] Xue, L. (2012). Pattern formation in a predator–prey model with spatial effect. *Physica A: Statistical Mechanics and its Applications*, 391(23):5987–5996.

[Yamaguchi et al., 1991] Yamaguchi, T., Kuhnert, L., Nagy-Ungvarai, Z., Mueller, S. C., and Hess, B. (1991). Gel systems for the Belousov-Zhabotinskii reaction. *The Journal of Physical Chemistry*, 95(15):5831–5837.

[Yamamoto, 1991] Yamamoto, William S., T. B. A. (1991). *Ay's Neuroanatomy of C. Elegans for Computation*. CRC Press, Boca Raton.

[Yoshimoto et al., 1993] Yoshimoto, M., Yoshikawa, K., and Mori, Y. (1993). Coupling among three chemical oscillators: Synchronization, phase death, and frustration. *Physical Review E*, 47(2):864–874.

[Zanette, 2001] Zanette, D. H. (2001). Critical behavior of propagation on small-world networks. *Physical Review E*, 64(5):050901.

[Zemanová et al., 2006] Zemanová, L., Zhou, C., and Kurths, J. (2006). Structural and functional clusters of complex brain networks. *Physica D: Nonlinear Phenomena*, 224(1):202–212.

[Zhabotinskii, 1964] Zhabotinskii, A. M. (1964). Periodic course of the oxidation of malonic acid in a solution (studies on the kinetics of belousov's reaction. *Biofizika*, 9:306–311.

USC UNIVERSIDADE DE SANTIAGO DE COMPOSTELA

[Zhabotinsky and Zaikin, 1973] Zhabotinsky, A. M. and Zaikin, A. N. (1973). Autowave processes in a distributed chemical system. *Journal of Theoretical Biology*, 40(1):45–61.

[Zhan et al., 2018] Zhan, X.-X., Liu, C., Sun, G.-Q., and Zhang, Z.-K. (2018). Epidemic dynamics on information-driven adaptive networks. *Chaos, Solitons, and Fractals*, 108:196–204.

[Zhao et al., 2020] Zhao, Z.-Y., Zhu, Y.-Z., Xu, J.-W., Hu, S.-X., Hu, Q.-Q., Lei, Z., Rui, J., Liu, X.-C., Wang, Y., Yang, M., Luo, L., Yu, S.-S., Li, J., Liu, R.-Y., Xie, F., Su, Y.-Y., Chiang, Y.-C., Zhao, B.-H., Cui, J.-A., Yin, L., Su, Y.-H., Zhao, Q.-L., Gao, L.-D., and Chen, T.-M. (2020). A five-compartment model of age-specific transmissibility of SARS-CoV-2. *Infectious Diseases of Poverty*, 9(1):117.

[Zwillinger, 2014] Zwillinger, Daniel, S. K. (2014). *CRC Standard Probability and Statistics Tables and Formulae, Student Edition*. CRC Press, Boca Raton.

USC
UNIVERSIDADE DE SANTIAGO DE COMPOSTELA

USC
UNIVERSIDADE
DE SANTIAGO
DE COMPOSTELA





From the collective behavior of many coupled units results the spontaneous emergence of certain dynamic properties that tend to increase the order in the system, such as coherent oscillations, structured pattern formations and biological waves. In this thesis, we revolve around the idea that the communication among the elements of a system transforms them into parts of something greater. Using numerical models, theoretical analysis and experimental setups, here we study the interplay between complexity at the interaction level and the global properties of the system.